Fighting Fire with Format: Exploiting Autoantigen Delivery to Combat Autoimmunity

By

J. Daniel Griffin

Submitted to the graduate degree program in Bioengineering Graduate Program and the Graduate Faculty of the University of Kansas in partial fulfillment of the requirements for the degree of Doctor of Philosophy.

_____

Chair: Dr. Cory Berkland

_____

Dr. Brandon DeKosky

_____

Dr. Prajna Dhar

_____

Dr. A.J. Mellott

_____

Dr. Elizabeth Friis

Date Defended: December 13th, 2019

The dissertation committee for J. Daniel Griffin certifies that this is the approved version of the following dissertation:

Fighting Fire with Format: Exploiting Autoantigen Delivery to Combat Autoimmunity

_____

Chairperson Dr. Cory Berkland

Date Approved: December 13th, 2019

Abstract

There is a dire need for next-generation approaches to treating autoimmune disease that can potently inhibit the autoreactive destruction of host tissue while conserving protective immune functions. Antigen-specific immunotherapies (ASIT) offer such promise by harnessing the same pathogenic epitopes attacked in autoimmunity to selectively suppress the autoreactive cells that cause disease. Formatting autoantigen for ASIT is not trivial, as no clinical immunotherapies of this class are currently approved for treating autoimmune disease despite decades of attempts. This dissertation sought to explore physical and chemical determinants of efficacy in ASITs as a contribution toward fostering a future of precisely tailored autoimmune interventions. In these works, three autoantigen formats are explored: soluble, particulate, and surface delivery – each within the context of murine experimental autoimmune encephalomyelitis (EAE). In chapter 2, the soluble antigen array (SAgA) was adopted as a platform to investigate the role of antigen valency in evoking B cell anergy to promote tolerance among mixed splenocytes. Analysis of SAgAs presenting discrete autoantigen valencies revealed that low-valency (but not monovalent) autoantigen was most capable of inhibiting B cell calcium mobilization, and this inhibition predicted tolerogenic effects in a mixed population of splenocytes. In chapter 3, particulate autoantigen delivery was explored by formulating a "functional" delivery system consisting of an antioxidant vitamin E emulsion. This formulation proved capable to suppress EAE *in vivo*, but mechanistic analyses suggested a driver of effect that differed from the originally hypothesized antioxidant function. These results motivated the invention of the antigen-specific immune decoys (ASIDs) reported in chapters 4 and 5. ASIDs were comprised of autoantigen restricted onto the surface of microporous collagenous biomaterials. Peptide-epitope decorated constructs prevented EAE *in vivo* by intercepting and exhausting autoreactive cells. Chapter 5 was an extension of this

work, where polyantigenic ASIDs were fabricated to present a comprehensive palette of autoantigens and account for the heterogeneity of authentic disease. Though capable of amplifying discrete antigen-specific cell subsets *ex vivo*, polyantigenic ASIDs apparently did not induce cellular exhaustion and failed to attenuate EAE as a result. Together, these works emphasize the importance of characteristics such as antigen valency and context. The ongoing exploration of the ASID platform provides a foundation for assessing the utility of engineered local microenvironments in immune-mediated disease.

Acknowledgments

Above all, thanks be to God. He is my strong tower and the light to my path.

I am forever indebted to the people who believed in me both leading up to and during my time as a Jayhawk; It is because of you that this dissertation was ever possible. It would be impossible to recount all of the ways that friends, peers, and mentors enabled this journey, but I will attempt to note a few here.

It is with tremendous gratitude that I thank my PhD advisor, Dr. Cory Berkland. Cory, you modeled for me what it means to be a man of intentionality, integrity, and tact in this field. You took me into your lab when I had little to offer, and I will never forget this outpouring of generosity you demonstrated to me. You taught me to internally define and strive for my own success in a world that longs for external laudations. Thank you for your guidance, investment, and friendship over the past four and a half years. I have immensely valued our conversations together.

Thank you to my parents, Richard and Teresa Griffin. Dad, you spoke encouragement into me from a very young age and instilled in me an appreciation for the true value of exceptional effort. Mom, you constantly and selflessly demonstrated sacrificial love to my siblings and I, and because of it we are able to chase our dreams today.

I am monumentally grateful to Madison 'Al' and Lila Self their gift that is the Self Graduate Fellowship. It is only because of their endless generosity and vision that I was able to complete this dissertation, both in the first place, but especially with the experiences and development that have prepared me to "make a real difference". Thank you to the fellowship staff for your dedication and for giving me the opportunity to participate in this extraordinary program. Fellow fellows, it has been tremendous to grow with you over the past four years and I am forever grateful for the relationships we have built together.

There is no lab quite like the Berkland lab - thank you to the lab mates who have made this such an enjoyable ride and have helped me so very much along the way. Jian Qian, Brad Sullivan, Brittany Hartwell, Lorena Napolitano, Chad Pickens, Shara Thati, Laura Northrup, Martin Leon, Matt Christopher, Jimmy Song, Melissa Mihalcin, Stephanie Johnson, Aric Huang, Sebastian Huayamares, Kyle Apley, Justin Ruffalo, Aparna Chakravarti, Mary Duncan, Bryce Stottlemire, Dakota Even, and Jon Whitlow, you have all enriched my graduate school experience beyond measure. Thank you as well to Michael Shao, Alex Sedlacek, and Deanna Diaz - the talented undergraduate students I had the privilege to work directly with.

Wally Meyer, thank you for the mentorship and support you invested into me. I am indebted to you for the thoughtful questions and careful attention you gave me in encouraging the tangible realization of Exodus Biosciences.

Thank you to Dr. Steve Jacobson. You took me in and showed me an entirely new world of research at the National Institutes of Health.

The School of Engineering have been greatly supportive over my time as a graduate student. I am fortunate to have been able to work with Anna Paradis and Lynn Villafuerte as a graduate engineering ambassador, and special thanks go to Denise Bridwell for ensuring the success of me, along with all the other students of the Bioengineering Graduate Program.

To my doctoral committee – Dr. Brandon DeKosky, Dr. Prajna Dhar, Dr. AJ Mellott, and Dr. Lisa Friis – thank you for your time, dedication, and feedback in edifying my development as a scientist and the dissertation herein.

This dissertation is dedicated to my mother and her battle with multiple sclerosis.

Table of Contents

1. Introduction 1

1.1 Autoantigen format directs the immune response: lessons from the clinic 2

1.2 Peripheral Autoimmunity is a Vicious Cycle 4

1.3 Route and Size -Dependent Biotransport Dictates the Destination of Parenterally Delivered Compounds. 7

1.4 Allergy Immunotherapies as the Foundation for Antigen-Specific Approaches to Autoimmunity. 12

1.5 Autoantigens Embody Physicochemical Profiles that Differ from Allergens 16

1.6 Immunological Fates for Delivered Autoantigen are Determined by Format 20

1.6.1 Systemic Drainage 22

1.6.2 Lymphatic Transport 22

1.6.3 Injection Site Retention 23

1.7 Strategies for Circumventing Delivery and Distribution Obstacles 24

1.7.1 Intranodal delivery 24

1.7.2 Transdermal delivery 25

1.8 Next-Generation Approaches to Formatting Autoantigen for Optimizing ASIT 25

1.8.1 Soluble Delivery 26

1.8.2 Colloidal Delivery 26

1.8.3 Depot Delivery 27

1.9 Conclusions 27

1.10 References 28

2. Acute B-Cell Inhibition by Soluble Antigen Arrays is Valency-Dependent and Predicts Immunomodulation in Splenocytes 35

2.1 Introduction 36

2.2 Materials and Methods 38

2.2.1 Materials 38

2.2.2 Synthesis and Characterization of Varied Valency Conjugates 39

2.2.3 Raji B Cell Culture 39

2.2.4 Induction of EAE 40

2.2.5 Spleen Harvest and Splenocyte Isolation 40

2.2.6 Fluorescent Staining and Flow Cytometry 41

2.2.7 Measurement of Cytokines 41

2.2.8 Measurement of Cellular Metabolism 42

2.2.9 Statistical Analysis 42

2.3 Results 42

2.3.1 Synthesis of Varied-Valency Conjugates 42

2.3.2 Inhibition of Short-Term B-cell Response is Valency-Dependent. 44

2.3.3 Low-Valency Conjugates Induce Downstream Anergy in Mixed EAE Splenocytes. 46

2.4 Discussion 50

2.5 Conclusions 54

2.6 Supporting Information 55

2.7 Acknowledgments 60

2.8 References 60

3. Tocopherol Emulsions as Functional Autoantigen Delivery Vehicles Evoke Therapeutic Efficacy in Experimental Autoimmune Encephalomyelitis 64

3.1 Introduction 65

3.2 Materials and Methods 67

3.2.1 Materials 67

3.2.2 Preparation of ETPGS Emulsions 68

3.2.3 Characterizing Size and Peptide Release from ETPGS Emulsions 69

3.2.4 Measurement of ETPGS Antioxidant Power 70

3.2.5 Acute Antioxidant Effect in a Model APC 70

3.2.6 Induction of EAE and Therapeutic Study 71

3.2.7 Tissue Harvest and Splenocyte Isolation 72

3.2.8 Measurement of Cytokines 72

3.2.9 Measurement of Cellular Metabolism 73

3.2.10 Fluorescent Staining and Flow Cytometry 73

3.2.11 Detection of Anti-PLP IgG 74

3.2.12 Statistical Analysis 74

3.3 Results 74

3.3.1 Characterization of the ETPGS Formulation 75

3.3.2 ETPGS influences oxidative stress in vitro 77

3.3.3 ETPGS-facilitated autoantigen delivery delays and suppresses EAE in vivo 79

3.3.4 Ex vivo splenocyte cytokines and populations in ETPGS+PLP efficacy 81

3.3.5 Autoantibodies are largely restricted to the periphery in mice treated with ETPGS+PLP 85

3.4 Discussion 86
3.5 Conclusions 89
3.6 Supporting Information 90
3.7 Acknowledgments 92
3.8 References 93
4. Antigen-Specific Immune Decoys Intercept and Exhaust Autoimmunity to Prevent Disease 98
4.1 Introduction 99
4.2 Materials and Methods 101
4.2.1 Materials 101
4.2.2 Synthesis of ASIDs 102
4.2.3 Characterizing ASIDs 103
4.2.4 Induction of EAE and Therapeutic Study 103
4.2.5 Detection of Anti-PLP IgG 104
4.2.6 Spleen Harvest and Splenocyte Isolation 104
4.2.7 Sponge Harvest and Spongeocyte Isolation 105
4.2.8 Fluorescent Staining and Flow Cytometry 105
4.2.9 Measurement of Cellular Metabolism 106
4.2.10 Measurement of Cytokines 106
4.2.11 Histology 106
4.2.12 Statistical Analysis 106
4.3 Results 107
4.3.1 Synthesis and Functional Characterization of ASIDs 107

4.3.2 Subcutaneous Implantation of ASIDs prevents EAE in vivo 109
4.3.3 ASID Infiltrates undergo Apoptosis upon PLP Rechallenge 112
4.3.4 ASIDs Return Exhausted Immune Cells to Secondary Lymphoid Organs 115
4.3.5 Antigen-Specific Exhaustion Persists after PLP rechallenge 118
4.3.6 Pro-inflammatory Cytokines are Elevated in ASID-Treated Splenocytes at Day 14 and 25 121
4.4 Discussion 124
4.5 Conclusions 127
4.6 Supplementary Information 127
4.7 Acknowledgements 138
4.8 References 138
5. Polyantigenic Immune Decoys Amplify Antigen-Specific Cell Populations but do not Suppress Experimental Autoimmune Encephalomyelitis 143
5.1 Introduction 144
5.2 Materials and Methods 146
5.2.1 Materials 147
5.2.2 Preparation of Gelatin Methacrylate 148
5.2.3 Fabrication of Homogenate-GelMA Scaffolds 148
5.2.4 Synthesis of plpGelatin Materials 148
5.2.5 Characterizing Complex Decoys 149
5.2.6 Retained Antigen-Specificity Analysis 149
5.2.7 Induction of EAE and Therapeutic Study 150
5.2.8 Detection of Anti-PLP IgG 150

5.2.9 Spleen Harvest and Splenocyte Isolation 151
5.2.10 Ex Vivo Screening with EAE Splenocytes 151
5.2.11 Fluorescent Staining and Flow Cytometry 152
5.2.12 Resazurin Cell Metabolism Assay 152
5.2.13 Statistical Analysis 152
5.3 Results 152
5.3.1 Fabrication of Complex Decoys 152
5.3.2 mbhGelatin Decoys are Persistent Depots that Incorporate Primary Tissue Homogenate and Retain Antigen-Specificity 154
5.3.3 mbhGelatin Decoys Elicit a Cellular Response and Amplify Antigen-Specific B cells ex vivo 157
5.3.4 EAE splenocytes are largely unchanged by prophylactic mbhGelatin implantation 161
5.4 Discussion 164
5.5 Conclusions 168
5.6 Acknowledgments 168
5.7 References 168
6. Conclusions and Future Directions 172
6.1 Conclusions 173
6.2 Future Directions 176

1. Introduction

As prepared for peer-reviewed submission

Griffin, J. Daniel, Jimmy Y. Song, Brandon J. DeKosky, and Cory J. Berkland. "Autoantigen format directs the immune response: lessons from the clinic." *Manuscript in Preparation* (2019).

1.1 Autoantigen format directs the immune response: lessons from the clinic

Autoimmune disease has long persisted as a difficult and costly problem in modern medicine. Indeed, the American Autoimmune Related Diseases Association estimates that these diseases such as Multiple Sclerosis (MS), Type 1 Diabetes (T1D), and nearly one hundred others collectively affect over 50 million Americans and cost upwards of $100 billion to treat each year. A major criticism of this exorbitant treatment burden is that it does not adequately stifle disease presentations; contemporary therapeutics largely serve only to suppress symptoms without addressing the causative factors that drive autoimmunity[1, 2]. In this review, we will explore biotransport considerations for antigen-specific immunotherapies (ASIT) and glean insights for designing safe and potent autoimmune treatments. We will begin by analyzing the physicochemical properties of several predominant allergens, as desensitization therapies have provided the foundation for ASITs. We will highlight key differences between these properties and those of autoantigens to suggest design parameters for ASITs of the future to ultimately optimize clinical success.

Prevailing treatment strategies across many autoimmune diseases involve the administration of immunosuppressive drugs. These compounds broadly compromise host immunity – healthy and aberrant alike[3]. While the virtue of these approaches is a slowing of disease progression, a steep tradeoff demanded by these routes is the ablation of protective immune function as well[4]. Glucocorticoids have been widely applied to suppress inflammatory function against a plethora of autoimmune diseases, though they are marked by increased patient susceptibility to infection[5]. In MS, natalizumab is proven to significantly reduce relapse rates, however this monoclonal antibody is also well known for imposing the risk of progressive multifocal leukoencephalopathy (PML) - a life-threatening result of the opportunistic JC virus

becoming activated[6]. Similarly severe risks exist with Rituxumab, a B-cell depleting immunotherapy that has been deployed for a plurality of autoimmune diseases such as Rheumatoid Arthritis (RA), T1D, and MS[7].

The push for precision medicine is a major initiative that has built excitement and momentum especially in the arena of cancer, but it likewise captivates immense promise for autoimmunity[8, 9]. Breakthroughs of precision approaches to cancer have come by way of leveraging the genetic anomalies that are hallmark of specific kinds of tumors. Capitalizing on these discrepancies has enabled the design of delivery systems that can specifically target and eliminate malignancies with potent chemotherapeutics, and these approaches have radically transformed previously hopeless prognoses[10, 11]. Autoimmunity, however, has yet to see clinical success stories in the form of precision medicines. This setback is in part due to the fact that unlike cancers, the autoreactive cells that perpetuate disease can be phenotypically indistinguishable from healthy immune cells. The result has been an absence of targeted immunotherapies for autoimmune disease. Even Ocrelizumab, one recently approved drug for MS, works by broadly deleting B cells from patients[12]. Although more targeted, this approach has already been plagued by the same kinds of adversities as its predecessors from past decades[13, 14].

Though autoimmune cells can appear similar to typical functional immune cell types, their detrimentality can be defined by a fundamental difference in the antigen receptor specificity[15, 16]. The immune system serves to exact homeostasis by maintaining recognition of "self" and "non-self" antigens through highly specific T cell and B cell receptors (TCRs and BCRs, respectively)[17]. In the development of healthy immune cell progenitors, antigen receptors are selected by positive- and negative-filtering checkpoints[18, 19]. These tolerance mechanisms typically serve to remove or inactivate autoreactive T and B cells, though they are indelibly compromised when autoimmunity

ensues[20, 21]. Antigen-specific immunotherapy (ASIT) invokes a meaningful stride toward precision in treating autoimmunity through the promise of selectively targeting cells that escape tolerance[22].

ASITs, in the context of autoimmunity, direct immunomodulation to the autoreactive cells that propagate disease[23]. This precision is accomplished by delivering formulations that incorporate the very same autoantigens responsible for the self-directed tissue destruction taking place. While the precision implications of ASITs are readily grasped from the cell-targeting that comes from delivering autoantigen, deeper mechanistic characteristics are critical to consider. Autoantigens and their constitutive epitopes widely vary in terms of physicochemical properties such as size, charge, and solubility, and these differences can vastly impact the way ASIT formulations are trafficked throughout the body and elicit effect[24]. In this review, we explore these physicochemical drivers of effect that hold great importance for the design of effective ASITs with potential for treating authentic human disease.

1.2 Peripheral Autoimmunity is a Vicious Cycle

To understand antigen-specific approaches for the desensitization of aberrant autoimmunity, we must first review the underpinning mechanisms that propagate disease in the first place. In the cycle of autoimmunity, the faulty immune response is primed in secondary lymphoid organs and exacted in tissue compartments rich with cognate autoantigens (**Fig. 1**)[25]. In the origination of autoimmune destruction, an initial or ongoing insult disrupts tissue (**Fig. 1.1**)[26]. Damaged tissue both releases autoantigen and provokes innate arms of the immune system. Disrupted autoantigen is able to passively or actively drain to lymphoid organs (**Fig. 1.2a**) by following transport phenomena that will be covered in greater depth later on (**Fig. 2**). Also, however, innate arms of immunity are engaged through the tissue compartment becomes an

inflammatory microenvironment (**Fig. 1.2b**). Tissue damage generates a host of immune-boosting cues including reactive oxygen species and damage-associated molecular patterns that stimulate sentinel cells such as dendritic cells (DCs), macrophages (mφ), and monocytes to take up antigen and become activated[27]. With this activation comes a subsequent migration to regional lymph nodes; "active transport" implies antigen conveyed by this mechanism. (**Fig. 3**).

Once at the lymph node, autoantigen may undergo further processing to reach the T and B cell zones[28]. In these locales, follicular antigen presenting cells are capable to present autoantigen to cognate naïve CD4+ T helper cells (**Fig. 1.4**). Naïve T helper cells will become stimulated if antigen presentation occurs with the simultaneous ligation of B7 pathway surface proteins[29]. These proteins include CD80 and CD86 on the surface of antigen presenting B cells and DCs which can bind CD28 on T cells to propagate their activation[30]. Depending on T helper subtype and intranodal cues such as cytokines, these activated cells are compelled to proliferate and promote an effector-driven immune response through receptor and cytokine signaling (**Fig. 4.5**)[31]. While a plethora of finely-tuned antigen-specific effector responses can ensue, they can broadly be categorized by cellular or humoral responses in nature. Cellular immune responses are characterized by T helper 1 and 17 type responses which are recognizable by secreted inflammatory cytokines such as IL-2, IFN-γ, TNF-α, IL-23 and IL-17[32, 33]. Responses of this nature are most commonly indicated in autoimmune disease, as they stimulate phagocytic innate immune cells such as mφ to engulf target cells or debris[34]. Humoral immune responses recruit B cells into the effector response; these directive signals promoted through cytokines such as IL-4, IL-6, and IL-10 trigger antibody secretion by terminally differentiated plasma cells[35]. The ensuing antibody production is efficient to bind and label free antigen. Humoral immunity is recognized to play an increasingly important role in some autoimmune diseases such as Neuromyelitis Optica and MS[36, 37].

Nevertheless, when effector responses are triggered, these activated cells home back to antigen-rich compartments to cause autoreactive damage and reinitiate the autoimmune cycle once more by renewing the production of immunogenic factors (**Fig. 1.6**)[38]. The cyclic nature of autoimmune potentiation may illustrate the relapsing-remitting pattern followed by many of these diseases. However, this thematic scheme likewise demonstrates the potential for ASIT to influence the immune system. Antigen processing, presentation, and signaling occurs in secondary lymphoid organs, and these tissues represent a priority target in modulating the aberrant response. It is critical to target ASIT to the lymphatics not just for their directive role in propagating immunity, but also for the inherent probability of interacting with T and B cells that possess cognate antigen receptors. The body has an estimated $10^{12\text{-}18}$ discrete theoretical T and B cell receptor specificities[39-41] . In peripheral blood, only 2% of all lymphocytes are estimated to be circulating at any given time[42]. Since an overwhelming majority of clonalities are present in the lymphatics, the importance of reaching these organs to evoke potent, successful effects is yet further emphasized.

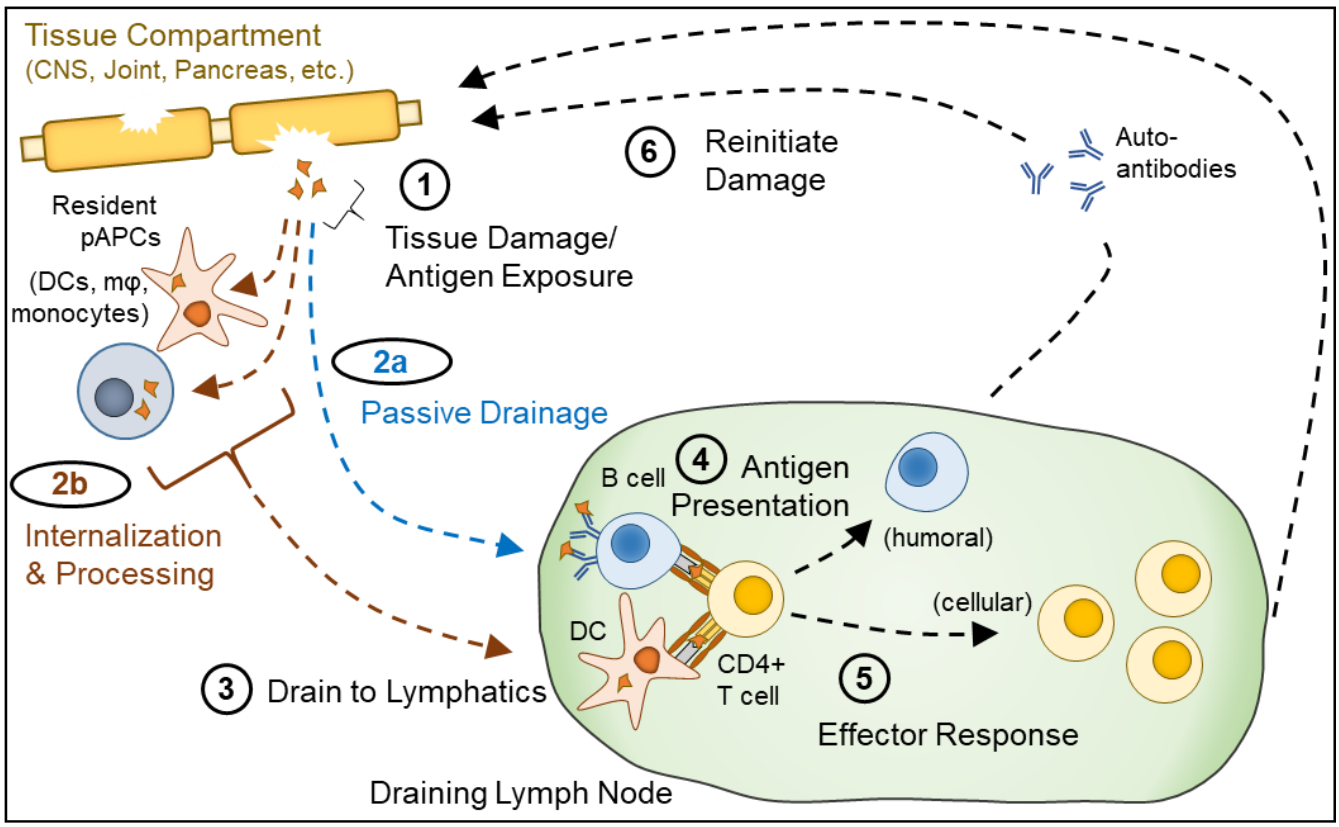

Figure 1. Mechanisms of peripheral autoimmunity. Damaged tissue releases autoantigen (**1**) that either drains directly to lymphatics (**2a**) or is internalized by resident professional antigen presenting cells (pAPCs, **2b** and **3**). In the secondary lymphoid organs, follicular pAPCs process and present antigen to naïve T helper cells in the presence of costimulatory signals (**4**). Naïve T cells become stimulated to proliferate and differentiate a cellular or humoral effector response (**5**). These activated effectors egress from lymphatics and eventually home to antigen-rich tissue compartments once more, where more damage can be caused and the cycle of autoimmunity is renewed (**6**).

1.3 Route and Size -Dependent Biotransport Dictates the Destination of Parenterally Delivered Compounds.

It is critical to understand the transport phenomena that that must be harnessed for delivery to immunologically directive tissues. Particularly with delivered allergy and antigen formulations, many administration routes have been investigated, but each presents its own unique delivery considerations. In this review, we will refine our analysis to focus on parental routes administration, as non-injected delivery introduces complex facets of mucosal immunity that have been well-reviewed in the past[43-45]. Our scope includes interstitial and intravenous (IV) strategies, which have been clinically investigated for both allergy and autoimmunity (**Fig. 2**). Interstitial administration indicates formulations delivered directly into tissue parenchyma and envelops common routes such as subcutaneous (SC), intramuscular (IM), and intradermal (ID) injection (**Fig. 2a**).

Interstitial delivery is appealing for its ease of administration and proven successes over a century-long history in vaccines and allergy[46, 47]. This route can exploit extracellular matrix (ECM) properties and sentinel cell populations to deliver formulations to draining lymph nodes. The ECM largely consists of an interpenetrating network of collagen and glycosaminoglycan polymers and is able to hinder leakage from the injection site in a size-dependent manner. Both diffusion and convection can drive transport through the ECM. Albumin serves as an excellent reference (molecular weight 69 kDa, size 3.5 nm) in that compounds smaller than this protein can rapidly diffuse from the injection site and reach systemic circulation through the blood pool while the transport for larger entities is driven by convective flow[48]. A negative pressure gradient exists in the interstitium that drains to the lymphatics. When particles are larger than the size of albumin, this convective flow dominates over diffusive transport and enables accumulation at lymph nodes. Importantly, however, when administered moieties exceed 100 nm in size, transport is restricted by the ECM (in humans)[48]. Structures of this size persist at the injection site as depots and must

rely on active transport by innate immune cells to reach lymphoid organs. An important note is that actively transported antigen can be difficult to harness for immunosuppressive function, however, due to its particulate nature[49]. We will discuss this perspective later in the review.

Indeed, entities between the size of 4-100 nm are generally able to reach lymph nodes from the interstitium by convective flow, but reaching these organs alone is not sufficient for affecting immunity. Lymph nodes are contained by a capsule that excludes much of the extranodal content that would otherwise intrude from systemic circulation. The T and B cell zones where immunity is potentiated lie within nodal sinuses that are protected by the subcapsular space and its resident macrophages and dendritic cells[28]. Herein, a second barrier is embodied that must be considered for ultimately delivering ASITs via interstitial routes. Conduits at this interface largely determine the penetration of free antigen into the nodal cortex with a 70 kDa cutoff[50]. The size of these channels once again represents a reference point similar to albumin, though shape and flexibility can confer access to larger compounds[51, 52]. Entities between 10-100 nm reaching the subcapsular space are mostly excluded excepting transport by subcapsular innate immune cells[53]. Most of the active internalization by these macrophages and dendritic cells is Fc-mediated, meaning antigen bound with antibody can reach the cortex. However, these complexes are poised to be immunogenic as part of natural immunological cues.

A set of delivery principles can also be surmised for the IV administration of antigen formulations as well (**Fig. 2b**). Compounds injected directly to the blood stream can be deposed by the spleen, renal elimination, or liver processing. The spleen is poised as an immunologic filter from which systemic circulation is policed[54]. Delivery and penetration into this organ resembles the requirements for lymph nodes; moieties 4-200 nm in size are capable of reaching the spleen,

but only those between 4 to 10 nm can traverse conduits into the cortex. Small compounds (<4-6 nm) are subject to renal excretion and do not persist to significantly influence immunity[55].

Though antigens between 4-200 nm are able to reach the spleen, blood flow highly favors liver processing. Blood flow through the spleen is typically 5-10% of cardiac output while the liver draws up to 5-fold more blood[56]. Liver delivery has drawn interest for ASIT delivery due to its immunologically privileged nature that is conferred by unique cell subsets including Kupffer cells and liver sinusoidal endothelial cells[57]. For example, researchers have tuned properties such as size and charge to produce formulations that preferentially accumulate in the liver[58]. This design is important for ASIT, because autoantigen relegated to the liver has been applied to enact tolerance against autoimmune mouse models[59, 60]. Liver accumulation and retention is maximized with very large particles that exceed 200 nm in size, and persistence enables the longitudinal activation of tolerogenic mechanisms. In the case of 4-200 nm structures, exposure is less conducive to immunological effects because liver accumulation is not as pronounced.

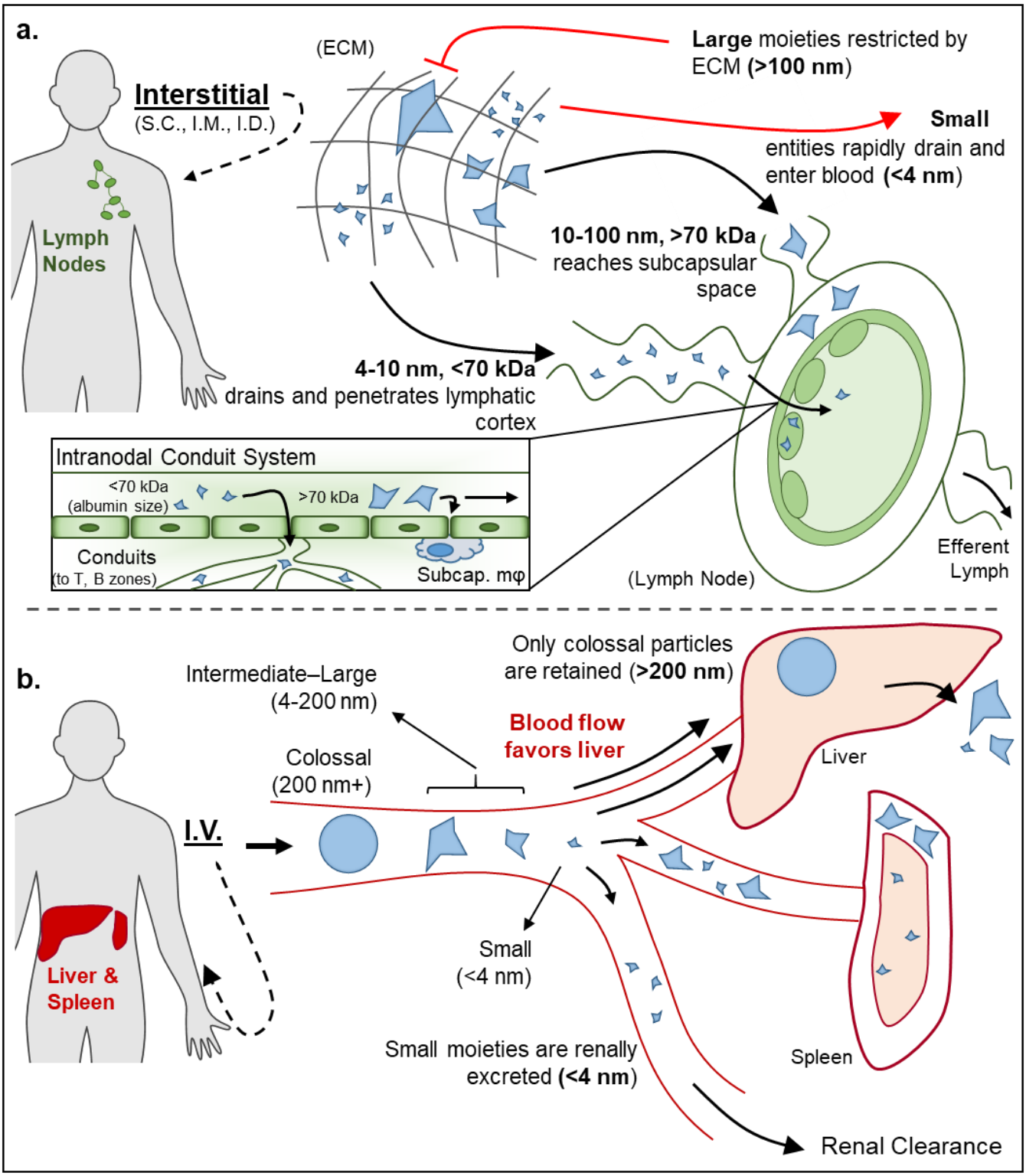

Figure 2. Parental routes of administration for influencing immunity. a. interstitial antigen transport is dictated by two major barriers. First, the ECM can serve to restrict the trafficking of

large entities greater than 100 nm in size. Small antigens less than 4 nm are subject to being lost to systemic circulation. Compounds between 4-100 nm can travel by convective transport to the lymph node, but only molecules between 4-10 nm are capable of traversing conduits into the directive T and B cell zones of lymph node parenchyma. b. IV administration poses the opportunity for antigen to reach the liver, spleen, or kidneys. Particles greater than 200 nm preferentially accumulate and are retained in the liver, but formulations 4-200 nm can also be processed via this route. The same 4-200 nm formulations can reach the spleen, and penetration into its cortex is dictated by the same principles as the lymph nodes. Finally, antigens less than 4 nm are subject to clearance by renal excretion.

1.4 Allergy Immunotherapies as the Foundation for Antigen-Specific Approaches to Autoimmunity.

With an understanding of the delivery parameters that influence the ability of formulations to access and influence the immune system, we can now look to practical examples for how aberrant immunity is modulated. ASIT as a strategy for addressing autoimmunity stems from historically successful applications in allergy desensitization therapies where hypersensitivity immune responses take place[61]. As such, we will assess historical underpinnings of allergy hyposensitization therapies and implications for ASIT applied to autoimmune disease. While recent ASIT strategies encompass a broad scope of approaches and delivery systems incorporating biomaterials, immunomodulatory drugs, and adjuvants, we have refined our focus here to the clinical delivery of allergen and autoantigen immunotherapies without co-delivery of drugs to enable the thorough analysis of physicochemical implications of these components. We aim to use this distilled approach to extrapolate a meaningful supposition about the clinical successes of

allergen-specific immunotherapies in contrast with the continued elusiveness of autoantigen ASIT implementation. Through understanding the role of autoantigen contextualization in directing the immune response, we propose that next-generation ASITs can be formatted for optimized action against autoimmune disease.

The first allergy immunotherapy was implemented with success in 1911 when Leonard Noon and John Freemen desensitized patients to grass allergy (known as hay fever at the time)[62, 63]. In this seminal trial, the physicians subcutaneously administered grass pollen extract in regular intervals while increasing allergen dose over time to build resistance. This framework of repeated and escalating dose has overall remained essentially the same and informed allergy immunotherapies for the century since. Today there are 19 FDA-approved, standardized subcutaneous allergen desensitization regimens[64].

With such broad and repeated demonstrations of effective allergen-specific immunotherapy regimens, it is important to explore the underlying characteristics driving these successes to enable rationalization against the comparative lack of breakthroughs within autoimmunity. Parameters such as size, charge and solubility each can play critical roles in directing the interaction between allergens and the immune system, and as such we have organized these data among three prominent allergens (**Table 1**).

Somewhat conserved physicochemical properties are evident across allergens. In terms of molecular weight (MW), extract fractions average 25.8, 21.4, and 21.0 kDa for timothy grass, peanut, and domestic cat, respectively. MW does not exceed 65.4 kDa (Ara h 1) across all allergens, though the minimum MW bottoms out at 2.6 kDa (Ara h 6). Isoelectric points (PI) are generally found at or below physiological pH between allergens. A PI of 10.5 was the maximum observed in the set (Ara h 11), while values did not go below 3.84 (Phl p 7). Finally, grand average

of hydropathicity (GRAVY) was used to roughly infer the water solubility of allergens through summing the hydropathy values of amino acids in the sequences. The GRAVY score describes the hydrophobicity of a given protein; larger, positive values generally mean the compound is insoluble while negative values imply hydrophilicity[65]. Interestingly, allergen extracts are mostly water soluble, displaying negative GRAVY scores.

Allergen	Extract Fraction	GenBank ID	MW (kDa, calculated)	PI (calculated)	GRAVY Score (calculated)
Phleum prantense **(Timothy Grass)**	**Phl p (avg)**		**25.8**	**5.90**	**-0.179**
	Phl p 1	P43213	28.5	6.12	-0.433
	Phl p 2	P43214.1	13.4	4.28	-0.124
	Phl p 4	ABB78007.1	58.2	9.37	-0.127
	Phl p 5	CCD28287.1	31.1	7.5	0.195
	Phl p 6	CAA81608.1	13.9	5.08	0.041
	Phl p 7	CAA76887.1	8.7	3.84	-0.283
	Phl p 11	Q8H6L7.1	33.7	6.23	-0.562
	Phl p 12	CAA54686.1	19.1	4.78	-0.141
	Phl p 13*	CAB42886.1	30	7.33	-0.364
Arachis hypogaea **(Peanut)**	**Ara h (avg)**		**21.4**	**7.35**	**-0.316**
	Ara h 1	AAB00861.1	65.4	6.91	-1.07
	Ara h 2	AAN77576.1	13.4	5.91	-1.22
	Ara h 3	AAD47382.1	54.1	5.29	-0.891
	Ara h 5	AAD55587.1	17.8	4.26	-0.078
	Ara h 6	ABQ96216.1	2.6	6.1	-0.821
	Ara h 7	AAD56719.1	19.6	5.8	-1.015

	Ara h 8	AAQ91847.1	17	4.73	-0.365
	Ara h 9	ABX56711.1	11.6	9.15	0.572
	Ara h 10	AAU21499.2	9.5	10.07	0.153
	Ara h 11	AAZ20276.1	10.8	10.5	0.451
	Ara h 14	AAK13449.1	18.4	10.28	0.259
	Ara h 15	AAU21501.1	16.9	9.22	0.238
	Fel d (avg)		**21.0**	**5.09**	**-0.170**
***Felis domesticus* (Domestic Cat)**	Fel d 1	AAC37318.1, AAC41616.1	17.8	4.5	0.265
	Fel d 2	CAA59279.1	38.3	5.27	-0.340
	Fel d 3	AAL49391.1	7.7	4.37	-0.584
	Fel d 4	AAS77253.1	15.9	4.62	-0.050
	Fel d 7	ADK56160.1	20.2	4.56	-0.521
	Fel d 8	ADM15668.1	25.9	7.24	0.209

Table 1. Physicochemical properties of model allergens. Molecular Weight (MW), Isoelectric Point (PI), and Grand Average of Hydropathy (GRAVY) are reported for protein extract fractions where full amino acid sequences are available. Allergen extract fractions were identified by searching allergen.org for the major allergen (ex. *Felis domesticus*). MW and PI were calculated using the PepCalc.com online tool. GRAVY score was determined using the calculator at gravy-calculator.de.

Together, allergen extracts paint a cohesive picture about conserved properties that may point to their utility for desensitization. For the most part these extracts fall squarely in a size distribution between 10-70 kDa – precisely the range which facilitates lymphatic drainage and penetration while likely being excluded from the blood pool when administered as subcutaneous

or intramuscular injections (**Fig. 2**). Indeed, the desensitization regimens approved by the FDA enable the interstitial delivery of mixed extracts. Allergens are generally not extremely charged; these extracts possess PIs at or below physiological pH such that they carry a neutral or slightly negative charge. An absence of highly positively charged fractions means fibrillization and innate immunogenicity are generally circumvented. With these charge properties and net negative GRAVY scores, allergens avoid aggregation due to poor solubility and remain at a size that facilitates lymphatic transport and prevents the formation of large, immunogenic aggregates.

1.5 Autoantigens Embody Physicochemical Profiles that Differ from Allergens

While allergens appear to present with similar characteristics, autoimmune antigens come with many different size, charge, and solubility properties appreciable across several disease pathologies (**Table 2**). Myelin autoantigens including proteolipid protein (PLP), myelin oligodendrocyte glycoprotein (MOG), and myelin basic protein (MBP) are associated with MS. Their molecular weights are 30, 28.2 and 11.57 kDa, respectively, while each is positively charged at physiological pH. These autoantigens are found embedded within the fatty myelin sheath, and as such PLP and MOG display considerable hydrophobicity. Conversely, MBP presents with a highly water-soluble GRAVY score that is likely conveyed by its significantly positive physiological charge. T1D presents glutamate decarboxylase (GAD), preproinsulin, and 60 kDa heat shock protein (HSP60) as conserved autoantigens. Among these proteins, a negative charge is presented at physiological pHs. GAD and HSP60 are both somewhat soluble in water, while preproinsulin is slightly hydrophobic. RA autoreactivity includes specificity for 40 kDa heat shock protein (HSP40), which is negatively charged and slightly soluble. The thyrotropin receptor autoantigen in Grave's disease is large (86.8 kDa), neutrally charged, and presents a positive

GRAVY score. In Hashimoto's disease, a similar thyroid-directed autoimmunity, thyroglobulin is a colossal (304.8 kDa), but hydrophilic protein. Aquaporin 4 in neuromyelitis optica is moderately sized at 34.8 kDa, neutrally charged, and considerably hydrophobic.

A number of clinical trials have been launched to investigate interstitial and IV delivery of autoantigenic epitopes within these proteins. Soluble antigen is reported as capable to skew immunity toward a regulatory phenotype and confer bystander immunosuppression effects. As such, a majority of injected autoantigen therapies within human MS patients has taken place using fragments of the soluble MBP protein. One phase III study investigated the immunodominant $MBP_{82\text{-}98}$ epitope in 612 secondary-progressive MS patients possessing genetic dispositions for reactivity to the MBP protein in particular[66]. Over the two-year period, the epitope was safe and well tolerated during twice-yearly bolus administration, but no clinical benefit was observed. An alternate dose escalation study assessed the efficacy of a cocktail containing four MBP epitopes (30-44, 83-99, 130-144, and 140-154). While only 16 weeks long, a decrease in gadolinium-enhancing lesions was evident[67].

In T1D, many insulin variants have been clinically evaluated. A 2002 study investigated the subcutaneous administration of insulin to first degree family members of T1D patients to assess its ability to prevent disease, though no success was realized[68]. Likewise, an altered peptide ligand of the insulin B chain did not confer effect for newly-diagnosed patients[69]. Another study followed newly-diagnosed patients over 12 months as they were administered a proinsulin peptide[70]. Here, patients receiving the peptide did not exhibit significant adverse events and their glucoregulatory insulin requirements did not increase over the interval, suggesting some therapeutic benefit. Another T1D study administered a HSP460 peptide to patients[71]. While safe and well tolerated, the study was retracted due to biostatistical misconduct that distorted clinical differences between

the treatment and placebo groups. In patients with Grave's disease, two peptides were intradermally injected for a Phase I study lasting 18 weeks[72]. While injection site swelling and pain were observed, the formulation was generally well tolerated and led to an improvement of disease-related biomarkers.

Disease	Epitopes	GenBank ID /Reference	MW (kDa, calc.)	PI (calc.)	GRAVY Score (calc.)	Clin. Resp.
MS	**Proteolipid Protein**	**AAA60117.1**	**30**	**8.11**	**0.559**	
	Myelin Oligodendrocyte Glycoprotein	**CAA52617.1**	**28.2**	**8.43**	**0.114**	
	Myelin Basic Protein	**AAC41944.1**	**17.8**	**11.57**	**-1.039**	
	82-98	[66]	2	6.75	-0.441	**-**
	30-44	[67]	1.7	9.94	-0.800	**++**
	83-99	[67]	2	8.85	-0.329	**++**
	130-144	[67]	1.7	10	-1.067	**++**
	140-154	[67]	1.6	8.59	0.160	**++**
T1D	**Glutamate Decarboxylase**	**AAB59427.1**	**67**	**7.11**	**-0.334**	
	Preproinsulin	**AAA59172.1**	**12**	**4.97**	**0.193**	
	Insulin	[68]	5.8	5.3	0.217	**-**
	Insulin B (9-23)	[69]	1.7	6.71	0.433	**-**
	Proinsulin peptide	[70]	1.9	8.75	0.133	**++**
	Heat Shock Protein 60	**P10809.2**	**61.1**	**5.46**	**-0.076**	
	DiaPep277	[71]	2.4	3.54	0.713	*****
RA	**Heat Shock Protein 40**	**BAA12819.1**	**38**	**8.91**	**-0.715**	
Grave's	**Thyrotropin Receptor**	**AAA36783.1**	**86.8**	**6.58**	**0.066**	

	5D-K1	[72]	2.5	10.61	-1.314	+
	9B-N	[72]	1.3	6.71	-0.253	+
Hashimoto's	**Thyroglobulin**	**CAA29104.1**	**304.8**	**5.25**	**-0.276**	
Neuromyelitis Optica	**Aquaporin 4**	**AAH22286.1**	**34.8**	**7.41**	**0.420**	

Table 2. Size, charge, and solubility properties for autoimmune antigens and interstitial/IV epitope treatments that have been clinical investigated. Property values were calculated using the same methodologies as in Table 1. Here, clinical responses are denoted with the following identifiers: (-) no therapeutic outcome, (+) biomarker improvement, and (++) clinical improvement. *The DiaPep277 study was retracted due to biostatistical misconduct.

In previously outlining allergen properties, a consistent trend of moderately sized (10-70 kDa), slightly negatively charged (PI 5-7.4), hydrophilic (GRAVY < -0.15) fractions were observable. Such trends are not as evident in autoantigens. Many autoantigens are also moderately sized, but several including Thyroglobulin and Thyrotropin are well over the 70 kDa threshold. Charge properties are widely dispersed; unlike with allergens, autoantigens such as PLP, MOG, MBP, and HSP40 exhibit PIs greater than 8, conferring a positive charge at physiological pH, while others such as GAD and Preproinsulin resemble more neutral, allergen-like charges. GRAVY scores are also highly variable. Ranges across autoantigens are dispersed from -1.013 (MBP) to 0.559 (PLP).

Further inference about allergen and autoantigen discrepancies can be gained by taking a perspective of MW, PI, and GRAVY scores holistically, rather than discretely. Very few autoantigenic proteins embody the full trifecta of size, charge, and solubility properties embodied by allergens. For example, while MBP is moderately sized (17.8 kDa) and theoretically water soluble (GRAVY -1.039), it carries an extreme positive charge which is known to be immunogenic

and disrupt cell membranes. Preproinsulin is likewise moderately sized (12 kDa) and it's PI mirrors allergens (4.97), but it presents with hydrophobicity (GRAVY 0.193) that creates the possibility of aggregation *in situ* that would likewise be immunogenic[73]. Such unfavorable characteristics may pose safety and tolerability obstacles to the prospects of full-protein autoantigen administration. Clinical ASIT researchers have rather incorporated smaller peptide epitopes of immunodominant antigen regions to incorporate greater specificity to formulations. Peptide epitopes harnessed for parental interstitial and IV ASITs may neutralize safety concerns that may arise from whole-protein autoantigen. MBP epitopes present charges that are slightly attenuated over full MBP. Thytotropin peptides cut down on the colossal size of the autoantigen. But is there a cost to electing these variants? What are the tradeoffs of size, charge, and solubility properties in the context of autoantigen delivery?

1.6 Immunological Fates for Delivered Autoantigen are Determined by Format

The physical and chemical properties of delivered autoantigens are paramount in dictating distribution, kinetics, and immunological effect (**Fig 2**). These properties can together outweigh the primary intent of targeted interaction with autoreactive cells when they are not properly defined. The format of autoantigens can direct their distribution or retention in tissues, and these fates and ultimate immunological effects are dictated by physicochemical properties (**Fig. 3**).

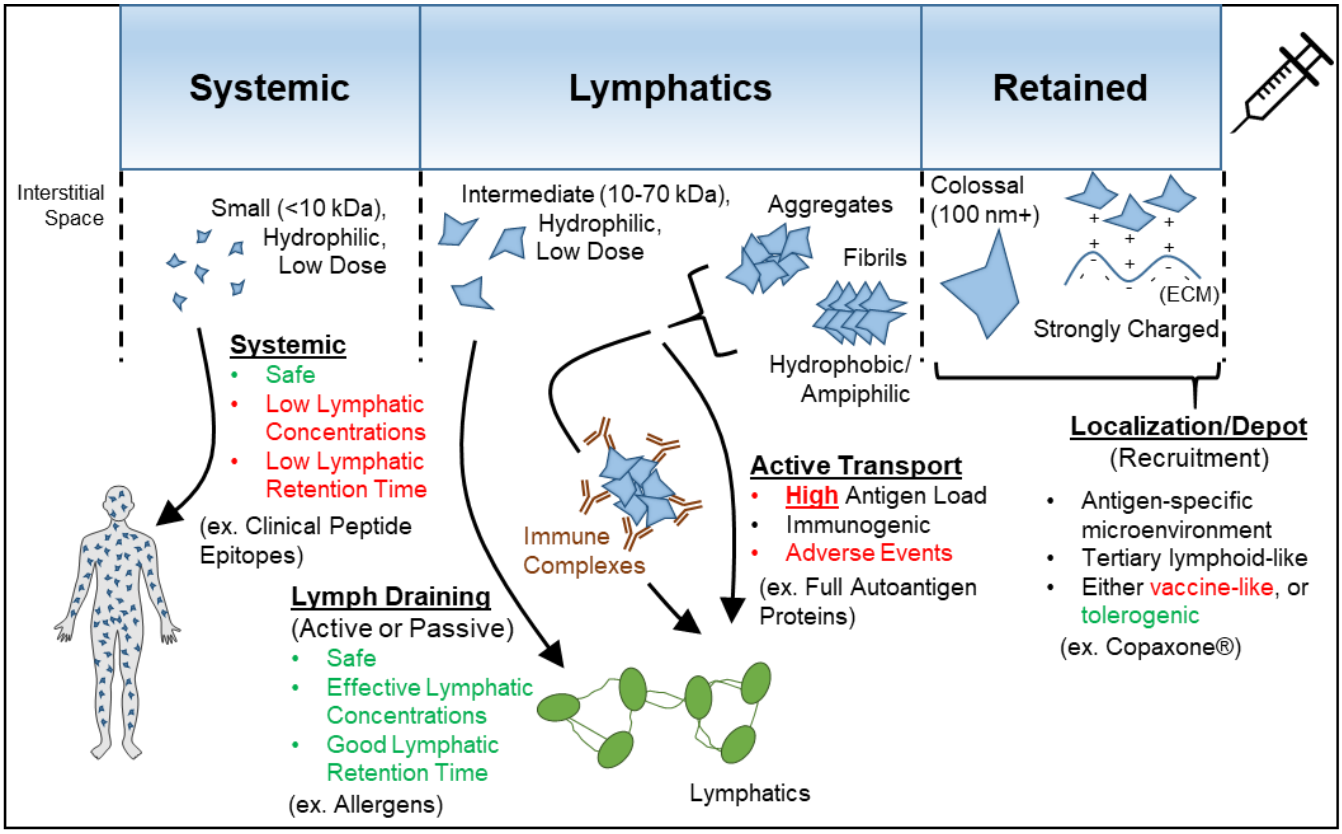

Figure 3. Autoantigen format dictates transport and can inform the resulting immune response. Small, hydrophilic entities that are interstitially delivered my replicate allergen regimens at low doses, but the peptide epitopes used are typically too small to be excluded from systemic exposure. As a result, low lymphatic loading and retention occurs, and efficacy becomes elusive. Conversely, anergizing lymphatic-draining formulations can be harnessed with intermediately-sized (10-70 kDa), hydrophilic moieties that most closely resemble allergens. Antigens with this format are excluded from the blood and can achieve loading into lymph nodes in a low-density format that is most conducive for tolerance. Conversely, antigens that are net-hydrophobic or prone to fibril formation form immune complexes or are actively transported to the lymphatics, which entices an immunogenic response that introduces risks for autoimmune ASITs. Finally, large entities exceeding 100 nm are restricted by the ECM and retained near the site of injection. Likewise, entities with a strong positive charge can be retained through electrostatic interactions with the

negatively charged ECM. When formulations are retained, the innate immune system is recruited, and microenvironment (stimulatory or tolerogenic) directs the immune response.

1.6.1 Systemic Drainage

Small, hydrophilic autoantigens and epitopes are destined for loss to the blood pool and systemic circulation. Low lymphatic loading results. For this reason, safety is maximized as antigen overstimulation and anaphylaxis are avoided, however potency in desensitization is also reduced. Many autoantigen epitopes that have been clinically investigated are classifiable under this fate. One of the major benefits of ASIT is the improved safety profile over global immunomodulatory drugs; as such, the development of a new class of immunotherapy mandates safety as a main priority. The epitope-alone strategies reviewed here consistently fall well below the 10 kDa cutoff for lymphatic drainage. Clinical results from these interventions are favorable in early-phase studies as they are safe and well tolerated, however efficacy has yet to be fully carried over to a full FDA approval for autoantigen epitopes.

1.6.2 Lymphatic Transport

Lymph-draining formulations pose the opportunity to maximize autoantigen colocalization with directive immune populations. However, the resulting dose in lymphoid organs is extremely important to consider in directing immunity, as parameters such as valency and density can highly impact the nature of the resulting immune response. Indeed, the seminal allergy desensitization work that led to autoimmune ASITs was based on a low, but progressively escalating dose over time. This regimen is conducive to the physicochemical properties of allergens; intermediately-sized (10-70 kDa), water-soluble allergen extract fractions are able to drain to and penetrate within lymph nodes for the retained delivery of controlled, low valency antigen. Autoantigen

physicochemical properties are not always conducive to the same routes. Immunogenic vaccines, in contrast, use adjuvants such as alum and MF59 to incorporate a high density of antigen in particulate formulations to trigger stimulatory processing and presentation by antigen-presenting cells[74]. The hydrophobic nature of some antigens such as PLP, MOG, and aquaporin 4 means these proteins are susceptible to aggregation after injection. Large aggregates of autoantigen complexes can confer the same immunogenic effects as adjuvant delivery systems, causing antigen-presenting cells to present high densities of antigen at lymph nodes via active transport[73]. Alternatively, in antibody-mediated autoimmunities, the aggregated autoantigen can invoke the formation of equally immunogenic immune complexes in the blood and interstitium[75]. Unduly concentrated autoantigen loads pose danger and could lead to anaphylactic or adverse events. While hydrophobic aggregation is one mechanism of these unintended effects, amphiphilic autoantigens or peptide epitopes can cause fibrils that embody similar nucleation events[76]. Even net hydrophiles are susceptible to the formation of particulates when regions of hydrophobicity are present[77].

1.6.3 Injection Site Retention

Some physicochemical properties may lead to the outright retention of formulations at the injection site. Human ECM restricts diffusion for entities that exceed 100 nm. While delivered autoantigens do not reach this threshold alone, significant aggregation or self-assembly can lead to macrostructures that are retained at the site of injection. Extreme positive charges can also retain autoantigen through electrostatic complexation with negatively-charged ECM components. Glatiramer acetate (Copaxone®) is a random chain of the four most prominent amino acids contained in MBP and is an FDA-approved injectable immunotherapy for MS patients[78]. While this formulation's precise mechanism of action is unknown, we recently detailed that glatiramer acetate is highly retained at its site of injection through the electrostatic interaction of its many

lysine residues with negatively-charged glycosaminoglycans such as hyaluronic acid[79]. MBP, which is what glatiramer acetate was initially designed to mimic, expresses an even more polarized PI of 11.57 and shows that charge should be considered even though it confers a favorable calculated hydrophobicity.

Retained autoantigen can be a versatile tool for modulating immunity. With the formation of a depot at the injection site comes the recruitment of innate immune cells, and the accumulation of these actors can ultimately resemble tertiary lymphoid organs that form in disease states such as cancer and MS[80, 81]. The instructive immunity that results from the formation of these structures is highly determined by cues from the microenvironment.

1.7 Strategies for Circumventing Delivery and Distribution Obstacles

1.7.1 Intranodal delivery

While the focus of our review is contained to the interstitial and IV administration of autoantigen-alone, several notable strategies exist to sidestep the inherent delivery constraints imposed by size, charge, and solubility. Interstitial injection may be favored over other routes for its ease and established history in allergy and vaccines, but intranodal injection directly administers antigen to target tissues. The principles governing the engineering of the lymphatic microenvironment have been well-reviewed in the past[82] and may favor systemic immune tolerance[83]. It has been maintained that biomaterial delivery systems are necessary to increase lymphatic retention and sustained kinetics after intranodal delivery. In one study, researchers administered 165 patients with alum-adsorbed grass pollen allergen either subcutaneously for 54 times over three years or just three intranodal injections over two months[84]. Striking results were obtained where tolerance in the intranodal group was attained in just four months compared to the

more intensive three-year plan. Further, these outcomes were achieved with just 1/1300 of the cumulative dose required for subcutaneous desensitization, and fewer adverse events were observed in the intranodal group. A study by the same group showed similar results for cat allergy. After just three intranodal injections over two months, nasal tolerance to cat allergen was increased 74-fold[85]. These results highlight the importance of lymphoid organs as necessary target tissues in ASIT and illuminate the promise of direct intranodal administration.

1.7.2 Transdermal delivery

Another notable strategy for overcoming ASIT delivery constraints is the controlled release of autoantigen through transdermal patches. As previously mentioned, autoantigen epitopes below 10 kDa are likely to enter systemic circulation, thus bolus subcutaneous injections are not conducive to lymphatic loading and retention. Transdermal delivery offers a potential alternative to reformatting antigen for optimized trafficking. Here, the sustained depot release of epitopes can facilitate gradual lymphatic dosing. It is further hypothesized that transdermal administration can target resident Langerhans cells for active nodal transport[86]. These interventions have already shown some successes in the realm of autoimmunity. For MS, a study was conducted where patients were administered three immunodominant epitopes (MBP_{85-99}, MOG_{35-55}, and $PLP_{139-155}$) via the transdermal route[87]. Over one year, patch-treated patients exhibited significantly fewer clinical signs of disease progression than the placebo-treated cohort, and researchers observed a 66.5% reduction in gadolinium-enhancing lesions over the interval.

1.8 Next-Generation Approaches to Formatting Autoantigen for Optimizing ASIT

Clinical explorations of allergen and autoantigen immunotherapies shed light on delivery considerations, which should be harnessed in aiming to desensitize autoimmunity. Lymphatic

homing is paramount for evoking therapeutic effects. Interstitial and intranodal routes of administration appear to be most conducive for these effects, as splenic accumulation via the IV route is difficult to balance with hepatic accumulation. Physicochemical discrepancies between allergens and prominent autoantigens prompts the pursuit of next-generation ASITs that incorporate delivery systems and biomaterials to format the latter for optimal interfacing with tolerance mechanisms.

1.8.1 Soluble Delivery

Immunogens that are below 100 kDa and hydrophilic are purported to be naturally tolerogenic[88]. Formatting autoantigens and their epitopes to more closely mirror these size and solubility properties should, therefore, enhance lymphatic delivery and amplify immune tolerance. Of course, inherent physicochemical autoantigen properties cannot be inherently changed, however net molecular properties can be modified using appropriate chemical modifications or carriers. Our group has employed polymers to solubilize antigen epitopes and control their valency properties to invoke immune tolerance pathways[89-96]. The size adjustment conferred to autoantigens enables exclusion from direct absorption into circulation while the solubility and spacing of antigen engages mechanisms of tolerance.

1.8.2 Colloidal Delivery

A vast majority of autoimmune-targeted ASITs have recruited nanoparticulate delivery systems to deliver antigens and immunomodulatory drugs to lymph nodes. These systems incorporate polymers, metals, or emulsions to spatiotemporally restrict autoantigen and facilitate drainage to lymphoid organs as well as interaction with tissue-resident pAPCs. Notably, many vehicle materials are adapted from more mature fields such as cancer immunotherapy . Such delivery systems can invoke innate immunogenicity that is overlooked in applications where

inflammation is desirable[97, 98]. Some strategies for overcoming vehicle detriments for autoimmune ASITs involves developing functional vehicles that are formulated using immunologically instructive signals as constitutive building blocks[99, 100]. Others have utilized the ability of colloids to deliver drugs, such as immunosuppressants, to counteract any inherent immunogenicity and to direct downsteam response pathways.

1.8.3 Depot Delivery

Immunologically-directive microenvironments are a powerful tool for evoking either inflammatory or regulatory responses[101, 102]. Another strategy for autoimmune ASITs is to intentionally retain autoantigen at the site of administration. Localization of autoantigens at the site of administration recruits pAPCs and cognate immune cells, encouraging processing at a locus that can be engineered with immunomodulatory signals. Though not delivering autoantigen, recent work by the Hubbell group showed the power of localized immunotherapies by homing anti-TNF-α antibodies to collagen-rich inflammatory microenvironments and suppressing a mouse model of RA[103]. By skewing the inflammatory cues at the site of autoimmune destruction and autoantigen processing, disease was stifled. Depot-based autoantigen delivery systems may be further refined with the exploration of more immunological cues to control the inflammatory fates of autoantigen processing *in situ*.

1.9 Conclusions

ASIT represents a compelling step toward precision medicine to treat autoimmune diseases. To date, many formulations have sought to interrupt the vicious cycle of autoimmunity by delivering the same autoantigens and epitopes implicated in disease. To date, however, no comparable ASITs are available for treating autoimmunity. ASIT underpinnings could learn from

historical successes in allergy, where a plethora of FDA-standardized allergen desensitization regimens are available. The physicochemical properties of allergen extracts differ substantially from those of autoantigens and their constitutive epitopes. Allergens are generally found between 10-70 kDa in size with neutral or slightly negative charge and good water solubility. Autoantigens and their epitopes rarely express all three of these qualities, and these properties may confound their local transport *in vivo*. These discrepancies emphasize the role of molecular properties and delivery systems for developing ASITs to treat human autoimmune diseases.

1.10 References

1. Miller, S. D.; Turley, D. M.; Podojil, J. R., Antigen-specific tolerance strategies for the prevention and treatment of autoimmune disease. *Nat. Rev. Immunol.* **2007,** *7* (9), 665-677.
2. Aly, T.; Devendra, D.; Eisenbarth, G. S., Immunotherapeutic approaches to prevent, ameliorate, and cure type 1 diabetes. *Am. J. Ther.* **2005,** *12* (6), 481-490.
3. Rosenblum, M. D.; Gratz, I. K.; Paw, J. S.; Abbas, A. K., Treating human autoimmunity: current practice and future prospects. *Science translational medicine* **2012,** *4* (125), 125sr1-125sr1.
4. Riminton, D. S.; Hartung, H.-P.; Reddel, S. W., Managing the risks of immunosuppression. *Curr. Opin. Neurol.* **2011,** *24* (3), 217-223.
5. Reddy, S.; Wanchu, A.; Gupta, V.; Bambery, P., Profile of opportunistic infections among patients on immunosuppressive medication. *APLAR Journal of Rheumatology* **2006,** *9* (3), 269-274.
6. Ransohoff, R. M., Natalizumab and PML. *Nat. Neurosci.* **2005,** *8* (10), 1275.
7. Salliot, C.; Dougados, M.; Gossec, L., Risk of serious infections during rituximab, abatacept and anakinra treatments for rheumatoid arthritis: meta-analyses of randomised placebo-controlled trials. *Ann. Rheum. Dis.* **2009,** *68* (1), 25-32.
8. Bluestone, J. A.; Tang, Q., Immunotherapy: making the case for precision medicine. American Association for the Advancement of Science: 2015.
9. Dugger, S. A.; Platt, A.; Goldstein, D. B., Drug development in the era of precision medicine. *Nature reviews Drug discovery* **2018,** *17* (3), 183.
10. Arnedos, M.; Vicier, C.; Loi, S.; Lefebvre, C.; Michiels, S.; Bonnefoi, H.; Andre, F., Precision medicine for metastatic breast cancer—limitations and solutions. *Nature reviews Clinical oncology* **2015,** *12* (12), 693.
11. Guerin, M.; Sabatier, R.; Goncalves, A., Trastuzumab emtansine (Kadcyla (®)) approval in HER2-positive metastatic breast cancers. *Bull. Cancer* **2015,** *102* (4), 390-397.
12. Kausar, F.; Mustafa, K.; Sweis, G.; Sawaqed, R.; Alawneh, K.; Salloum, R.; Badaracco, M.; Niewold, T. B.; Sweiss, N. J., Ocrelizumab: a step forward in the evolution of B-cell therapy. *Expert Opin. Biol. Ther.* **2009,** *9* (7), 889-895.

13. Chaudhuri, A., Ocrelizumab in multiple sclerosis: risks and benefits. *The Lancet* **2012,** *379* (9822), 1196-1197.
14. Kappos, L.; Leppert, D.; Tinbergen, J.; Gerber, M.; Hauser, S., Risk of infections and malignancies after treatment with anti-CD20 monoclonal antibodies: ocrelizumab and rituximab in rheumatoid arthritis and multiple sclerosis. *Mult. Scler.* **2012,** *18*, 424.
15. Owens, G. P.; Ritchie, A. M.; Burgoon, M. P.; Williamson, R. A.; Corboy, J. R.; Gilden, D. H., Single-cell repertoire analysis demonstrates that clonal expansion is a prominent feature of the B cell response in multiple sclerosis cerebrospinal fluid. *J. Immunol.* **2003,** *171* (5), 2725-2733.
16. Posnett, D.; Gottlieb, A.; Bussel, J.; Friedman, S.; Chiorazzi, N.; Li, Y.; Szabo, P.; Farid, N.; Robinson, M., T cell antigen receptors in autoimmunity. *J. Immunol.* **1988,** *141* (6), 1963-1969.
17. Lemke, H., Immune Response regulation by antigen receptors' clone-specific nonself parts. *Front. Immunol.* **2018,** *9*, 1471.
18. Mueller, D. L., Mechanisms maintaining peripheral tolerance. *Nat. Immunol.* **2010,** *11* (1), 21.
19. Owen, J. A.; Punt, J.; Stranford, S. A., *Kuby immunology*. WH Freeman New York: 2013.
20. Goverman, J. M., Immune tolerance in multiple sclerosis. *Immunol. Rev.* **2011,** *241* (1), 228-240.
21. Kamradt, T.; Mitchison, N. A., Tolerance and autoimmunity. *N. Engl. J. Med.* **2001,** *344* (9), 655-664.
22. Peakman, M.; Dayan, C. M., Antigen-specific immunotherapy for autoimmune disease: fighting fire with fire? *Immunology* **2001,** *104* (4), 361.
23. Northrup, L.; Christopher, M. A.; Sullivan, B. P.; Berkland, C., Combining antigen and immunomodulators: Emerging trends in antigen-specific immunotherapy for autoimmunity. *Adv Drug Deliv Rev* **2016,** *98*, 86-98.
24. Irvine, D. J.; Swartz, M. A.; Szeto, G. L., Engineering synthetic vaccines using cues from natural immunity. *Nature materials* **2013,** *12* (11), 978.
25. Hampton, H. R.; Chtanova, T., Lymphatic Migration of Immune Cells. *Front Immunol* **2019,** *10* (1168).
26. Rosenblum, M. D.; Remedios, K. A.; Abbas, A. K., Mechanisms of human autoimmunity. *The Journal of Clinical Investigation* **2015,** *125* (6), 2228-2233.
27. Mohammad Hosseini, A.; Majidi, J.; Baradaran, B.; Yousefi, M., Toll-Like Receptors in the Pathogenesis of Autoimmune Diseases. *Adv Pharm Bull* **2015,** *5* (Suppl 1), 605-614.
28. Roozendaal, R.; Mempel, T. R.; Pitcher, L. A.; Gonzalez, S. F.; Verschoor, A.; Mebius, R. E.; von Andrian, U. H.; Carroll, M. C., Conduits mediate transport of low-molecular-weight antigen to lymph node follicles. *Immunity* **2009,** *30* (2), 264-276.
29. Itano, A. A.; Jenkins, M. K., Antigen presentation to naive CD4 T cells in the lymph node. *Nature Immunology* **2003,** *4* (8), 733-739.
30. Ellis, J. H.; Burden, M. N.; Vinogradov, D. V.; Linge, C.; Crowe, J. S., Interactions of CD80 and CD86 with CD28 and CTLA4. *The Journal of Immunology* **1996,** *156* (8), 2700-2709.
31. Arai, K.-i.; Lee, F.; Miyajima, A.; Miyatake, S.; Arai, N.; Yokota, T., Cytokines: coordinators of immune and inflammatory responses. *Annual review of biochemistry* **1990,** *59* (1), 783-836.

32. Dardalhon, V.; Korn, T.; Kuchroo, V. K.; Anderson, A. C., Role of Th1 and Th17 cells in organ-specific autoimmunity. *Journal of Autoimmunity* **2008,** *31* (3), 252-256.
33. Damsker, J. M.; Hansen, A. M.; Caspi, R. R., Th1 and Th17 cells: adversaries and collaborators. *Ann N Y Acad Sci* **2010,** *1183*, 211-221.
34. Fujiwara, N.; Kobayashi, K., Macrophages in inflammation. *Current Drug Targets-Inflammation & Allergy* **2005,** *4* (3), 281-286.
35. Medina, K. L., Overview of the immune system. In *Handbook of clinical neurology*, Elsevier: 2016; Vol. 133, pp 61-76.
36. Miller, J. R.; Burke, A. M.; Bever, C. T., Occurrence of oligoclonal bands in multiple sclerosis and other CNS diseases. *Annals of Neurology* **1983,** *13* (1), 53-58.
37. Lennon, V. A.; Wingerchuk, D. M.; Kryzer, T. J.; Pittock, S. J.; Lucchinetti, C. F.; Fujihara, K.; Nakashima, I.; Weinshenker, B. G., A serum autoantibody marker of neuromyelitis optica: distinction from multiple sclerosis. *The Lancet* **2004,** *364* (9451), 2106-2112.
38. Webb, M.; Tham, C.-S.; Lin, F.-F.; Lariosa-Willingham, K.; Yu, N.; Hale, J.; Mandala, S.; Chun, J.; Rao, T. S., Sphingosine 1-phosphate receptor agonists attenuate relapsing–remitting experimental autoimmune encephalitis in SJL mice. *Journal of Neuroimmunology* **2004,** *153* (1), 108-121.
39. Robins, H. S.; Campregher, P. V.; Srivastava, S. K.; Wacher, A.; Turtle, C. J.; Kahsai, O.; Riddell, S. R.; Warren, E. H.; Carlson, C. S., Comprehensive assessment of T-cell receptor β-chain diversity in αβ T cells. *Blood* **2009,** *114* (19), 4099-4107.
40. Chu, N. D.; Bi, H. S.; Emerson, R. O.; Sherwood, A. M.; Birnbaum, M. E.; Robins, H. S.; Alm, E. J., Longitudinal immunosequencing in healthy people reveals persistent T cell receptors rich in highly public receptors. *BMC Immunology* **2019,** *20* (1), 19.
41. Briney, B.; Inderbitzin, A.; Joyce, C.; Burton, D. R., Commonality despite exceptional diversity in the baseline human antibody repertoire. *Nature* **2019,** *566* (7744), 393-397.
42. Battaglia, A.; Ferrandina, G.; Buzzonetti, A.; Malinconico, P.; Legge, F.; Salutari, V.; Scambia, G.; Fattorossi, A., Lymphocyte populations in human lymph nodes. Alterations in CD4+ CD25+ T regulatory cell phenotype and T-cell receptor Vbeta repertoire. *Immunology* **2003,** *110* (3), 304-312.
43. Jalava, K.; Eko, F. O.; Riedmann, E.; Lubitz, W., Bacterial ghosts as carrier and targeting systems for mucosal antigen delivery. *Expert review of vaccines* **2003,** *2* (1), 45-51.
44. Mestecky, J.; Michalek, S.; Moldoveanu, Z.; Russell, M., Routes of immunization and antigen delivery systems for optimal mucosal immune responses in humans. *Behring Institute Mitteilungen* **1997,** (98), 33-43.
45. Shakya, A. K.; Chowdhury, M. Y. E.; Tao, W.; Gill, H. S., Mucosal vaccine delivery: Current state and a pediatric perspective. *Journal of Controlled Release* **2016,** *240*, 394-413.
46. Stern, A. M.; Markel, H., The history of vaccines and immunization: familiar patterns, new challenges. *Health affairs* **2005,** *24* (3), 611-621.
47. Krishna, M.; Huissoon, A., Clinical immunology review series: an approach to desensitization. *Clinical & Experimental Immunology* **2011,** *163* (2), 131-146.
48. Irvine, D. J.; Swartz, M. A.; Szeto, G. L., Engineering synthetic vaccines using cues from natural immunity. *Nature Materials* **2013,** *12*, 978.
49. Benne, N.; van Duijn, J.; Kuiper, J.; Jiskoot, W.; Slütter, B., Orchestrating immune responses: How size, shape and rigidity affect the immunogenicity of particulate vaccines. *Journal of Controlled Release* **2016,** *234*, 124-134.

50. Gretz, J. E.; Norbury, C. C.; Anderson, A. O.; Proudfoot, A. E.; Shaw, S., Lymph-borne chemokines and other low molecular weight molecules reach high endothelial venules via specialized conduits while a functional barrier limits access to the lymphocyte microenvironments in lymph node cortex. *Journal of Experimental Medicine* **2000,** *192* (10), 1425-1440.
51. Thomas, S. N.; Schudel, A., Overcoming transport barriers for interstitial-, lymphatic-, and lymph node-targeted drug delivery. *Current Opinion in Chemical Engineering* **2015,** *7*, 65-74.
52. Reddy, S. T.; Berk, D. A.; Jain, R. K.; Swartz, M. A., A sensitive in vivo model for quantifying interstitial convective transport of injected macromolecules and nanoparticles. *J Appl Physiol (1985)* **2006,** *101* (4), 1162-9.
53. Phan, T. G.; Grigorova, I.; Okada, T.; Cyster, J. G., Subcapsular encounter and complement-dependent transport of immune complexes by lymph node B cells. *Nature immunology* **2007,** *8* (9), 992.
54. Mebius, R. E.; Kraal, G., Structure and function of the spleen. *Nature reviews immunology* **2005,** *5* (8), 606.
55. Choi, H. S.; Liu, W.; Misra, P.; Tanaka, E.; Zimmer, J. P.; Itty Ipe, B.; Bawendi, M. G.; Frangioni, J. V., Renal clearance of quantum dots. *Nature biotechnology* **2007,** *25* (10), 1165-1170.
56. Karlstadt, R. G.; Hogan, D. L.; Foxx-Orenstein, A. M. Y., 36 - Normal Physiology of the Gastrointestinal Tract and Gender Differences. In *Principles of Gender-Specific Medicine*, Legato, M. J., Ed. Academic Press: San Diego, 2004; pp 377-396.
57. Crispe, I. N., Hepatic T cells and liver tolerance. *Nature Reviews Immunology* **2003,** *3* (1), 51-62.
58. Hirn, S.; Semmler-Behnke, M.; Schleh, C.; Wenk, A.; Lipka, J.; Schäffler, M.; Takenaka, S.; Möller, W.; Schmid, G.; Simon, U.; Kreyling, W. G., Particle size-dependent and surface charge-dependent biodistribution of gold nanoparticles after intravenous administration. *Eur J Pharm Biopharm* **2011,** *77* (3), 407-416.
59. Lüth, S.; Huber, S.; Schramm, C.; Buch, T.; Zander, S.; Stadelmann, C.; Brück, W.; Wraith, D. C.; Herkel, J.; Lohse, A. W., Ectopic expression of neural autoantigen in mouse liver suppresses experimental autoimmune neuroinflammation by inducing antigen-specific Tregs. *The Journal of clinical investigation* **2008,** *118* (10), 3403-3410.
60. Carambia, A.; Freund, B.; Schwinge, D.; Bruns, O. T.; Salmen, S. C.; Ittrich, H.; Reimer, R.; Heine, M.; Huber, S.; Waurisch, C., Nanoparticle-based autoantigen delivery to Treg-inducing liver sinusoidal endothelial cells enables control of autoimmunity in mice. *Journal of hepatology* **2015,** *62* (6), 1349-1356.
61. Arefieva, A.; Smoldovskaya, O.; Tikhonov, A.; Rubina, A. Y., Allergy and autoimmunity: Molecular diagnostics, therapy, and presumable pathogenesis. *Mol. Biol.* **2017,** *51* (2), 194-204.
62. Ring, J.; Gutermuth, J., 100 years of hyposensitization: history of allergen-specific immunotherapy (ASIT). *Allergy* **2011,** *66* (6), 713-724.
63. Freeman, J., Further observations on the treatment of hay fever by hypodermic inoculations of pollen vaccine. *The Lancet* **1911,** *178* (4594), 814-817.
64. Jutel, M.; Kosowska, A.; Smolinska, S., Allergen immunotherapy: past, present, and future. *Allergy Asthma Immunol. Res.* **2016,** *8* (3), 191-197.

65. Kyte, J.; Doolittle, R. F., A simple method for displaying the hydropathic character of a protein. *Journal of Molecular Biology* **1982,** *157* (1), 105-132.
66. Freedman, M. S.; Bar-Or, A.; Oger, J.; Traboulsee, A.; Patry, D.; Young, C.; Olsson, T.; Li, D.; Hartung, H. P.; Krantz, M.; Ferenczi, L.; Verco, T., A phase III study evaluating the efficacy and safety of MBP8298 in secondary progressive MS. *Neurology* **2011,** *77* (16), 1551.
67. Chataway, J.; Martin, K.; Barrell, K.; Sharrack, B.; Stolt, P.; Wraith, D. C., Effects of ATX-MS-1467 immunotherapy over 16 weeks in relapsing multiple sclerosis. *Neurology* **2018,** *90* (11), e955-e962.
68. Effects of insulin in relatives of patients with type 1 diabetes mellitus. *N Engl J Med* **2002,** *346* (22), 1685-91.
69. Walter, M.; Philotheou, A.; Bonnici, F.; Ziegler, A.-G.; Jimenez, R.; Group, N. B. I. S., No effect of the altered peptide ligand NBI-6024 on beta-cell residual function and insulin needs in new-onset type 1 diabetes. *Diabetes Care* **2009,** *32* (11), 2036-2040.
70. Alhadj Ali, M.; Liu, Y. F.; Arif, S.; Tatovic, D.; Shariff, H.; Gibson, V. B.; Yusuf, N.; Baptista, R.; Eichmann, M.; Petrov, N.; Heck, S.; Yang, J. H. M.; Tree, T. I. M.; Pujol-Autonell, I.; Yeo, L.; Baumard, L. R.; Stenson, R.; Howell, A.; Clark, A.; Boult, Z.; Powrie, J.; Adams, L.; Wong, F. S.; Luzio, S.; Dunseath, G.; Green, K.; O'Keefe, A.; Bayly, G.; Thorogood, N.; Andrews, R.; Leech, N.; Joseph, F.; Nair, S.; Seal, S.; Cheung, H.; Beam, C.; Hills, R.; Peakman, M.; Dayan, C. M., Metabolic and immune effects of immunotherapy with proinsulin peptide in human new-onset type 1 diabetes. *Sci Transl Med* **2017,** *9* (402).
71. Raz, I.; Ziegler, A. G.; Linn, T.; Schernthaner, G.; Bonnici, F.; Distiller, L. A.; Giordano, C.; Giorgino, F.; de Vries, L.; Mauricio, D.; Procházka, V.; Wainstein, J.; Elias, D.; Avron, A.; Tamir, M.; Eren, R.; Peled, D.; Dagan, S.; Cohen, I. R.; Pozzilli, P., Treatment of Recent-Onset Type 1 Diabetic Patients With DiaPep277: Results of a Double-Blind, Placebo-Controlled, Randomized Phase 3 Trial. *Diabetes Care* **2014,** *37* (5), 1392.
72. Pearce, S. H. S.; Dayan, C.; Wraith, D. C.; Barrell, K.; Olive, N.; Jansson, L.; Walker-Smith, T.; Carnegie, C.; Martin, K. F.; Boelaert, K.; Gilbert, J.; Higham, C. E.; Muller, I.; Murray, R. D.; Perros, P.; Razvi, S.; Vaidya, B.; Wernig, F.; Kahaly, G. J., Antigen-Specific Immunotherapy with Thyrotropin Receptor Peptides in Graves' Hyperthyroidism: A Phase I Study. *Thyroid* **2019,** *29* (7), 1003-1011.
73. Moussa, E. M.; Panchal, J. P.; Moorthy, B. S.; Blum, J. S.; Joubert, M. K.; Narhi, L. O.; Topp, E. M., Immunogenicity of therapeutic protein aggregates. *Journal of pharmaceutical sciences* **2016,** *105* (2), 417-430.
74. Pasquale, A. D.; Preiss, S.; Silva, F. T. D.; Garçon, N., Vaccine adjuvants: from 1920 to 2015 and beyond. *Vaccines* **2015,** *3* (2), 320-343.
75. Szakal, A.; Holmes, K.; Tew, J., Transport of immune complexes from the subcapsular sinus to lymph node follicles on the surface of nonphagocytic cells, including cells with dendritic morphology. *The Journal of Immunology* **1983,** *131* (4), 1714-1727.
76. Mastrotto, F.; Bellato, F.; Andretto, V.; Malfanti, A.; Garofalo, M.; Salmaso, S.; Caliceti, P., Physical PEGylation to prevent insulin fibrillation. *Journal of pharmaceutical sciences* **2019**.
77. Zhang, F.; Du, H. N.; Zhang, Z. X.; Ji, L. N.; Li, H. T.; Tang, L.; Wang, H. B.; Fan, C. H.; Xu, H. J.; Zhang, Y., Epitaxial growth of peptide nanofilaments on inorganic surfaces: Effects of interfacial hydrophobicity/hydrophilicity. *Angewandte Chemie International Edition* **2006,** *45* (22), 3611-3613.

78. Neuhaus, O.; Farina, C.; Wekerle, H.; Hohlfeld, R., Mechanisms of action of glatiramer acetate in multiple sclerosis. *Neurology* **2001,** *56* (6), 702-708.
79. Song, J. Y.; Larson, N. R.; Thati, S.; Torres-Vazquez, I.; Martinez-Rivera, N.; Subelzu, N. J.; Leon, M. A.; Rosa-Molinar, E.; Schöneich, C.; Forrest, M. L., Glatiramer acetate persists at the injection site and draining lymph nodes via electrostatically-induced aggregation. *Journal of controlled release* **2019,** *293*, 36-47.
80. Sautès-Fridman, C.; Petitprez, F.; Calderaro, J.; Fridman, W. H., Tertiary lymphoid structures in the era of cancer immunotherapy. *Nature Reviews Cancer* **2019,** *19* (6), 307-325.
81. Neyt, K.; Perros, F.; GeurtsvanKessel, C. H.; Hammad, H.; Lambrecht, B. N., Tertiary lymphoid organs in infection and autoimmunity. *Trends in Immunology* **2012,** *33* (6), 297-305.
82. Andorko, J. I.; Hess, K. L.; Jewell, C. M., Harnessing Biomaterials to Engineer the Lymph Node Microenvironment for Immunity or Tolerance. *The AAPS Journal* **2015,** *17* (2), 323-338.
83. Tostanoski, Lisa H.; Chiu, Y.-C.; Gammon, Joshua M.; Simon, T.; Andorko, James I.; Bromberg, Jonathan S.; Jewell, Christopher M., Reprogramming the Local Lymph Node Microenvironment Promotes Tolerance that Is Systemic and Antigen Specific. *Cell Reports* **2016,** *16* (11), 2940-2952.
84. Senti, G.; Prinz Vavricka, B. M.; Erdmann, I.; Diaz, M. I.; Markus, R.; McCormack, S. J.; Simard, J. J.; Wüthrich, B.; Crameri, R.; Graf, N.; Johansen, P.; Kündig, T. M., Intralymphatic allergen administration renders specific immunotherapy faster and safer: a randomized controlled trial. *Proc Natl Acad Sci U S A* **2008,** *105* (46), 17908-17912.
85. Senti, G.; Crameri, R.; Kuster, D.; Johansen, P.; Martinez-Gomez, J. M.; Graf, N.; Steiner, M.; Hothorn, L. A.; Grönlund, H.; Tivig, C., Intralymphatic immunotherapy for cat allergy induces tolerance after only 3 injections. *Journal of Allergy and Clinical Immunology* **2012,** *129* (5), 1290-1296.
86. Jurynczyk, M.; Walczak, A.; Jurewicz, A.; Jesionek-Kupnicka, D.; Szczepanik, M.; Selmaj, K., Immune regulation of multiple sclerosis by transdermally applied myelin peptides. *Ann Neurol* **2010,** *68* (5), 593-601.
87. Walczak, A.; Siger, M.; Ciach, A.; Szczepanik, M.; Selmaj, K., Transdermal application of myelin peptides in multiple sclerosis treatment. *JAMA Neurol* **2013,** *70* (9), 1105-9.
88. Dintzis, R. Z.; Okajima, M.; Middleton, M.; Greene, G.; Dintzis, H. M., The immunogenicity of soluble haptenated polymers is determined by molecular mass and hapten valence. *The Journal of Immunology* **1989,** *143* (4), 1239-1244.
89. Hartwell, B. L.; Pickens, C. J.; Leon, M.; Northrup, L.; Christopher, M. A.; Griffin, J. D.; Martinez-Becerra, F.; Berkland, C., Soluble antigen arrays disarm antigen-specific B cells to promote lasting immune tolerance in experimental autoimmune encephalomyelitis. *Journal of Autoimmunity* **2018,** *93*, 76-88.
90. Sestak, J. O.; Fakhari, A.; Badawi, A. H.; Siahaan, T. J.; Berkland, C., Structure, size, and solubility of antigen arrays determines efficacy in experimental autoimmune encephalomyelitis. *The AAPS journal* **2014,** *16* (6), 1185-1193.
91. Hartwell, B. L.; Smalter Hall, A.; Swafford, D.; Sullivan, B. P.; Garza, A.; Sestak, J. O.; Northrup, L.; Berkland, C., Molecular dynamics of multivalent soluble antigen arrays support a two-signal co-delivery mechanism in the treatment of experimental autoimmune encephalomyelitis. *Molecular pharmaceutics* **2016,** *13* (2), 330-343.

92. Sestak, J. O.; Sullivan, B. P.; Thati, S.; Northrup, L.; Hartwell, B.; Antunez, L.; Forrest, M. L.; Vines, C. M.; Siahaan, T. J.; Berkland, C., Codelivery of antigen and an immune cell adhesion inhibitor is necessary for efficacy of soluble antigen arrays in experimental autoimmune encephalomyelitis. *Molecular Therapy-Methods & Clinical Development* **2014,** *1*, 14008.
93. Hartwell, B. L.; Pickens, C. J.; Leon, M.; Berkland, C., Multivalent Soluble Antigen Arrays Exhibit High Avidity Binding and Modulation of B Cell Receptor-Mediated Signaling to Drive Efficacy against Experimental Autoimmune Encephalomyelitis. *Biomacromolecules* **2017,** *18* (6), 1893-1907.
94. Thati, S.; Kuehl, C.; Hartwell, B.; Sestak, J.; Siahaan, T.; Forrest, M. L.; Berkland, C., Routes of administration and dose optimization of soluble antigen arrays in mice with experimental autoimmune encephalomyelitis. *Journal of pharmaceutical sciences* **2015,** *104* (2), 714-721.
95. Hartwell, B. L.; Martinez-Becerra, F. J.; Chen, J.; Shinogle, H.; Sarnowski, M.; Moore, D. S.; Berkland, C., Antigen-Specific Binding of Multivalent Soluble Antigen Arrays Induces Receptor Clustering and Impedes B Cell Receptor Mediated Signaling. *Biomacromolecules* **2016,** *17* (3), 710-722.
96. Kuehl, C.; Thati, S.; Sullivan, B.; Sestak, J.; Thompson, M.; Siahaan, T.; Berkland, C., Pulmonary administration of soluble antigen arrays is superior to antigen in treatment of experimental autoimmune encephalomyelitis. *Journal of pharmaceutical sciences* **2017,** *106* (11), 3293-3302.
97. Zhang, A. H.; Rossi, R. J.; Yoon, J.; Wang, H.; Scott, D. W., Tolerogenic nanoparticles to induce immunologic tolerance: Prevention and reversal of FVIII inhibitor formation. *Cell Immunol* **2016,** *301*, 74-81.
98. Yeste, A.; Nadeau, M.; Burns, E. J.; Weiner, H. L.; Quintana, F. J., Nanoparticle-mediated codelivery of myelin antigen and a tolerogenic small molecule suppresses experimental autoimmune encephalomyelitis. *Proc Natl Acad Sci U S A* **2012,** *109* (28), 11270-11275.
99. Tostanoski, L. H.; Chiu, Y.-C.; Andorko, J. I.; Guo, M.; Zeng, X.; Zhang, P.; Royal, W.; Jewell, C. M., Design of Polyelectrolyte Multilayers to Promote Immunological Tolerance. *ACS Nano* **2016,** *10* (10), 9334-9345.
100. Griffin, J. D.; Christopher, M. A.; Thati, S.; Salash, J. R.; Pressnall, M. M.; Weerasekara, D. B.; Lunte, S. M.; Berkland, C. J., Tocopherol Emulsions as Functional Autoantigen Delivery Vehicles Evoke Therapeutic Efficacy in Experimental Autoimmune Encephalomyelitis. *Molecular pharmaceutics* **2019,** *16* (2), 607-617.
101. Kim, J.; Li, W. A.; Choi, Y.; Lewin, S. A.; Verbeke, C. S.; Dranoff, G.; Mooney, D. J., Injectable, spontaneously assembling, inorganic scaffolds modulate immune cells in vivo and increase vaccine efficacy. *Nature biotechnology* **2015,** *33* (1), 64-72.
102. Griffin, J. D.; Song, J. Y.; Huang, A.; Sedlacek, A. R.; Flannagan, K. L.; Berkland, C. J., Antigen-specific immune decoys intercept and exhaust autoimmunity to prevent disease. *Biomaterials* **2019,** *222*, 119440.
103. Katsumata, K.; Ishihara, J.; Mansurov, A.; Ishihara, A.; Raczy, M. M.; Yuba, E.; Hubbell, J. A., Targeting inflammatory sites through collagen affinity enhances the therapeutic efficacy of anti-inflammatory antibodies. *Science Advances* **2019,** *5* (11), eaay1971.

2. Acute B-Cell Inhibition by Soluble Antigen Arrays is Valency-Dependent and Predicts Immunomodulation in Splenocytes

As published in *Biomacromolecules*

Griffin, J. Daniel, Martin A. Leon, Jean R. Salash, Michael Shao, Brittany L. Hartwell, Chad J. Pickens, Joshua O. Sestak, and Cory Berkland. "Acute B-Cell Inhibition by Soluble Antigen Arrays is Valency-Dependent and Predicts Immunomodulation in Splenocytes." *Biomacromolecules* (2019).

2.1 Introduction

Antigen presentation, especially with regards to valency (the number of antigens presented) can be a powerful therapeutic tool for either stimulating or suppressing immunity. More importantly, tuning ligand density on a macromolecule or colloid can vastly amplify or diminish immune signaling down either pathway [1-5]. Targeting antigen-specific cell surface receptors may also provide a targeted approach to directing immune responses. Moving from monovalent antigen toward a multivalent antigen display can increase therapeutic potency by virtue of increasing receptor engagement through avidity [6-9]. Investigation of both density and valency-dependent immunity matured in the late 1970s with seminal work by Howard Dintzis which illustrated starkly different immunological outcomes. By tuning properties including molecular size and ligand valency, Dintzis observed that large (>100 kD) polymers grafted with high ligand density (>20 ligands/polymer, or 1 ligand per 5 kD) were immunogenic while smaller constructs (<100 kD) with similar or lower valency (<20 ligands/polymer) tended to be tolerogenic in nature [10-13].

Central to this work was a focus on B-cells as potent directors of immunity. Nanoparticles target dendritic cells through nonspecific uptake that is mainly due to transport phenomena where depot formation at injection sites necessitates active transport by these sentinels to secondary lymphoid organs [14-17], but antigen-grafted polymers are uniquely able to target antigen-specific B-cell receptors by virtue of solubility (facilitating passive transport to B-cell rich lymph nodes), backbone flexibility, and retained ligand functionality [18]. Much has been done to elucidate the signaling events triggered by occupation of B-cell receptors (BCR), especially in the area of valency-dependent receptor clustering [19, 20]. Work by Kiessling and others has shown BCR clustering events as determinants of cell response, which has reflected many of Dintzis' findings regarding the relationship between valency and immunogenicity [18, 21]. For example, increased

avidity afforded by multivalent ligands was linked to the degree of BCR clustering as a driving factor dictating the B-cell response [22, 23]. B-cells are known to be potent initiators of immunity [24], and the successful treatment of autoimmunity through depletion of these populations has reinforced their pathological role in directing the broader immune system [25-27].

Soluble Antigen Arrays (SAgAs) exhibit size and valency characteristics of tolerogenic compounds espoused by Dintzis and others. SAgAs are constructed using antigenic peptides conjugated to a linear, polymeric hyaluronic acid (HA) backbone as antigen-specific immunotherapy (ASIT) for combating autoimmunity [28, 29]. Initially SAgAs were developed as a platform for displaying antigen alongside inhibitors of inflammatory immune responses [30-33], though recent mechanistic work has suggested the inhibitors may be somewhat dispensable. These studies have illustrated the integral role of antigen-specific binding and clustering of BCRs for effect [34-36]. Past work has focused almost exclusively on SAgAs made using a 16-20 kD HA backbone displaying roughly 10 copies of antigenic peptide ($PLP_{139-151}$) and 10 copies of a peptide (LABL) that inhibits binding of intracellular cell-adhesion molecule-1 (ICAM-1) [37]. This work has gone far to expand our understanding of how multivalent polymers evoke immunological tolerance through the antigen-specific binding and clustering of BCRs [34-36]. Past studies have shown these events anergize B cells by decreasing calcium flux, downregulating costimulatory molecule CD86 and skewing cytokines toward a regulatory phenotype [35]. Notably, valency has never been experimentally probed in this system where this avid engagement of B cells and clustering of BCRs has been identified as a central to the SAgA mechanism.

Here, we hypothesized that titrating peptide valency could modulate initial B-cell behavior and ultimately tune downstream cellular immune responses in mixed splenocytes. To investigate this supposition, we modified a 16 kD hyaluronic acid backbone and employed click chemistry [38,

[39] to synthesize a small library of SAgAs with discrete valencies for evaluation in both a B-cell *in vitro* model as well as an *ex vivo* experimental autoimmune encephalomyelitis (EAE) splenocyte assay. Furthermore, we tested the contribution of LABL as a secondary adhesion ligand by investigating the effects of SAgAs conjugated with only $PLP_{139-151}$ antigen as well as those conjugated with both $PLP_{139-151}$ and LABL.

2.2 Materials and Methods

2.2.1 Materials

Hyaluronic acid (HA) sodium salt (MW 16 kDa) was purchased from Lifecore Biomedical (Chaska, MN). 11-azido-3,6,9-trioxaundecan-1-amine (NH_2-PEG_3-N_3), *N*-hydroxysuccinimide, *N*-(3-dimethylaminopropyl)-N′-ethylcarbodiimide hydrochloride (EDC), 2-(*N*-morpholino)ethane-sulfonic acid sodium salt (MES), tris(3-hydroxypropyltriazolylmethyl)amine, and sodium ascorbate (NaAsc) were purchased from Sigma-Aldrich (St. Louis, MO). Copper(II) sulfate pentahydrate ($CuSO_4 \cdot 5H_2O$) was purchased from Acros Organics (Geel, Belgium). Alkyne-functionalized peptides with an *N*-terminal 4-pentynoic acid (homopropargyl, hp) modification, $hpPLP_{139-151}$ (hp-HSLGKWLGHPDKF-OH) and hpLABL (hp-ITDGEATDSG-OH) were purchased from Biomatik (Cambridge, ON, Canada). Unmodified $PLP_{139-151}$ (NH2-HSLGKWLGHPDKF-OH) used for rechallenge was purchased from PolyPeptide Laboratories (San Diego, CA). Fluo-4 AM was purchased from Thermo Fisher Scientific (Waltham, MA). Raji B-cells were obtained from American Type Culture Collection (ATCC, Manassas, VA). Affinity purified F(ab')2 fragment goat anti-human IgM was purchased from Jackson ImmunoResearch Laboratories (West Grove, PA). Incomplete Freund's adjuvant (IFA) and killed *Mycobacterium tuberculosis* strain H37RA were purchased from Difco (Sparks, MD). Pertussis toxin was

purchased from List Biological Laboratories (Campbell, CA). R-phycoerythrin (PE)/Cy7-conjugated anti-mouse CD3, PE-conjugated anti-mouse CD86, FITC-conjugated anti-mouse CD80, and respective isotype control antibodies were purchased from BioLegend (San Diego, CA). All other chemicals and reagents were analytical grade and used as received.

2.2.2 Synthesis and Characterization of Varied Valency Conjugates

$SAgA_{PLP}$ and $SAgA_{PLP:LABL}$ were synthesized using click chemistry as previously reported [35], where varied valency was attained by varying reactant hpPLP and hpLABL equivalents per HA-azide and assessing conjugation by RP-HPLC. Briefly, a two-step procedure was used to synthesize the conjugates used in this study. 16 kD sodium hyaluronate was reacted with 3-(ethyliminomethyleneamino)-N,N-dimethylpropan-1-amine (EDC) and N-hydroxysuccinimide (NHS) before the addition of $H_2N\text{-}PEG_3\text{-}N_3$. The product was dialyzed and lyophilized to yield hyaluronan-$PEG_3\text{-}N_3$ (HA). $hpPLP_{139\text{-}151}$ and/or hpLABL were reacted with azide-modified HA in 50 mM phosphate buffer at room temperature over 24h in the presence of tris(3-hydroxypropyltriazolylmethyl)amine (THPTA), copper (II) sulfate pentahydrate ($CuSO_4 \cdot 5H_2O$), and sodium ascorbate (NaAsc). SAgAs were analyzed quantitatively by RP-HPLC to assess target conjugation efficiencies (**Supp. Fig. 1**).

2.2.3 Raji B Cell Culture

Raji B-cells were cultured in RPMI-1640 media with L-glutamine, 10% fetal bovine serum (FBS), and 1% penicillin/streptomycin (P/S) at 37 °C and 5% CO_2. Calcium flux was performed only after cells reached confluency after 2 weeks of culture and before 8 passages were reached. Cells were split 1:10 once every 3 days, and calcium flux was performed on the second day after splitting (Raji B-cells in saturated culture at day 3 did not consistently respond to IgM stimulation).

Calcium Flux Experiments Calcium flux experiments were conducted as previously reported by our group [36]. Briefly, Raji B-cells were loaded with 5 μM Fluo-4 for 30 minutes at room temperature. Cells were washed and resuspended in Hank Balanced Salt Solution (HBSS) before establishing a baseline fluorescence level on the flow cytometer for 60s. Raji B-cells were stimulated with 20 μg/mL goat anti-human IgM, and stimulated fluorescence was measured for another 60s. Stimulated cells were then treated with varied valency conjugates (dosed on a 353.18 μM PLP basis), and fluorescence was read for an additional 180s. Data were analyzed by FlowJo, Kaluza, and GraphPad Prism.

2.2.4 Induction of EAE

EAE was induced as previously described [40, 41] in 4-6 week-old, female SJL/J mice from Envigo Laboratories. Mice were housed under specified, pathogen-free conditions at the University of Kansas and under an approved protocol by the University's Institutional Animal Care and Use Committee. EAE was induced by subcutaneously administering mice with 200 μg of PLP in a 0.2 mL emulsion of Complete Freund's Adjuvant (CFA). The CFA mixture was produced from equal volumes of PBS and IFA containing killed Mycobacterium tuberculosis strain H37RA at a final concentration of 4 mg/mL. The immunization was administered as four, 50 μL injections above the shoulders and the flanks. An additional 200 ng of pertussis toxin was given intraperitoneally on the same day of immunization (day 0) as well as day 2 post-immunization. Mice were weighed each day of the study and monitored with clinical scores starting on day 7.

2.2.5 Spleen Harvest and Splenocyte Isolation

Splenocytes were harvested from EAE and healthy control mice at peak of disease (Day 12 post-induction). Spleen harvest and splenocyte isolation was conducted as previously reported [35]. Briefly, spleens were passed through a wire mesh using the rubber stopper of a sterile 1 mL

syringe in RPMI-1640 media. The strained cellular extracts were centrifuged, and the cell pellet was resuspended in red blood cell lysis buffer. The cells were incubated on ice for 3.5 minutes to lyse splenic red blood cells. The lysis reaction was stopped by adding 10 mL RPMI 1640 media containing 10% FBS to the mixture before centrifuging. The remaining splenocyte pellets were resuspended in fresh media (RPMI 1640 media containing 10% FBS and 1% Penicillin-Streptomycin) and plated in 24-well cell culture plates at a cell density of $3x10^6$ cells/well as well as a 96-well format at $1x10^6$ cells/well. Varied valency conjugates were introduced in triplicate (both for EAE and healthy control splenocytes and in two sets per group for flow cytometry and cytokines, respectively) to each well at 141.3 µM to replicate dosing from past studies, as well as 25 µM PLP. Each cell culture was incubated for 72 hours at 37 °C in a CO_2 (5%) incubator.

2.2.6 Fluorescent Staining and Flow Cytometry

Splenocytes were collected from 24-well plates after 72 hours and stained with fluorescent antibodies according to manufacturer recommendations. Cells were washed with 1 mL of RPMI-1640 + 5% FBS before centrifuging and resuspending in 50 µL of 20 µg/mL TruStain fcX blocking antibody (anti-mouse CD16/32 antibody, Biolegend). Cells were incubated on ice for 30 minutes before adding the fluorescent antibodies and isotype controls in 50 µL for 1 hour. For flow cytometry data collection, 30,000 cells per sample were detected using a BD FACSFusion cytometer. Data were analyzed using Kaluza, FlowJo, and GraphPad Prism software.

2.2.7 Measurement of Cytokines

Following the 72-hour incubation, splenocytes in a 96-well culture plate were centrifuged. Supernatants were collected for cytokine analysis (GM-CSF, IFN- γ, IL-2, IL-21, IL-6, IL-10, IL-17, IL-23, TNF-α). Marker levels were detected using a U-Plex assay kit according to manufacturer instructions (Meso Scale Discovery). Briefly, each plate was coated with 50 µL of multiplex

coating solution consisting of linkers and biotinylated capture antibodies for each cytokine and incubated on a shaker at 700 rpm for 1 hour at room temperature. Following a 3X wash step with 150 µL PBS containing 0.05% Tween 20, 25 µL of diluent and 25 µL of sample was added to each well and incubated again for 1 hour on a shaker at room temperature. Detection antibody was then added at 50 µL/well and incubated for 1 hour. Finally, each assay plate was read using the QuickPlex multiplex plate reader (Meso Scale Discovery).

2.2.8 Measurement of Cellular Metabolism

Resazurin (7-hydroxy-3H-phenoxazin-3-one 10-oxide) was incubated with centrifuged splenocytes leftover from cytokine supernatant collection to determine cellular metabolism. 75 µM resazurin was introduced to splenocyte cultures and incubated for 3 hours. Metabolic reductive capacity was observed by viewing changes in fluorescence at excitation 560, emission 590 (Spectramax M5, Molecular Devices). Background fluorescence were taken using RPMI media and subtracted out from splenocyte readings for analysis.

2.2.9 Statistical Analysis

Statistical evaluation was performed using one- and two-way analysis of variance (ANOVA), followed by Tukey and Sidak multiple comparison tests. Statistical significance for all analyses was set at $p<0.05$. All statistical analyses were performed using GraphPad Software (GraphPad Software Inc.).

2.3 Results

2.3.1 Synthesis of Varied-Valency Conjugates

Soluble antigen arrays displaying antigen ($SAgA_{PLP}$) or antigen plus inhibitor ($SAgA_{PLP:LABL}$) were synthesized by click chemistry using previously described methods [35].

Reactant quantities of PLP and LABL peptides were titrated to yield constructs of varied valency, defined by percent ligand occupancy of the 42 azide-modified sites of a 16 kD HA backbone and calculated by RP-HPLC (**Fig. 1**, **Supp. Fig. 1**). $SAgA_{PLP}$ was synthesized in a single batch, where peptide conjugation deviated less than 5% from the desired conjugation efficiencies of 10%, 30%, 50%, 70%, and 90% occupancy. For the $SAgA_{PLP:LABL}$, the same efficiencies were targeted for overall valency, though backbone occupancy was equally divided between PLP and LABL. Single batch synthesis of these constructs maintained conjugation accuracy within 5%, excepting 90% $SAgA_{PLP:LABL}$, where average peptide conjugation peaked at 82%.

	Target Conj.		Approx. MW (kDa)	Peptide:HA		TOTAL	
				PLP	LABL	#	%
$SAgA_{PLP}$	10%	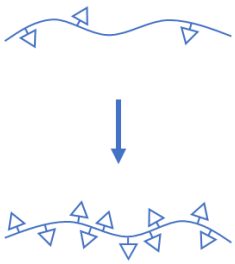	31.4	4.2	0	4.2	10%
	30%		46.0	13.3	0	13.3	32%
	50%		56.4	19.8	0	19.8	47%
	70%		72.5	29.9	0	29.9	71%
	90%		82.8	36.3	0	36.3	86%
$SAgA_{PLP:LABL}$	10%	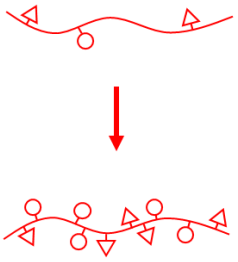	30.9	2.7	1.8	4.5	11%
	30%		41.6	7.2	5.2	12.4	29%
	50%		53.5	10.8	11.1	21.9	52%
	70%		63.0	14.4	14.7	29.1	69%
	90%		71.1	18.2	16.6	34.8	82%
		△ - PLP ○ - LABL					

Figure. 1. Synthesis of varied valency conjugates. Antigen-only ($SAgA_{PLP}$) and antigen plus inhibitor ($SAgA_{PLP:LABL}$) conjugates were synthesized by click chemistry according to varied

target conjugation efficiencies for each 16 kD HA backbone. RP-HPLC was used for characterization, and calculated peptide conjugations are reported.

2.3.2 Inhibition of Short-Term B-cell Response is Valency-Dependent.

To investigate acute valency-dependent effects of $SAgA_{PLP}$ and $SAgA_{PLP:LABL,}$ an immortalized B-cell line (Raji B cells) were loaded with a calcium-indicating fluorochrome and stimulated with anti-IgM fragments [20]. Influx of Ca^{2+} ions to B cells is critical for propagating immunity, and past SAgA studies have demonstrated the inhibition of this stimulatory signaling event [36]. Here, Stimulated B-cells showed distinctly increased peak fluorescence over baseline (**Fig 2A**). Following SAgA treatment, a brief spike was consistently observed in Fluo-4 signal intensity and monitoring over the course of three minutes illustrated a net reduction that was normalized against untreated controls (**Fig. 2B**). The degree of reduction by $SAgA_{PLP}$ and $SAgA_{PLP:LABL}$ varied in a valency-dependent manner (**Fig. 2C**). In the one-signal $SAgA_{PLP}$ constructs, reduction trended inversely with valency, and the 10% construct elicited a significantly higher reduction in calcium signal than both 70% and 90% $SAgA_{PLP}$. A similar trend was realized in the $SAgA_{PLP:LABL}$ cohort; 10% $SAgA_{PLP:LABL}$ reduced Fluo-4 signal significantly more than 70% and 90% $SAgA_{PLP:LABL}$, while 30%, 50%, and 70% constructs each outperformed 90% $SAgA_{PLP:LABL}$. Between $SAgA_{PLP}$ and $SAgA_{PLP:LABL}$, dosing was maintained on a basis of PLP concentration (*i.e.* the total molar dose of $SAgA_{PLP:LABL}$ was roughly double $SAgA_{PLP}$). For the HA alone control group, molar dose was selected to be equivalent to that of the lowest valency SAgA in this study such that this group would convey the highest relative number of molecules in solution.

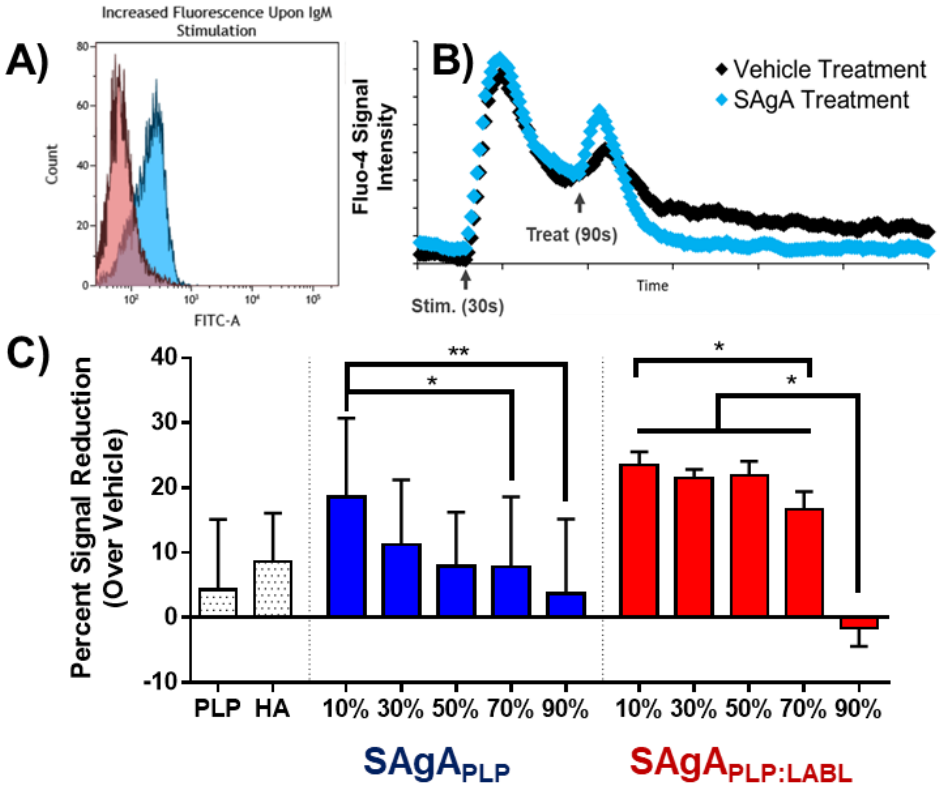

Figure. 2. Calcium flux was used as a measure of acute B-cell response by varied valency conjugates. **A)** Raji B-cells were loaded with Fluo-4 as a fluorescent calcium indicator and stimulated with IgM. Fluo-4 signal was increased from baseline (left) after stimulation (right). **B)** Acute B-cell inhibition was measured by stimulating Raji B-cells for 60 s, followed by treatment with varied valency conjugates. After treatment, mean fluorescence intensity was monitored for 180s and compared to the 60 second stimulation period. **C)** Reduced calcium signaling by one-signal varied valency conjugates ($SAgA_{PLP}$, blue), two-signal varied valency conjugates ($SAgA_{PLP:LABL}$, red), monovalent PLP and azide-modified HA alone (white). (n > 3/group, *p < 0.05, **p < 0.01).

2.3.3 Low-Valency Conjugates Induce Downstream Anergy in Mixed EAE Splenocytes

Next, varied valency conjugates were tested against EAE splenocytes to investigate whether the findings of acute B-cell inhibition could predict outcomes in a more complex system. Splenocytes were harvested from healthy mice and from EAE mice at peak of disease. We incubated cells with a rechallenge of autoantigen epitope $PLP_{139-151}$ to prompt stimulation of antigen-specific immunity in the presence of varied valency SAgAs. After a 72 hour incubation, samples were labeled for costimulatory markers CD86 and CD80 to assess the activation states of antigen-presenting cells (including B-cells). CD3 was also labeled in the panel to probe fluctuations in T cells (**Fig. 3**, **Supp. Fig. 3**). This study was conducted in two separate animal experiments, so population changes were reported as normalized to respective vehicle controls for comparison. For both $SAgA_{PLP}$ and $SAgA_{PLP:LABL}$ treatments, valency correlated with CD86 expression at 72 hours. Only low valency conjugates (10% $SAgA_{PLP}$, 10% $SAgA_{PLP:LABL}$ and 30% $SAgA_{PLP:LABL)}$ were statistically similar to healthy controls for each replicate, though all SAgAs tested elicited a decreased expression of this costimulatory marker (**Fig. 3A**). Interestingly, CD80 expression showed the inverse; the same low valency conjugates exhibited the highest CD80 expression, which may have indicated a regulatory phenotype when taken in conjunction with decreased CD86 and higher levels of T cells [42-45]. The 10% $SAgA_{PLP}$ treatment doubled CD80 expression compared to the healthy control, and 10% and 30% $SAgA_{PLP:LABL}$ remained comparable to the healthy control. When comparing the healthy control and all SAgAs, an increase in CD80 expression was consistently observed (**Fig. 3B**). SAgA treatment generally increased CD3+ populations with the exception of 70% and 90% $SAgA_{PLP}$ (**Fig. 3C**). Additional analysis of

CD86 dot plots for the historically reported, 50% conjugated $SAgA_{PLP:LABL}$ compared with low valency 10% $SAgA_{PLP:LABL}$ revealed substantial CD86 downregulation (**Fig. 3D**).

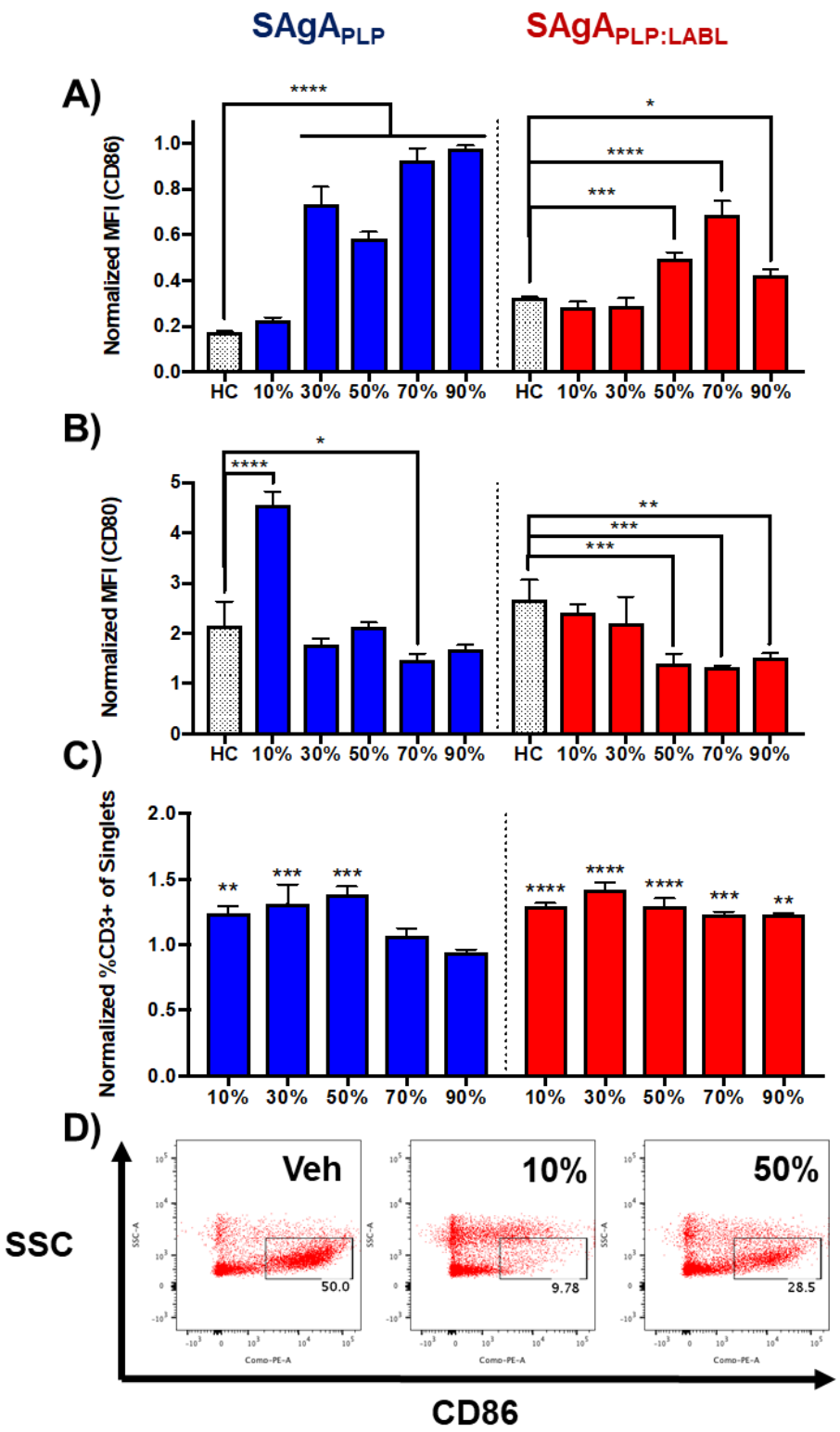

Figure. 3. Mixed splenocytes were harvested from EAE mice at peak of disease, treated with varied valency conjugates, and rechallenged with 25 μM PLP for 72h. Following the incubation,

cells were fluorescently labeled and analyzed by flow cytometry, where changes in **A)** CD86, **B)** CD80, and **C)** CD3 were compared to healthy control splenocytes (HC). All values are expressed in terms of fold-change as compared to vehicle treated EAE splenocytes. **D)** CD86 changes are shown by dot plot for PBS-treated EAE spenocytes, as well as those treated with low-valency $SAgA_{PLP:LABL}$ or $SAgA_{PLP:LABL}$ of typical valency from previous reports. (n = 3/group, *p < 0.05, **p < 0.01, ***p < 0.001, ****p < 0.0001).

Changes in cell metabolism were also investigated in splenocytes treated with varied valency conjugates (**Fig. 4**). Elevated metabolism is a hallmark of a stimulated immune response, so here we assessed decreases in metabolism to indicate inhibited immunity. The resazurin metabolic assay was employed toward this end, as this compound is reduced to fluorescent resorfurin in the presence of NADH, thus allowing quantification of cell respiration. In EAE splenocytes (**Fig. 4A**), $SAgA_{PLP}$, but not $SAgA_{PLP:LABL}$ evoked significant decreases in resazurin metabolism. Notably, in healthy splenocytes (**Fig. 4B**), only low valency 10% $SAgA_{PLP}$ did *not* increase metabolism, while $SAgA_{PLP:LABL}$ treatment largely did not affect metabolic outcomes. Cytokine analysis was also performed for EAE splenocytes treated with $SAgA_{PLP}$ and $SAgA_{PLP:LABL}$ (**Fig. 4C, Supp. Fig. 4**). These biomarkers provide signals, which can indicate the stimulatory or tolerogenic nature of an immune response. Interestingly, two distinct signatures were apparent. $SAgA_{PLP}$ was characterized by non-valency discriminate increases in IL-6 and anti-inflammatory Il-10, with a decrease in T cell proliferation suggested by reduced Il-2. However, low valency conjugates elicited smaller increases in Il-17 and Il-12, indicating less inflammation and costimulatory antigen-presentation. Inflammatory Il-17 production was markedly increased

by cells treated with $SAgA_{PLP:LABL}$ conjugates, and the cytokines Il-6 and TNF-α increased to a lesser extent.

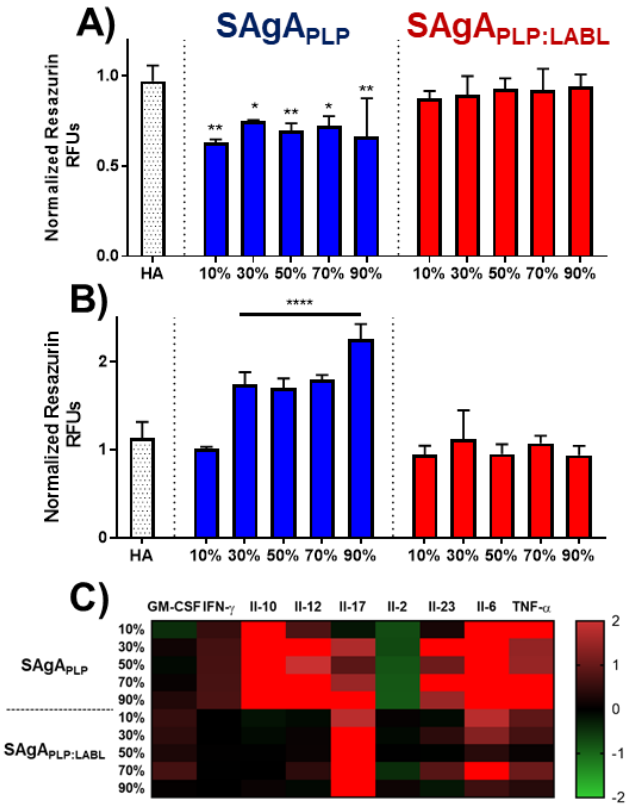

Figure. 4. A) EAE splenocytes treated with varied valency conjugates and 25 μM PLP rechallenge. Groups were incubated with resazurin after 72 hr to assess differences in cell metabolism. **B)** Likewise, healthy splenocytes were treated with varied valency conjugates and 25 μM PLP and subsequently incubated with resazurin after 72 hr. **C)** Supernatants were collected from conjugate-treated EAE splenocytes and analyzed for GM-CSF, IFN- γ, Il-10, Il-12, Il-17, Il-2, Il-23, Il-6, and TNF-α. (n = 3/group, *p < 0.05, **p < 0.01, ***p < 0.001, ****p < 0.0001).

2.4 Discussion

While the number of antigens is an important characteristic for directing the type and magnitude of immune response [1-3], the valency at which antigens are presented along a polymeric

backbone requires further exploration. In recent work by Arthur *et al.*, allogenic responses to blood transfusions were exacerbated by red blood cells containing high levels of alloantigen, but stifled by cells engineered to carry a low level of alloantigen [4]. In 2018, the Jewell group showed that quantum dots displaying low antigen density were superior to those loaded with high levels of antigen in terms of evoking tolerance [5]. Interestingly, this work focused on the modulation of dendritic cells as a mechanism, where nonspecific endocytosis drives effect. Certainly, nonspecific dendritic cell modulation was shown to be feasible in our system as well [35], but SAgAs are differentially capable of antigen-specific B-cell receptor engagement by virtue of a flexible, soluble polymeric backbone. In our present study, we evaluated the titration of antigen valency using this system, where distinct antigen-specific modulation of B-cells has been reported in autoimmune disease models [34-36].

The work presented here built from the mechanistic foundations that have positioned B cells as key targets of the SAgA mechanism [34-36]. In past work elucidating these insights, we found SAgAs to be capable of specifically engaging B cells and inhibiting the acute (*t* = minutes) influx of Ca^{2+} ions necessary to propagate immunity [36]. Later, we found these short-term changes observed *ex vivo* were correlated to *in vivo* efficacy [34]. and *Ex vivo* costimulatory marker downregulation and a humoral skewing of immunity were also correlated to *in vivo* SAgA mechanisms of EAE prevention [35].

Here, both acute-phase (**Fig. 2**) and downstream response (**Fig. 3, Fig. 4**) assays showed immunomodulatory outcomes were that were highly dependent on SAgA antigen valency (**Fig. 5**). For the short-term reduction of calcium signaling in Raji B-cells, both $SAgA_{PLP}$ and $SAgA_{PLP:LABL}$ showed an inverse relationship of similar magnitudes between calcium inhibition and PLP valency (**Fig. 5A**). Similar trending was observed when mixed EAE splenocytes were treated with SAgAs

for 72 hours. CD86+ cells decreased with valency, meaning $SAgA_{PLP}$ and $SAgA_{PLP:LABL}$ of low PLP conjugation translated to the highest reductions of this costimulatory marker (**Fig. 5B**). Together, these data suggest that low valency, but not monovalent, antigen display is able to evoke the most potent immunosuppressive effects in both the acute and downstream frames of immunity.

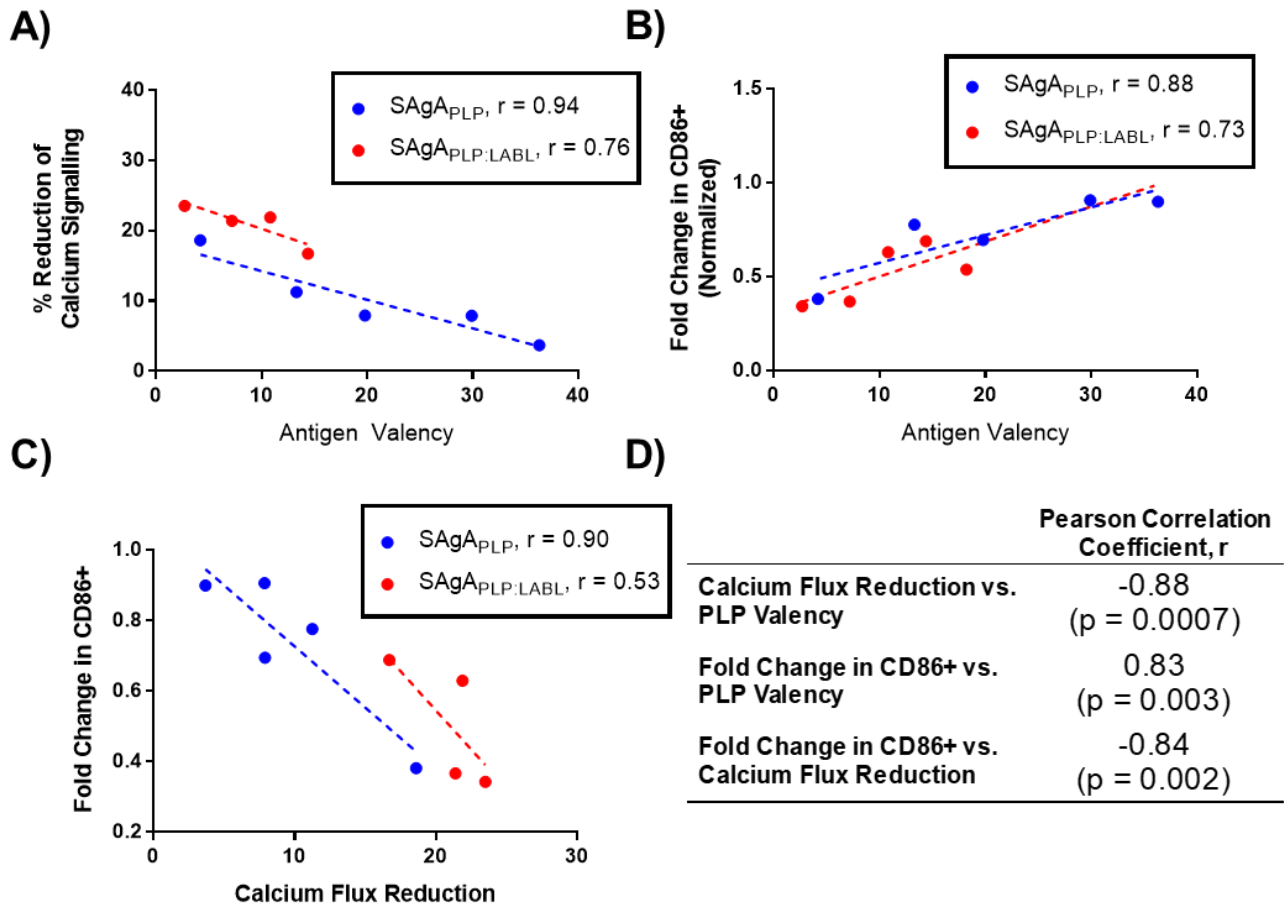

	Pearson Correlation Coefficient, r
Calcium Flux Reduction vs. PLP Valency	-0.88 (p = 0.0007)
Fold Change in CD86+ vs. PLP Valency	0.83 (p = 0.003)
Fold Change in CD86+ vs. Calcium Flux Reduction	-0.84 (p = 0.002)

Figure. 5. Inhibitory outcomes from treating EAE splenocytes with varied valency conjugates were assessed according to PLP valency, including **A)** acute inhibition of B-cells and **B)** CD86 expression. Pearson correlation coefficients were calculated for each comparison. **C)** Correlation between acute B-cell inhibition and downstream CD86+ expression was also investigated. **D)** The relationship between PLP valency, calcium flux reduction, and CD86 expression changes was collectively analyzed to form a correlation matrix where Pearson correlation coefficients were

expressed. In Figures 5A and 5C, data points for 90% $SAgA_{PLP:LABL}$ are omitted for clarity, but readouts from this group are applied for the analysis in Figures 5D.

Interestingly, $SAgA_{PLP:LABL}$ showed an apparent advantage over $SAgA_{PLP}$ in acute phase calcium inhibition that was not observed in the splenocyte experiments (**Fig. 5A**). While not statistically definitive, this discrepancy could be due to increased binding avidity afforded by the inclusion of LABL, which may allow $SAgA_{PLP:LABL}$ to engage and persist at the cell surface through binding ICAM-1 in addition to B-cell receptors. This marginal increase in short-term performance does not appear to critical to downstream effect, as CD86 downregulation of $SAgA_{PLP:LABL}$ mirrored $SAgA_{PLP}$ (**Fig. 4B**). The splenocyte experiment demonstrated a clear valency-dependent trend was maintained wherein the lowest valency $SAgA_{PLP}$ and $SAgA_{PLP:LABL}$ reduced CD86 expression to the greatest extent. Notably, this effect was found to *inversely* trend with CD80, another common marker of costimulation (**Fig. 3B**). While initially unexpected, reports have indicated CD80 in the absence of CD86, directs inhibition of T cells when regulatory T and B subsets are prevalent [42-45]. The potential for this phenomenon to explain the data we observed is substantiated by an overall increase in T cell populations (possibly reflecting an increase in T_{regs} caused by SAgA treatment, **Fig. 3C**), though future studies are necessary to evaluate fully.

Generally, incubation of EAE splenocytes with SAgAs led to a decreased metabolism after 72 hours (**Fig. 4A**). In healthy splenocytes, 10% $SAgA_{PLP}$ and all $SAgA_{PLP:LABL}$ exhibited resazurin levels comparable to vehicle-treated control, but $SAgA_{PLP}$ of valency 30% and higher caused an elevated metabolism. This finding may be due to the higher antigen number of $SAgA_{PLP}$ over $SAgA_{PLP:LABL}$ triggering more immunogenicity, though this change did not translate to a stimulated immune response overall (**Supp. Fig. 3**). Cytokine responses between $SAgA_{PLP}$ and

$SAgA_{PLP:LABL}$ seemed distinct, possibly highlighting a difference in signaling pathways created by the inclusion of LABL (**Fig. 4C**). In $SAgA_{PLP}$, a robust Il-10 response with the elevation of many other markers was consistent with past work, but the increased Il-17 response in $SAgA_{PLP:LABL}$ treated splenocytes was atypical. Differences in cytokines did not, however, translate to altered cell phenotypes (**Fig. 3**).

Adding to the valency dependencies outlined in this work, acute B cell calcium flux inhibition was found to be highly correlative of CD86 expression in a mixed population of splenocytes (**Fig. 5C**). The implication of this observation further substantiates our past investigations of B cells as a key target of SAgAs for effect. While other mechanisms may aid in SAgA efficacy, fold change in calcium flux in this experiment proved informative for long-term (72 hours) outcomes in a more complex, mixed system of splenocytes. Ultimately, correlations between antigen valency, calcium flux reduction, and CD86 expression were all highly significant (**Fig. 5D**).

2.5 Conclusions

SAgAs were found to be capable of modulating B-cell calcium signaling and mixed splenocyte CD86 expression in a valency-dependent fashion. SAgAs were most effective when antigen valency was low, reflecting Dintzis' "rules" with greater resolution than previously elucidated [46]. SAgAs displaying 4-7 PLP were most effective, overshadowing the conventional, albeit effective SAgA constructs displaying 10 PLP, which have been the focal point of our prior studies. Furthermore, the level of acute B-cell inhibition studied in isolation correlated with downregulation of CD86 in splenocytes. Together, studies indicated SAgA valency was an

important driver of immune response, which casts light on the role of valency when designing antigen-specific immunotherapies.

2.6 Supporting Information

Supporting information is available. Figures include HPLC quantification of peptide conjugation, flow cytometry analysis, additional healthy splenocyte data, and raw cytokine results.

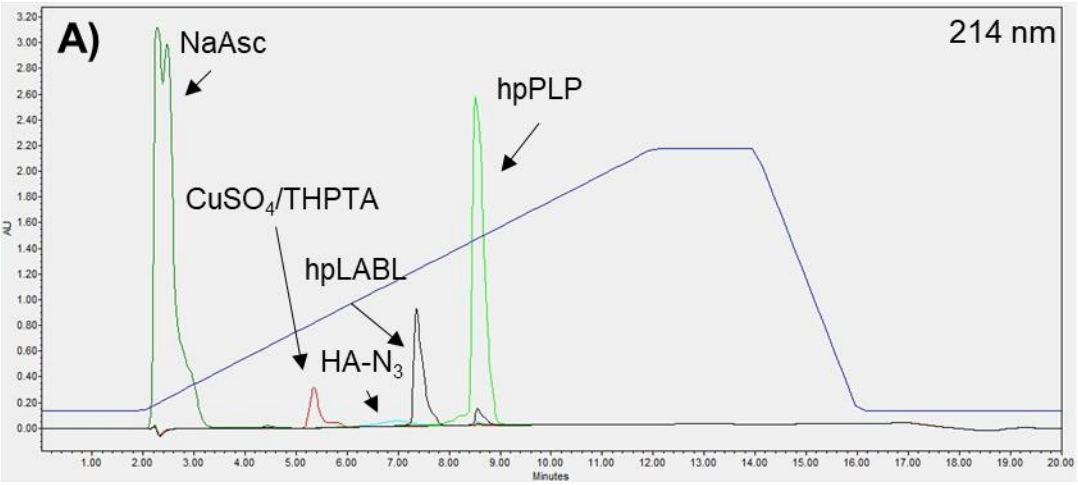

C) $$Number_{conj.} = \left(\frac{n_{peptide}}{n_{HA}}\right)\left(1 - \frac{PA_{post}}{PA_{pre}}\right)$$

Supp. Fig. 1. All varied valency construct conjugation efficiencies were determined using a 20 minute Reverse-Phase HPLC method employing a 95/5 to 30/70 aqueous:organic gradient scheme on a C4 RP column. **A)** Individual click reaction component peak retention times (HA-N_3, $CuSO_4$/THPTA, NaAsc, hpPLP, and hpLABL) are represented. **B)** Varied valency construct reaction mixtures were sampled before beginning reactions (Pre, green), after the reaction (Post, brown), and after dialysis (black), and **C)** conjugation efficiency was calculated by taking the molar (*n*) ratio of peptide:HA and multiplying by the reduction in peak area (PA) from Pre to Post reaction.

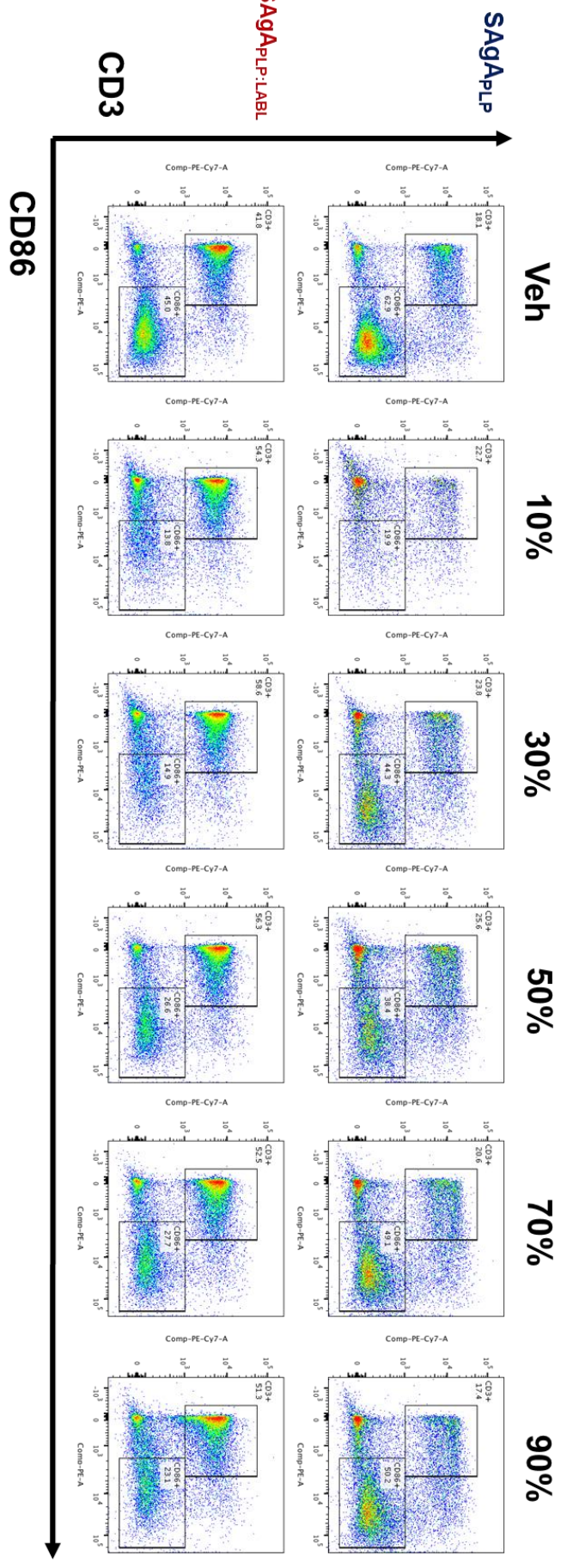
SAgAPLP
SAgAPLP:LABL
CD3
CD86
Veh
10%
30%
50%
70%
90%
Comp-PE-Cy7-A
Comp-PE-A

Supp. Fig. 2. Cytometric population analysis for EAE splenocytes treated with varied valency $SAgA_{PLP}$ (top) and $SAgA_{PLP:LABL}$ (bottom) yielded valency-dependent changes in CD86 and CD3.

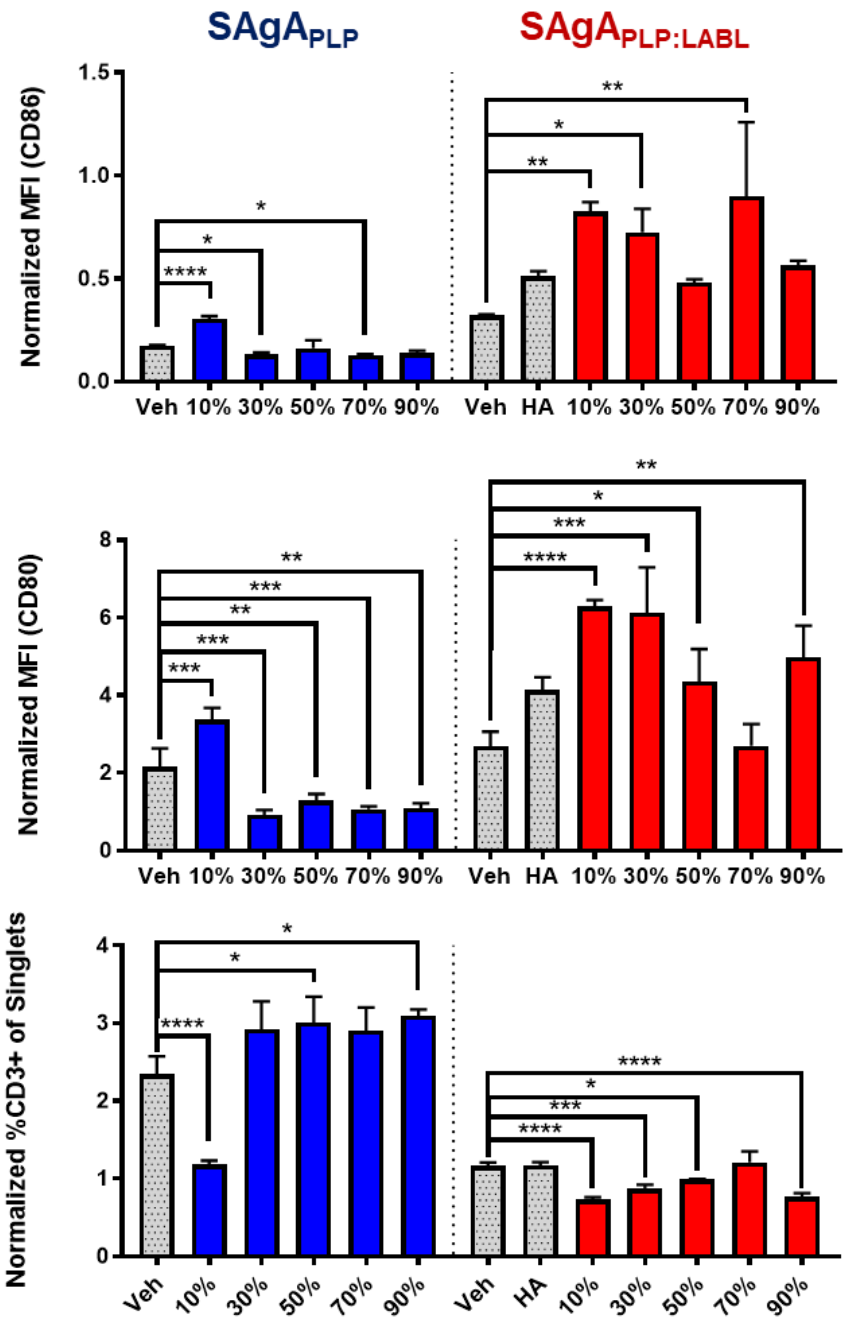

Supp. Fig. 3. Changes in **A)** CD86, **B)** CD80, and **C)** CD3 expression were measured in healthy splenocytes treated with varied valency conjugates. (*n* = 3/group, *p < 0.05, **p < 0.01, ***p < 0.001, ****p < 0.0001).

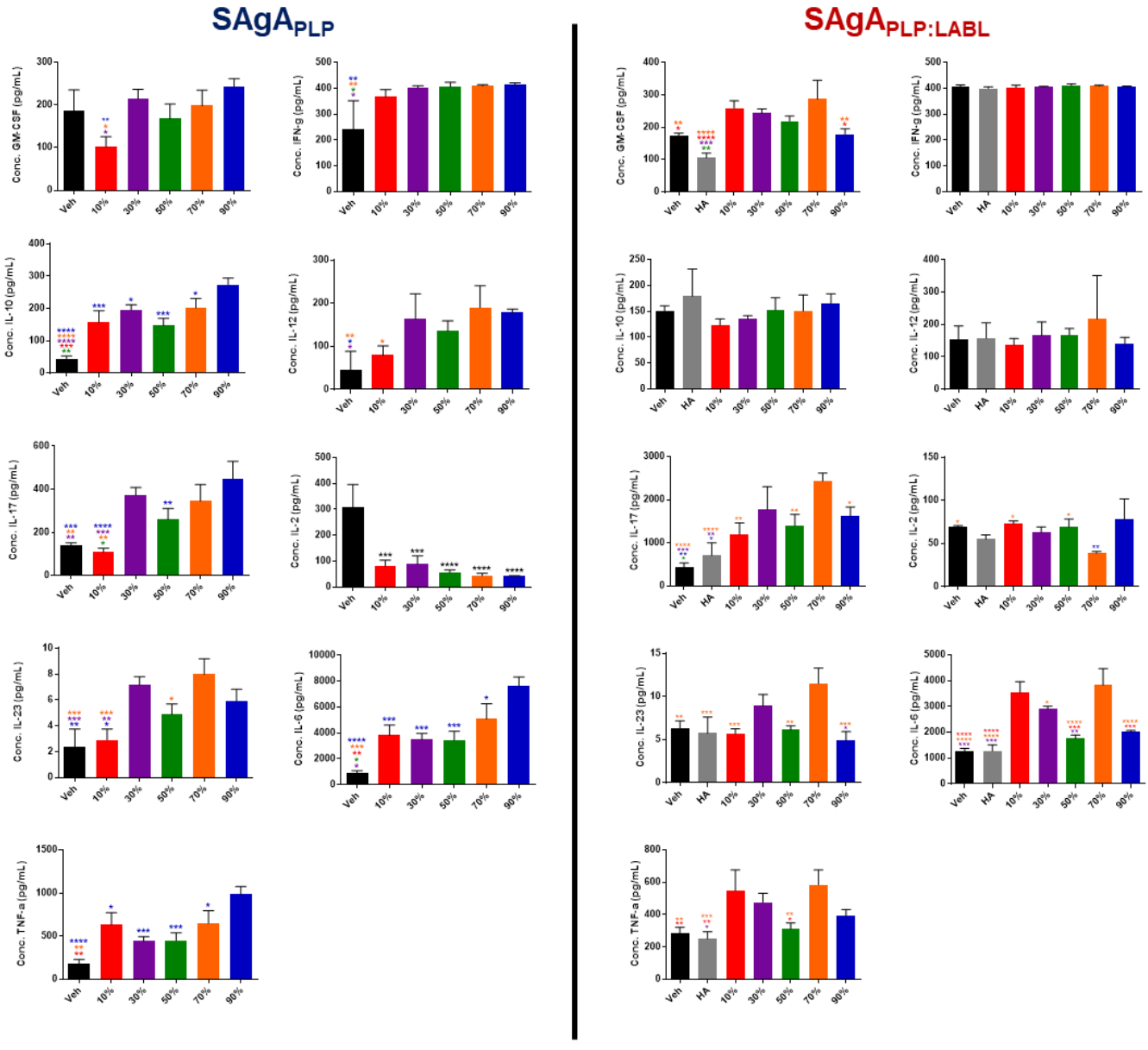

Supp. Fig. 4. Cytokines collected from EAE splenocytes treated with varied valency conjugates are reported in terms of concentration (pg/mL) with significance. (n = 3/group, *p < 0.05, **p < 0.01, ***p < 0.001, ****p < 0.0001).

2.7 Acknowledgments

JDG and BLH were supported by the Madison and Lila Self Graduate Fellowship at the University of Kansas. Also, authors MAL and CJP gratefully acknowledge support from the National Institutes of Health Graduate Training Program in Dynamic Aspects of Chemical Biology Grant (T32 GM008545) from the National Institutes of General Medical Sciences.

2.8 References

1. Hartwell, B. L.; Antunez, L.; Sullivan, B. P.; Thati, S.; Sestak, J. O.; Berkland, C., Multivalent nanomaterials: learning from vaccines and progressing to antigen-specific immunotherapies. *J. Pharm. Sci.* **2015,** *104* (2), 346-361.
2. Bachmann, M. F.; Jennings, G. T., Vaccine delivery: a matter of size, geometry, kinetics and molecular patterns. *Nat. Rev. Immunol.* **2010,** *10* (11), 787.
3. Gestwicki, J. E.; Cairo, C. W.; Strong, L. E.; Oetjen, K. A.; Kiessling, L. L., Influencing receptor− ligand binding mechanisms with multivalent ligand architecture. *J. Am. Chem. Soc.* **2002,** *124* (50), 14922-14933.
4. Arthur, C. M.; Patel, S. R.; Smith, N. H.; Bennett, A.; Kamili, N. A.; Mener, A.; Gerner-Smidt, C.; Sullivan, H. C.; Hale, J. S.; Wieland, A.; Youngblood, B.; Zimring, J. C.; Hendrickson, J. E.; Stowell, S. R., Antigen Density Dictates Immune Responsiveness following Red Blood Cell Transfusion. *J. Immunol.* **2017,** *198* (7), 2671-2680.
5. Hess, K. L.; Oh, E.; Tostanoski, L. H.; Andorko, J. I.; Susumu, K.; Deschamps, J. R.; Medintz, I. L.; Jewell, C. M., Engineering Immunological Tolerance Using Quantum Dots to Tune the Density of Self-Antigen Display. *Adv. Funct. Mater.* **2017,** *27* (22), 1700290.
6. Minguet, S.; Dopfer, E.-P.; Schamel, W. W. A., Low-valency, but not monovalent, antigens trigger the B-cell antigen receptor (BCR). *Int. Immunol.* **2010,** *22* (3), 205-212.
7. Nielsen, U. B.; Adams, G. P.; Weiner, L. M.; Marks, J. D., Targeting of bivalent anti-ErbB2 diabody antibody fragments to tumor cells is independent of the intrinsic antibody affinity. *Cancer Res.* **2000,** *60* (22), 6434-40.
8. Adams, G. P.; Tai, M.-S.; McCartney, J. E.; Marks, J. D.; Stafford, W. F.; Houston, L. L.; Huston, J. S.; Weiner, L. M., Avidity-Mediated Enhancement of In vivo Tumor Targeting by Single-Chain Fv Dimers. *Clin. Cancer Res.* **2006,** *12* (5), 1599-1605.

9. Kubetzko, S.; Balic, E.; Waibel, R.; Zangemeister-Wittke, U.; Pluckthun, A., PEGylation and multimerization of the anti-p185HER-2 single chain Fv fragment 4D5: effects on tumor targeting. *J. Biol. Chem.* **2006,** *281* (46), 35186-201.
10. Dintzis, H. M.; Dintzis, R. Z.; Vogelstein, B., Molecular determinants of immunogenicity: the immunon model of immune response. *Proc. Natl. Acad. Sci.* **1976,** *73* (10), 3671-3675.
11. Dintzis, R. Z.; Middleton, M. H.; Dintzis, H. M., Studies on the immunogenicity and tolerogenicity of T-independent antigens. *J. Immunol.* **1983,** *131* (5), 2196-2203.
12. Dintzis, R. Z.; Middleton, M. H.; Dintzis, H. M., Inhibition of anti-DNP antibody formation by high doses of DNP-polyacrylamide molecules; effects of hapten density and hapten valence. *J. Immunol.* **1985,** *135* (1), 423-427.
13. Dintzis, R. Z.; Okajima, M.; Middleton, M.; Greene, G.; Dintzis, H., The immunogenicity of soluble haptenated polymers is determined by molecular mass and hapten valence. *J. Immunol.* **1989,** *143* (4), 1239-1244.
14. Manolova, V.; Flace, A.; Bauer, M.; Schwarz, K.; Saudan, P.; Bachmann, M. F., Nanoparticles target distinct dendritic cell populations according to their size. *Eur. J. Immunol.* **2008,** *38* (5), 1404-1413.
15. Reddy, S. T.; Rehor, A.; Schmoekel, H. G.; Hubbell, J. A.; Swartz, M. A., In vivo targeting of dendritic cells in lymph nodes with poly (propylene sulfide) nanoparticles. *J. Control. Release* **2006,** *112* (1), 26-34.
16. Uto, T.; Wang, X.; Sato, K.; Haraguchi, M.; Akagi, T.; Akashi, M.; Baba, M., Targeting of antigen to dendritic cells with poly (γ-glutamic acid) nanoparticles induces antigen-specific humoral and cellular immunity. *J. Immunol.* **2007,** *178* (5), 2979-2986.
17. Maldonado, R. A.; LaMothe, R. A.; Ferrari, J. D.; Zhang, A.-H.; Rossi, R. J.; Kolte, P. N.; Griset, A. P.; O'Neil, C.; Altreuter, D. H.; Browning, E.; Johnston, L.; Farokhzad, O. C.; Langer, R.; Scott, D. W.; von Andrian, U. H.; Kishimoto, T. K., Polymeric synthetic nanoparticles for the induction of antigen-specific immunological tolerance. *Proc. Natl. Acad. Sci.* **2015,** *112* (2), E156-E165.
18. Puffer, E. B.; Pontrello, J. K.; Hollenbeck, J. J.; Kink, J. A.; Kiessling, L. L., Activating B Cell Signaling with Defined Multivalent Ligands. *ACS Chem. Biol.* **2007,** *2* (4), 252-262.
19. Fleire, S. J.; Goldman, J. P.; Carrasco, Y. R.; Weber, M.; Bray, D.; Batista, F. D., B Cell Ligand Discrimination Through a Spreading and Contraction Response. *Science* **2006,** *312* (5774), 738-741.
20. Minguet, S.; Klasener, K.; Schaffer, A. M.; Fiala, G. J.; Osteso-Ibanez, T.; Raute, K.; Navarro-Lerida, I.; Hartl, F. A.; Seidl, M.; Reth, M.; Del Pozo, M. A., Caveolin-1-dependent nanoscale organization of the BCR regulates B cell tolerance. *Nat. Immunol.* **2017,** *18* (10), 1150-1159.
21. Cairo, C. W.; Gestwicki, J. E.; Kanai, M.; Kiessling, L. L., Control of Multivalent Interactions by Binding Epitope Density. *J. Am. Chem. Soc.* **2002,** *124* (8), 1615-1619.
22. Kiessling, L. L.; Gestwicki, J. E.; Strong, L. E., Synthetic multivalent ligands in the exploration of cell-surface interactions. *Curr. Opin. Chem. Biol.* **2000,** *4* (6), 696-703.
23. Gestwicki, J. E.; Cairo, C. W.; Strong, L. E.; Oetjen, K. A.; Kiessling, L. L., Influencing Receptor−Ligand Binding Mechanisms with Multivalent Ligand Architecture. *J. Am. Chem. Soc.* **2002,** *124* (50), 14922-14933.
24. Lund, F. E.; Randall, T. D., Effector and regulatory B cells: modulators of CD4+ T cell immunity. *Nat. Rev. Immunol.* **2010,** *10* (4), 236.

25. Franks, S. E.; Getahun, A.; Hogarth, P. M.; Cambier, J. C., Targeting B cells in treatment of autoimmunity. *Curr. Opin. Immunol.* **2016,** *43*, 39-45.
26. Liossis, S.-N. C.; Sfikakis, P. P., Rituximab-induced B cell depletion in autoimmune diseases: potential effects on T cells. *Clin. Immunol.* **2008,** *127* (3), 280-285.
27. Milo, R., Therapeutic strategies targeting B-cells in multiple sclerosis. *Autoimmun. Rev.* **2016,** *15* (7), 714-718.
28. Berkland, C.; Sestak, J.; Siahaan, T., Bifunctional conjugate compositions and associated methods. Google Patents: 2013.
29. Sestak, J.; Mullins, M.; Northrup, L.; Thati, S.; Laird Forrest, M.; Siahaan, T. J.; Berkland, C., Single-step grafting of aminooxy-peptides to hyaluronan: A simple approach to multifunctional therapeutics for experimental autoimmune encephalomyelitis. *J. Control. Release* **2013,** *168* (3), 334-340.
30. Sestak, J. O.; Sullivan, B. P.; Thati, S.; Northrup, L.; Hartwell, B.; Antunez, L.; Forrest, M. L.; Vines, C. M.; Siahaan, T. J.; Berkland, C., Codelivery of antigen and an immune cell adhesion inhibitor is necessary for efficacy of soluble antigen arrays in experimental autoimmune encephalomyelitis. *Mol Ther Methods Clin Dev* **2014,** *1*, 14008.
31. Hartwell, B. L.; Smalter Hall, A.; Swafford, D.; Sullivan, B. P.; Garza, A.; Sestak, J. O.; Northrup, L.; Berkland, C., Molecular Dynamics of Multivalent Soluble Antigen Arrays Support a Two-Signal Co-delivery Mechanism in the Treatment of Experimental Autoimmune Encephalomyelitis. *Mol. Pharm.* **2016,** *13* (2), 330-43.
32. Northrup, L.; Sestak, J. O.; Sullivan, B. P.; Thati, S.; Hartwell, B. L.; Siahaan, T. J.; Vines, C. M.; Berkland, C., Co-delivery of autoantigen and b7 pathway modulators suppresses experimental autoimmune encephalomyelitis. *Aaps j* **2014,** *16* (6), 1204-13.
33. Northrup, L.; Christopher, M. A.; Sullivan, B. P.; Berkland, C., Combining antigen and immunomodulators: Emerging trends in antigen-specific immunotherapy for autoimmunity. *Adv. Drug Del. Rev.* **2016,** *98*, 86-98.
34. Hartwell, B. L.; Pickens, C. J.; Leon, M.; Berkland, C., Multivalent Soluble Antigen Arrays Exhibit High Avidity Binding and Modulation of B Cell Receptor-Mediated Signaling to Drive Efficacy against Experimental Autoimmune Encephalomyelitis. *Biomacromolecules* **2017,** *18* (6), 1893-1907.
35. Hartwell, B. L.; Pickens, C. J.; Leon, M.; Northrup, L.; Christopher, M. A.; Griffin, J. D.; Martinez-Becerra, F.; Berkland, C., Soluble antigen arrays disarm antigen-specific B cells to promote lasting immune tolerance in experimental autoimmune encephalomyelitis. *J. Autoimmun.* **2018,** *93*, 76-88.
36. Hartwell, B. L.; Martinez-Becerra, F. J.; Chen, J.; Shinogle, H.; Sarnowski, M.; Moore, D. S.; Berkland, C., Antigen-Specific Binding of Multivalent Soluble Antigen Arrays Induces Receptor Clustering and Impedes B Cell Receptor Mediated Signaling. *Biomacromolecules* **2016,** *17* (3), 710-722.
37. Yusuf-Makagiansar, H.; Anderson, M. E.; Yakovleva, T. V.; Murray, J. S.; Siahaan, T. J., Inhibition of LFA-1/ICAM-1 and VLA-4/VCAM-1 as a therapeutic approach to inflammation and autoimmune diseases. *Med. Res. Rev.* **2002,** *22* (2), 146-167.
38. Nandivada, H.; Jiang, X. W.; Lahann, J., Click chemistry: Versatility and control in the hands of materials scientists. *Adv. Mater.* **2007,** *19* (17), 2197-2208.
39. Pickens, C. J.; Johnson, S. N.; Pressnall, M. M.; Leon, M. A.; Berkland, C. J., Practical Considerations, Challenges, and Limitations of Bioconjugation via Azide-Alkyne Cycloaddition. *Bioconjug. Chem.* **2018,** *29* (3), 686-701.

40. Northrup, L.; Griffin, J. D.; Christopher, M. A.; Antunez, L. R.; Hartwell, B. L.; Pickens, C. J.; Berkland, C., Co-delivery of autoantigen and dexamethasone in incomplete Freund's adjuvant ameliorates experimental autoimmune encephalomyelitis. *J. Control. Release* **2017,** *266*, 156-165.
41. Griffin, J. D.; Christopher, M. A.; Thati, S.; Salash, J. R.; Pressnall, M. M.; Weerasekara, D. B.; Lunte, S. M.; Berkland, C. J., Tocopherol Emulsions as Functional Autoantigen Delivery Vehicles Evoke Therapeutic Efficacy in Experimental Autoimmune Encephalomyelitis. *Molecular pharmaceutics* **2019,** *16* (2), 607-617.
42. Zheng, Y.; Manzotti, C. N.; Liu, M.; Burke, F.; Mead, K. I.; Sansom, D. M., CD86 and CD80 differentially modulate the suppressive function of human regulatory T cells. *J. Immunol.* **2004,** *172* (5), 2778-2784.
43. Nova-Lamperti, E.; Fanelli, G.; Becker, P. D.; Chana, P.; Elgueta, R.; Dodd, P. C.; Lord, G. M.; Lombardi, G.; Hernandez-Fuentes, M. P., IL-10-produced by human transitional B-cells down-regulates CD86 expression on B-cells leading to inhibition of CD4+ T-cell responses. *Sci. Rep.* **2016,** *6*, 20044.
44. Manzotti, C. N.; Tipping, H.; Perry, L. C.; Mead, K. I.; Blair, P. J.; Zheng, Y.; Sansom, D. M., Inhibition of human T cell proliferation by CTLA-4 utilizes CD80 and requires CD25+ regulatory T cells. *Eur. J. Immunol.* **2002,** *32* (10), 2888-2896.
45. Sansom, D. M.; Manzotti, C. N.; Zheng, Y., What's the difference between CD80 and CD86? *Trends Immunol.* **2003,** *24* (6), 313-318.
46. Dintzis, R. Z.; Okajima, M.; Middleton, M. H.; Dintzis, H. M., Inhibition of antibody formation by receptor cross-linking: the molecular characteristics of inhibitory haptenated polymers. *Eur. J. Immunol.* **1990,** *20* (1), 229-232.

3. Tocopherol Emulsions as Functional Autoantigen Delivery Vehicles Evoke Therapeutic Efficacy in Experimental Autoimmune Encephalomyelitis

As published in *Molecular Pharmaceutics*

Griffin, J. Daniel, Matthew A. Christopher, Sharadvi Thati, Jean R. Salash, Melissa M. Pressnall, Dhanushka B. Weerasekara, Susan M. Lunte, and Cory J. Berkland. "Tocopherol Emulsions as Functional Autoantigen Delivery Vehicles Evoke Therapeutic Efficacy in Experimental Autoimmune Encephalomyelitis." *Molecular pharmaceutics* (2019).

3.1 Introduction

Current therapeutic approaches to autoimmune diseases such as multiple sclerosis (MS) are largely relegated to symptom management alone, and the most effective drugs evoke efficacy by imposing global immunosuppression [1-3]. This immunosuppression leaves patients susceptible to life-threatening side effects such as opportunistic infections and malignancies [4-7]. Indeed, there is a clear history of positive correlation between drug effectiveness and risk for adverse outcomes in the clinical treatment of MS [6, 8]. Antigen-specific immunotherapy (ASIT) has proven itself compelling as a means to more selectively disarm autoimmunity without global immunosuppression. Recent trends suggest co-delivery of autoantigen with an immunomodulatory drug may target autoreactive cells to overcome the conventional efficacy/safety trade-off in autoimmune therapeutics [9-13].

Co-delivering ASIT and an immune modulator requires spatiotemporal restriction of antigen and drug to ensure processing in the same immunological context for eliciting potent, antigen-specific outcomes [14, 15]. To accomplish this necessity of space-time proximity, formulations have historically utilized vehicles from applications such as vaccines, cancer immunotherapy, and sustained-release drug delivery [16-20]. While the polymers and metals that make up these vehicles are often touted as biocompatible and immunologically inert, co-delivery applications for autoimmunity have periodically shown negative outcomes for vehicle control groups in measures such as autoantibody titers and clinical disease severity [21, 22]. These studies each reported overall promising therapeutic results, perhaps by overcoming deleterious vehicle effects on immunity via the immunosuppression imparted through the inclusion of drug. Ultimately, works such as these have resulted in a paradigm that inclusion of immunosuppressive drugs is required to overcome inherent immunogenicity of formulations.

In recent work, co-delivery of autoantigen and dexamethasone in incomplete Freund's adjuvant was shown to ameliorate experimental autoimmune encephalomyelitis (EAE), a murine model of relapsing-remitting multiple sclerosis [23]. Nevertheless, incomplete Freund's adjuvant is substantially toxic in humans and has even been used to *induce* EAE in primates [24], suggesting poor feasibility in terms of practical therapeutic application for autoimmune diseases such as MS. It seems an efficacious ASIT to combat autoimmunity should utilize components of a co-delivery system optimally tolerable to humans. Furthermore, ASIT delivery vehicles that also exhibit desirable immunological function may simplify formulation, yielding a more translatable approach to restore immune tolerance.

Tocopherol emulsions (ETPGS) consisting of vitamin E oil and a PEGylated vitamin E surfactant (D-α-Tocopherol polyethylene glycol 1000 succinate, TPGS) in an aqueous continuous phase have been approved as safe pharmaceutical adjuvants since 2005 [25, 26]. The original application for ETPGS was the sustained delivery of paclitaxel as a chemotherapeutic agent, but since its emergence, the formulation has been pervasively modified and applied in other applications such as intestinal permeation enhancement and copolymerization [27, 28]. Because it has already been approved in humans, tolerability is known when considering it as a potential vehicle. In addition, the wealth of various ETPGS formulations explored in many discrete biomedical applications indicate the physical properties of the suspension are highly tunable. For particulate ASIT delivery approaches in cancer, autoimmunity, and vaccines, the immunotherapeutic effect is most commonly evoked through nonspecific uptake of the formulation by antigen-presenting cells (APCs), leading to downstream inflammation or tolerance by processing of antigen in the context of immunostimulatory or suppressive compounds [29-31]. Since ETPGS droplet size is versatile, suspensions can be created at mean diameters under 500 nm for optimal APC uptake [32].

Importantly, ETPGS can be tuned to have a mean diameter still greater than 100 nm to enable APC interaction to occur while increasing formulation persistence at the site of injection [33-35]. The flexibility of ETPGS for ASIT delivery is augmented by the fact vitamin E is an effective antioxidant. The propagation of an immune response is driven by a cascade of inflammatory events [36, 37]. By staving off inflammation, antioxidant compounds can skew immune responses toward tolerance [27, 38].

Herein, we report on the application of ETPGS to deliver autoantigen and ameliorate EAE *in vivo*. Efficacy was determined by comparing disease scores and weights of EAE mice. The immune response was characterized by quantifying cytokine responses in splenocytes and by shifts in autoantibody responses in blood and in tissues from the central nervous systems in mice. Finally, real-time measurement of oxidation in antigen presenting cells was conducted to more deeply understand the mechanism of ETPGS as an ASIT delivery vehicle.

3.2 Materials and Methods

3.2.1 Materials

$PLP_{139-151}$ (PLP), the antigenic peptide used, was purchased from Biomatik (Cambridge, ON, Canada). For the induction of EAE, incomplete Freund's adjuvant (IFA) and killed *Mycobacterium tuberculosis* strain H37RA were purchased from Difco (Sparks, MD) as well as pertussis toxin, purchased from List Biological Laboratories (Campbell, CA). Murine RAW 264.7 cells (ATCC® TIB71™) along with Dulbecco's Modified Eagle's Medium (DMEM), phenol red-free DMEM, fetal bovine serum (FBS), and penicillin/streptomycin antibiotic solution were procured from American Type Culture Collection (ATCC, Manassas, VA, USA) and Atlanta Biologicals (Flowery Branch, GA, USA). Diethyldithiocarbamate (DDC), 2-methoxyestradiol (2-

ME), phorbol 12-myristate 13- acetate (PMA), phosphate-buffered saline (PBS), lipopolysaccharide (LPS, from *Escherichia coli* 0111:B4), sodium dodecyl sulfate (SDS), and bovine serum albumin (BSA) were purchased from Sigma-Aldrich (St. Louis, MO, USA). Interferon-γ (IFN-γ) was obtained from Calbiochem (Gibbstown, NJ, USA). 4-Amino-5-methylamino-2',7'-difluorofluorescein diacetate (DAF-FM DA) and MitoSOX Red were supplied from Life Technologies (Carlsbad, CA, USA). For flow cytometry, Alexa Fluor® 488-conjugated anti-mouse CD3, Alexa Fluor® 647-conjugated anti-mouse CD19, and Pacific Blue™-conjugated anti-mouse CD11c, and matched isotype controls were purchased from Biolegend (San Diego, CA). Goat HRP-conjugated anti-Mouse IgG for ELISAs was also purchased from Biolegend (San Diego, CA). Vitamin E and TPGS were received from Sigma Aldrich (St. Louis, MO). Other chemicals and reagents used for these studies were analytical grade and used as received.

3.2.2 Preparation of ETPGS Emulsions

ETPGS emulsions were prepared by adding TPGS to 1X phosphate-buffered saline (PBS), and agitating overnight at 42.5°C. If PLP was required, the peptide was then dissolved in the mixture before the aqueous phase was gently pipetted to a tube containing α-tocopherol mineral oil. Next, the tube containing α-tocopherol, TPGS and PBS (with or without PLP) was sonicated using a Fisher Scientific™ Sonic Dismembrator Model 500 with a 10 second *on*, 2 second *off* cadence (30% intensity) for 2 minutes, dipping the emulsion mixture in an ice bath during *off* periods to maintain temperature. After sonication, the emulsion was poured into a glass scintillation vial for storage, either on ice or at 4°C. For recipe development, amounts used of α-tocopherol, TPGS and PBS were systematically varied, though final proportions used for the ETPGS emulsions in these studies were 2:1 α-tocopherol:TPGS ultimately constituting 10% of a 10:90 oil-in-water emulsion.

3.2.3 Characterizing Size and Peptide Release from ETPGS Emulsions

Dynamic light scattering (DLS) was used to size ETPGS emulsions. Six ETPGS emulsions were fabricated (three with PLP, three without) and submitted to a NanoBrook Omni DLS to measure mean particle diameter and half-width for each formulation.

For imaging via transmission electron microscopy (TEM), 5 µl of ETPGS or ETPGS+PLP was placed onto 300 mesh copper grids with ultrathin carbon film. The wet grids were air-dried for several minutes prior to being examined under TEM. The emulsions were examined by bright-field and dark-field transmission electron microscopy (TEM) using an FEI Tecnai F20 transmission electron microscope at an electron acceleration voltage of 200 kV. High resolution images were captured using a standardized, normative electron dose and a constant defocus value from the carbon-coated surfaces.

To characterize peptide release, 4 mL of ETPGS emulsion containing PLP was inserted into regenerated cellulose dialysis tubing (6000-8,000 MWCO, 30 µm wall thickness, Fisherbrand Dialysis Tubing). This sealed tubing was submerged in 100 mL of PBS within a glass vessel and capped to prevent evaporation. Likewise, the same schematic was used for PBS containing PLP at the same concentration as a control. Release vessels were kept at 37°C with gentle shaking by an incubator (79 rpm, Excella E24 Incubator Shaker, New Brunswick Scientific). For sample collection, 1 mL was taken from the 100 mL bulk fluid of the release vessels and replaced with 1 mL of fresh PBS. Characterization of PLP concentration in samples was performed using reverse-phase HPLC (Waters 2796 Bioseparations Module, Waters Corp) on a C_4 analytical column (Waters XBridge Protein BEH column, 300 Å, 3.5 µm, 4.6 mm x 150 mm, 10-500 K). Samples were eluted with mobile phases A (100% water with 0.05% trifluoroacetic acid (TFA)) and B (100% acetonitrile with 0.05% TFA) with a linear gradient of

95% A to 30% A over 20 minutes at a constant flow of 1 mL/min. PLP was detected at 280 nm and DEX was detected at 240 nm with a dual wavelength absorbance detector (Waters 2487 Dual λ Absorbance Detector, Waters Corp). Data was collected and processed using Empower 3 Software (Waters Corp). Concentration losses of peptide from sampling and PBS re-addition were accounted for when data were analyzed.

3.2.4 Measurement of ETPGS Antioxidant Power

For assessing antioxidant capabilities of ETPGS emulsions, the ferric-ion reducing antioxidant power (FRAP) assay was utilized as previously established [39]. Briefly, ETPGS with and without PLP was prepared, diluted 1:1000 and titrated at various concentrations in duplicate into FRAP reagent containing Fe(III). Fe(III) conversion to Fe(II) was measured by reading samples at a wavelength of 593 nm (Spectramax M5, Molecular Devices) over various time points.

3.2.5 Acute Antioxidant Effect in a Model APC

The acute effects of ETPGS on reactive nitrogen and oxygen species (RNOS) in RAW 264.7 cells were measured using a previously established, highly sensitive microfluidic assay [40, 41]. Briefly, RAW 264.7 macrophages were cultured in 25 cm^3 flasks and maintained at a density of $5x10^6$ cells/flask. The cells were stimulated with IFN-γ (600 U/mL) and LPS (100ng/mL), and incubated for 20 hours. Cells were then treated with 0.1% (v/v) ETPGS and incubated for another 60 minutes. Fluorescent probes DAF-FM DA and MitoSOX were loaded into cells at concentrations of 10 μM, each to indicate NO and superoxide species, respectively. Also included in the loading were superoxide dismutase inhibitors DDC (1 mM) and 2-ME (10 μM). After loading, cells were harvested, washed and lysed. The lysate was injected into a preconditioned PDMS/glass microfluidic device, and Labview software was used to collect and analyze data.

3.2.6 Induction of EAE and Therapeutic Study

Female SJL/J mice, 4-5 weeks of age were obtained from Envigo Laboratories and housed at the University of Kansas under specified, pathogen-free conditions. Female SJL/J mice are a well characterized and established strain known to exhibit a relapsing-remitting pattern of MS-like disease when immunized against the $PLP_{139-151}$ epitope [42-44]. All live-mouse protocols were approved by the University of Kansas Institutional Animal Care and Use Committee. For the induction of EAE, mice were subcutaneously administered with 200 μg of PLP in a 0.2 mL emulsion of Complete Freund's Adjuvant (CFA). The CFA mixture was comprised of equal volumes of PBS and IFA also containing killed Mycobacterium tuberculosis strain H37RA at a final concentration of 4 mg/mL. This immunization was given as four, 50 μL injections above the shoulders and the flanks. Additionally, 200 ng of pertussis toxin was given intraperitoneally on the same day of immunization (day 0) as well as day 2 post-immunization. The data presented are comprised of three independent *in vivo* studies; each group was comprised of 12-15 mice in total. Treatments were administered as 100 μL subcutaneous injections on days 4, 7 and 10 of the study. For the PLP and ETPGS+PLP groups, antigen was dosed at 200 nmol. ETPGS and ETPGS+PLP treatments were injected within 30 minutes of fabrication. One of the 15 PBS control mice was excluded from the study due to starting weight outside of the appropriate range. Two of 15 ETPGS+PLP mice died within 24 hours of receiving the third treatment injection due to unclear circumstances and were excluded from the study as well. Disease progression was assessed on a five-point clinical scale including: 0, no clinical evidence of disease; 1, tail weakness or limp tail; 2, paraparesis (weakness or incomplete paralysis of one or two hind limbs); 3, paraplegia (complete paralysis of two hind limbs); 4, paraplegia with forelimb weakness or paralysis; and 5, moribund. Body weight was taken each day as well.

3.2.7 Tissue Harvest and Splenocyte Isolation

Mouse spleens were harvested from EAE mice on day 25 post-immunization as previously described [23, 45, 46]. Briefly, the spleens were first passed through a wire mesh using the rubber end of a sterile 1 mL syringe plunger and collected in 5 mL of RPMI 1640 media. The cellular extracts were centrifuged, and the resulting cell pellet was resuspended in 3.5 mL of 1X Gey's lysis solution. The cells were incubated on ice for 3.5 minutes to lyse splenic red blood cells. The lysis reaction was stopped with the addition of 10 mL RPMI 1640 media containing 10% FBS and centrifuged at 1,100 x g for 5 minutes. The remaining splenocyte pellets were resuspended in fresh media (RPMI 1640 media containing 10% FBS and 1% Penicillin-Streptomycin) and plated in 96-well cell culture plates at a cell density of $1x10^6$ cells/well in a final volume of 200 µL, and in 12-well cell culture plates at a density of $5x10^6$ cells/well and 1 mL volume. Plain media or 25 µM PLP was immediately introduced to cells. Stimulated cell cultures were incubated for 96 hours at 37°C in a CO_2 (5%) incubator.

Additionally, serum was taken from mice during sacrifice by accessing the caudal vena cava. Spinal cords were harvested, weighed, and homogenized with the Fisher Scientific™ Sonic Dismembrator Model 500 in PBS. The amount of PBS added was determined to create 50 mg homogenized central nervous tissue (hCNS) per 500 µL of PBS stocks. Serum and hCNS samples were stored at -20°C.

3.2.8 Measurement of Cytokines

After 96 hours of incubation, splenocytes in a 96-well culture plate were centrifuged, and supernatants were collected for cytokine analysis (GM-CSF, IFN- γ, IL-2, IL-21, IL-4, IL-10, IL-15, IL-17, IL-23, TNF-α). Marker levels were detected using a U-Plex assay kit according to manufacturer instructions (Meso Scale Discovery). Briefly, each plate was coated with 50 µL of

multiplex coating solution consisting of linkers and biotinylated capture antibodies for each cytokine and incubated on a shaker at 700 rpm for 1 hour at room temperature. Following a 3-time wash step with 150 µL PBS containing 0.05% Tween 20, 25 µL of diluent and 25 µL of sample was added to each well and incubated again for 1 hour on a shaker at room temperature. Detection antibody was then added at 50 µL/well and incubated for 1 hour. Finally, each assay plate was read using the QuickPlex multiplex plate reader (Meso Scale Discovery).

3.2.9 Measurement of Cellular Metabolism

Resazurin (7-hydroxy-3H-phenoxazin-3-one 10-oxide) was used to determine cellular metabolism. 75 µM resazurin was introduced to splenocyte cultures and incubated for 3 hours. Metabolic reductive capacity was observed by viewing changes in fluorescence at excitation 560, emission 590 (Spectramax M5, Molecular Devices). Background fluorescence were taken using RPMI media and subtracted out from splenocyte readings for analysis.

3.2.10 Fluorescent Staining and Flow Cytometry

Splenocytes were collected from 12-well plates at 96 hours and stained with fluorescent antibodies. $1x10^6$ cells were washed with 1 mL of wash buffer (RPMI 1640 media containing 5% FBS) before being centrifuged and resuspended in 50 µL of block buffer containing 20 µg/mL TruStain fcX (anti-mouse CD16/32 antibody, Biolegend) in wash buffer. Cells were incubated on ice for 30 minutes before adding the fluorescent antibodies and isotype controls in 50 µL at 2x the manufacturer recommended concentration for 1 hour. For flow cytometry data collection, 30,000 cells per sample were detected using a BD FACSFusion cytometer. Data were analyzed using Kaluza Software.

3.2.11 Detection of Anti-PLP IgG

PLP-specific IgG titers were assessed in an ELISA format [47]. 1µg/mL PLP was dissolved in an isoelectric (pH 9.5) solution of 50 mM $NaHCO_3$. This coating buffer was seeded on Immulon 2HB 96-well plates and incubated overnight at 4°C. Plates were then blocked at 37°C for 1 hour with 1% (w/v) bovine serum albumin (BSA) plus 0.5% Tween 20 after washing unbound component with the same procedure as used in the multiplex assays. Serum and hCNS samples were then introduced and serially diluted 1:1 across seven concentrations. After another 1 hour incubation (37°C), plates were again washed, and HRP-conjugated anti-mouse IgG (BioLegend) was added at 0.1 µg per 100 µL and incubated again for 1 hour at 37°C. Washing the plates once more, 100 µL of TrueBlue substrate was added and plates were covered and shaken at 75 rpm and room temperature for 15 minutes. Enzymatic conversion was stopped with 100 µL 2N H_2SO_4 and the plate was read at 450/540 nm (Spectramax M5, Molecular Devices). For analyzing titer, linear regions across sample titration readings were fitted with linear regressions and extrapolated to their 1X concentration for comparison across samples.

3.2.12 Statistical Analysis

Statistical evaluation of data was performed using two-way analysis of variance (ANOVA), followed by Tukey and Sidak multiple comparison tests. The criteria for statistical significance for all analyses was set at $p<0.05$. All statistical analyses were performed using GraphPad Software (GraphPad Software Inc.).

3.3 Results

3.3.1 Characterization of the ETPGS Formulation

To develop ETPGS as a functional co-delivery vehicle, a formulation recipe was empirically derived by altering proportions of vitamin E, TPGS, and phosphate-buffered saline. By measuring fabricated particle diameters by DLS, outcomes were reconciled against the design criteria for an emulsion to contain droplets between 100-500 nm. Ultimately, a stable emulsion was obtained with 10% oil in PBS (w/w) and 2:1 E:TPGS (w/w, **Fig. 1A,B**). The selected formulation was evaluated by fabricating three replicate emulsions, both alone and when formulated with PLP (**Fig. 1B**). The ETPGS recipe alone yielded a mean diameter of 263.2 nm, and with the inclusion of PLP, the emulsion increased in mean size to 303.1 nm. Droplet half-width decreased from 52.3 nm to 32.8 nm, suggesting that PLP may be surface active. The emulsions were sized again after one month at 4°C storage; negligible changes in droplet size were observed (data not shown). To image the association of PLP with ETPGS and confirm incorporation of the peptide into the formulation, transmission electron microscopy (TEM) was carried out, which suggested PLP accumulation at the oil-water interface (**Fig. 1C**). Peptide incorporation was further confirmed using elemental analysis to visualize nitrogen content within the oil phase of ETPGS with PLP, but not ETPGS alone (**Supp. Fig. 1**). A peptide release study was conducted to verify temporal restriction of peptide with the ETPGS formulation as well (**Supp. Fig. 2**)

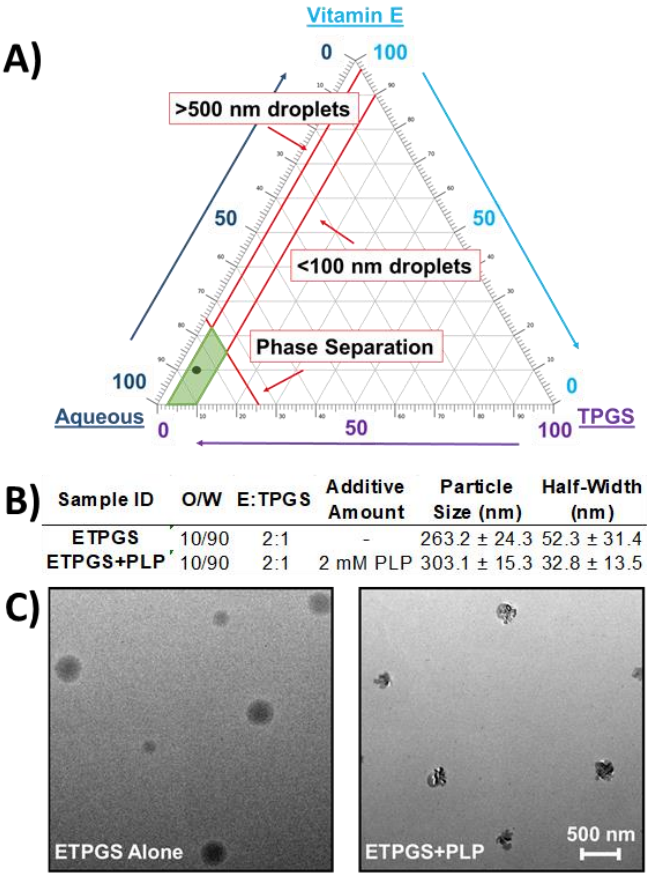

Sample ID	O/W	E:TPGS	Additive Amount	Particle Size (nm)	Half-Width (nm)
ETPGS	10/90	2:1	-	263.2 ± 24.3	52.3 ± 31.4
ETPGS+PLP	10/90	2:1	2 mM PLP	303.1 ± 15.3	32.8 ± 13.5

Fig. 1. Formulation of a tocopherol-based vehicle for antigen delivery. A.) Emulsion fabrication using varied proportions of Vitamin E, TPGS and PBS enabled the construction of a ternary phase diagram, where scale denotes percent composition of each component. B.) Favorable component proportions were used to fabricate emulsions both with (ETPGS+PLP) and without (ETPGS) PLP for sizing *via* dynamic light scattering (n = 3/group) DLS sizes and half-widths are presented in terms of average size ± standard deviation. C.) formulations of ETPGS alone (left) and ETPGS+PLP (right) were also imaged with TEM to verify antigen incorporation into the emulsion. The lower right scale bar represents 500 nm for both formulations.

3.3.2 ETPGS influences oxidative stress in vitro

To assess the antioxidant capacity of ETPGS emulsions, the ferric-ion reducing antioxidant power (FRAP) assay was selected as a colorimetric indicator of functionality. ETPGS with and without PLP was fabricated and titrated into FRAP reagent. After 10 minutes, a linear concentration dependence was recognized for all components (**Fig. 2A**). Over time, both ETPGS and ETPGS+PLP achieved similar reductions in ferric ions (**Fig. 2B**). Moving from these preliminary results in the simple FRAP system, acute antioxidant effects of ETPGS were measured *in vitro* in a model APC line. LPS-stimulated RAW 264.7 macrophages showed substantial levels of MitoSOX Red, but cells treated with ETPGS displayed markedly suppressed the analyte (**Fig. 2C**). Notably, while ETPGS treatment resulted in an apparent overall decrease of reactive oxygen species, a slight increase of reactive nitrogen species was observed. A third, unknown product peak formed likely as the result of a reaction between ETPGS and an indicator dye.

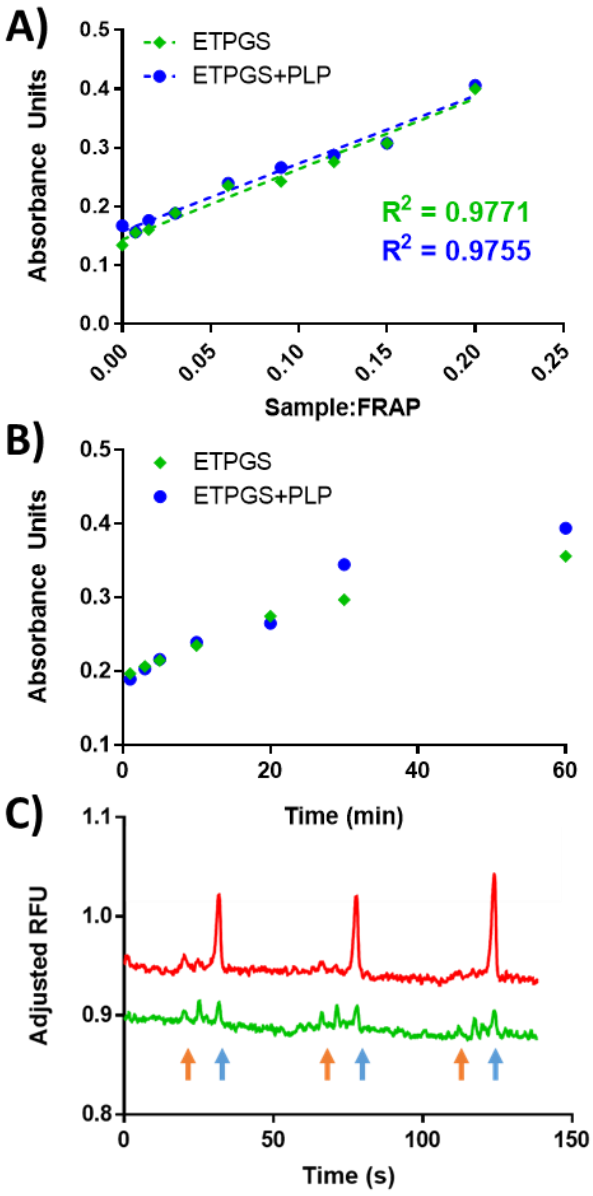

Fig. 2. *In vitro* antioxidant power analyses for ETPGS formulations. Ferric ion reducing antioxidant power results yielded A.) linear relationships between reduction and sample dilutions (reported for t = 10 minutes), and B.) reduction kinetics over time (reported at sample:FRAP ratio 0.09). ETPGS alone is represented by green diamonds, ETPGS+PLP is represented by blue circles. C.) Acute measurement of reactive nitrogen and oxygen species in stimulated RAW 264.7 cells

alone (red), and ETPGS-treated cells (green) for three repeat runs, each. Superoxide peaks are identified with blue arrows, while reactive nitrogen peaks are denoted by orange arrows.

3.3.3 ETPGS-facilitated autoantigen delivery delays and suppresses EAE in vivo

Next, ETPGS formulated with autoantigen was tested for efficacy against EAE *in vivo*. This ETPGS+PLP group was evaluated against ETPGS alone, PLP alone, and PBS control groups with treatment administrations occurring on days 4, 7 and 10 post EAE induction. Clinical scoring and weight data were collected, and are reflected in **Fig. 3A-C and 3D-F**, respectively. PBS treated control mice exhibited disease onset at 9 days post-induction and reached peak severity (in both weight and clinical score) by day 14. Among PLP-treated mice, disease severity was largely suppressed as reflected by both scoring and weight, but disease onset occurred at a similar time to those in the PBS control group and was seemingly prolonged when compared to PBS control mice. ETPGS vehicle treatment alone substantially delayed the onset of EAE with clinical scores not occurring until day 13 and peak severity evident on day 16 as opposed to day 14 in the PBS control mice. Treatment consisting of ETPGS+PLP delayed disease presentation even further with symptoms not appearing until day 15 and a peak at day 19. Disease severity was also suppressed, evidenced by lower clinical scores and significantly higher weights even at the end of the 25-day study. In fact, ETPGS+PLP treatment resulted in greater than 50% of mice showing no signs of EAE at all (**Fig. 4A**). Cumulative scores were tallied for each treatment group and are presented in **Fig. 4B**. ETPGS+PLP treatment indeed significantly suppressed the accumulation of clinical scores when compared to PBS control and ETPGS alone, but significance was not realized between ETPGS+PLP and PLP alone due to high variability in PLP treatment efficacy.

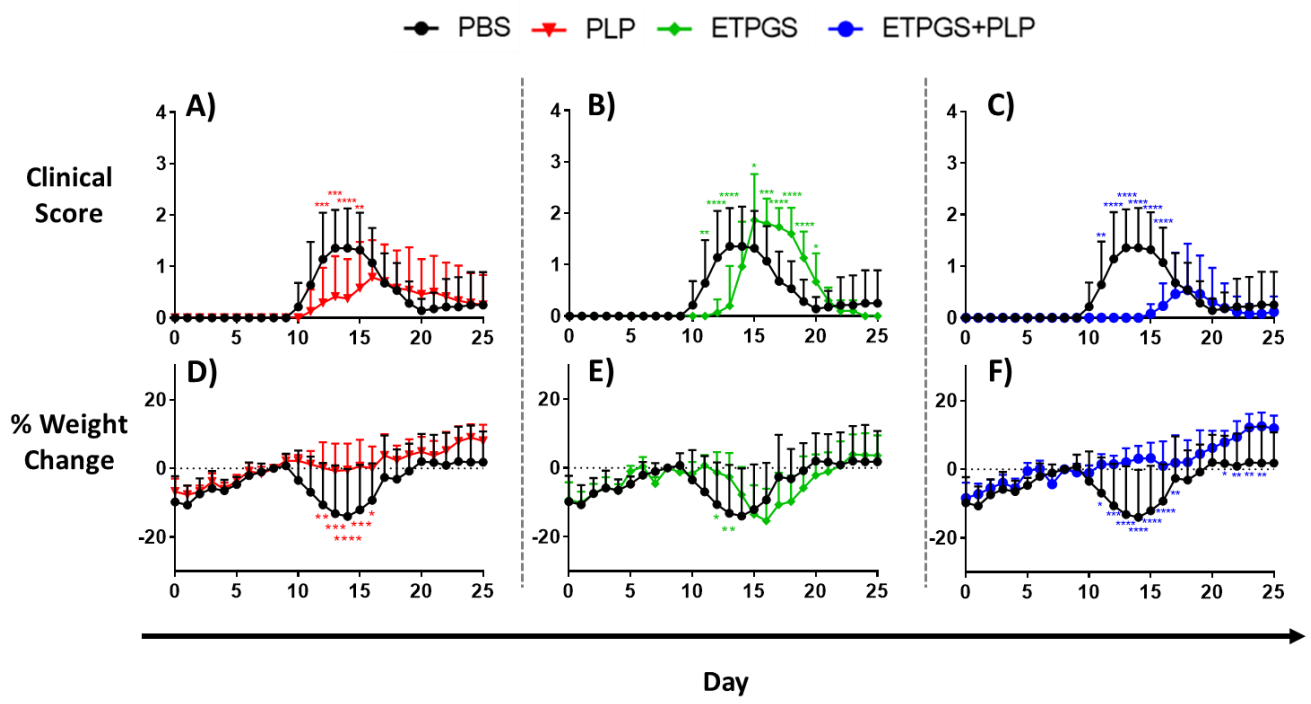

Fig. 3. Clinical disease scores (A-C) and weight changes (D-F) in EAE mice given treatment components. Disease score and weight change data for the PBS control treatment are compared to those of PLP treatment (A and D, respectively), ETPGS alone treatment (B and E), and ETPGS+PLP treatment (C and F). All treatments were administered on days 4, 7 and 10 post-disease induction. Each group consisted of n = 12-15 mice combined from three independent trials (*$p < 0.05$, **$p < 0.01$, ***$p < 0.001$, ****$p < 0.0001$ as compared to PBS). Error bars are reported as standard deviation among samples.

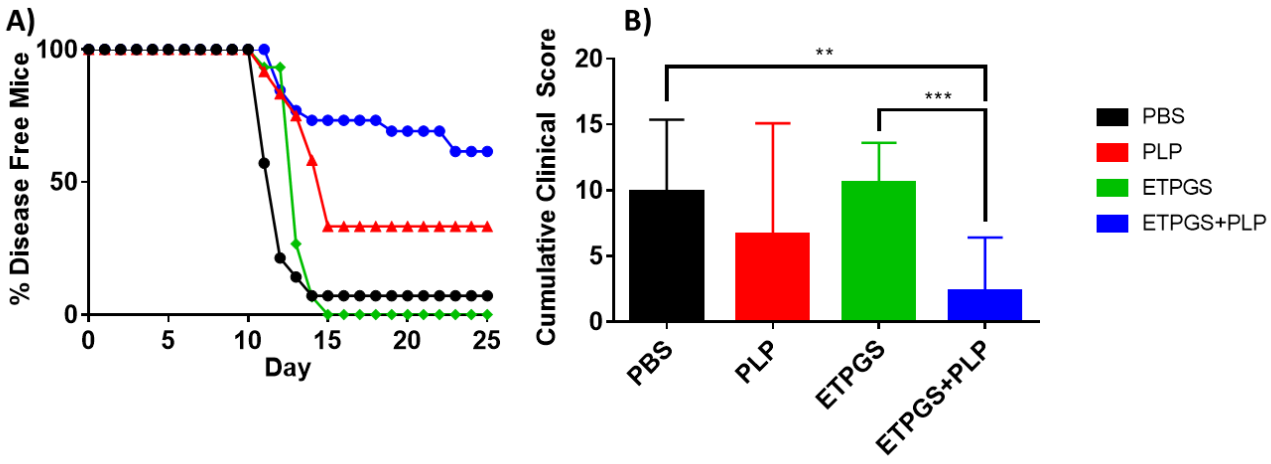

Fig. 4. Clinical scoring data were analyzed by A.) disease onset by group, as determined by proportion of mice having exhibited *any* clinical score by the day of each time point, and B.) area under the scoring curve for each treatment group. (n = 12-15 mice/group, *p < 0.05, **p < 0.01, ***p < 0.001). Error bars are reported as standard deviation among samples.

3.3.4 Ex vivo splenocyte cytokines and populations in ETPGS+PLP efficacy

On day 25 of the EAE study, all mice were sacrificed and splenocytes were isolated for *ex vivo* analysis. Isolated splenocytes were cultured for 96 hours either with or without a 25 µM autoantigen rechallenge. At the end of the incubation, cytokines were assessed by MSD multiplex and cell metabolism was measured via resazurin (**Fig. 5**). Cell populations were also probed using flow cytometry (**Fig. 6**).

Surprisingly, a highly conserved trend was observed across many cytokines included in the study. ETPGS+PLP group splenocytes consistently exhibited elevated levels of cytokines when compared to PBS control cells, both in terms of tolerogenic and inflammatory cytokines. The most robust cytokine responses evoked in ETPGS+PLP splenocytes were in IL-21 and IL-10 (**Fig. 5D** and **5F**), where significant elevation was recognized over all other groups. Responses in the PLP

group were statistically similar to those in PBS. ETPGS group splenocytes showed higher levels of IL-2 than those from PBS control mice (**Fig. 5C**). Interestingly, cell metabolism was significantly elevated in splenocytes from the ETPGS and ETPGS+PLP treatment groups (**Fig. 5K**). This observation, combined with the conserved cytokine trend, mirrors the delayed disease presentations that were observed in clinical measures.

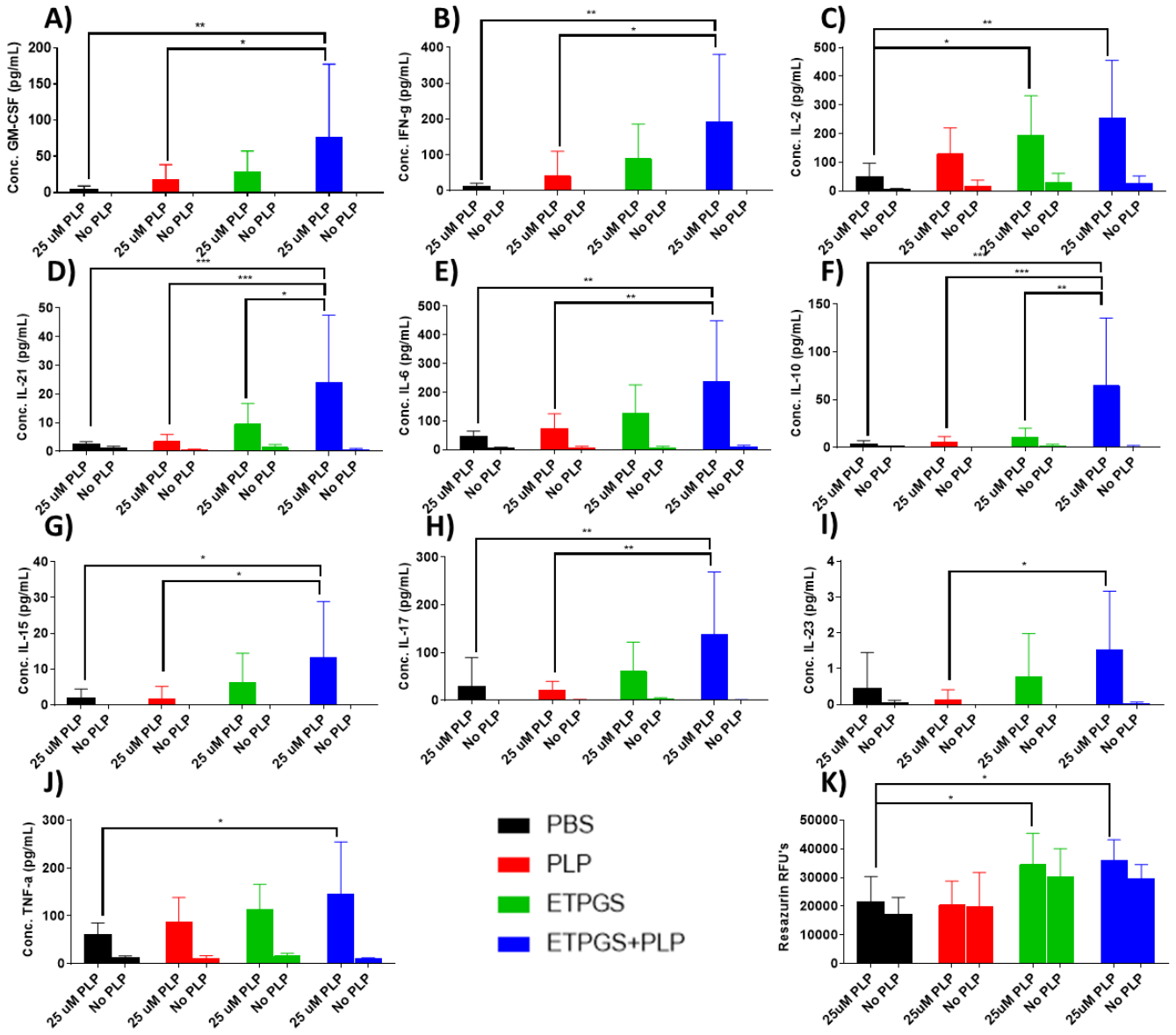

Fig. 5. Splenocytes were harvested on day 25 from EAE mice treated *in vivo* with PBS, PLP, ETPGS alone, or ETPGS+PLP. Splenocytes were incubated for 96h with or without a 25 μM PLP rechallenge. Supernatant cytokine levels of A.) GM-CSF, B.) IFN-γ, C.) Il-2, D.) Il-21, E.) Il-6, F.) Il-10, G.) Il-15, H.) Il-17, I.) Il-23, and J.) TNF-α were determined and K.) cell metabolism was measured *via* resazurin. (n = 5-6 mice/group, *p < 0.05, **p < 0.01, ***p < 0.001, ****p< 0.0001). Error bars are reported as standard deviation among samples.

From cell phenotyping metrics, unchallenged splenocyte populations showed some significant differences (**Fig. 6A-C**). Samples from the ETPGS treatment group had slightly decreased numbers of T cells (CD3+) compared to the PLP group, and a higher B cell (CD19+) count than PBS and PLP splenocytes. However, antigen-challenged cell population differences were not present among T, B, or dendritic cells (CD3+, CD19+, and CD11c+, respectively). A rhodamine-conjugated PLP was also used to probe cells capable of interacting with autoantigen, particularly by surface recognition of PLP-specific B cells (**Fig. 6D**). Again, resting cells displayed significant differences with PLP, ETPGS and ETPGS+PLP populations showing lower amounts of cells triggering events in the PLP channel. Upon antigen rechallenge, all groups showed similar levels of interaction with PLP. In previous ASIT studies investigating co-delivery systems, differences in a unique population of CD19+CD11c+ "autoimmune-associated B cells" have been observed and have been believed to contribute to tolerogenic outcomes. The same population was gated in this study (**Fig. 6E**), but no statistically relevant differences were found. Finally, T-to-B cell ratio was assessed for each group (**Fig. 6F**), and ETPGS was found to show a B cell-skewed proportionality compared to other groups in unchallenged populations, but not upon rechallenge.

ETPGS+PLP trended similarly to the ETPGS group, but was not significantly different than PBS or PLP splenocytes.

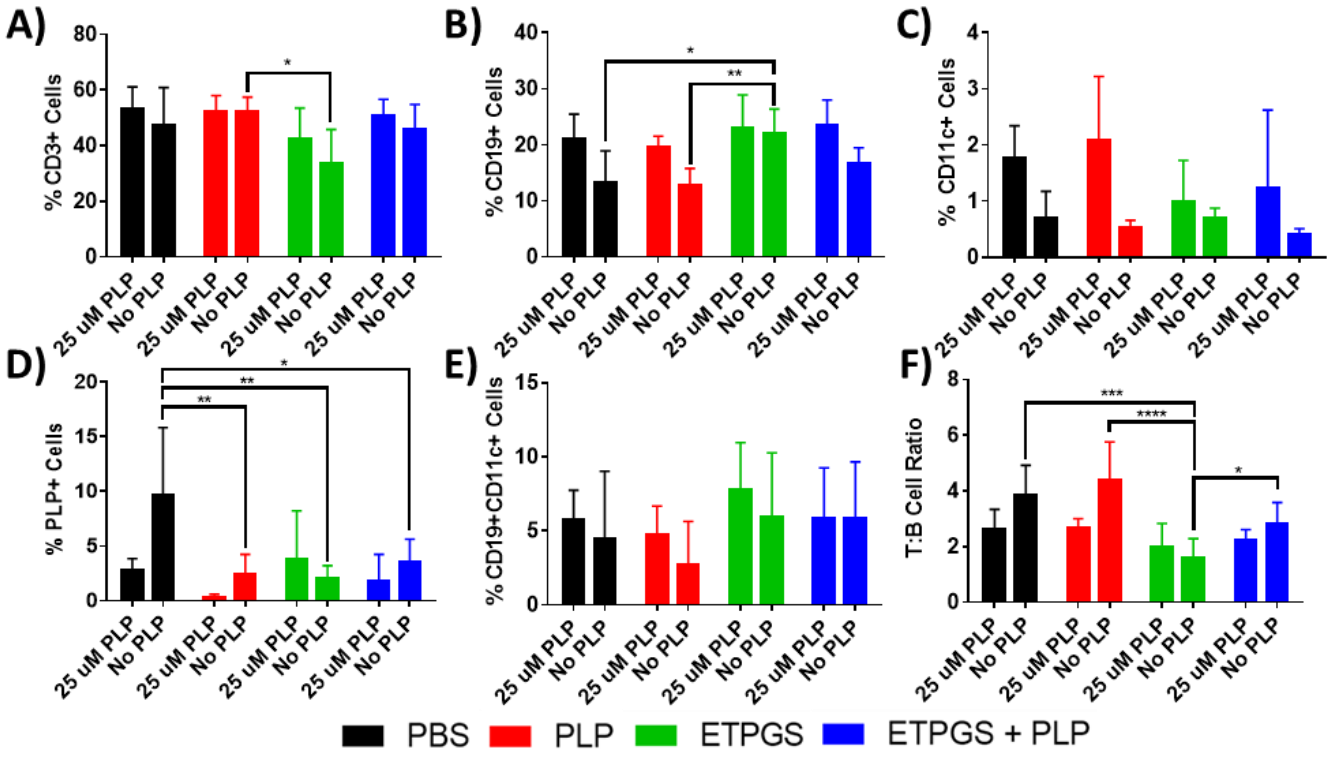

Fig. 6. Splenocytes were harvested on day 25 from EAE mice treated *in vivo* with PBS, PLP, ETPGS alone, or ETPGS+PLP. Splenocytes were incubated for 96h with or without a 25 µM PLP rechallenge. The cells were stained with antibodies for CD3 (Alexa Fluor 488), CD19 (Alexa Fluor 647), and CD11c (Brilliant Violet 421), as well as a Rhodamine-labeled PLP. Stained splenocytes were analyzed by flow cytometry. Cell populations were evaluated for A.) T-cells (CD3+), B.) B-cells (CD19+), C.) Dendritic cells (CD11c+), D.) PLP-specific cells (PLP+), and E.) Autoimmune-associated B-cells (CD19+CD11c+). Also analyzed was F.) ratio of T cells (CD3+) to B cells (CD19+) for each group. (n = 5-6 mice/group, *p < 0.05, **p < 0.01, ***p < 0.001, ****p< 0.0001). Error bars are reported as standard deviation among samples.

3.3.5 Autoantibodies are largely restricted to the periphery in mice treated with ETPGS+PLP

To compare evidence of immunity between the periphery and central nervous system, serum and hCNS were harvested and probed for anti-PLP IgG by ELISA (**Fig. 7**). In the serum (**Fig. 7A**) and hCNS (**Fig.** 7B) alone, no statistically significant differences existed between groups, though tissues from the PLP and ETPGS+PLP treated mice exhibited titers that trended higher than the PBS and ETPGS alone groups. However, when comparing the ratio of serum-to-hCNS anti-PLP titer (**Fig. 7C**), a stark difference was realized; ETPGS+PLP group titer ratios were markedly higher than those in any other group.

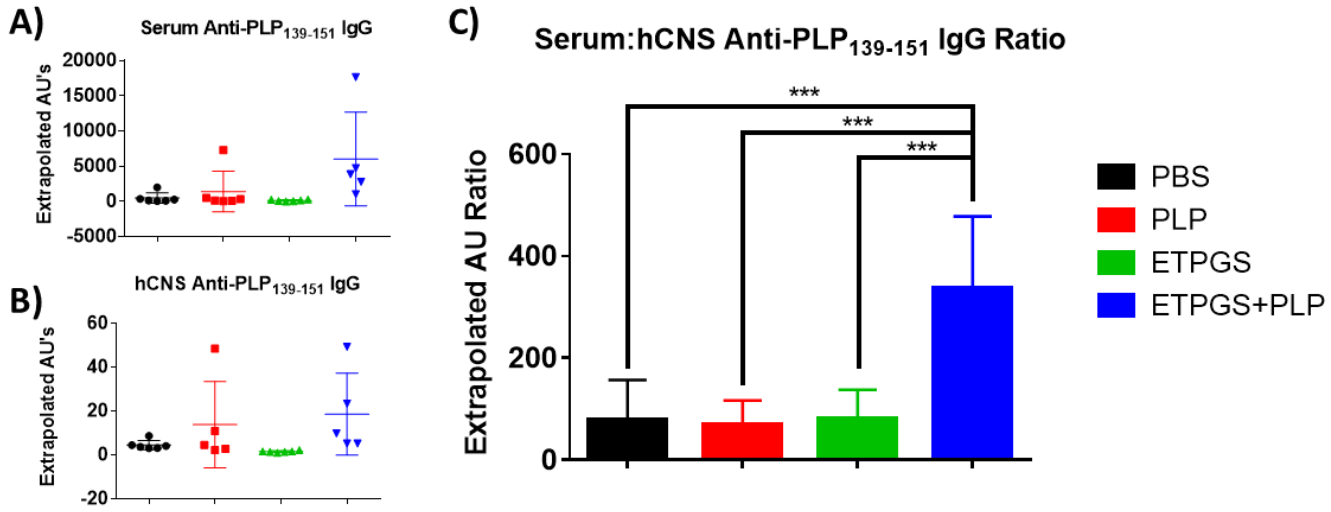

Fig. 7. On day 25 of the *in vivo* study, blood and spinal cords were collected from EAE mice treated with PBS, PLP, ETPGS alone, or ETPGS+PLP. Serum was isolated from blood, and spinal cords were homogenized and centrifuged to collect hCNS supernatants. Anti-PLP IgG titers were detected by ELISA for both A.) serum and B.) hCNS. C.) Ratio of serum to hCNS titers for each mouse was also determined. (n = 5-6 mice/group, *p < 0.05, **p < 0.01, ***p<0.001). Error bars are reported as standard deviation among samples.

3.4 Discussion

While autoantigen delivery as immunotherapy has shown tremendous capability to ameliorate autoimmunity across numerous disease models, past applications have pointed to the necessity for the inclusion of immunomodulatory molecules (i.e. immunosuppressant, adjuvant, etc.), such that the co-delivery of antigen and drug together can elicit maximal therapeutic effectiveness [21, 22]. Delivery vehicles have been used to restrict these components to the same immunological context, but many of these vessels can evoke adverse inflammation, or are regarded as inert at best. In this work, we present ETPGS as a functional vehicle for autoantigen delivery, potentially dispensing the need for additional drugs or adjuvants. By comparing ETPGS+PLP treatment to ETPGS and PLP alone, we evaluated this formulation's capacity to diminish EAE *in vivo*.

The development of an ETPGS formulation of appropriate size and stability was empirically derived by varying recipe components (**Fig. 1A**). TPGS content highly influenced emulsion droplet sizes, and oil-in-water content had a large bearing on stability. Formulations with greater than 25% oil were not stable over time or temperature. A 10% oil-in-water, 2:1 ETPGS recipe created stable emulsions that were in the ~250-300 nm range (**Fig 1B**) and advanced for further study. PLP was found to be compatible for incorporation with ETPGS, as evidenced by TEM (**Fig. 1C, Supp. Fig. 1**) and peptide release (**Supp. Fig. 2**). ETPGS was confirmed to have antioxidant function *in vitro* by the FRAP assay (**Fig. 2A),** and the inclusion of PLP did not affect its reductive capacity (**Fig. 2B**). This antioxidant capability was further shown to definitively influence reactive nitrogen and oxygen species production by macrophages *in vitro*.

Moving to an *in vivo* murine model of multiple sclerosis, a synergistic effect was realized by treating EAE mice with ETPGS+PLP. PLP treatment alone led to a suppressed, but prolonged disease state (**Fig. 3A, D**), while ETPGS treatment resulted in a delayed, though fully severe presentation of EAE (**Fig 3. B, E**). Formulation of ETPGS with PLP as a treatment ultimately delayed disease even further compared to ETPGS alone, and the severity was dampened to a greater extent than in the PLP group, particularly evidenced by fewer days of clinical scores and statistical improvement in weight data at the end of the study **(Fig. 3C, F**). These effects were most pronounced in disease incidence, where markedly more ETPGS+PLP mice showed no clinical evidence of disease than any other group (**Fig. 4A**).

Undoubtedly, there was therapeutic benefit to delivering PLP with ETPGS as a vehicle, and this effect suggested that these vitamin E emulsions are functionally contributive toward combating EAE. Despite this clinical success, *ex vivo* mechanistic measures proved somewhat confounding. ETPGS+PLP cytokine data showed robust production of markers such as IL-10 (**Fig. 5F**) and IL-6 (**Fig. 5E**), which in combination have been shown to be productive toward ameliorating EAE [48-50]. The conserved trend of increased ETPGS+PLP cytokine production of both IFN-γ (**Fig. 5B)** and TNF-α (**Fig. 5J**) was perplexing in that each of these are known to be inversely correlated with IL-10 and IL-6, respectively [51, 52]. In this study, these cytokines among all others assessed were all elevated in the ETPGS+PLP splenocytes (**Fig. 5A-J**). Furthermore, cell population data were also inconclusive for discerning any induction of tolerance as a mechanism for ETPGS+PLP (**Fig. 6**). Significant differences between groups only existed in unchallenged splenocyte populations, and re-exposure to PLP consistently led to similar levels of T, B and dendritic cells as well as PLP-recognizing cells (**Fig. 6A-D**). In a previous study, therapeutic success was achieved when delivering PLP and dexamethasone with IFA, and

differences in a distinct population of CD19+CD11c+ were seen [23]. These differences were believed to be mechanistically contributive, though in this work, no population differences in this subtype were observed (**Fig. 6E**).

Though cytokine and phenotype readouts were largely inconclusive, it remains evident that ETPGS+PLP treatment enacted therapeutic efficacy, albeit perhaps not through the antioxidant mechanism first hypothesized. Extending from the universally elevated cytokine trends, it was apparent that ETPGS+PLP group splenocytes may have been more metabolically active than those from other groups. This assertion is substantiated by resazurin data (**Fig. 6K**), where cellular metabolism seems to correlate with temporal differences in disease presentation and resolution. While PBS and PLP groups began showing disease symptoms on the same day, the delays in both ETPGS and ETPGS+PLP onsets may translate to incompletely resolved, or "exhausted" splenocytes on day 25 at harvest. Since ETPGS+PLP mice got sick at the latest point in the study, it is reasonable to consider the splenocytes of this group may have been in a more stimulated state, affecting elevated cytokine levels and resazurin readouts.

To reconcile observed delays in disease, we considered diversion of cells to the injection site as an explanation. One notable clinical observation of the ETPGS and ETPGS+PLP treatments was that they formed a depot at the injection site. The persistence of emulsion in the subcutaneous space was intended to draw immunological attention. This attraction of immune infiltrates could contribute to a prioritization of ETPGS and consequentially explain the slight delay in disease onset for ETPGS mice. Furthermore, the instance of encountering autoantigen in the periphery (as with the ETPGS+PLP treated mice) could trigger proliferation of PLP-specific cells before reaching the central nervous system (CNS). This off-site proliferation, preceding migration to the CNS, could result in therapeutic efficacy against the clinical onset of EAE. In fact, glatiramer

acetate, one of the most established MS treatments, is characterized by injection site inflammation occurring in up to 60% of patients receiving it [53, 54]. The swollen nodules observed at the injection site of EAE mice may follow a similar mechanism.

Anti-PLP IgG titers were probed in both the periphery (serum) and central compartment (hCNS) of the mice from the study (**Fig. 7**). Natural antibodies are unable to cross the blood brain barrier [55], so quantities were measured in both compartments as long-lasting evidence of autoimmunity between each location. While no statistical differences were definite in serum or hCNS autoantibodies discretely, the ratio of serum-to-hCNS titer yielded a distinct separation where ETPGS+PLP treated mice exhibited a markedly higher proportion of autoantibodies restricted to the periphery. These findings give credence to the possibility that ETPGS+PLP could create a lasting immunological decoy at the injection site. It is notable, however, that compartmental antibody titers trended higher compared to other groups for ETPGS+PLP as well. This information highlights the possibility that immunity could potentially also be shifted from a T helper type-1 (cellular) response to that of Th2 (humoral) response, which is known to be beneficial toward ameliorating EAE and MS [56, 57]. Future investigation into the subclass of IgG response will be beneficial to discern skewed immunity by ETPGS+PLP, as IgG1/IgG2a ratio could provide information about the potentially protective nature of an IgG response in addition to its magnitude [58, 59]. In all, the data collected in this study suggest that both a decoy effect and immunomodulation could be potential factors in the efficacy of ETPGS+PLP.

3.5 Conclusions

The development of autoantigen delivery vehicles that also functionally direct the immune response would provide substantial benefit to ASIT for autoimmune diseases. In the past,

conventional vehicles such as Freund's adjuvant have fallen short of clinical success [14, 23]. In this work, the ability of tocopherol emulsions to act as functional vehicles for antigen delivery was investigated. PLP delivered by ETPGS was efficacious to ameliorate EAE *in vivo* as evidenced by a decrease in disease incidence as well as severity. While trends of skewed cytokine responses were not evident in splenocytes from ETPGS+PLP treated mice compared to controls, anti-PLP IgG was slightly elevated and significantly relegated to the periphery, potentially indicating a therapeutic shift to Th2-mediated immunity and restriction of autoimmune effectors from the CNS compartment. Overall, these data indicate that ETPGS can act as a functional delivery vehicle, making it a compelling candidate for further study. The pharmaceutical development of MF59 as an emulsion-based vaccine adjuvant has shown that large-scale manufacturing of pharmaceutical emulsions can be feasible in practice [60, 61], but it will be critical to further elucidate the mechanistic potential of ETPGS in general, as well as in the context of authentic autoimmune disorders.

Moving forward, it is pertinent to further study the mechanistic drivers of therapeutic success in ETPGS as an antigen-delivery system. Evidence such as acute *in vitro* inhibition of RNOS production by macrophages and robust IL-10 generation in EAE splenocytes support an antioxidant mechanism, but cytokine and cell populations should be more carefully explored in secondary lymphoid organs, CNS tissues, and at the site of administration before drawing firm conclusions. The decoy effect is substantiated by delayed disease onsets and the restriction of anti-PLP IgG to the periphery over the CNS, but more work is needed to assess the validity of this phenomenon as a mechanism to correct autoimmunity.

3.6 Supporting Information

Supporting information is available: **Supp. Fig. 1** Scanning electron microscopy and elemental analysis of ETPGS formulations. **Supp. Fig. 2** PLP Release from ETPGS formulation. **Supp. Fig. 3** Overlaid clinical scoring and weight data from *in vivo* study.

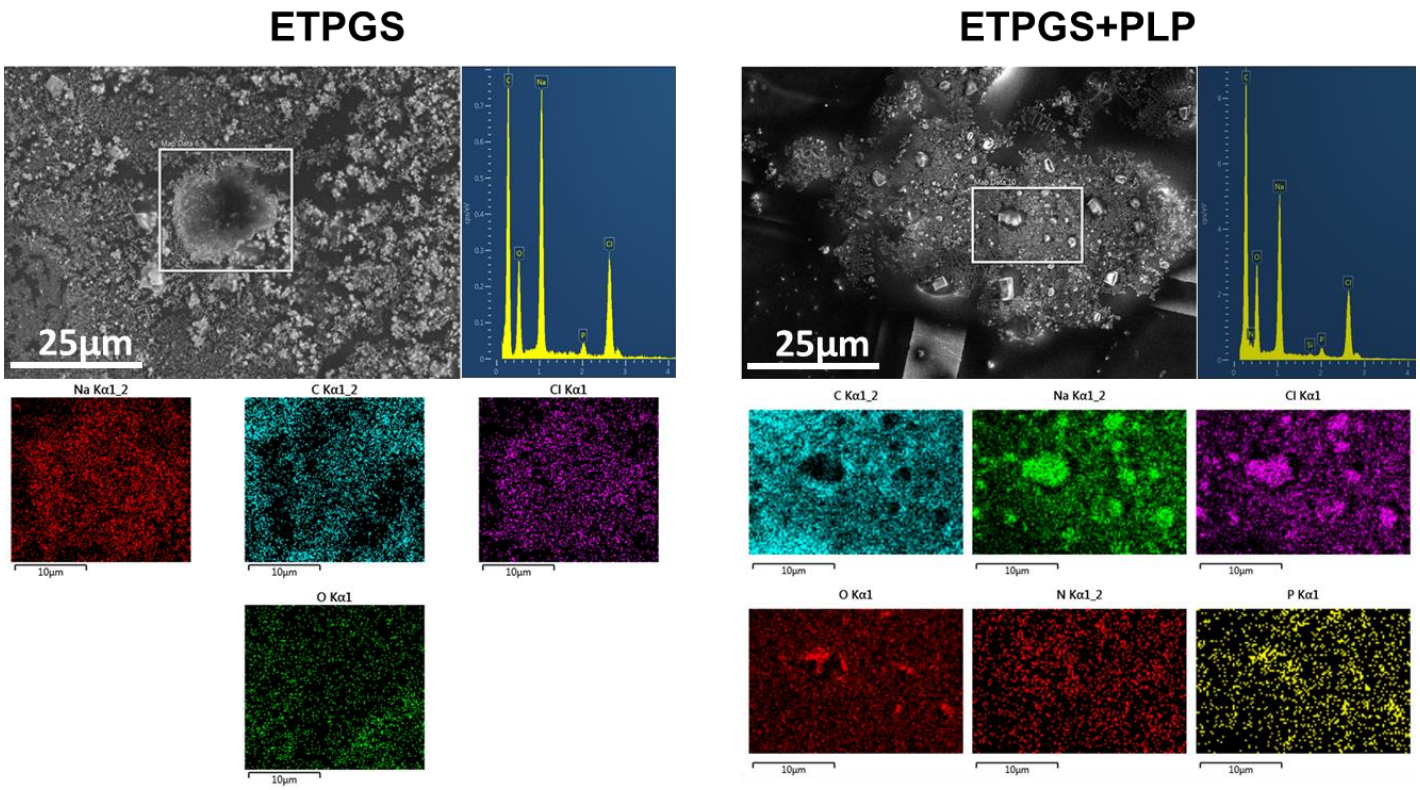

Supp. Fig. 1. Elemental Analysis of Scanning Electron Microscopy for ETPGS alone (Left) and ETPGS+PLP (Right). ETPGS+PLP, but not ETPGS alone, contains nitrogen in the dried oil phase, which is indicative of peptide incorporation to the formulation.

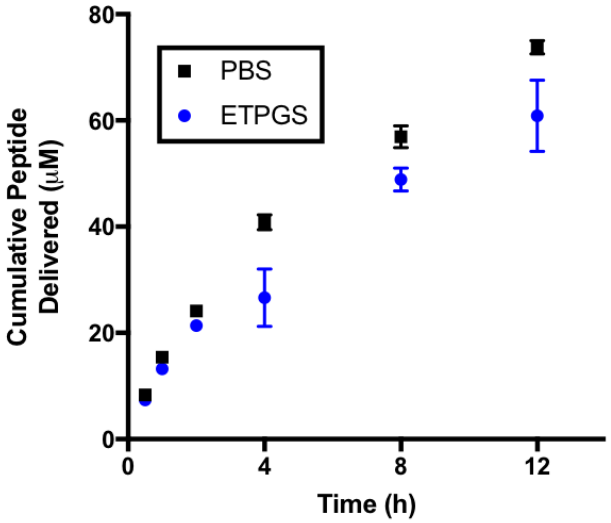

Supp. Fig. 2. Peptide release from dialysis tubing containing 4 mL of either PBS or ETPGS with PLP into 100 mL of bulk PBS. Peptide released into the bulk was sampled and analyzed by HPLC. PLP incorporation to ETPGS yielded a slightly impeded delivery over time as compared to PBS.

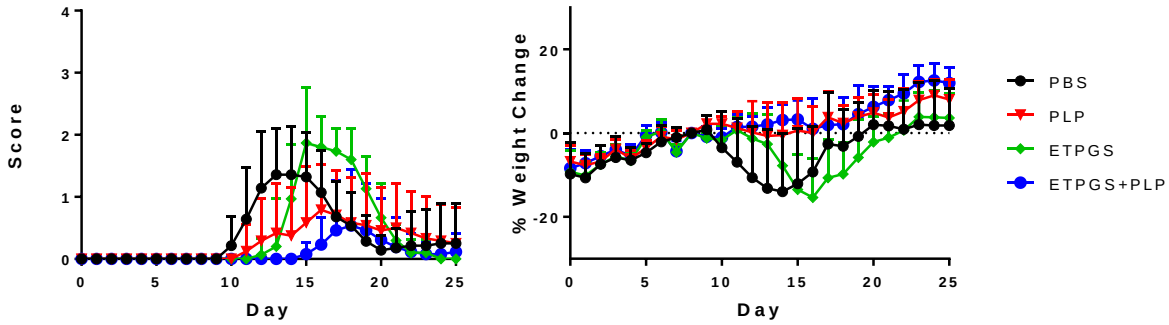

Supp. Fig. 3. Overlaid clinical scoring and weight change data for EAE mice treated with either PBS, PLP, ETPGS, or ETPGS+PLP. Statistics are not represented.

3.7 Acknowledgments

JDG was supported by the Madison and Lila Self Graduate Fellowship at the University of Kansas. MAC was supported by Biotechnology Predoctoral Training Program at the University of

Kansas. The authors would like to thank Michael Shao and Alexander Sedlacek for their assistance in executing the autoantibody detection assays and ferric ion reducing antioxidant power assays. Additional acknowledgement is due to Francisco J. Martinez-Becerra of the Kansas Vaccine Institute at the University of Kansas for resources and assistance with flow cytometry and MSD multiplex cytokine analysis, as well as Prem S. Thapa of the Microscopy and Analytical Imaging Laboratory at the University of Kansas for his assistance in executing TEM for emulsion imaging. Karen Peltier of the Tertiary Oil Recovery Program at the University of Kansas assisted ETPGS particle sizing with the NanoBrook Omni DLS. NSF grant #CHE-1411993 and COBREP20GM103638 supported authors DBW and SML to carry out the acute RNOS measurements.

3.8 References

1. Lim, S. Y.; Constantinescu, C. S., Current and future disease-modifying therapies in multiple sclerosis. *Int J Clin Pract* **2010,** *64* (5), 637-50.
2. Loleit, V.; Biberacher, V.; Hemmer, B., Current and future therapies targeting the immune system in multiple sclerosis. *Curr Pharm Biotechnol* **2014,** *15* (3), 276-96.
3. Comi, G.; Radaelli, M.; Soelberg Sørensen, P., Evolving concepts in the treatment of relapsing multiple sclerosis. *The Lancet* **2017,** *389* (10076), 1347-1356.
4. Clifford, D. B.; De Luca, A.; Simpson, D. M.; Arendt, G.; Giovannoni, G.; Nath, A., Natalizumab-associated progressive multifocal leukoencephalopathy in patients with multiple sclerosis: lessons from 28 cases. *The Lancet. Neurology* **2010,** *9* (4), 438-46.
5. Iaffaldano, P.; D'Onghia, M.; Trojano, M., Safety profile of Tysabri: international risk management plan. *Neurological Sciences* **2009,** *30* (2), 159.
6. Rommer, P. S.; Zettl, U. K.; Kieseier, B.; Hartung, H. P.; Menge, T.; Frohman, E.; Greenberg, B. M.; Hemmer, B.; Stuve, O., Requirement for safety monitoring for approved multiple sclerosis therapies: an overview. *Clin Exp Immunol* **2014,** *175* (3), 397-407.
7. Havrdova, E.; Horakova, D.; Kovarova, I., Alemtuzumab in the treatment of multiple sclerosis: key clinical trial results and considerations for use. *Therapeutic advances in neurological disorders* **2015,** *8* (1), 31-45.
8. Minagar, A., Current and future therapies for multiple sclerosis. *Scientifica (Cairo)* **2013,** *2013*, 249101.
9. Hartwell, B. L.; Antunez, L.; Sullivan, B. P.; Thati, S.; Sestak, J. O.; Berkland, C., Multivalent nanomaterials: learning from vaccines and progressing to antigen-specific immunotherapies. *Journal of pharmaceutical sciences* **2015,** *104* (2), 346-61.

10. Maldonado, R. A.; LaMothe, R. A.; Ferrari, J. D.; Zhang, A. H.; Rossi, R. J.; Kolte, P. N.; Griset, A. P.; O'Neil, C.; Altreuter, D. H.; Browning, E.; Johnston, L.; Farokhzad, O. C.; Langer, R.; Scott, D. W.; von Andrian, U. H.; Kishimoto, T. K., Polymeric synthetic nanoparticles for the induction of antigen-specific immunological tolerance. *Proc Natl Acad Sci U S A* **2015,** *112* (2), E156-65.
11. Yeste, A.; Nadeau, M.; Burns, E. J.; Weiner, H. L.; Quintana, F. J., Nanoparticle-mediated codelivery of myelin antigen and a tolerogenic small molecule suppresses experimental autoimmune encephalomyelitis. *Proceedings of the National Academy of Sciences* **2012,** *109* (28), 11270-11275.
12. Tostanoski, Lisa H.; Chiu, Y.-C.; Gammon, Joshua M.; Simon, T.; Andorko, James I.; Bromberg, Jonathan S.; Jewell, Christopher M., Reprogramming the Local Lymph Node Microenvironment Promotes Tolerance that Is Systemic and Antigen Specific. *Cell Reports* **2016,** *16* (11), 2940-2952.
13. Hartwell, B. L.; Pickens, C. J.; Leon, M.; Berkland, C., Multivalent Soluble Antigen Arrays Exhibit High Avidity Binding and Modulation of B Cell Receptor-Mediated Signaling to Drive Efficacy against Experimental Autoimmune Encephalomyelitis. *Biomacromolecules* **2017,** *18* (6), 1893-1907.
14. Northrup, L.; Christopher, M. A.; Sullivan, B. P.; Berkland, C., Combining antigen and immunomodulators: Emerging trends in antigen-specific immunotherapy for autoimmunity. *Adv Drug Deliv Rev* **2016,** *98*, 86-98.
15. Shakya, A. K.; Nandakumar, K. S., Antigen-Specific Tolerization and Targeted Delivery as Therapeutic Strategies for Autoimmune Diseases. *Trends in biotechnology* **2018,** *36* (7), 686-699.
16. Moon, J. J.; Huang, B.; Irvine, D. J., Engineering Nano- and Microparticles to Tune Immunity. *Advanced Materials* **2012,** *24* (28), 3724-3746.
17. Sahdev, P.; Ochyl, L. J.; Moon, J. J., Biomaterials for Nanoparticle Vaccine Delivery Systems. *Pharmaceutical Research* **2014,** *31* (10), 2563-2582.
18. Irvine, D. J.; Swartz, M. A.; Szeto, G. L., Engineering synthetic vaccines using cues from natural immunity. *Nature materials* **2013,** *12* (11), 978-990.
19. Allison, A. C.; Byars, N. E., Immunological adjuvants: desirable properties and side-effects. *Molecular immunology* **1991,** *28* (3), 279-84.
20. Mohan, T.; Verma, P.; Rao, D. N., Novel adjuvants & delivery vehicles for vaccines development: A road ahead. *The Indian Journal of Medical Research* **2013,** *138* (5), 779-795.
21. Zhang, A.-H.; Rossi, R. J.; Yoon, J.; Wang, H.; Scott, D. W., Tolerogenic nanoparticles to induce immunologic tolerance: Prevention and reversal of FVIII inhibitor formation. *Cellular Immunology* **2016,** *301*, 74-81.
22. Yeste, A.; Nadeau, M.; Burns, E. J.; Weiner, H. L.; Quintana, F. J., Nanoparticle-mediated codelivery of myelin antigen and a tolerogenic small molecule suppresses experimental autoimmune encephalomyelitis. *Proc Natl Acad Sci U S A* **2012,** *109* (28), 11270-11275.
23. Northrup, L.; Griffin, J. D.; Christopher, M. A.; Antunez, L. R.; Hartwell, B. L.; Pickens, C. J.; Berkland, C., Co-delivery of autoantigen and dexamethasone in incomplete Freund's adjuvant ameliorates experimental autoimmune encephalomyelitis. *Journal of Controlled Release* **2017,** *266*, 156-165.
24. Haanstra, K. G.; Jagessar, S. A.; Bauchet, A.-L.; Doussau, M.; Fovet, C.-M.; Heijmans, N.; Hofman, S. O.; van Lubeek-Veth, J.; Bajramovic, J. J.; Kap, Y. S.; Laman, J. D.; Touin, H.; Watroba, L.; Bauer, J.; Lachapelle, F.; Serguera, C.; 't Hart, B. A., Induction of

Experimental Autoimmune Encephalomyelitis With Recombinant Human Myelin Oligodendrocyte Glycoprotein in Incomplete Freund's Adjuvant in Three Non-human Primate Species. *Journal of Neuroimmune Pharmacology* **2013,** *8* (5), 1251-1264.
25. Zhao, L.; Feng, S. S., Enhanced oral bioavailability of paclitaxel formulated in vitamin E-TPGS emulsified nanoparticles of biodegradable polymers: In vitro and in vivo studies. *Journal of pharmaceutical sciences* **2010,** *99* (8), 3552-3560.
26. Mu, L.; Feng, S., A novel controlled release formulation for the anticancer drug paclitaxel (Taxol®): PLGA nanoparticles containing vitamin E TPGS. *Journal of controlled release* **2003,** *86* (1), 33-48.
27. Guo, Y.; Luo, J.; Tan, S.; Otieno, B. O.; Zhang, Z., The applications of Vitamin E TPGS in drug delivery. *European Journal of Pharmaceutical Sciences* **2013,** *49* (2), 175-186.
28. Mi, Y.; Liu, Y.; Feng, S.-S., Formulation of docetaxel by folic acid-conjugated d-α-tocopheryl polyethylene glycol succinate 2000 (Vitamin E TPGS 2k) micelles for targeted and synergistic chemotherapy. *Biomaterials* **2011,** *32* (16), 4058-4066.
29. Steinman, R. M.; Turley, S.; Mellman, I.; Inaba, K., The Induction of Tolerance by Dendritic Cells That Have Captured Apoptotic Cells. *The Journal of Experimental Medicine* **2000,** *191* (3), 411-416.
30. Banchereau, J.; Steinman, R. M., Dendritic cells and the control of immunity. *Nature* **1998,** *392* (6673), 245-52.
31. Roche, P. A.; Furuta, K., The ins and outs of MHC class II-mediated antigen processing and presentation. *Nature Reviews. Immunology* **2015,** *15* (4), 203-216.
32. Foged, C.; Brodin, B.; Frokjaer, S.; Sundblad, A., Particle size and surface charge affect particle uptake by human dendritic cells in an in vitro model. *International Journal of Pharmaceutics* **2005,** *298* (2), 315-322.
33. Manolova, V.; Flace, A.; Bauer, M.; Schwarz, K.; Saudan, P.; Bachmann, M. F., Nanoparticles target distinct dendritic cell populations according to their size. *European Journal of Immunology* **2008,** *38* (5), 1404-1413.
34. He, C.; Hu, Y.; Yin, L.; Tang, C.; Yin, C., Effects of particle size and surface charge on cellular uptake and biodistribution of polymeric nanoparticles. *Biomaterials* **2010,** *31* (13), 3657-3666.
35. Rice-Ficht, A. C.; Arenas-Gamboa, A. M.; Kahl-McDonagh, M. M.; Ficht, T. A., Polymeric particles in vaccine delivery. *Current Opinion in Microbiology* **2010,** *13* (1), 106-112.
36. Korn, T.; Mitsdoerffer, M.; Kuchroo, V. K., Immunological basis for the development of tissue inflammation and organ-specific autoimmunity in animal models of multiple sclerosis. *Results Probl Cell Differ* **2010,** *51*, 43-74.
37. Murta, V.; Ferrari, C. C., Influence of Peripheral inflammation on the progression of multiple sclerosis: evidence from the clinic and experimental animal models. *Mol Cell Neurosci* **2013,** *53*, 6-13.
38. Huq, R.; Samuel, E. L.; Sikkema, W. K.; Nilewski, L. G.; Lee, T.; Tanner, M. R.; Khan, F. S.; Porter, P. C.; Tajhya, R. B.; Patel, R. S., Preferential uptake of antioxidant carbon nanoparticles by T lymphocytes for immunomodulation. *Scientific reports* **2016,** *6*.
39. Benzie, I. F. F.; Strain, J. J., The Ferric Reducing Ability of Plasma (FRAP) as a Measure of "Antioxidant Power": The FRAP Assay. *Analytical Biochemistry* **1996,** *239* (1), 70-76.
40. Hulvey, M. K.; Frankenfeld, C. N.; Lunte, S. M., Separation and Detection of Peroxynitrite Using Microchip Electrophoresis with Amperometric Detection. *Analytical Chemistry* **2010,** *82* (5), 1608-1611.

41. Caruso, G.; Fresta, C. G.; Siegel, J. M.; Wijesinghe, M. B.; Lunte, S. M., Microchip electrophoresis with laser-induced fluorescence detection for the determination of the ratio of nitric oxide to superoxide production in macrophages during inflammation. *Analytical and Bioanalytical Chemistry* **2017**, 1-10.
42. McCarthy, D. P.; Richards, M. H.; Miller, S. D., Mouse models of multiple sclerosis: experimental autoimmune encephalomyelitis and Theiler's virus-induced demyelinating disease. *Methods in molecular biology (Clifton, N.J.)* **2012,** *900*, 381-401.
43. Papenfuss, T. L.; Rogers, C. J.; Gienapp, I.; Yurrita, M.; McClain, M.; Damico, N.; Valo, J.; Song, F.; Whitacre, C. C., Sex differences in experimental autoimmune encephalomyelitis in multiple murine strains. *Journal of Neuroimmunology* **2004,** *150* (1), 59-69.
44. Raine, C. S.; Cannella, B.; Duijvestijn, A. M.; Cross, A. H., Homing to central nervous system vasculature by antigen-specific lymphocytes. II. Lymphocyte/endothelial cell adhesion during the initial stages of autoimmune demyelination. *Laboratory investigation; a journal of technical methods and pathology* **1990,** *63* (4), 476-89.
45. Sestak, J. O.; Sullivan, B. P.; Thati, S.; Northrup, L.; Hartwell, B.; Antunez, L.; Forrest, M. L.; Vines, C. M.; Siahaan, T. J.; Berkland, C., Codelivery of antigen and an immune cell adhesion inhibitor is necessary for efficacy of soluble antigen arrays in experimental autoimmune encephalomyelitis. *Molecular Therapy - Methods & Clinical Development* **2014,** *1*, 14008.
46. Northrup, L.; Sestak, J. O.; Sullivan, B. P.; Thati, S.; Hartwell, B. L.; Siahaan, T. J.; Vines, C. M.; Berkland, C., Co-delivery of autoantigen and b7 pathway modulators suppresses experimental autoimmune encephalomyelitis. *AAPS J* **2014,** *16* (6), 1204-13.
47. Nagelkerken, L.; Blauw, B.; Tielemans, M., IL-4 abrogates the inhibitory effect of IL-10 on the development of experimental allergic encephalomyelitis in SJL mice. *International immunology* **1997,** *9* (9), 1243-51.
48. Bettelli, E.; Prabhu Das, M.; Howard, E. D.; Weiner, H. L.; Sobel, R. A.; Kuchroo, V. K., IL-10 Is Critical in the Regulation of Autoimmune Encephalomyelitis as Demonstrated by Studies of IL-10- and IL-4-Deficient and Transgenic Mice. *The Journal of Immunology* **1998,** *161* (7), 3299.
49. McGeachy, M. J.; Bak-Jensen, K. S.; Chen, Y.; Tato, C. M.; Blumenschein, W.; McClanahan, T.; Cua, D. J., TGF-β and IL-6 drive the production of IL-17 and IL-10 by T cells and restrain TH-17 cell–mediated pathology. *Nature Immunology* **2007,** *8*, 1390.
50. Kimura, A.; Kishimoto, T., IL-6: regulator of Treg/Th17 balance. *Eur J Immunol* **2010,** *40* (7), 1830-5.
51. Tilg, H.; Trehu, E.; Atkins, M. B.; Dinarello, C. A.; Mier, J. W., Interleukin-6 (IL-6) as an anti-inflammatory cytokine: induction of circulating IL-1 receptor antagonist and soluble tumor necrosis factor receptor p55. *Blood* **1994,** *83* (1), 113-8.
52. Fiorentino, D. F.; Zlotnik, A.; Mosmann, T. R.; Howard, M.; Garra, A., IL-10 inhibits cytokine production by activated macrophages. *The Journal of Immunology* **1991,** *147* (11), 3815.
53. Soós, N.; Shakery, K.; Mrowietz, U., Localized Panniculitis and Subsequent Lipoatrophy with Subcutaneous Glatiramer Acetate (Copaxone®) Injection for the Treatment of Multiple Sclerosis. *American journal of clinical dermatology* **2004,** *5* (5), 357-359.
54. Edgar, C. M.; Brunet, D. G.; Fenton, P.; McBride, E. V.; Green, P., Lipoatrophy in patients with multiple sclerosis on glatiramer acetate. *The Canadian journal of neurological sciences. Le journal canadien des sciences neurologiques* **2004,** *31* (1), 58-63.

55. Pardridge, W. M., The Blood-Brain Barrier: Bottleneck in Brain Drug Development. *NeuroRX* **2005,** *2* (1), 3-14.
56. Fletcher, J. M.; Lalor, S. J.; Sweeney, C. M.; Tubridy, N.; Mills, K. H., T cells in multiple sclerosis and experimental autoimmune encephalomyelitis. *Clin Exp Immunol* **2010,** *162* (1), 1-11.
57. Legroux, L.; Arbour, N., Multiple Sclerosis and T Lymphocytes: An Entangled Story. *Journal of neuroimmune pharmacology : the official journal of the Society on NeuroImmune Pharmacology* **2015,** *10* (4), 528-46.
58. Uyttenhove, C.; Arendse, B.; Stroobant, V.; Brombacher, F.; Van Snick, J., Development of an anti-IL-12 p40 auto-vaccine: protection in experimental autoimmune encephalomyelitis at the expense of increased sensitivity to infection. *European Journal of Immunology* **2004,** *34* (12), 3572-3581.
59. Komiyama, Y.; Nakae, S.; Matsuki, T.; Nambu, A.; Ishigame, H.; Kakuta, S.; Sudo, K.; Iwakura, Y., IL-17 Plays an Important Role in the Development of Experimental Autoimmune Encephalomyelitis. *The Journal of Immunology* **2006,** *177* (1), 566.
60. Haensler, J., Manufacture of Oil-in-Water Emulsion Adjuvants. In *Vaccine Adjuvants: Methods and Protocols*, Fox, C. B., Ed. Springer New York: New York, NY, 2017; pp 165-180.
61. Schijns, V.; O'Hagan, D., *Immunopotentiators in Modern Vaccines*. Academic Press: 2016.

4. Antigen-Specific Immune Decoys Intercept and Exhaust Autoimmunity to Prevent Disease

As published in *Biomaterials*

Griffin, J. Daniel, Jimmy Y. Song, Aric Huang, Alexander R. Sedlacek, Kaitlin L. Flannagan, and Cory J. Berkland. "Antigen-Specific Immune Decoys Intercept and Exhaust Autoimmunity to Prevent Disease." *Biomaterials* (2019).

4.1 Introduction

Central to the propagation of adaptive immunity is the maturation of antigen-specific responses in secondary lymphoid organs (SLOs) such as the spleen and lymph nodes [1-3]. Following these initiatory events, antigen-specific populations are amplified, egress from SLOs, and traffic to antigen-rich locales [4, 5] for further stimulation and effector action [6-8]. Acute adaptive immunity is robust, but short-lived for the rapid clearance of pathogens and abnormal cells. Following the steep deployment of a response, immune cells can become exhausted as a checkpoint mechanism. Under these conditions, functional capacity is diminished and apoptosis may ensue [9-11]. Together, the migratory circuit between SLOs and diseased tissue coupled with the exhaustible nature of immunity is a hallmark of relapsing-remitting autoimmune diseases such as multiple sclerosis (MS) [12-15]. In such diseases and their experimental models, a vicious cycle is entrenched where aberrant autoantigen-specific effectors are primed, trafficked to disease-specific sites, and further stimulated to cause damage before returning to SLOs and regaining functionality [16-18].

Some of the most clinically effective immunotherapies for MS work by blockading the migratory circuit between peripheral SLOs and the central nervous system [19, 20]. Preventing egress from SLOs or blocking infiltration of myelin-specific immune populations can preserve host tissue integrity and stifle autoimmune destruction. These disease-modifying therapies are, however, nonspecific in their mechanism. The trafficking of entire populations of immune cells is broadly hindered, which severely handicaps both disease-relevant and healthy immune functions alike. Patients receiving such immunotherapies are subjected to risks of life-threatening infection that can far outweigh therapeutic benefits [21-23]. Antigen-specific immunotherapies may offer an appealing improvement to the state of conventional treatments, promising to selectively disarm autoreactive cells while preserving healthy immune function.

Conventional migration-inhibiting immunotherapies broadly block cellular egress from lymph nodes [19] or extravasation across the blood brain barrier [20]. Conversely, an antigen-specific approach may necessitate selectively attracting autoimmune cells or autoantibodies to a surrogate locale for sequestration. Engineered implantable biomaterials have emerged for evoking therapeutic, antigen-specific immune responses against cancer and autoimmunity alike [24-30]. These materials create a unique niche [31-36] of antigen to recruit and tune antigen-presenting populations for activation or tolerance, often by including a stimulatory adjuvant or immunosuppressive drug [37-45].

We designed and tested a novel biomaterial, which mimics etiologic autoantigens via covalent surface conjugation of a peptide epitope to microporous collagen sponges. Collagen provided an appealing substrate for our application because of the immunologically benign nature and widespread use of collagen sponges [46]. Antigen-Specific Immune Decoys (ASIDs) were designed to short-circuit the SLO-host tissue circuit by sequestering autoreactive effector cells from circulation, ultimately preserving host organs. Using murine experimental autoimmune encephalomyelitis (EAE) as a model, we set forth to evaluate the prophylactic, subcutaneous implantation of ASIDs for preventing paralysis *in vivo*. Analyzing cell isolates from both sponges and spleens, we explored the hypothesis that these constructs could work by intercepting T cell proliferation in the periphery. Ultimately, we discovered that ASIDs overstimulated immunity and exploited antigen-specific exhaustion as a mechanism for therapeutic effect (**Fig. 1**).

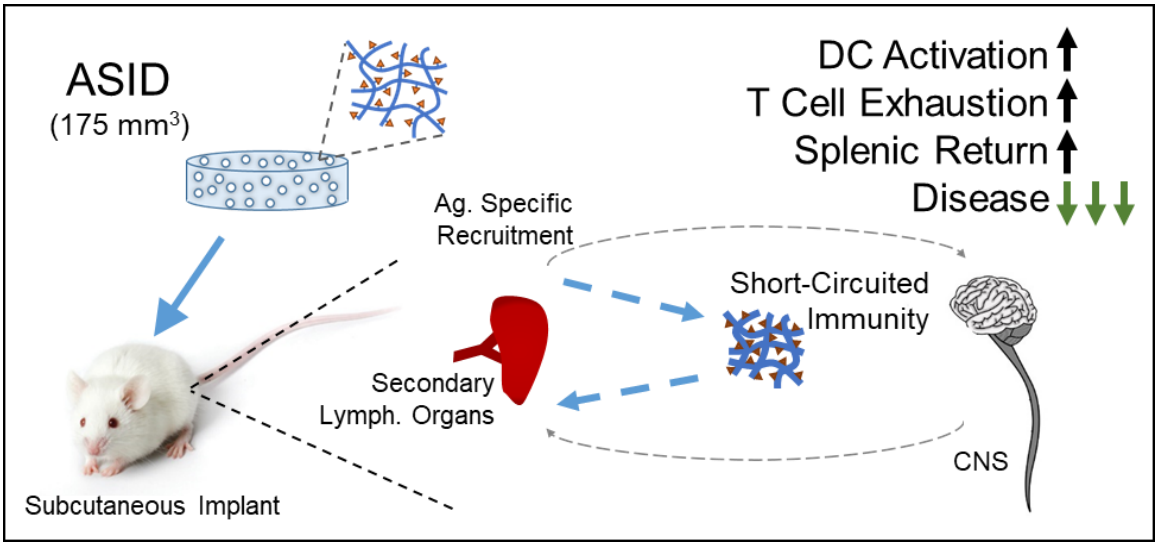

Figure 4. Autoimmunity is primed in secondary lymphoid organs and travels to disease-implicated tissues. ASIDs were designed to intercept this response and exhaust it prematurely, leaving host tissue intact.

4.2 Materials and Methods

4.2.1 Materials

Microporous collagen sponges (4 mm and 21 mm, columnar pore architecture) were purchased from Advanced Biomatrix (San Diego, CA). 2,5-dioxopyrrolidin-1-yl 1-azido-3,6,9,12-tetraoxapentadecan-15-oate (azido-PEG4-NHS Ester) was purchased from Click Chemistry Tools (Scottsdale, AZ). Tris(3-hydroxypropyltriazolylmethyl)amine (THPTA), and sodium ascorbate (NaAsc) were purchased from Sigma-Aldrich (St. Louis, MO). Copper (II) sulfate pentahydrate ($CuSO_4 \cdot 5H_2O$) was purchased from Acros Organics (Geel, Belgium). Alkyne-functionalized PLP with an *N*-terminal 4-pentynoic acid (homopropargyl, hp) modification, $hpPLP_{139-151}$ (hp-HSLGKWLGHPDKF-OH) was purchased from Biomatik (Cambridge, ON, Canada). Unmodified $PLP_{139-151}$ (NH2-HSLGKWLGHPDKF-OH) used for EAE induction, rechallenge assays, and anti-

PLP IgG ELISA was purchased from PolyPeptide Laboratories (San Diego, CA). Incomplete Freund's adjuvant (IFA) and killed *Mycobacterium tuberculosis* strain H37RA were purchased from Difco (Sparks, MD). Pertussis toxin was purchased from List Biological Laboratories (Campbell, CA). R-phycoerythrin (PE)/Cy7-conjugated anti-mouse CD3, PE-conjugated anti-mouse CD86, FITC-conjugated anti-mouse CD80, and respective isotype control antibodies were purchased from BioLegend (San Diego, CA). All other chemicals and reagents were analytical grade and used as received.

4.2.2 Synthesis of ASIDs

Collagen sponges (4 mm or ¼ sections of 21 mm diameters) were modified by reacting in a 2 mg/ml solution of 2,5-dioxopyrrolidin-1-yl 1-azido-3,6,9,12-tetraoxapentadecan-15-oate (azido-PEG4-NHS ester) in 50 mM HEPES buffer at pH 8.3 for 4 hours at room temperature. Subsequently, the sponges were washed five times with deionized water. The washed sponges were then placed in an solution of N-(6-(diethylamino)-9-(2-(prop-2-yn-1-ylcarbamoyl)phenyl)-3H-xanthen-3-ylidene)-N-ethylethanaminium (Rhodamine-alkyne, 1.22 mM) or $hpPLP_{139-151}$ (1.22 mM, 2 mg/mL) in pH 8.3 HEPES, followed by the addition of a premixed solution of tris-hydroxypropyltriazolylmethylamine (THPTA, 4.5 mM) and copper (II) sulfate pentahydrate (0.8 mM). Finally, sodium ascorbate (16 mM) was added to begin the reaction. The reaction was carried out overnight at room temperature. The sponges were then washed 5 times with deionized water and stored in 100% ethanol. The unmodified sponges were treated with the same procedure outlined above, with the omission of azido-PEG4-NHS ester. For *in vivo* studies, sponges were washed five times over the course of a day in 1X PBS and stored overnight at 4C in a solution of 1200 ng/mL of mouse GM-CSF.

4.2.3 Characterizing ASIDs

Scanning Electron Microscopy (SEM) was employed at 150X magnification to approximate collagen pore size. SEM images were taken on an FEI Technai F20 XT Field Emission Transmission Electron Microscope with dehydrated collagen sponges. PLP conjugation to collagen sponges was determined using a 20 minute Reverse-Phase HPLC method employing a 95/5 to 30/70 aqueous:organic gradient scheme on a C4 RP column. PLP conjugation was assessed by sampling "pre" and "post" reaction mixtures from before and after the addition of sodium ascorbate, respectively. Peptide conjugated was indirectly determined by comparing the percentage loss of the PLP peak area (8.9 minutes) from "pre" to "post" reaction. H_2O + 0.05% trifluoroacetic acid was used as the aqueous phase, and acetonitrile + 0.05% trifluoroacetic acid was used for the organic. Functional characterization of ASIDs was completed by incubating PLP-conjugated and unconjugated sponges with 1:100 anti-$PLP_{139-151}$ IgG positive mouse serum for 1 hour at room temperature. Sponges were washed, and bound anti-$PLP_{139-151}$ IgG was detected with HRP-conjugated anti-mouse IgG.

4.2.4 Induction of EAE and Therapeutic Study

EAE was induced as previously described [47, 48] in 4-6 week-old, female SJL/J mice from Envigo Laboratories. Mice were housed under specified, pathogen-free conditions at the University of Kansas with authorization approved under a protocol passed by the University's Institutional Animal Care and Use Committee. EAE was induced by subcutaneous administration of 200 µg of unmodified $PLP_{139-151}$ in 200 µL of Complete Freund's Adjuvant (CFA) emulsion. The CFA mixture was produced from equal volumes of PBS and IFA containing killed Mycobacterium tuberculosis strain H37RA at a final concentration of 4 mg/mL. The immunization was administered as four, 50 µL injections above the shoulders and the flanks. Additionally, 200

ng of pertussis toxin was administered as an intraperitoneal injection on the same day of immunization (day 0) as well as day 2 post-induction. For therapeutic study, mice received a subcutaneous implantation surgery between the shoulder blades on Day 7. Mice were weighed each day of the study and monitored with clinical scores starting on day 7. Disease progression was assessed on a five-point clinical scale including: 0, no clinical evidence of disease; 1, tail weakness or limp tail; 2, paraparesis (weakness or incomplete paralysis of one or two hind limbs); 3, paraplegia (complete paralysis of two hind limbs); 4, paraplegia with forelimb weakness or paralysis; and 5, moribund.

4.2.5 Detection of Anti-PLP IgG

PLP-specific IgG titers were assessed in an ELISA format as previously described [48, 49]. Briefly, 1µg/mL PLP was dissolved in a pH 9.5 solution of 50 mM $NaHCO_3$. This coating buffer was seeded on Immulon 2HB 96-well plates and incubated overnight at 4°C. Plates were then blocked with 1% (w/v) bovine serum albumin (BSA). Serum and homogenized central nervous system tissue (hCNS) were then introduced and serially diluted 1:1 across seven concentrations starting at 1:100. After washing, HRP-conjugated anti-mouse IgG (BioLegend) was added at 0.1 µg per 100 µL. After a final washing regimen, 100 µL of TrueBlue substrate was added, and plates were covered and shaken at 250 rpm and room temperature for 15 minutes. Enzymatic conversion was stopped with 100 µL 2N H_2SO_4 and the plate was read at 450/540 nm (Spectramax M5, Molecular Devices). For analyzing titer, linear regions across sample titration readings were fitted with linear regressions and extrapolated to their 1X concentration for comparison across samples.

4.2.6 Spleen Harvest and Splenocyte Isolation

Spleen harvest and splenocyte isolation was conducted as previously reported [50]. Briefly, spleens were passed through a wire mesh using the rubber stopper of a sterile 1 mL syringe in 1X

PBS. The strained cellular extracts were centrifuged, and the cell pellet was resuspended in red blood cell lysis buffer. The cells were incubated on ice for 3.5 minutes to lyse splenic red blood cells. The lysis reaction was stopped by adding 10 mL RPMI 1640 media containing 10% FBS to the mixture before centrifuging. The remaining splenocyte pellets were resuspended in fresh media (RPMI 1640 media containing 10% FBS and 1% Penicillin-Streptomycin) and counted for further analysis and experimentation.

4.2.7 Sponge Harvest and Spongeocyte Isolation

Cellular infiltrates to ASIDs and Blank Sponges were isolated by retrieving sponges from the subcutaneous space. In an Eppendorf tube, sponges were either chemically digested using 0.5 mg/mL Liberase TL (Sigma Aldrich, St. Louis, MO) in HBSS or mechanically disrupted with microscissors. The resulting freed cell suspension was then passed through a 70 µm strainer. The suspension was pelleted, replenished with 1 mL of RPMI 1640 media containing 10% FBS and 1% Penicillin-Streptomycin, and cells were counted for further processing and plating.

4.2.8 Fluorescent Staining and Flow Cytometry

Splenocytes were collected from 24-well plates after 96 hours and stained with fluorescent antibodies according to manufacturer recommendations. Cells were washed with 1X PBS + 5% FBS + 0.1% sodium azide before being incubated for 20 minutes with Zombie Aqua viability stain (Biolegend) at room temperature. Following the incubation, fluorescent antibodies and isotype controls were added for 30 minutes on ice. For flow cytometry data collection, 100,000 cells per sample were targeted using a BD FACSFusion cytometer. Data were analyzed using FlowJo and GraphPad Prism software.

4.2.9 Measurement of Cellular Metabolism

75 µM Resazurin (7-hydroxy-3H-phenoxazin-3-one 10-oxide) was incubated with splenocytes in a 96 well plate for 3 hours. Metabolic reductive capacity was observed by viewing changes in fluorescence at excitation 560, emission 590 (Spectramax M5, Molecular Devices). Background fluorescence was taken using RPMI media and subtracted out from splenocyte readings for analysis.

4.2.10 Measurement of Cytokines

Following a 96-hour incubation, splenocytes in a 96-well culture plate were centrifuged. Supernatants were collected for cytokine analysis (GM-CSF, IFN- γ, IL-2, IL-21, IL-6, IL-10, IL-17, IL-23, TNF-α). Marker levels were detected using a U-Plex assay kit according to manufacturer instructions (Meso Scale Discovery). Each assay plate was read using the QuickPlex multiplex plate reader (Meso Scale Discovery).

4.2.11 Histology

Resected sponges and tissues were cryoembedded with Tissue-Plus O.C.T. Compound (FisherSci) and sectioned into 20 µm on microscope slides in triplicate. Slides were fixed in 10% neutral buffered formalin for 10 minutes, and Masson's trichrome stain (Sigma Aldrich) was conducted.

4.2.12 Statistical Analysis

Statistical evaluation was performed using one-way analysis of variance (ANOVA), followed by Tukey and Sidak multiple comparison tests. Statistical significance for all analyses was set at $p<0.05$. All statistical analyses were performed using GraphPad Software (GraphPad Software Inc.).

4.3 Results

4.3.1 Synthesis and Functional Characterization of ASIDs

We designed ASIDs as an implantable depot displaying covalently-coupled autoantigen. Microporous collagen sponges were selected as a scaffolding material due to their immunologically inert nature, widespread clinical utility since the 1970s [46], and commercial availability. The sponges we obtained for this work consisted of type I collagen with a columnar pore architecture (**Supp. Fig. 1a**). We hypothesized primary amine moieties would be chemically accessible on the surface of these collagenous materials (**Fig. 2a**) and pore diameters of ~200 μm would facilitate unhindered cell infiltration and nutrient transfer (**Fig. 2b**). To qualitatively assess surface accessibility of primary amines, a bifunctional NHS-PEG4-Azide linker was installed to collagen sponges, and rhodamine-alkyne was successfully conjugated using copper (I)-catalyzed azide-alkyne cycloaddition (**Fig. 2c**). Likewise using the same chemistry, a homopropargyl version of model autoantigen $PLP_{139-151}$ (hpPLP) was coupled to the collagen sponges to synthesize ASIDs. We indirectly quantified peptide conjugation efficiency by HPLC and determined 1.5 mgs of PLP was conjugated per 175 mm^3 collagen sponge (**Supp. Fig. 1b**). Accounting for the surface area of the microporous collagen sponges (2,000 mm^2), we estimate that antigen density was 0.468 $nmol/mm^2$ on the implant.

The functionality of conjugated autoantigen was then validated. ASID and Blank collagen sponges were each incubated in anti-PLP IgG-positive mouse serum. HRP-conjugated anti-mouse IgG was used to detect bound autoantibody (**Fig. 2d**), and the ASID, but not Blank sponge, showed successful capture. Additionally, EAE splenocytes were harvested at peak of disease and cultured *ex vivo* with ASIDs. Functional outcomes were compared with cells stimulated with 25 μM soluble $PLP_{139-151}$ as well as vehicle control (**Fig. 2e-g**). After 96 hours, splenocytes cultured with ASID

exhibited a significantly elevated metabolism over vehicle control (**Fig. 2e**), and CD86 expression levels were analogous to cells stimulated with soluble antigen (**Fig. 2f**). Likewise, soluble PLP and ASIDs generated robust IL-17 secretion, though only ASID culturing enabled high IL-12 after the incubation, indicating sustained APC activity (**Fig. 2g**).

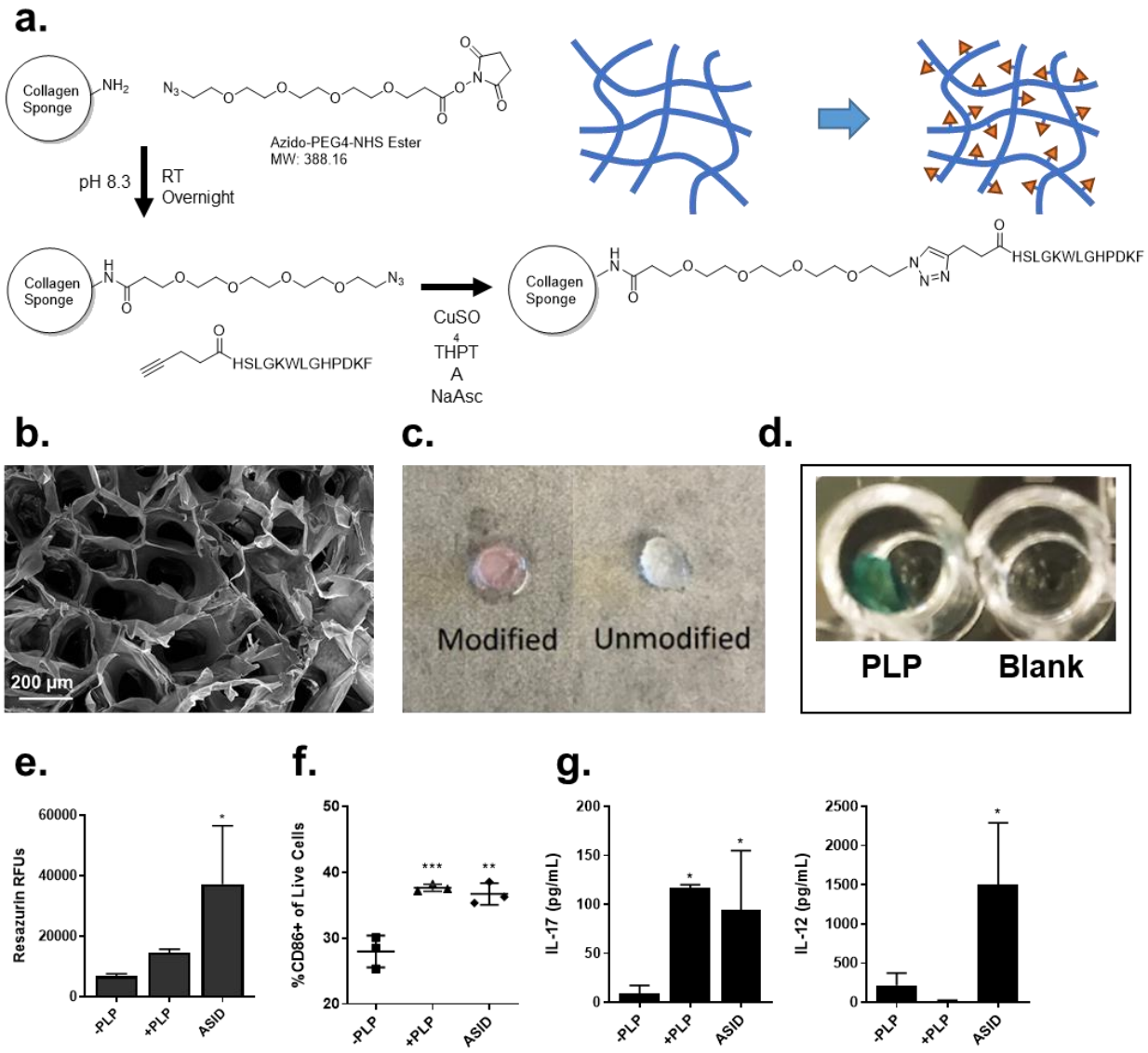

Figure 5. Synthesis and characterization of immunologically active PLP-conjugated ASIDs. **a)** The synthesis reaction scheme modified surface primary amines on collagen sponges with an azide-functional PEG linker subsequently clicked to homopropargyl $PLP_{139-151}$. **b)** Microporous

collagen sponges were used, and 150X SEM imaging showed an average pore size of approximately 200 μm. **c)** To visualize surface accessibility of primary amine moieties, rhodamine-alkyne was installed (left) and imaged compared to a Blank sponge (right), where dye conjugation could be confirmed. **d)** ASID with surface-conjugated PLP (left) captured anti-PLP IgG (note blue color) from mouse serum and a Blank collagen sponge (right) did not. **e)** Day 12 EAE Splenocyte metabolism was measured after incubation with vehicle (-PLP), soluble antigen (+PLP), or ASID. ASIDs significantly elevated metabolism over vehicle-treated splenocytes after 96 hours. **f)** Under the same conditions, CD86 expression was measured by flow cytometry, where ASIDs likewise upregulated costimulation in a manner similar to that of soluble antigen. **g)** In the same experiment, quantification of cytokine production showed that inflammatory IL-17 (left) was elevated by both +PLP and ASID treatment, however APC-indicating IL-12 (right) was only stimulated by incubation with ASIDs. (Statistical analysis was performed against –PLP as a control. n = 3/group, *$p < 0.05$, **$p < 0.01$, ***$p < 0.001$).

4.3.2 Subcutaneous Implantation of ASIDs prevents EAE in vivo

To investigate ASID therapeutic capacity, we subcutaneously implanted EAE mice with these constructs between the shoulder blades on day 7 post-induction, prior to the onset of symptoms (**Fig. 3a**). Healthy mice were also implanted with ASID to assess whether decoys themselves would stimulate an immune response. All implanted sponge constructs were sterilized and soaked overnight in a solution of 1200 ng/mL mouse GM-CSF prior to implantation to create impetus for cell infiltration and to normalize for inflammatory discrepancies that may have arisen from variability in surgery. This GM-CSF soaking concentration was informed by past work [51] and designed to be subtherapeutic in dose (roughly 200 ng per sponge). ASIDs highly suppressed

EAE *in vivo*, both in terms of significant scoring reduction as well as weight loss (**Fig. 3b-d**). Only two of four ASID mice showed any EAE symptoms at all, and none exhibited substantial paralysis which is defined as a clinical score of 2 or greater (**Fig. 3e**). Blank sponge implantation and Mock Surgery had no significant clinical effect on disease course, as these mice did not vary as compared to EAE alone with no surgical procedure or treatment. Control disease in this study was severe, as one mouse from the Blank group and one mouse from the Mock Surgery group each succumbed to disease at its peak. Strikingly, weight gain in EAE mice treated with ASID mirrored that of the healthy mice that were completely unhindered by disease (**Fig. 3c**).

At the conclusion of the study, serum and whole brain homogenates were collected. Anti-$PLP_{139-151}$ IgG ELISA was used as previously described [48, 49, 52] to detect relative autoantibody titers between the periphery (serum) and CNS (homogenized whole brain, **Fig. 3f, Supp. Fig. 2**). EAE mice implanted with an ASID presented with an elevated serum anti-PLP titer that did not translate to significant increases in CNS autoantibody.

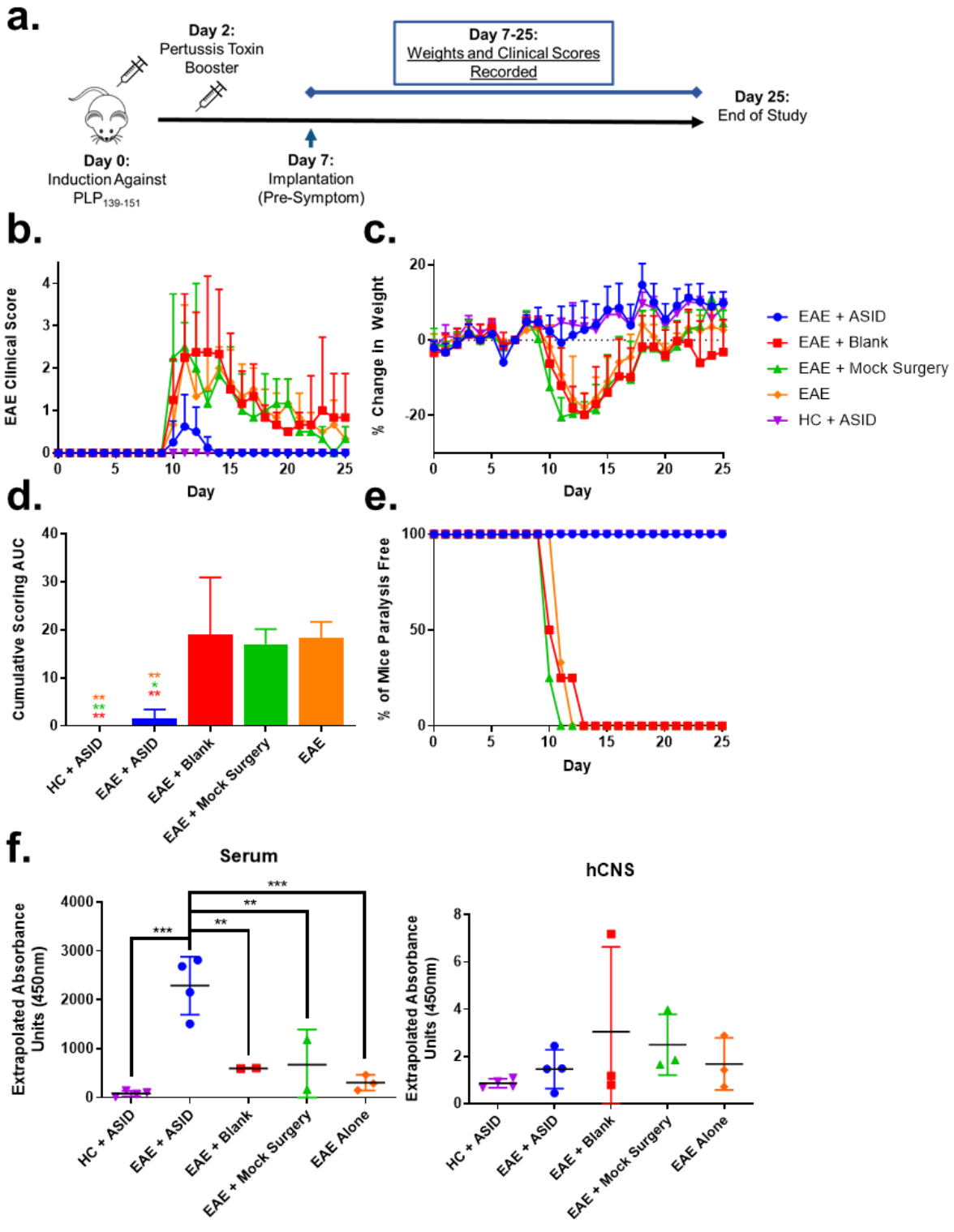

Figure 6. Therapeutic Evaluation of ASIDs against EAE in vivo. **a)** Mice were induced with EAE (excluding the HC, healthy controls group). On day 7, before symptoms began, mice were

subcutaneously implanted with either an ASID or Blank Collagen Sponge, given Mock Surgery, or no treatment (EAE alone). **b)** Clinical Scoring and **c)** Weight change data were collected over the course of 25 days and demonstrated that ASID implantation significantly suppressed disease and did not induce autoimmunity in healthy mice. **d)** Cumulative clinical score was calculated and compared between groups, reinforcing the significance of ASID effect. **e)** Additionally, disease incidence was stratified by presence of disease at or above a clinical score of 2, where ASID implantation completely prevented incidence of severe symptoms. **f)** After the study, serum and hCNS were collected from mice, and anti-PLP IgG titer was compared. ASID-implanted EAE mice exhibited a significantly elevated serum titer of anti-PLP IgG, but there was no change in hCNS titer (n = 3-4/group, *$p < 0.05$, **$p < 0.01$, ***$p < 0.001$).

4.3.3 ASID Infiltrates undergo Apoptosis upon PLP Rechallenge

We hypothesized the persistent, antigen-specific depot in ASIDs could selectively sequester autoreactive cell populations responsible for propagating autoimmunity to prevent disease. To evaluate this proposed decoy mechanism, we implanted EAE mice with *both* a Blank collagen sponge as well as an ASID on day 7 post-induction **(Fig. 4a**). Sponges and spleens were harvested at typical disease onset (day 10) or peak of disease (day 14). Cells were isolated and rechallenged with 25 μM PLP for 96 hours. At day 10, there were no significant differences in resazurin cell metabolism across splenocytes and sponge isolates (**Fig. 4b**), though ASIDs were considerably more degraded than Blank sponges (**Fig. 4c**). At day 14, metabolism in ASID infiltrates was roughly halved as compared to the Blank sponge and spleen **(Fig. 4b**). These results were initially surprising as we expected PLP-specific cells isolated from ASIDs to elicit a greater metabolic response upon rechallenge. To further investigate, harvested sponges were

cryosectioned and Masson's trichrome staining was used to assess morphological differences (**Fig. 4c**). Reflecting resazurin metabolism data, few differences were observable at day 10 (though ASID sections showed relatively more cell infiltrates). In contrast, ASID infiltrates appeared disjointed and unhealthy at the day 14 timepoint, while Blank sponge sections showed apparently healthy, ordered cell structures. Bright field microscopy of isolated splenocytes and spongeocytes after 96-hour PLP rechallenge corroborated apoptotic allusions. ASID isolates at the day 14 timepoint were clearly dying off in comparison to the Blank isolates and splenocytes.

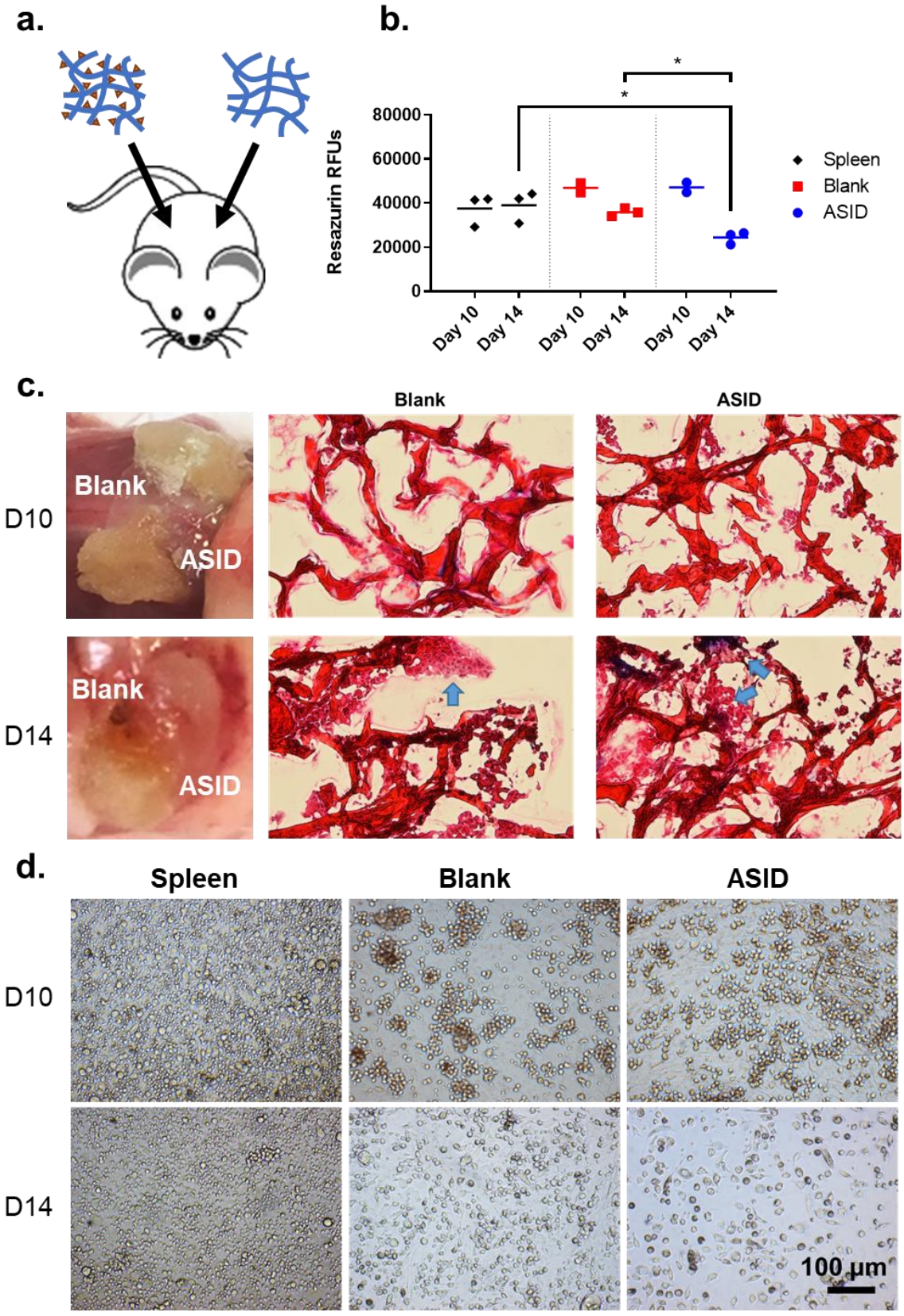
a.
b.
Resazurin RFUs
80000
60000
40000
20000
0
Day 10
Day 14
Day 10
Day 14
Day 10
Day 14
*
*
Spleen
Blank
ASID
c.
Blank
ASID
D10
D14
Blank
ASID
Blank
ASID
d.
Spleen
Blank
ASID
D10
D14
100 µm

Figure 7. Same-animal sponge infiltrate analysis. **a)** On day 7 post-induction, EAE mice received both an ASID and Blank Sponge separately placed in the subcutaneous space. **b)** At both onset (day 10) and peak (day 14) of disease, sponges and spleens were retrieved and challenged with 25 μM PLP. After 96 hours, metabolism was measured, and showed that while few differences were appreciable at day 10, the day 14 timepoint demonstrated that metabolism was significantly decreased in ASID cell infiltrates. **c)** Resected sponges were imaged upon retrieval and cryosectioned for trichrome histology on day 10 (top) and day 14 (bottom). Here, healthy and ordered cell structures were observed in the Blank construct by day 14, but ASID infiltrates were disordered and misshapen. **d)** These observations were conserved in splenocytes (left) and spongeocytes (Blank, middle, and ASID, right) after being isolated from the same mouse and rechallenged with 25 μM PLP. After 96 hours, splenocytes and Blank sponge infiltrates appeared largely healthy, however death was abundantly prevalent in ASID isolates (n = 3 biological replicates per group, $*p < 0.05$).

4.3.4 ASIDs Return Exhausted Immune Cells to Secondary Lymphoid Organs

In the same-animal implant experiment (**Fig. 4**), we noticed that secondary lymphoid organs appeared substantially engorged at times in disease course when splenopenia is typical, due to autoimmune cell egress to the CNS (**Supp. Fig. 3**). To further probe this phenomenon as a potential mechanistic underpinning of ASID efficacy, we implanted EAE mice with either an ASID, Blank sponge, or Mock Surgery on day 7 post-induction and harvested at peak of disease on day 14 (**Fig. 5a**). ASID-implanted mouse spleens were larger than those of the other groups by a factor of 4, and a similar size discrepancy in lymph nodes was evident (**Fig. 5b, Supp. Fig. 4**). The largest numbers of splenocytes were also harvested from these spleens, where yields averaged a multiple

of two and four times those from Mock and Blank controls, respectively. Cells were also isolated from sponges, and ASID isolates numbered roughly 5 million cells per construct while Blank infiltrates were on the order of 10,000 cells per sponge (**Fig. 5b**).

Isolated splenocytes and spongeocytes were rechallenged with media alone, 25 µM PLP, or 2.5 µg/mL of mitogenic Concanavalin A (ConA) for 96 hours (**Fig. 5c**). Unchallenged ASID splenocytes showed a significantly higher level of metabolism after the incubation (compared to controls), but the inclusion of PLP or ConA abrogated this increase. In the sponges, ASID isolates exhibited metabolism that was not exhaustive in response to PLP or ConA, and was significantly elevated over Blank sponge isolates, but these cells were much lower in number as mentioned above (**Fig. 5b**).

Flow cytometry was used to phenotype splenocytes immediately after harvest (**Fig. 5d, e)**. Moving from our previous same-animal experiment and observations of enlarged spleens, we hypothesized that ASIDs may have worked to evoke antigen overstimulation to exhaust the EAE autoimmune response and prematurely return perpetrating cells to secondary lymphoid organs. In accordance with our hypothesis, we found T (CD3+) and B (CD19+) cell populations to be significantly depleted in ASID spleens compared to those of Mock Surgery (**Fig. 5d**). Seemingly conflicting with these decreased levels of effector subsets, though, was an increase in CD11c+ APCs (**Fig. 5d**) and comparable levels of CD86+CD80+ costimulatory expression (**Fig. 5e**).

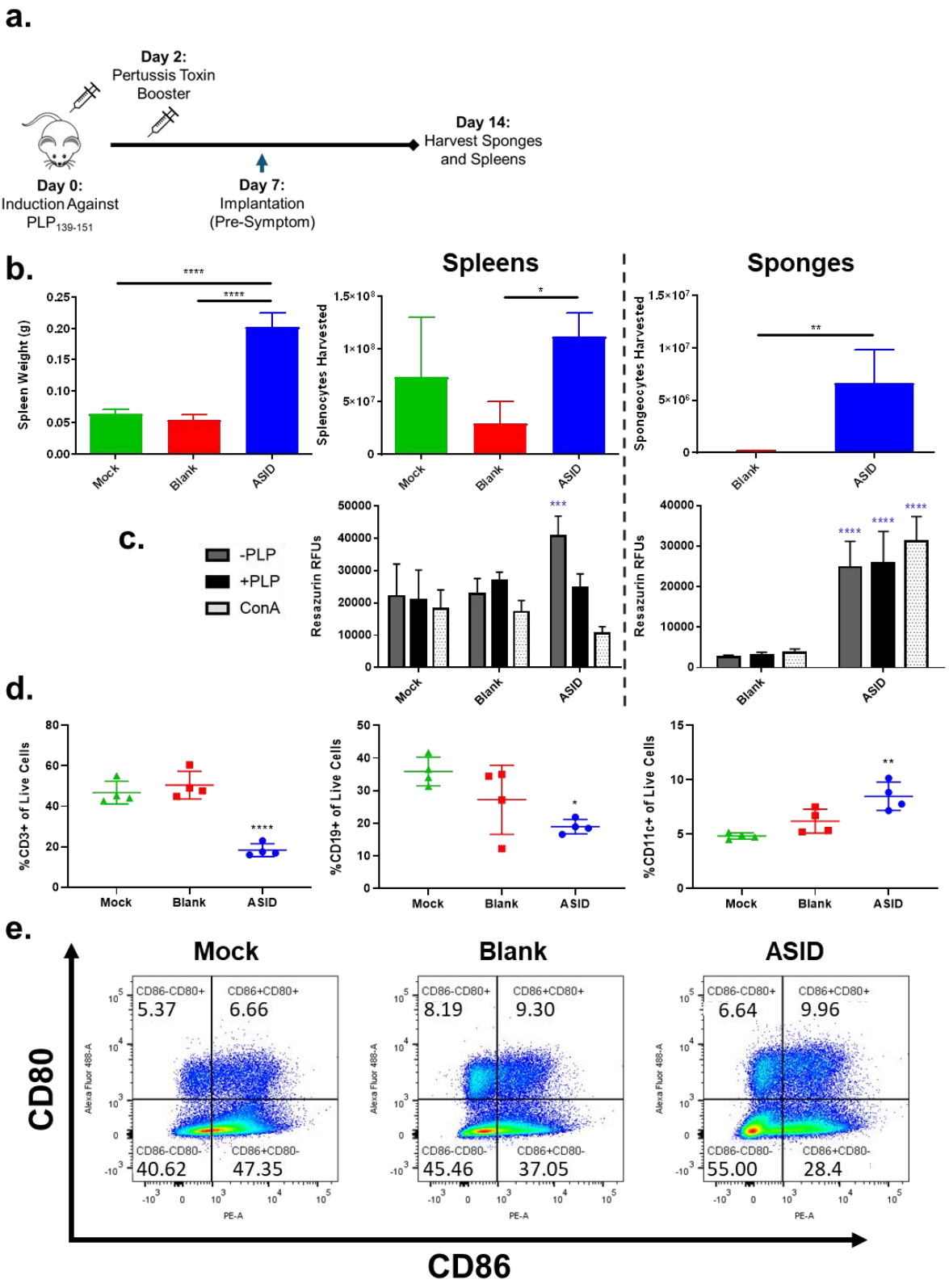
a.
Day 2:
Pertussis Toxin
Booster
Day 14:
Harvest Sponges
and Spleens
Day 0:
Induction Against
PLP139-151
Day 7:
Implantation
(Pre-Symptom)
b.
Spleens
Sponges
Spleen Weight (g)
Splenocytes Harvested
Spongeocytes Harvested
Mock
Blank
ASID
c.
-PLP
+PLP
ConA
Resazurin RFUs
d.
%CD3+ of Live Cells
%CD19+ of Live Cells
%CD11c+ of Live Cells
e.
Mock
Blank
ASID
CD86-CD80+
CD86+CD80+
CD86-CD80-
CD86+CD80-
5.37
6.66
40.62
47.35
8.19
9.30
45.46
37.05
6.64
9.96
55.00
28.4
CD80
CD86
Alexa Fluor 488-A
PE-A

Figure 8. Differences in composition at peak of disease. **a)** EAE mice were implanted with ASID, Blank Sponge, or Mock Surgery. On day 14, spleens were harvested. **b)** Spleen weights were compared at harvest (left) in addition to isolated splenocyte (middle) and spongeocyte (right) counts. ASIDs both recruited the most spongeocytes and induced significant spleen engorgement. **c)** Cell isolates from spleens (left) and sponges (right) were incubated with vehicle (-PLP), 25 µM PLP (+PLP), or 2.5 µg/mL Concanavalin A (ConA) for 96 hours and cell metabolism was measured. ASID splenocytes exhibited high metabolism when incubated with vehicle, but PLP rechallenge diminished this elevation. In spongeocytes, metabolism was largely conserved across all three treatments. **d)** Flow cytometry was used to phenotype splenocytes for CD3 (left), CD19 (middle), and CD11c (right), and splenocytes from ASID implanted mice were found to be relatively depleted of T and B cell subsets. Additionally, CD11c+ populations were increased in ASID spleens as compared to controls. **e)** CD80 and CD86 were also observed between groups, where CD86+CD80+ costimulation was slightly elevated by Blank sponges and ASIDs. (Statistical analysis was performed against the Mock group as a control. n = 4 biological replicates group, *$p < 0.05$, **$p < 0.01$, ***$p < 0.001$, ****$p<0.0001$).

4.3.5 Antigen-Specific Exhaustion Persists after PLP rechallenge

Moving from baseline phenotyping, day 14 splenocytes were also rechallenged with 25 µM PLP for 96 hours. After the incubation, many baseline trends persisted (**Fig. 6a**). ASID splenocyte CD3+ T cells remained lower in proportion to controls both with and without rechallenge, though CD19+ B cells were relatively similar at this time point. CD11c+ APCs were significantly elevated when incubated with vehicle media, but not significantly different when challenged with antigen. However, an inverted antigen rechallenge trend was appreciable; the

inclusion of PLP led to expanded CD11c+ populations in Mock and Blank controls, but led to a decrease when included with ASID splenocytes **(Fig. 6a**). Despite this decrease, the CD11c+ proportion of rechallenged ASID splenocytes was slightly higher than those of the controls. Costimulation was promoted upon rechallenge without exception across groups, but PLP rechallenge in ASID splenocytes promoted exorbitantly higher levels of CD80+ as well as CD86+CD80+ double positive cells (**Fig. 6a**).

One major limitation of the EAE model is a lack of tools for probing antigen-specificity. In recent years, our group has published a multivalent nanomaterial known as the soluble antigen array (SAgA), which has been developed as an antigen-specific immunotherapy [53-56]. SAgAs evoke efficacy by specifically engaging surface-bound B cell receptors [50, 57-59]. In this study, we hypothesized that fluorescently labeled SAgAs could identify antigen-specific B cells much in the same way that MHC-tetramers are employed for T cells. By including SAgAs with other fluorescent antibodies, we developed a method in which antigen-specific cells could be identified by gating on CD19 (**Fig. 6b, Supp. Fig 4**). Extrapolating this protocol allowed identification of antigen-specific subsets of B cells in EAE splenocytes **(Fig. 6c**). CD19+CD11c+ autoimmune-associated B cells (ABCs) have been reported as potent, antigen-specific instigators of immunity in EAE and autoimmune disease alike [47, 50, 60]. Interestingly, ASID splenocytes showed significantly elevated proportions of this population when incubated with vehicle (**Fig. 6c**), though much like resazurin (**Fig. 4b, Fig. 5c**), these cells were diminished by PLP rechallenge. The SAgA probe verified this trend was conserved within the antigen-specific CD19+CD11c+ ABC subset, but not the broader CD19+ B cell population.

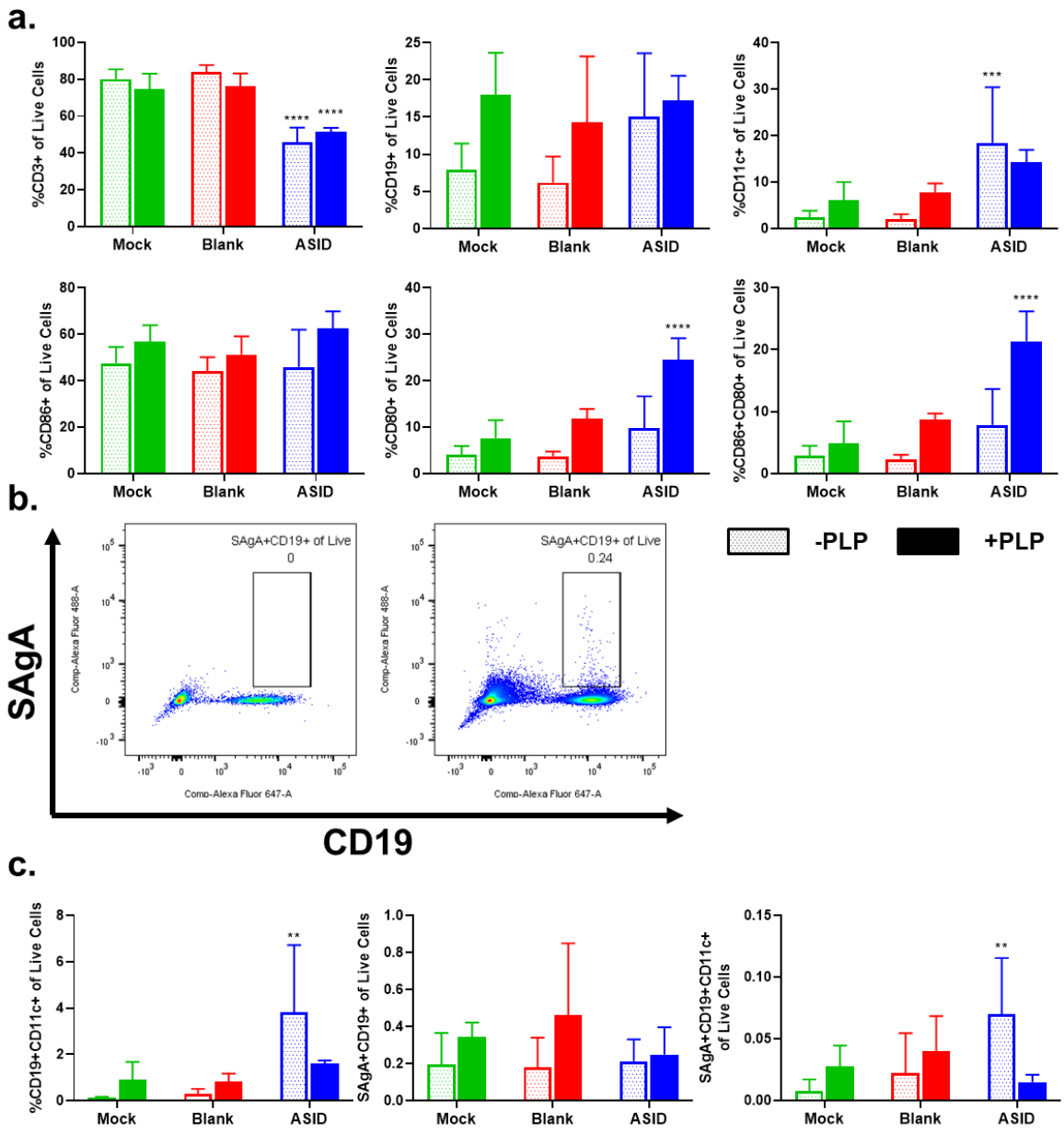

Figure 9. PLP rechallenge response among harvested splenocytes. **a)** From the previous experiment, excess splenocytes were phenotyped after 96 hours of vehicle (-PLP, open bars) or 25 µM PLP treatment (+PLP, solid bars) for CD3, CD19, and CD11c (top row, left to right) as well as costimulatory markers CD86, CD80 and double positive CD86+CD80+ populations (bottom row, left to right). Similar trends to the baseline analysis were appreciable; CD3+ T cell

proportions were suppressed in ASID spleens, but CD11c+ populations were slightly more prevalent. **b)** SAgAs were used to reliably tag antigen-specific B-cells and ultimately **c)** probe disease-relevant ABCs (left), SAgA+ B cells (middle), and SAgA+ ABCs (right). Within ASID splenocytes, the ABC subset showed a considerable decrease in prevalence in response to antigen rechallenge. (Statistical analysis was performed against the Mock group as a control. n = 4 biological replicates per group, *p < 0.05, **p < 0.01, ***p < 0.001, ****p<0.0001).

4.3.6 Pro-inflammatory Cytokines are Elevated in ASID-Treated Splenocytes at Day 14 and 25

In addition to phenotypic changes in response to antigen rechallenge, we assessed cytokine responses in splenocytes harvested on day 14 or 25 and cultured with 25 μM PLP or vehicle for 96 hours (+PLP reported in **Fig. 7a,** -PLP and absolute concentrations in **Supp. Fig. 8**). At day 14, ASID mice showed increased in pro-inflammatory cytokines GM-CSF, IFN-γ, and IL-6 as compared to the Mock Surgery group, while splenocytes from mice implanted with a Blank sponge largely secreted less of each analyte screened. At day 25, ASID-treated splenocytes still exhibited elevated levels of pro-inflammatory cytokines IFN-γ, IL-15, IL-17, and IL-6, though at this point, anti-inflammatory IL-10 was most profoundly upregulated.

We contextualized cytokine trends across a number of mechanistically indicative ratios (**Fig. 7b**). IL-2/IL-17 was used as a measure of T cell proliferation proportional to overall EAE inflammation. Mock Surgery and Blank-treated mice showed increases in T cell proliferation at day 14 which was resolved by day 25, but ASID treatment appears to have restricted IL-2 at peak of disease. This trend is in concordance the exhaustive mechanism suggested by our other experiments. IL-12/IL-2 was used to interrogate the balance between APCs and T cells. Consistent

with our earlier observations, ASID-treatment seems to cause an upward skew in this ratio, where APC levels are sustained while IL-2 is diminished. Finally, to investigate the observed increase of IL-10 from ASID splenocytes at day 25, IL-10/IFN-γ was employed to probe a potential tolerogenesis where anti-inflammatory IL-10 precludes pro-inflammatory IFN-γ production. Interestingly, despite these observed increases in IL-10, IFN-γ remains proportionally abundant such that this ratio fell well within the bounds of the controls.

Finally, we sought to discern whether ASID implantation would protect mice from the recurring paralysis that is characteristic of the $PLP_{139-151}$-EAE model. In our early studies, ASIDs and Blank sponges alike were found to be completely resorbed by day 25. We wondered if a durable therapeutic effect could be realized as a result of ASID-induced cell exhaustion (**Fig. 7c**). During the initial phase of disease, only one of three ASID recipients displayed any EAE symptoms, and each of the Mock Surgery cohort exhibited a fully severe initial presentation. Remarkably, all ASID-implanted mice were protected from recurrent disease through day 60 while two of three Mock Surgery mice displayed robust relapses on days 37 and 38 post-induction. *Ex vivo* analyses revealed few differences between splenocytes in response to PLP rechallenge (**Supp. Fig. 9**).

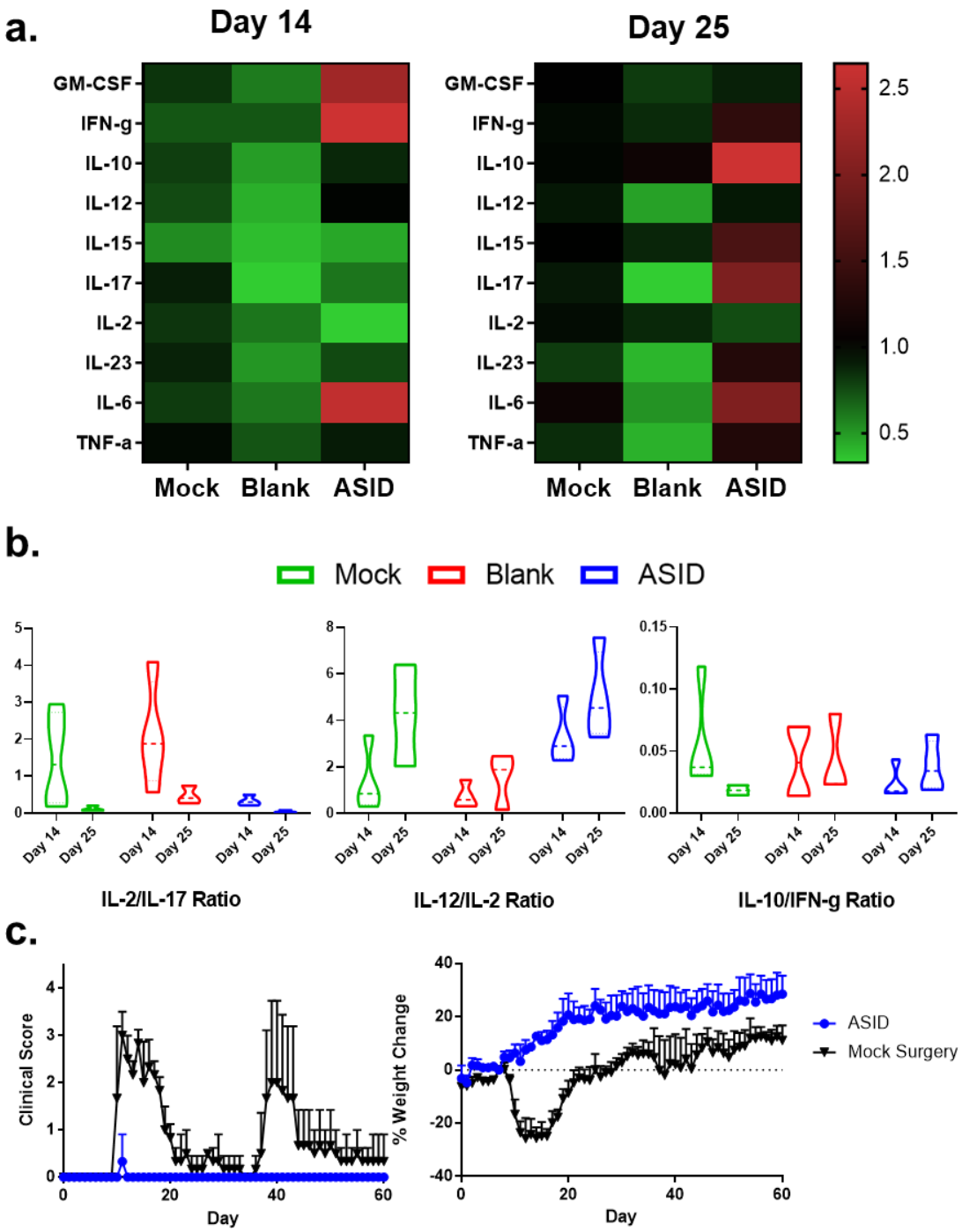

Figure 10. Cytokine changes in PLP challenged splenocytes. **a)** Day 14 (left) and day 25 splenocytes (right) were challenged for 96 hours with 25 µM PLP, and changes are expressed in terms of median fold-change with respect to Mock as a control. At day 14, inflammatory cytokines

GM-CSF, IFN-γ, and IL-6 abounded in ASID splenocytes, though IL-2 was suppressed. At day 25, both inflammatory and anti-inflammatory cytokines were elevated in the ASID cohort. **b)** Cytokine ratio analysis of IL-2/IL-17, IL-12/IL-2, and IL-10/IFN-γ (left to right) at both time points was used to provide greater resolution of inflammatory trends. Decreased ASID IL-17/IL-12 showed that despite increases in general inflammation, T cell proliferation did not occur. Additionally, IL-12/IL-2 was employed to investigate exhaustion, where increased antigen presentation (IL-12) did not stimulate T cell proliferation either. To rule out tolerogensis, IL-10/IFN-γ was employed, showing that ASID implantation did not evoke a response of that nature. **c**) Mice were implanted with either ASID (blue) or Mock Surgery (Black) on day 7 post-induction. By day 60 (after ASIDs had been completely resorbed), no ASID mice had relapsed, while two of three Mock Surgery mice displayed a fully severe recurrence of disease. (Statistical analysis was performed against the Mock group as a control. n = 3-4 biological replicates per group).

4.4 Discussion

Previous works exploring antigen-specific immunotherapies for autoimmunity delivered autoantigen in vastly differing ways, including soluble, insoluble, and biomaterial compositions. ASIDs utilize covalent attachment of autoantigen onto a microporous scaffold to inhibit EAE *in vivo* when implanted subcutaneously after disease induction, but before the appearance of symptoms. Past work exploring immunologically-active therapeutic biomaterials has mostly explored co-delivery formulations [27]. To our knowledge, ASIDs represent a first demonstration of antigen-specific immune cell sequestration for therapeutic effect. Recently, the Serwold group disseminated an implantable biomaterial soaked in autoantigen for the purpose of homing and enriching antigen-specific populations in models of Type 1 Diabetes, but interestingly, no

therapeutic effect was realized [35]. Our data also indicated antigen-specific cell infiltration into ASIDs (**Fig. 4, Fig. 5b**), but the therapeutic capacity we observed likely resulted from the specification of irreversible epitope conjugation to our constructs, which has been well described to enable antigen persistence and boost T cell stimulation [61]. In our example, such overstimulation proved itself a driver of effect through exhaustion and may explain our differential therapeutic success.

ASIDs elicited robust DC activation *ex vivo* (**Fig. 1e-g**). We initially hypothesized that this mechanism would solely facilitate the recruitment and sequestration of T and B effectors *in vivo*. When implanted, however, ASIDs spurred exhaustion and apoptosis within the constructs (**Fig. 3**). Evidence has emerged regarding the potential for "therapeutic exhaustion" by extrapolating a liability observed during chronic infection for possible benefit in autoimmunity [62]. In our studies, exhaustion was implicated in the prevention of disease. Spleen weights correlated highly with suppression of EAE, where engorgement was likely a consequence of ASID-induced exhaustion and return to SLOs (**Fig. 5b, Supp. Fig. 4** [14, 63]. The exhausted state of splenocytes in ASID-treated mice was corroborated by effector non-responsiveness to antigen rechallenge. Despite the presence of CD86+CD80+ active DCs (**Fig. 5d, e, and Fig. 6**), we observed an absence of IL-2 despite upregulation of other inflammatory markers such as IFN-γ (**Fig. 7a, b**). Interestingly, proliferation of resting (unchallenged) ABCs was diminished in the presence of PLP rechallenge (**Fig. 7c**). Abrogated proliferation was most severe in the antigen-specific population of this subset, suggesting that population changes may be driven by PLP-specific mechanisms. Autoimmunity was restricted to the periphery, exclusive of the CNS, as evident in the elevation of serum anti-PLP IgG, which was not observed in homogenized brain (**Fig. 3f**). In effect, the PLP-specific

response was short-circuited and exhausted in ASID-treated mice, which translated to therapeutic success.

Remarkably, no ASID-implanted EAE mice developed significant disease (score >1) over 60 days. All three Mock Surgery-receiving counterparts exhibited severe primary EAE, and two of these mice exhibited robust flare-ups over this interval after day 25 (**Fig. 7c**). After the initial 25-day efficacy study, ASID and Blank constructs had been completely degraded, so this experiment was conducted to observe relapsed autoimmunity that is typical of the $PLP_{139-151}$-EAE model. We originally expected ASID-treated mice to develop paralysis similarly to those given Mock Surgery by virtue of regained functionality after exhaustion, perhaps even at a higher rate or intensity of disease due to a delayed hypersensitivity reaction. In retrospect, initial disease prevention in ASID mice may have limited primary tissue inflammation and abrogated subsequent migration to the CNS. Alternatively, past work has shown that antigen, once trafficked to lymphoid organs, can persist for several months after exposure [64, 65]. Future studies in the ASID model should investigate the presence of autoantigen in engorged lymphoid organs, as persistence may enable the continued modulation of immunity even after the biomaterial has degraded.

Alternatively, ASID implantation could have induced differentially robust exhaustion similar to what is observed in chronic infection where clonal deletion or permanent anergy can ensue [18, 66-68]. In the EAE model employed here, immunity is generated against the $PLP_{139-151}$ epitope, a small fraction of the larger PLP antigen, which is ultimately one of many constitutive building blocks of the myelin sheath. As a result, $PLP_{139-151}$ density in the CNS is low and inaccessible relative to an ASID [69]. Conversely, $PLP_{139-151}$ density in ASIDs is high and by design, easily accessible to extravasating immune cells. Antigen density is known to highly dictate costimulation and downstream immunity [69-72], where excessively high density can drive

overstimulation and cell death [73-75]. Differences in these outcomes were evident between ASID-implanted mice and controls, especially in histological studies and bioassays of spongeocytes (**Fig. 4**). Future studies titrating the antigen density in ASIDs could provide an interesting design characteristic directing cell exhaustion for therapeutic benefit.

4.5 Conclusions

In clinical practice, some of the most effective MS therapeutics such as natalizumab and fingolimod work by inhibiting immune cell migration and trafficking to the CNS [19, 20]. Such drugs have a steep trade-off, risking life-threatening consequences of nonspecific immunosuppression for therapeutic efficacy [21-23]. By demonstrating the potential to affect immune cell migration in an antigen-specific fashion, our work suggests autoimmunity may be short-circuited in potent, yet safer ways. Additional studies will determine if ASID performance can be extrapolated to a broader palette of autoantigens and if therapeutic efficacy can be achieved when intervening at different points in the disease. The immunological mechanism of ASID capture, deactivation, and release of exhausted autoimmune cells offers a new paradigm to short circuit immune cell migration to prevent relapsing autoimmune diseases.

4.6 Supplementary Information

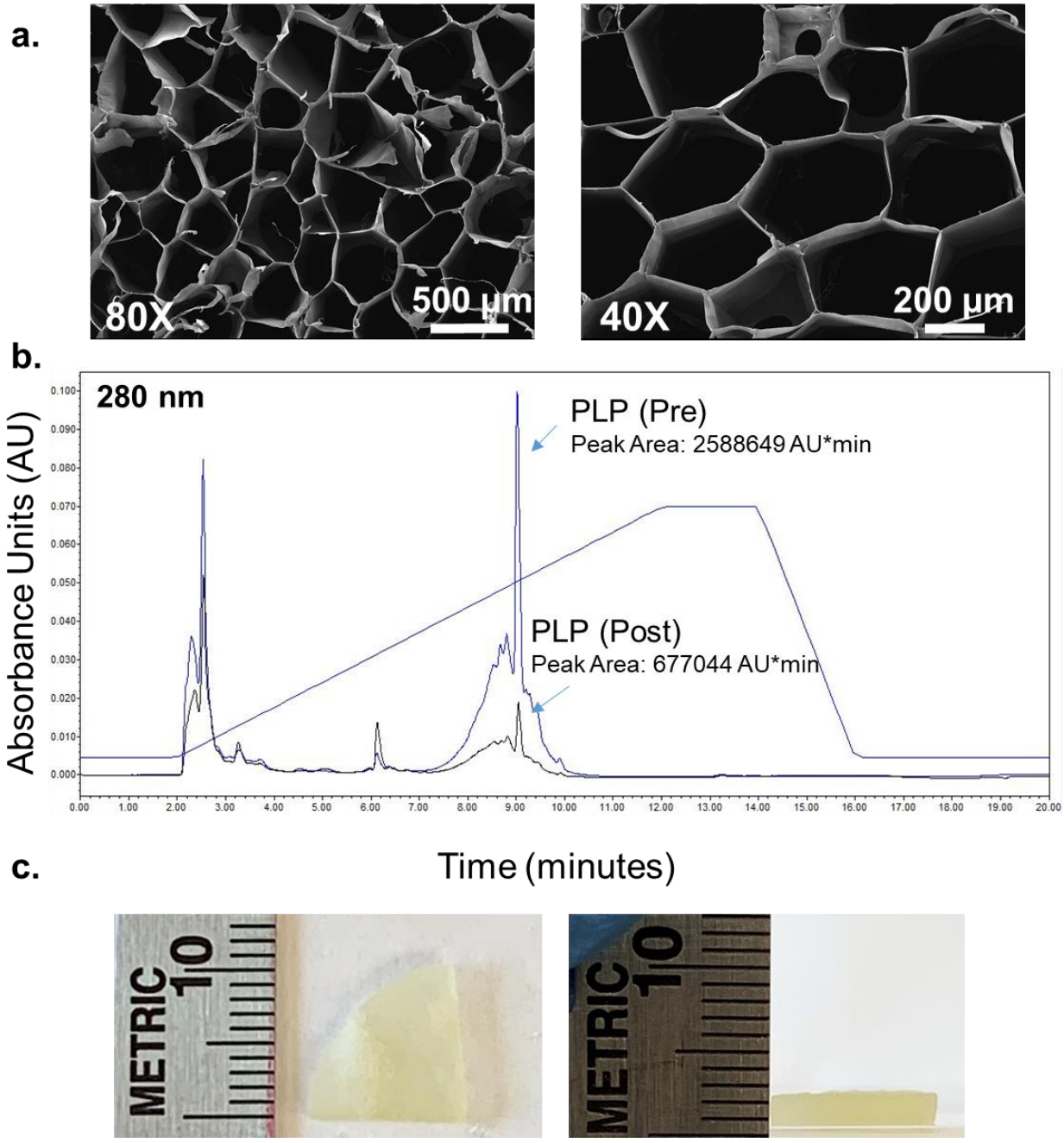

Supplementary Figure 1. Collagen sponges possess appealing porosity and are immunologically inert, making them suitable for the present application. **a.** 40X (left) and 80X (right) SEM images were provided with permission from Advanced Biomatrix to show columnar architecture and porosity such that surface area could be calculated (2,000 mm^2 per implant). **b.** RP-HPLC results for quantifying $PLP_{139\text{-}151}$ conjugation to collagen sponges. Pre and post reaction mixtures were sampled and PLP peak areas were determined (t =8.9 minutes. 73.8% of the 2 mgs (excess) of peptide in the reaction mixture was consumed from pre to post reaction, indicating that 1.5 mgs of peptide was conjugated to the material. **c.** Sponges used in the animal studies for this work were quarter cylinders of 21 mm diameter collagen sponges with height of 2 mm.

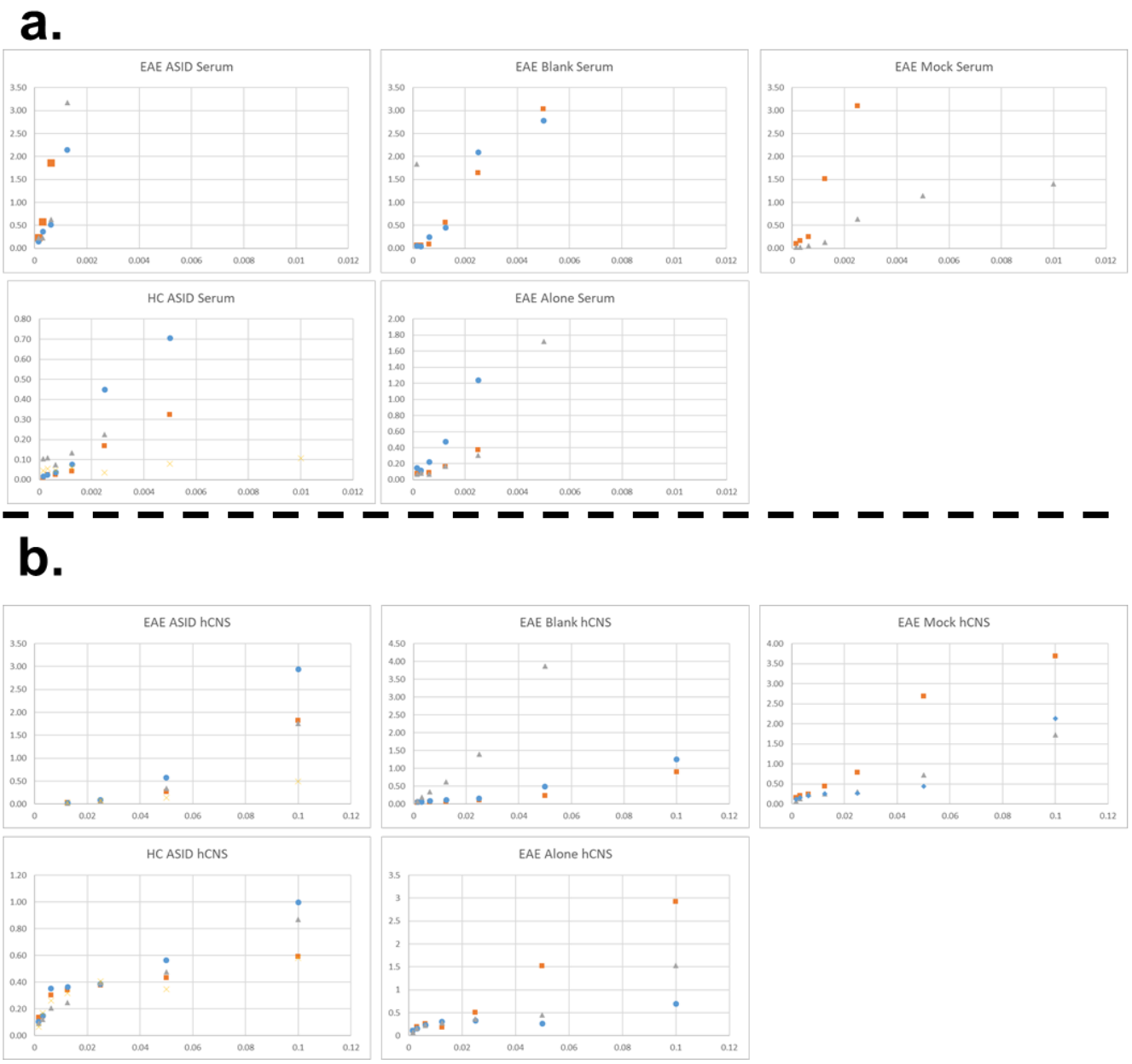

Supplementary Figure 2. Serum and hCNS autoantibody titers were detected by anti-PLP IgG ELISA. To compare relative titers, absorbance values were collected across seven dilutions, and the slopes of linear regions were calculated ($r > 0.8$) and compared. Both serum (**a**) and hCNS (**b**) were analyzed.

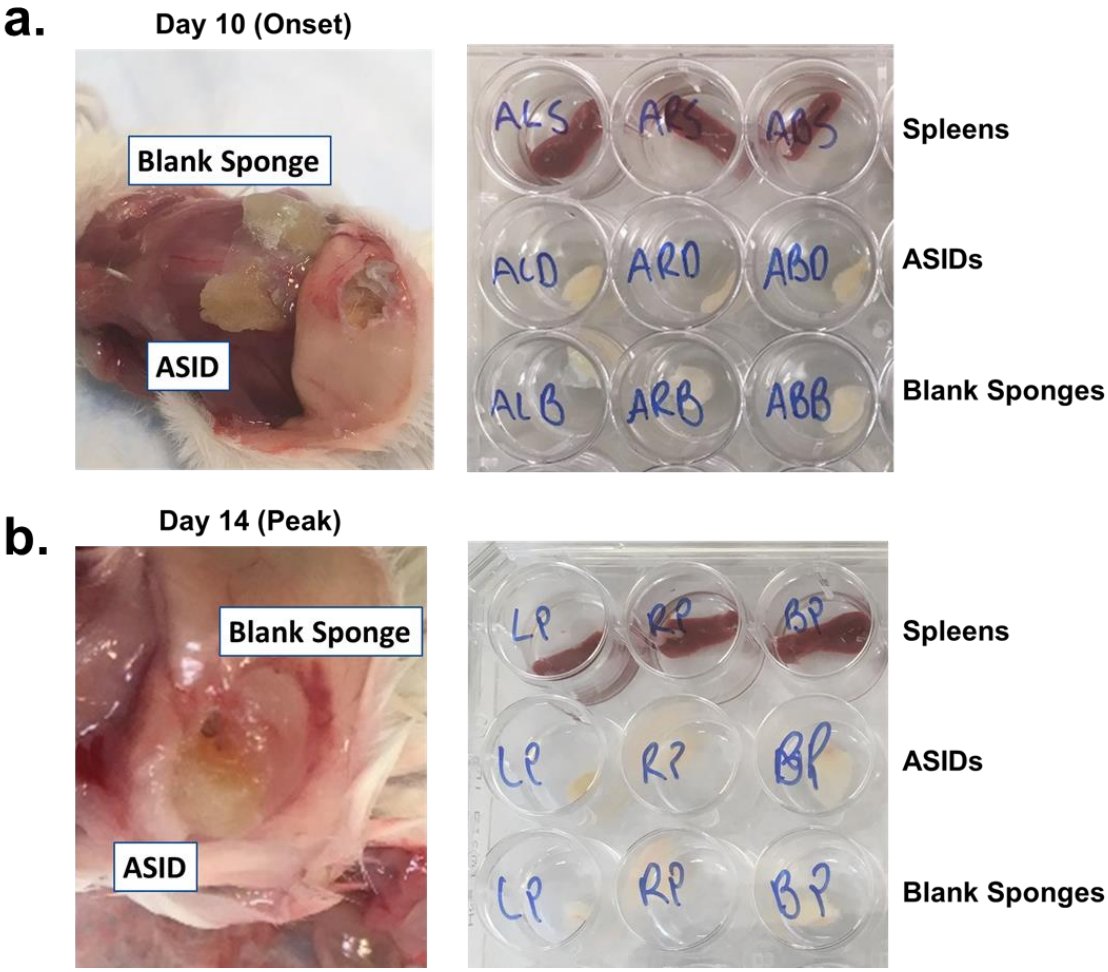

Supplementary Figure 3. In the same animal implant experiment, we observed engorged spleens at a time when secondary lymphoid organs are typically small. **a)** Day 10 and **b)** Day 14 sponges and spleens are pictured.

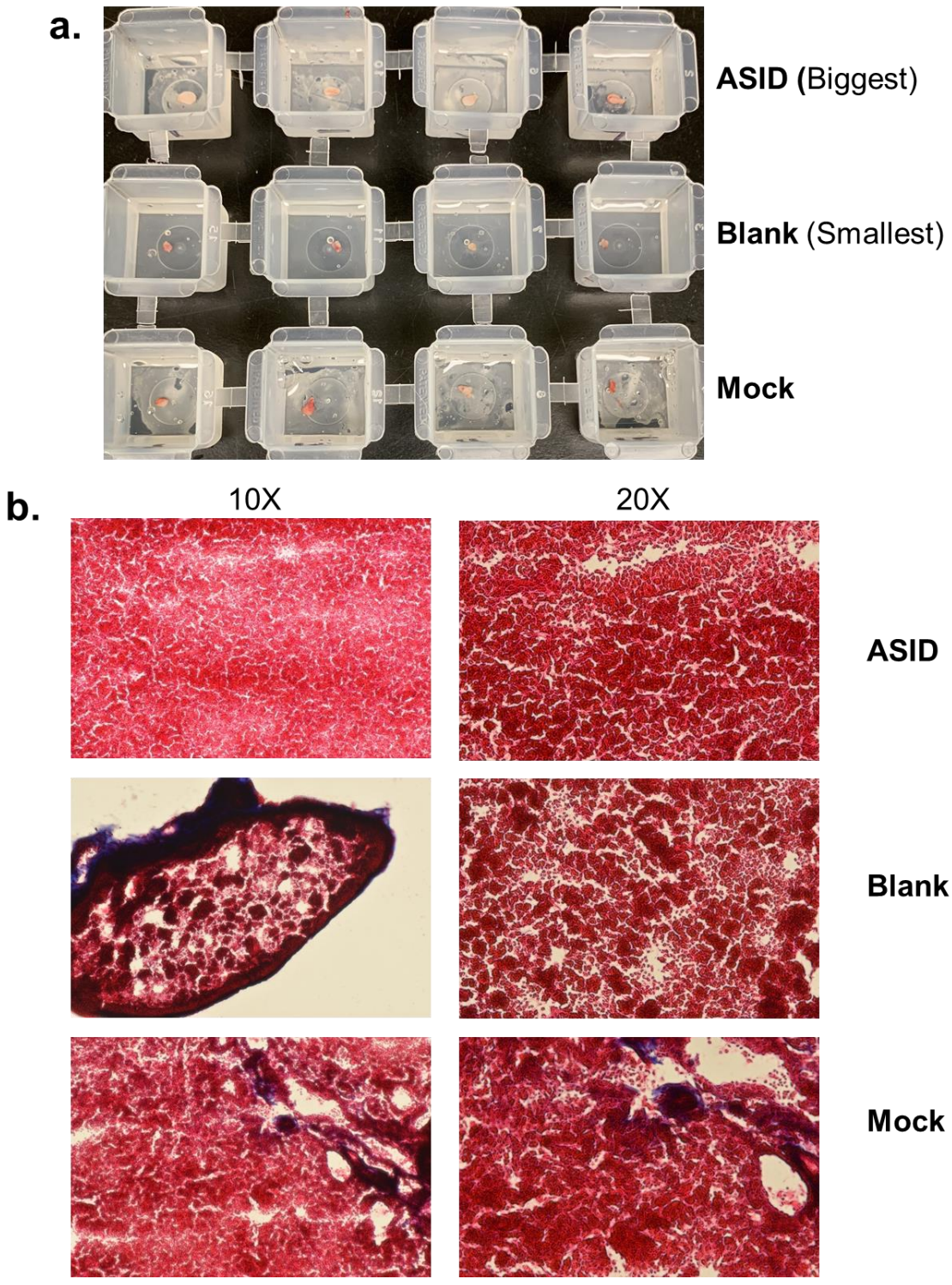

Supplementary Figure 4. EAE mice were implanted with either ASID, Blank Sponge, or Mock Surgery on Day 7 post induction. At day 14 (peak of disease), **a)** ASID popliteal lymph nodes were visibly swollen over Blank and Mock lymph nodes. **b)** Trichrome staining revealed a higher cell density in engorged ASID lymph nodes.

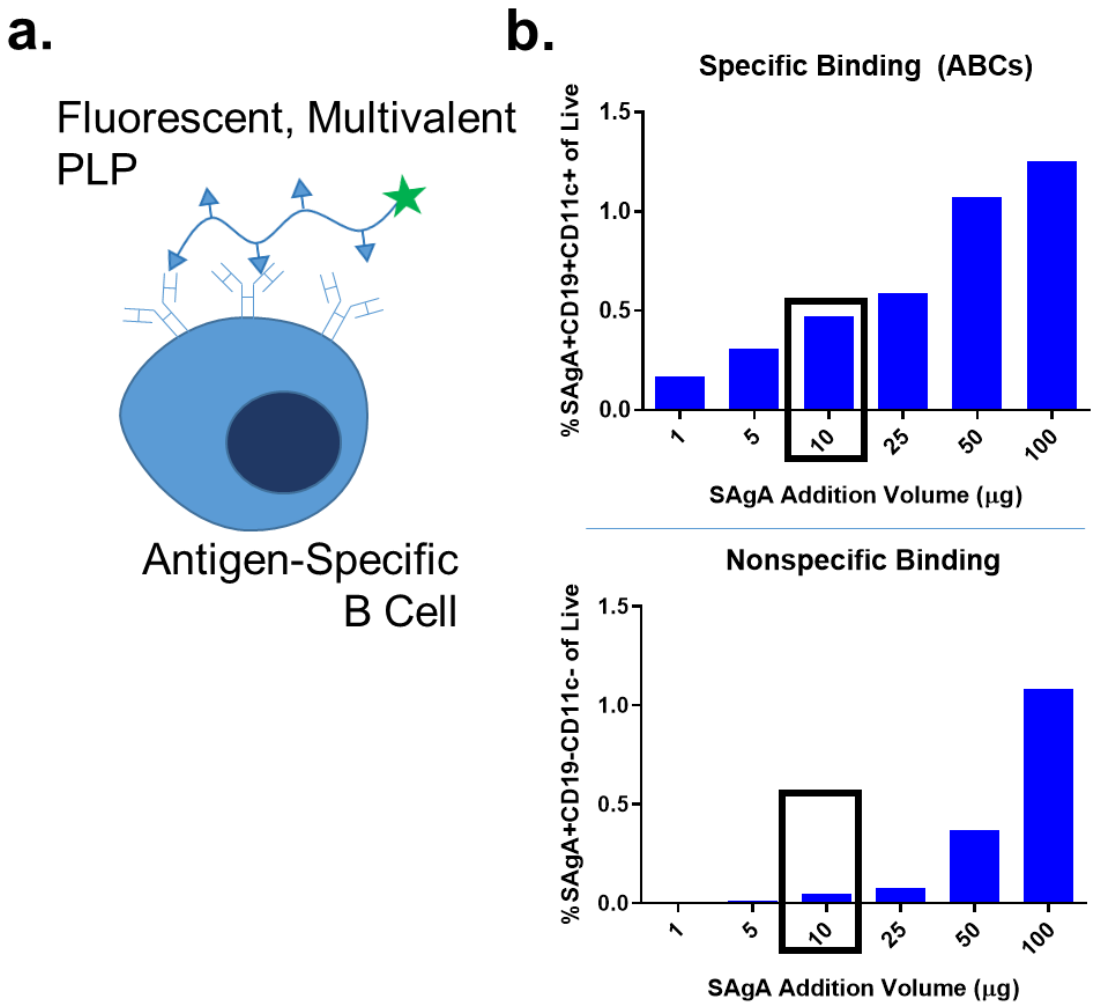

Supplementary Figure 5. Soluble Antigen Arrays (SAgAs) consist of autoantigen epitopes conjugated to a 16 kDa hyaluronic acid backbone. **a)** By incubating FITC-labeled SAgAs with EAE splenocytes, antigen-specific B cells were tagged through avid binding of the BCR. **b)** To determine a labeling method for fluorescent SAgAs, we titrated the amount of SAgA incubated per million splenocytes. Via flow cytometry, we measured antigen specific populations (ABCs, CD19+CD11c+) and nonspecific populations (CD19-CD11c-). 10 µg of SAgA per million splenocytes was selected as an appropriate labeling concentration, as it maximized specific binding while limiting nonspecific interactions.

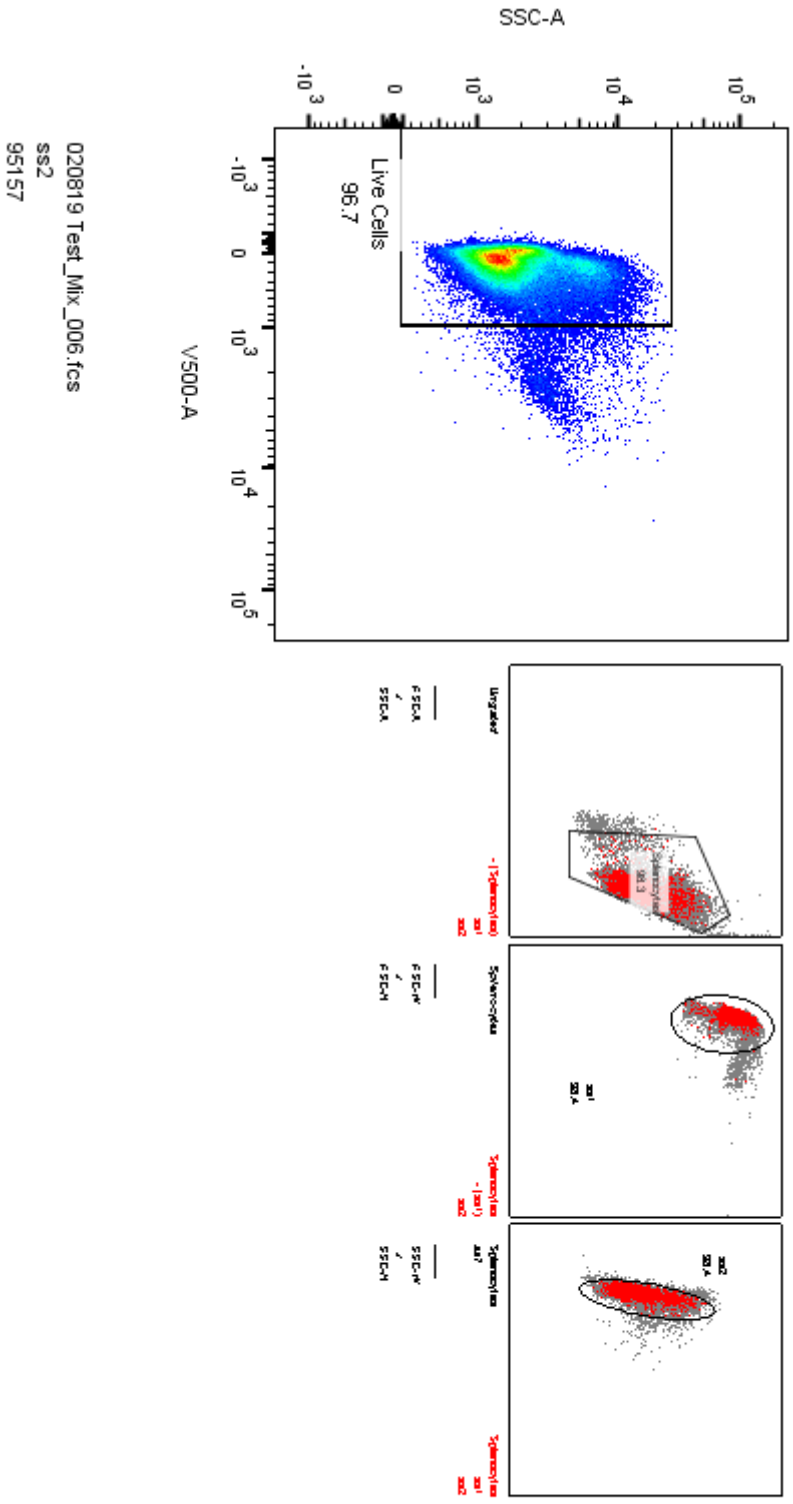

Supplementary Figure 6. Gating for flow cytometry live cell populations.

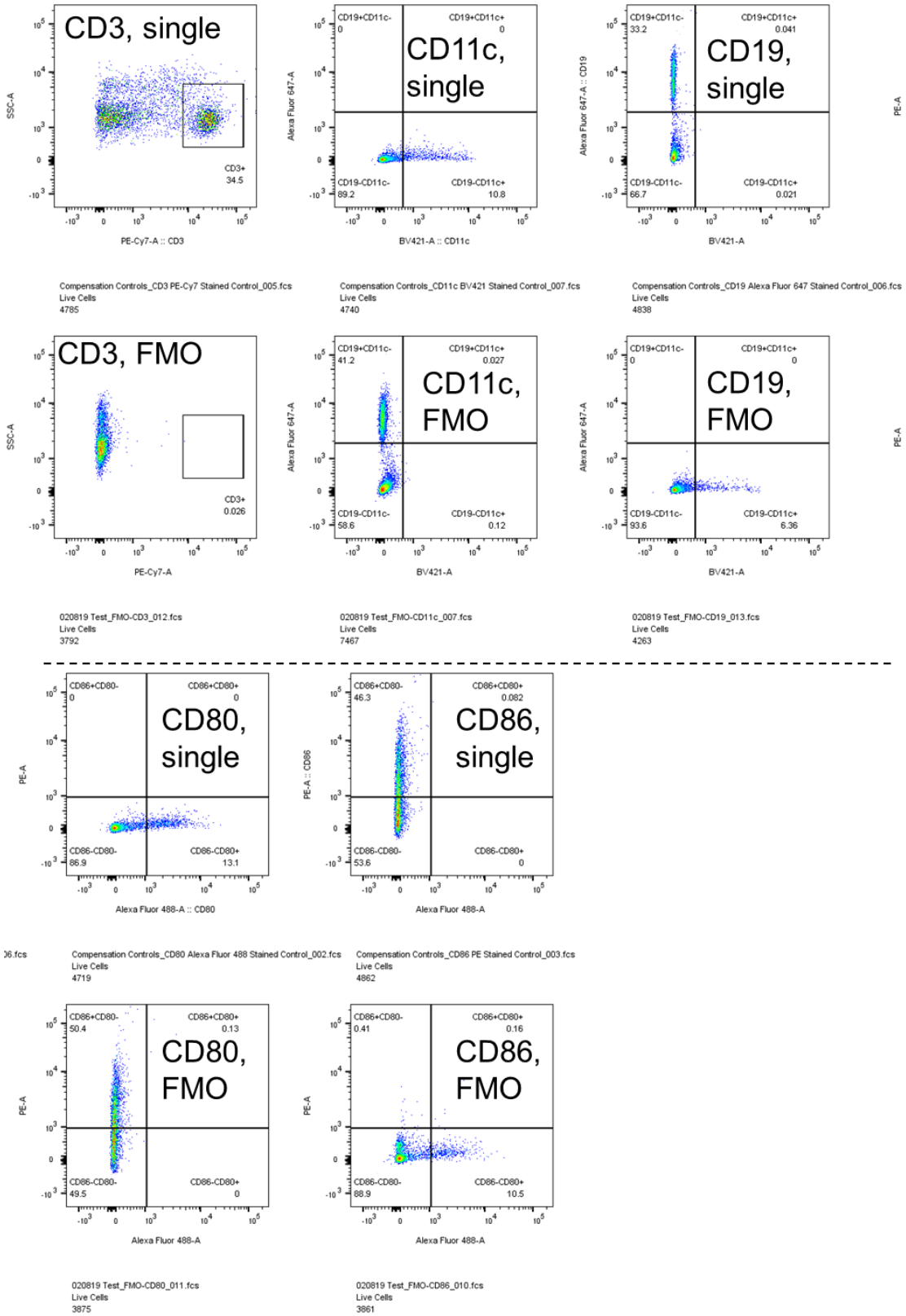
CD3, single
SSC-A
PE-Cy7-A :: CD3
CD3+
34.5
Compensation Controls_CD3 PE-Cy7 Stained Control_005.fcs
Live Cells
4785
CD11c, single
Alexa Fluor 647-A
BV421-A :: CD11c
CD19+CD11c-
0
CD19+CD11c+
0
CD19-CD11c-
89.2
CD19-CD11c+
10.8
Compensation Controls_CD11c BV421 Stained Control_007.fcs
Live Cells
4740
CD19, single
Alexa Fluor 647-A :: CD19
BV421-A
CD19+CD11c-
33.2
CD19+CD11c+
0.041
CD19-CD11c-
66.7
CD19-CD11c+
0.021
Compensation Controls_CD19 Alexa Fluor 647 Stained Control_006.fcs
Live Cells
4838
PE-A
CD3, FMO
SSC-A
PE-Cy7-A
CD3+
0.026
020819 Test_FMO-CD3_012.fcs
Live Cells
3792
CD11c, FMO
Alexa Fluor 647-A
BV421-A
CD19+CD11c-
41.2
CD19+CD11c+
0.027
CD19-CD11c-
58.6
CD19-CD11c+
0.12
020819 Test_FMO-CD11c_007.fcs
Live Cells
7467
CD19, FMO
Alexa Fluor 647-A
BV421-A
CD19+CD11c-
0
CD19+CD11c+
0
CD19-CD11c-
93.6
CD19-CD11c+
6.36
020819 Test_FMO-CD19_013.fcs
Live Cells
4263
PE-A
CD80, single
PE-A
Alexa Fluor 488-A :: CD80
CD86+CD80-
0
CD86+CD80+
0
CD86-CD80-
86.9
CD86-CD80+
13.1
CD86, single
PE-A :: CD86
Alexa Fluor 488-A
CD86+CD80-
46.3
CD86+CD80+
0.082
CD86-CD80-
53.6
CD86-CD80+
0
Compensation Controls_CD80 Alexa Fluor 488 Stained Control_002.fcs
Live Cells
4719
Compensation Controls_CD86 PE Stained Control_003.fcs
Live Cells
4862
CD80, FMO
PE-A
Alexa Fluor 488-A
CD86+CD80-
50.4
CD86+CD80+
0.13
CD86-CD80-
49.5
CD86-CD80+
0
020819 Test_FMO-CD80_011.fcs
Live Cells
3875
CD86, FMO
PE-A
Alexa Fluor 488-A
CD86+CD80-
0.41
CD86+CD80+
0.16
CD86-CD80-
88.9
CD86-CD80+
10.5
020819 Test_FMO-CD86_010.fcs
Live Cells
3861

Supplementary Figure 7. Gating for phenotypical populations. Shown are single stain controls (top) and FMO controls (bottom).

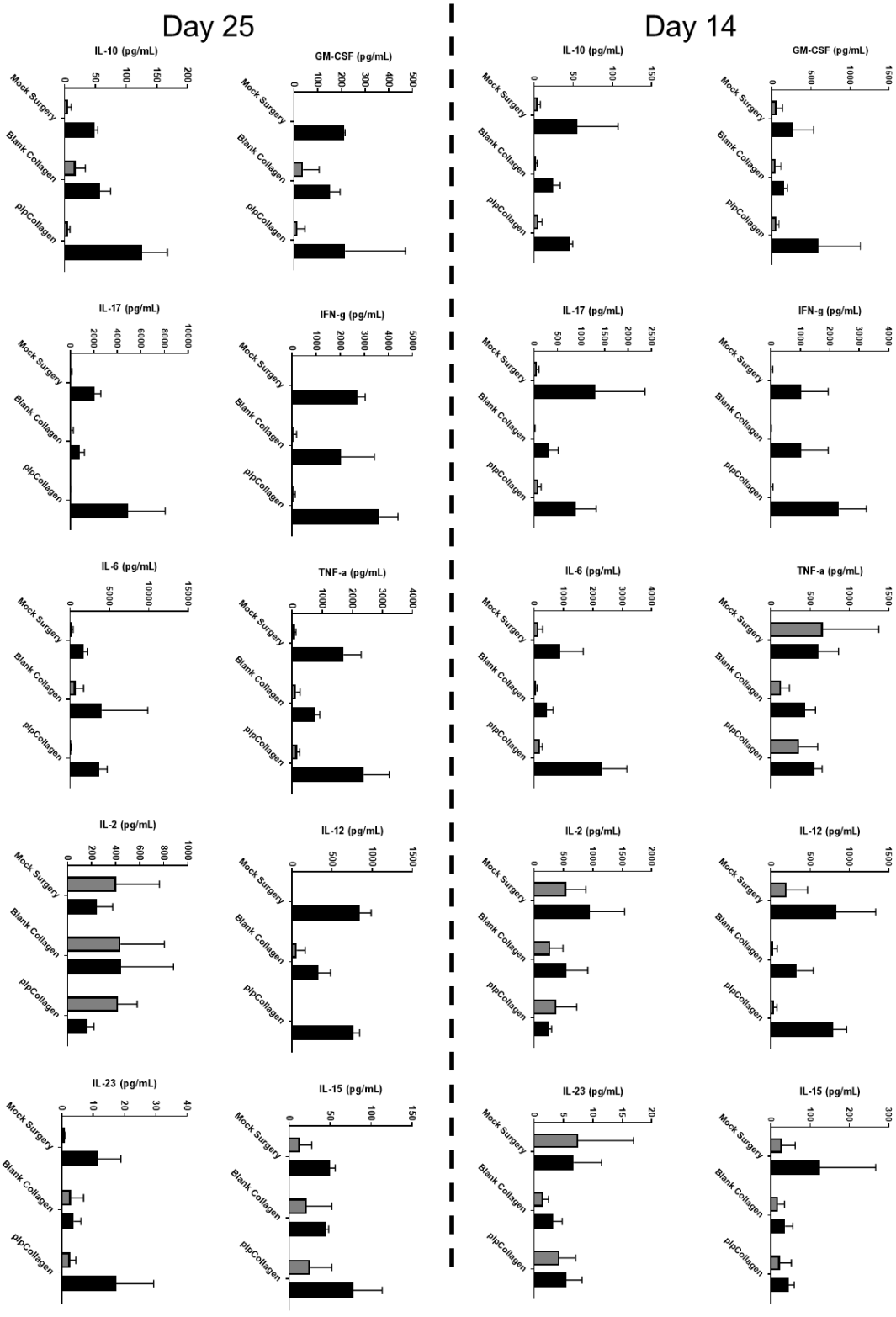
Day 25
Day 14
IL-10 (pg/mL)
GM-CSF (pg/mL)
IL-17 (pg/mL)
IFN-g (pg/mL)
IL-6 (pg/mL)
TNF-a (pg/mL)
IL-2 (pg/mL)
IL-12 (pg/mL)
IL-23 (pg/mL)
IL-15 (pg/mL)
Mock Surgery
Blank Collagen
plpCollagen

Supplementary Figure 8. Cytokine analyses are presented as absolute pg/mL values to supplement heatmap results presented in Figure 7. Samples incubated with 25 µM PLP (+PLP) are indicated by black bars, while samples incubated with vehicle alone (-PLP) are represented in gray.

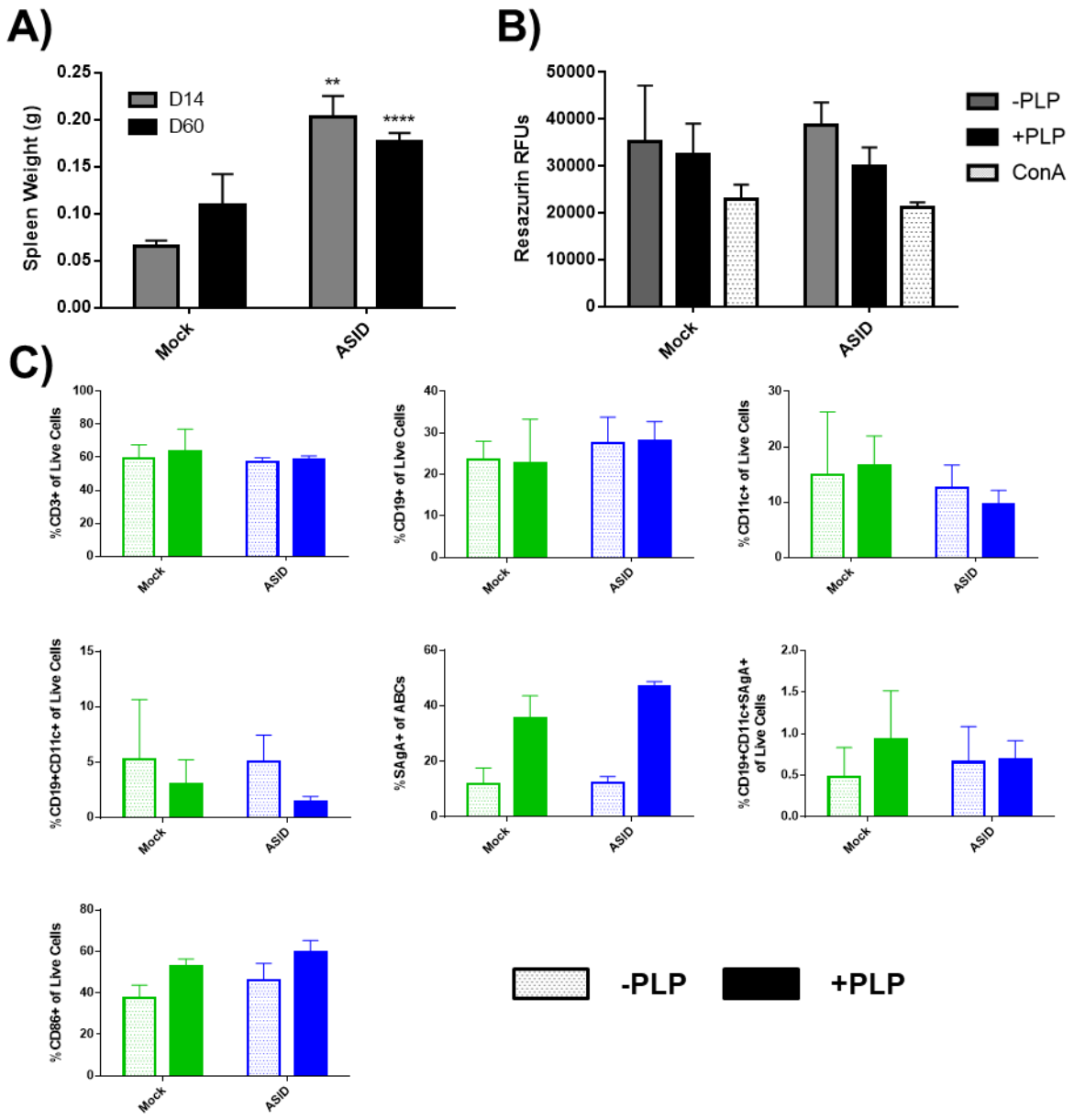

Supplementary Figure 9. PLP rechallenge response among harvested D60 splenocytes. **A)** Spleen weights were taken upon harvest and compared to D14 observations. **B)** Resazurin cell metabolism was measured after 96 hours of incubation with –PLP, +PLP, or ConA. **C)** Splenocytes were phenotyped after 96 hours of vehicle (-PLP, open bars) or 25 µM PLP rechallenged (+PLP, solid bars) for CD3, CD19, and CD11c (top row, left to right) as well as antigen-specific B cell

populations (middle row), and costimulation (CD86, bottom row). n = 3 biological replicates per group, *p < 0.05, **p < 0.01, ***p < 0.001, ****p<0.0001).

4.7 Acknowledgements

JDG was supported by the Madison and Lila Self Graduate Fellowship at the University of Kansas. JYS was supported by the Stella Fellowship of the Department of Pharmaceutical Chemistry at the University of Kansas. The authors would like to thank Dr. Steve Jacobson of the National Institutes of Health for his advisory role in study design, and for his continued interest in translating decoys for clinical applications. We would also like to thank Towne Walston, Sebastian Huayamares, and Michael Shao for their assistance in carrying out animal surgeries for this work, as well as Deanna Diaz for her help developing SAgAs as an antigen-specific B cell probe.

4.8 References

1. Stoolman, L. M., Adhesion molecules controlling lymphocyte migration. **1989**.
2. Duijvestijn, A.; Hamann, A., Mechanisms and regulation of lymphocyte migration. *Immunol. Today* **1989,** *10* (1), 23-28.
3. von Andrian, U. H.; Mempel, T. R., Homing and cellular traffic in lymph nodes. *Nat. Rev. Immunol.* **2003,** *3* (11), 867.
4. Butcher, E. C.; Picker, L. J., Lymphocyte Homing and Homeostasis. *Science* **1996,** *272* (5258), 60-67.
5. Sackstein, R.; Schatton, T.; Barthel, S. R., T-lymphocyte homing: an underappreciated yet critical hurdle for successful cancer immunotherapy. *Lab. Invest.* **2017,** *97* (6), 669.
6. Eriksson, U.; Ricci, R.; Hunziker, L.; Kurrer, M. O.; Oudit, G. Y.; Watts, T. H.; Sonderegger, I.; Bachmaier, K.; Kopf, M.; Penninger, J. M., Dendritic cell–induced autoimmune heart failure requires cooperation between adaptive and innate immunity. *Nat. Med.* **2003,** *9* (12), 1484.
7. Banchereau, J.; Pascual, V.; Palucka, A. K., Autoimmunity through cytokine-induced dendritic cell activation. *Immunity* **2004,** *20* (5), 539-550.
8. Iwasaki, A.; Medzhitov, R., Regulation of adaptive immunity by the innate immune system. *Science* **2010,** *327* (5963), 291-295.
9. Kahan, S. M.; Zajac, A. J., Immune exhaustion: past lessons and new insights from lymphocytic choriomeningitis virus. *Viruses* **2019,** *11* (2), 156.
10. Buchbinder, E. I.; Desai, A., CTLA-4 and PD-1 Pathways: Similarities, Differences, and Implications of Their Inhibition. *Am. J. Clin. Oncol.* **2016,** *39* (1), 98-106.

11. McKinney, E. F.; Smith, K. G., T-cell exhaustion: understanding the interface of chronic viral and autoinflammatory diseases. *Immunol. Cell Biol.* **2016,** *94* (10), 935-942.
12. Steinman, L., Multiple sclerosis: a two-stage disease. *Nat. Immunol.* **2001,** *2* (9), 762.
13. McKinney, E. F.; Lee, J. C.; Jayne, D. R.; Lyons, P. A.; Smith, K. G., T-cell exhaustion, co-stimulation and clinical outcome in autoimmunity and infection. *Nature* **2015,** *523* (7562), 612.
14. Pauken, K. E.; Wherry, E. J., Overcoming T cell exhaustion in infection and cancer. *Trends Immunol.* **2015,** *36* (4), 265-276.
15. McKinney, E. F.; Smith, K., Metabolic exhaustion in infection, cancer and autoimmunity. *Nat. Immunol.* **2018**, 1.
16. Fransson, M. E.; Liljenfeldt, L. S.; Fagius, J.; Tötterman, T. H.; Loskog, A. S., The T-cell pool is anergized in patients with multiple sclerosis in remission. *Immunology* **2009,** *126* (1), 92-101.
17. Von Herrath, M.; Sanda, S.; Herold, K., Type 1 diabetes as a relapsing–remitting disease? *Nat. Rev. Immunol.* **2007,** *7* (12), 988.
18. Rangachari, M.; Kuchroo, V. K., Using EAE to better understand principles of immune function and autoimmune pathology. *J. Autoimmun.* **2013,** *45*, 31-39.
19. Chun, J.; Hartung, H.-P., Mechanism of action of oral fingolimod (FTY720) in multiple sclerosis. *Clin. Neuropharmacol.* **2010,** *33* (2), 91.
20. Rudick, R. A.; Sandrock, A., Natalizumab: α4-integrin antagonist selective adhesion molecule inhibitors for MS. *Expert Rev. Neurother.* **2004,** *4* (4), 571-580.
21. Carson, K. R.; Focosi, D.; Major, E. O.; Petrini, M.; Richey, E. A.; West, D. P.; Bennett, C. L., Monoclonal antibody-associated progressive multifocal leucoencephalopathy in patients treated with rituximab, natalizumab, and efalizumab: a Review from the Research on Adverse Drug Events and Reports (RADAR) Project. *The lancet oncology* **2009,** *10* (8), 816-824.
22. Ransohoff, R. M., Natalizumab and PML. *Nat. Neurosci.* **2005,** *8* (10), 1275.
23. Pelletier, D.; Hafler, D. A., Fingolimod for multiple sclerosis. *N. Engl. J. Med.* **2012,** *366* (4), 339-347.
24. Hotaling, N. A.; Tang, L.; Irvine, D. J.; Babensee, J. E., Biomaterial strategies for immunomodulation. *Annu. Rev. Biomed. Eng.* **2015,** *17*, 317-349.
25. Irvine, D. J.; Swartz, M. A.; Szeto, G. L., Engineering synthetic vaccines using cues from natural immunity. *Nature materials* **2013,** *12* (11), 978.
26. Tostanoski, L. H.; Gosselin, E. A.; Jewell, C. M., Engineering tolerance using biomaterials to target and control antigen presenting cells. *Discov. Med.* **2016,** *21* (117), 403-410.
27. Bookstaver, M. L.; Tsai, S. J.; Bromberg, J. S.; Jewell, C. M., Improving vaccine and immunotherapy design using biomaterials. *Trends in immunology* **2018,** *39* (2), 135-150.
28. Koshy, S. T.; Mooney, D. J., Biomaterials for enhancing anti-cancer immunity. *Curr. Opin. Biotechnol.* **2016,** *40*, 1-8.
29. Mora-Solano, C.; Collier, J. H., Engaging adaptive immunity with biomaterials. *Journal of Materials Chemistry B* **2014,** *2* (17), 2409-2421.
30. Andorko, J. I.; Hess, K. L.; Jewell, C. M., Harnessing biomaterials to engineer the lymph node microenvironment for immunity or tolerance. *The AAPS journal* **2015,** *17* (2), 323-338.
31. Rao, S. S.; Bushnell, G. G.; Azarin, S. M.; Spicer, G.; Aguado, B. A.; Stoehr, J. R.; Jiang, E. J.; Backman, V.; Shea, L. D.; Jeruss, J. S., Enhanced survival with implantable

scaffolds that capture metastatic breast cancer cells in vivo. *Cancer Res.* **2016,** *76* (18), 5209-5218.
32. Aguado, B. A.; Caffe, J. R.; Nanavati, D.; Rao, S. S.; Bushnell, G. G.; Azarin, S. M.; Shea, L. D., Extracellular matrix mediators of metastatic cell colonization characterized using scaffold mimics of the pre-metastatic niche. *Acta Biomater.* **2016,** *33*, 13-24.
33. Lutolf, M.; Hubbell, J., Synthetic biomaterials as instructive extracellular microenvironments for morphogenesis in tissue engineering. *Nat. Biotechnol.* **2005,** *23* (1), 47.
34. Reddy, S. T.; Swartz, M. A.; Hubbell, J. A., Targeting dendritic cells with biomaterials: developing the next generation of vaccines. *Trends Immunol.* **2006,** *27* (12), 573-579.
35. Thelin, M. A.; Kissler, S.; Vigneault, F.; Watters, A. L.; White, D.; Koshy, S. T.; Vermillion, S. A.; Mooney, D. J.; Serwold, T.; Ali, O. A., In vivo enrichment of diabetogenic T cells. *Diabetes* **2017,** *66* (8), 2220-2229.
36. Verbeke, C. S.; Mooney, D. J., Injectable, pore-forming hydrogels for in vivo enrichment of immature dendritic cells. *Advanced healthcare materials* **2015,** *4* (17), 2677-2687.
37. Wang, H.; Mooney, D. J., Biomaterial-assisted targeted modulation of immune cells in cancer treatment. *Nature materials* **2018**, 1.
38. Kim, J.; Li, W. A.; Choi, Y.; Lewin, S. A.; Verbeke, C. S.; Dranoff, G.; Mooney, D. J., Injectable, spontaneously assembling, inorganic scaffolds modulate immune cells in vivo and increase vaccine efficacy. *Nature biotechnology* **2015,** *33* (1), 64-72.
39. Ali, O. A.; Doherty, E.; Bell, W. J.; Fradet, T.; Hudak, J.; Laliberte, M.-T.; Mooney, D. J.; Emerich, D. F., Biomaterial-based vaccine induces regression of established intracranial glioma in rats. *Pharm. Res.* **2011,** *28* (5), 1074-1080.
40. Lynn, G. M.; Laga, R.; Darrah, P. A.; Ishizuka, A. S.; Balaci, A. J.; Dulcey, A. E.; Pechar, M.; Pola, R.; Gerner, M. Y.; Yamamoto, A., In vivo characterization of the physicochemical properties of polymer-linked TLR agonists that enhance vaccine immunogenicity. *Nat. Biotechnol.* **2015,** *33* (11), 1201.
41. Bencherif, S. A.; Sands, R. W.; Ali, O. A.; Li, W. A.; Lewin, S. A.; Braschler, T. M.; Shih, T.-Y.; Verbeke, C. S.; Bhatta, D.; Dranoff, G., Injectable cryogel-based whole-cell cancer vaccines. *Nature communications* **2015,** *6*, 7556.
42. Smith, T. T.; Moffett, H. F.; Stephan, S. B.; Opel, C. F.; Dumigan, A. G.; Jiang, X.; Pillarisetty, V. G.; Pillai, S. P.; Wittrup, K. D.; Stephan, M. T., Biopolymers codelivering engineered T cells and STING agonists can eliminate heterogeneous tumors. *The Journal of clinical investigation* **2017,** *127* (6), 2176-2191.
43. Yoon, Y. M.; Lewis, J. S.; Carstens, M. R.; Campbell-Thompson, M.; Wasserfall, C. H.; Atkinson, M. A.; Keselowsky, B. G., A combination hydrogel microparticle-based vaccine prevents type 1 diabetes in non-obese diabetic mice. *Sci. Rep.* **2015,** *5*, 13155.
44. Verbeke, C. S.; Gordo, S.; Schubert, D. A.; Lewin, S. A.; Desai, R. M.; Dobbins, J.; Wucherpfennig, K. W.; Mooney, D. J., Multicomponent Injectable Hydrogels for Antigen-Specific Tolerogenic Immune Modulation. *Advanced healthcare materials* **2017,** *6* (6).
45. Zhang, W.; Gorantla, V. S.; Campbell, P. G.; Li, Y.; Yang, Y.; Komatsu, C.; Weiss, L. E.; Zheng, X. X.; Solari, M. G., Biopatterned CTLA4/Fc Matrices Facilitate Local Immunomodulation, Engraftment, and Glucose Homeostasis After Pancreatic Islet Transplantation. *Diabetes* **2016,** *65* (12), 3660-3666.
46. Chvapil, M., Collagen sponge: theory and practice of medical applications. *J. Biomed. Mater. Res.* **1977,** *11* (5), 721-741.

47. Northrup, L.; Griffin, J. D.; Christopher, M. A.; Antunez, L. R.; Hartwell, B. L.; Pickens, C. J.; Berkland, C., Co-delivery of autoantigen and dexamethasone in incomplete Freund's adjuvant ameliorates experimental autoimmune encephalomyelitis. *J. Control. Release* **2017,** *266*, 156-165.
48. Griffin, J. D.; Christopher, M. A.; Thati, S.; Salash, J. R.; Pressnall, M. M.; Weerasekara, D. B.; Lunte, S. M.; Berkland, C. J., Tocopherol Emulsions as Functional Autoantigen Delivery Vehicles Evoke Therapeutic Efficacy in Experimental Autoimmune Encephalomyelitis. *Molecular pharmaceutics* **2019,** *16* (2), 607-617.
49. Nagelkerken, L.; Blauw, B.; Tielemans, M., IL-4 abrogates the inhibitory effect of IL-10 on the development of experimental allergic encephalomyelitis in SJL mice. *Int. Immunol.* **1997,** *9* (9), 1243-51.
50. Hartwell, B. L.; Pickens, C. J.; Leon, M.; Northrup, L.; Christopher, M. A.; Griffin, J. D.; Martinez-Becerra, F.; Berkland, C., Soluble antigen arrays disarm antigen-specific B cells to promote lasting immune tolerance in experimental autoimmune encephalomyelitis. *J. Autoimmun.* **2018,** *93*, 76-88.
51. Ali, O. A.; Huebsch, N.; Cao, L.; Dranoff, G.; Mooney, D. J., Infection-mimicking materials to program dendritic cells in situ. *Nature Materials* **2009,** *8*, 151.
52. Potter, N.; Stephens, T., Humoral immune recognition of proteolipid protein (PLP)-specific encephalitogenic epitopes in the SJL/J mouse. *J. Neurosci. Res.* **1994,** *37* (1), 15-22.
53. Berkland, C.; Sestak, J.; Siahaan, T., Bifunctional conjugate compositions and associated methods. Google Patents: 2013.
54. Sestak, J. O.; Sullivan, B. P.; Thati, S.; Northrup, L.; Hartwell, B.; Antunez, L.; Forrest, M. L.; Vines, C. M.; Siahaan, T. J.; Berkland, C., Codelivery of antigen and an immune cell adhesion inhibitor is necessary for efficacy of soluble antigen arrays in experimental autoimmune encephalomyelitis. *Mol Ther Methods Clin Dev* **2014,** *1*, 14008.
55. Sestak, J.; Mullins, M.; Northrup, L.; Thati, S.; Laird Forrest, M.; Siahaan, T. J.; Berkland, C., Single-step grafting of aminooxy-peptides to hyaluronan: A simple approach to multifunctional therapeutics for experimental autoimmune encephalomyelitis. *J. Control. Release* **2013,** *168* (3), 334-340.
56. Sestak, J. O.; Fakhari, A.; Badawi, A. H.; Siahaan, T. J.; Berkland, C., Structure, size, and solubility of antigen arrays determines efficacy in experimental autoimmune encephalomyelitis. *AAPS J* **2014,** *16* (6), 1185-93.
57. Hartwell, B. L.; Martinez-Becerra, F. J.; Chen, J.; Shinogle, H.; Sarnowski, M.; Moore, D. S.; Berkland, C., Antigen-Specific Binding of Multivalent Soluble Antigen Arrays Induces Receptor Clustering and Impedes B Cell Receptor Mediated Signaling. *Biomacromolecules* **2016,** *17* (3), 710-722.
58. Hartwell, B. L.; Smalter Hall, A.; Swafford, D.; Sullivan, B. P.; Garza, A.; Sestak, J. O.; Northrup, L.; Berkland, C., Molecular Dynamics of Multivalent Soluble Antigen Arrays Support a Two-Signal Co-delivery Mechanism in the Treatment of Experimental Autoimmune Encephalomyelitis. *Mol. Pharm.* **2016,** *13* (2), 330-343.
59. Hartwell, B. L.; Pickens, C. J.; Leon, M.; Berkland, C., Multivalent Soluble Antigen Arrays Exhibit High Avidity Binding and Modulation of B Cell Receptor-Mediated Signaling to Drive Efficacy against Experimental Autoimmune Encephalomyelitis. *Biomacromolecules* **2017,** *18* (6), 1893-1907.

60. Rubtsov, A. V.; Rubtsova, K.; Kappler, J. W.; Jacobelli, J.; Friedman, R. S.; Marrack, P., CD11c-expressing B cells are located at the T cell/B cell border in spleen and are potent APCs. *J. Immunol.* **2015,** *195* (1), 71-79.
61. Li, W. A.; Lu, B. Y.; Gu, L.; Choi, Y.; Kim, J.; Mooney, D. J., The effect of surface modification of mesoporous silica micro-rod scaffold on immune cell activation and infiltration. *Biomaterials* **2016,** *83*, 249-256.
62. McKinney, E. F.; Smith, K. G., T cell exhaustion and immune-mediated disease—the potential for therapeutic exhaustion. *Curr. Opin. Immunol.* **2016,** *43*, 74-80.
63. Zinselmeyer, B. H.; Heydari, S.; Sacristán, C.; Nayak, D.; Cammer, M.; Herz, J.; Cheng, X.; Davis, S. J.; Dustin, M. L.; McGavern, D. B., PD-1 promotes immune exhaustion by inducing antiviral T cell motility paralysis. *J. Exp. Med.* **2013,** *210* (4), 757-774.
64. Kim, T. S.; Hufford, M. M.; Sun, J.; Fu, Y. X.; Braciale, T. J., Antigen persistence and the control of local T cell memory by migrant respiratory dendritic cells after acute virus infection. *J. Exp. Med.* **2010,** *207* (6), 1161-72.
65. Kedl, R. M.; Tamburini, B. A., Antigen archiving by lymph node stroma: A novel function for the lymphatic endothelium. *Eur. J. Immunol.* **2015,** *45* (10), 2721-2729.
66. Wherry, E. J., T cell exhaustion. *Nature immunology* **2011,** *12* (6), 492.
67. Ignatowicz, L.; Kappler, J.; Marrack, P., The effects of chronic infection with a superantigen-producing virus. *J. Exp. Med.* **1992,** *175* (4), 917-923.
68. Blattman, J. N.; Wherry, E. J.; Ha, S.-J.; Van Der Most, R. G.; Ahmed, R., Impact of epitope escape on PD-1 expression and CD8 T-cell exhaustion during chronic infection. *J. Virol.* **2009,** *83* (9), 4386-4394.
69. Jaini, R.; Popescu, D. C.; Flask, C. A.; Macklin, W. B.; Tuohy, V. K., Myelin antigen load influences antigen presentation and severity of central nervous system autoimmunity. *J. Neuroimmunol.* **2013,** *259* (1-2), 37-46.
70. Hess, K. L.; Oh, E.; Tostanoski, L. H.; Andorko, J. I.; Susumu, K.; Deschamps, J. R.; Medintz, I. L.; Jewell, C. M., Engineering Immunological Tolerance Using Quantum Dots to Tune the Density of Self-Antigen Display. *Adv. Funct. Mater.* **2017,** *27* (22), 1700290-n/a.
71. Arthur, C. M.; Patel, S. R.; Smith, N. H.; Bennett, A.; Kamili, N. A.; Mener, A.; Gerner-Smidt, C.; Sullivan, H. C.; Hale, J. S.; Wieland, A.; Youngblood, B.; Zimring, J. C.; Hendrickson, J. E.; Stowell, S. R., Antigen Density Dictates Immune Responsiveness following Red Blood Cell Transfusion. *J. Immunol.* **2017,** *198* (7), 2671-2680.
72. Griffin, J. D.; Leon, M. A.; Salash, J. R.; Shao, M.; Hartwell, B. L.; Pickens, C. J.; Sestak, J. O.; Berkland, C., Acute B-Cell Inhibition by Soluble Antigen Arrays is Valency-Dependent and Predicts Immunomodulation in Splenocytes. *Biomacromolecules*.
73. Moskophidis, D.; Lechner, F.; Pircher, H.; Zinkernagel, R. M., Virus persistence in acutely infected immunocompetent mice by exhaustion of antiviral cytotoxic effector T cells. *Nature* **1993,** *362* (6422), 758.
74. Schietinger, A.; Greenberg, P. D., Tolerance and exhaustion: defining mechanisms of T cell dysfunction. *Trends in immunology* **2014,** *35* (2), 51-60.
75. Moskophidis, D.; Laine, E.; Zinkernagel, R. M., Peripheral clonal deletion of antiviral memory CD8+ T cells. *Eur. J. Immunol.* **1993,** *23* (12), 3306-3311.

5. Polyantigenic Immune Decoys Amplify Antigen-Specific Cell Populations but do not Suppress Experimental Autoimmune Encephalomyelitis

As prepared for peer-reviewed submission

Griffin, J. Daniel, Sebastian Huayamares, Towne R. Walston, Jimmy Y. Song, Michael Shao, Alexander R. Sedlacek, Deanna L. Diaz, Aparna Chakravarti, and Cory J. Berkland. "Polyantigenic immune decoys amplify antigen-specific cell populations but do not suppress experimental autoimmune encephalomyelitis." *Manuscript in Preparation* (2019).

5.1 Introduction

Antigen-specific immunotherapies (ASIT) are an appealing supposition for treating autoimmune disease[1, 2]. Classically, autoimmunity has been treated through the nonspecific suppression of host immunity, which certainly dampens deleterious autoreactivity but also compromises protective functions of the immune system as well[3]. ASIT posits that the selective targeting of immunosuppression to the cell subsets responsible for disease could drastically improve safety and efficacy. Recent strategies have co-delivered autoantigen with drug to preferentially engage and deactivate cells with cognate receptors specific for self-tissue[4]. Despite many manifestations of these approaches, to date no autoimmune ASITs have advanced to clinical approval[5].

One obstacle to ASIT implementation could be the complexity of authentic human autoimmune disease that far exceeds what is capitulated by mouse models[6, 7]. Particularly, authentic autoimmunities are typically polyclonal and progression is accompanied by epitope spreading over years of disease[8, 9]. In Multiple Sclerosis (MS) where autoreactive cells attack myelin autoantigens in the CNS, over 100 potential autoantigens have been implicated to date and autoreactive specificities can vary greatly between patients[9, 10]. It is impractical to fabricate ASITs that discretely co-deliver all epitopes and it may be infeasible to tailor the formulations for personalized treatments. ASIT proponents have suggested bystander tolerance as a potential mechanism of therapeutic prowess[11-14], but formulations with single or several autoantigen epitopes have not exhibited definitive clinical successes. A format to introduce specificity to autoreactive immune cells while accounting for the heterogeneity of autoantigens would be of tremendous value.

In a recent report, we detailed antigen-specific immune decoys (ASIDs) as a biomaterial therapeutic with remarkable efficacy against experimental autoimmune encephalomyelitis (EAE), a mouse model of MS[15]. These peptide epitope-conjugated microporous collagen sponges were designed to recruit and sequester autoreactive cell populations to prevent disease. Evidence supported that these biomaterials were able to exhaust migrating effector cells after their egress from lymphatic organs but before reaching the central nervous system (CNS). This cellular exhaustion resulted in the premature return of immune cells to lymphoid organs and the hypersensitivity of these cell types that led to their deletion upon re-exposure to autoantigen. While ASIDs were designed as monoantigenic biomaterials in the first iteration, the format readily supports the inclusion of polyantigenic compositions. In the present work, we hypothesized that the integration of primary tissue into porous collagenous materials could represent a comprehensive palette for autoantigens while retaining discrete epitope antigenicity. We envisioned that such a material might elicit broad antigen-specific effects against heterogeneous, polyclonal autoimmune diseases.

In seeking to fabricate a polyantigenic, “complex” decoy that extends beyond the findings of our previous proteolipid protein (PLP)-conjugated “simple” system, several design parameters must be conserved. In building a decoy it is critical to create a persistent depot with a microporous architecture to ensure adequate cell and nutrient transfer both *in vivo* an *ex vivo*. To isolate the “decoy effect” as a therapeutic mechanism, an immunologically inert material is ideal. Further, antigen immobilization into the microstructure must be irreversible, such that sustained antigen release is not a driving mechanism of effect. Most important of all, however, is that incorporated antigen is functional and retains its ability to bind cognate receptors.

Gelatin was selected as a suitable substrate for the present application. Particularly, methacrylated gelatin polymers (gelatin methacrylate, GelMA) have been extensively applied in the literature for tissue engineering and drug delivery for their biocompatible and tissue-like characteristics[16, 17]. Some gelatin material variants have even been FDA-approved for wound-treatment[18]. Photocrosslinkability is particularly appealing for our application, because the sol-gel transformation enables mixing of polyantigenic primary tissues prior to microstructure formation to enable integration, as chemical conjugation is not feasible for a non-discrete, heterogeneous autoantigen composition. We hypothesized that introducing mouse brain homogenate (MBH) to a precursor solution of GelMA may enable the chemical integration of primary tissue into the resulting gel, as nondiscriminate free radicals generated during UV exposure may facilitate crosslinkage with gelatin polymers.

In the present work, we set forth to incorporate MBH into GelMA scaffolds to create complex immune decoys theoretically encompassing a full palette of the autoimmune epitopes in MS. We endeavored to build such a material, but pertinent questions would loom. Could a complex, homogenate containing antigen slurry biomaterial maintain discrete epitope functionality? Using EAE as a model disease of discrete antigen-specificity, we assessed cell *ex vivo* activation and amplification to evaluate this functionality. However, it would remain to be seen if discrete antigenicity would ultimately translate to clinical efficacy *in vivo*. Would complex decoys be able to instill the same immune exhaustion that was harnessed for therapeutic efficacy in the prior single-epitope iteration?

5.2 Materials and Methods

5.2.1 Materials

Gelatin type A from porcine skin, methacrylic anhydride, and Irgacure 2959 were purchased Sigma Aldrich (St. Charles, MO). Mouse brain material was obtained from SJL/J mice (Envigo, Cambridgeshire, UK) housed in specified, pathogen free conditions at the University of Kansas. Mouse brain homogenate was prepared adding 1X PBS to obtain a concentration of 1 g/mL. Using a sonicator probe, the mixture was homogenized for 2 minutes using 10 seconds on, 2 seconds off regimen. The resulting mouse brain homogenate was stored at -20°C. 2,5-dioxopyrrolidin-1-yl 1-azido-3,6,9,12-tetraoxapentadecan-15-oate (azido-PEG4-NHS Ester) was purchased from Click Chemistry Tools (Scottsdale, AZ). Tris(3-hydroxypropyltriazolylmethyl)amine (THPTA), and sodium ascorbate (NaAsc) were purchased from Sigma-Aldrich (St. Louis, MO). Copper (II) sulfate pentahydrate ($CuSO_4 \cdot 5H_2O$) was purchased from Acros Organics (Geel, Belgium). Alkyne-functionalized PLP with an *N*-terminal 4-pentynoic acid (homopropargyl, hp) modification, $hpPLP_{139-151}$ (hp-HSLGKWLGHPDKF-OH) was purchased from Biomatik (Cambridge, ON, Canada). Unmodified $PLP_{139-151}$ (NH2-HSLGKWLGHPDKF-OH) used for EAE induction, rechallenge assays, and anti-PLP IgG ELISA was purchased from PolyPeptide Laboratories (San Diego, CA). Incomplete Freund's adjuvant (IFA) and killed *Mycobacterium tuberculosis* strain H37RA were purchased from Difco (Sparks, MD). Pertussis toxin was purchased from List Biological Laboratories (Campbell, CA). PE/Cy7-conjugated anti-mouse CD3, PE-conjugated anti-mouse CD86, Alexa Fluor 647-conjugated anti-mouse CD19, and Brilliant Violet 421-conjugated anti-mouse CD11c were purchased from BioLegend (San Diego, CA). All other chemicals and reagents were analytical grade and used as received.

5.2.2 Preparation of Gelatin Methacrylate

A 10% (w/v) solution of porcine gelatin was prepared in PBS. The solution was warmed to 60°C and stirred vigorously as methacrylic anhydride was added dropwise (up to 8% of total gelatin content) to methacrylate the amine groups on gelatin polymers. After two hours of continued mixing, the solution was diluted with PBS and dialyzed (12-14 kDa cutoff) with deionized water for one week with twice daily water changes. The dialyzed GelMA was frozen at -80°C before being lyophilized to yield a purified solid product.

5.2.3 Fabrication of Homogenate-GelMA Scaffolds

The mbhGelatin scaffolds were produced by creating a 2X (14%) solution of GelMA containing an excess of Irgacure 2959 photocrosslinker and a 2X solution of mouse brain homogenate in 1X PBS that was proportional to GelMA content by weight. GelMA and homogenate-containing solutions were mixed in equal parts and added to wells of a 24-well plate. Using a UV light source, the mixtures were photocrosslinked for 7 minutes. Gelatin constructs were then frozen overnight at -80°C and lyophilized for storage.

5.2.4 Synthesis of plpGelatin Materials

PLP-conjugated materials were prepared as previously described[15]. Briefly, blank gelatin scaffolds were hydrated in pH 8.3, 50 mM HEPES buffer. 2 mg/mL azido-PEG4-NHS was added and the mixture was reacted for 4 hours at room temperature. The materials were washed 5 times in deionoized water before being placed in a solution of 2 mg/mL hpPLP$_{139\text{-}151}$ prior to the addition of a premixed solution of 4.5 mM THPTA and 0.8 mM copper (II) sulfate pentahydrate. Sodium ascorbate (16 mM) was added to commence the reaction, which was run overnight at room temperature. The resulting plpGelatin materials were washed 5 times in deionized water and stored in 100% ethanol. PLP conjugation to collagen sponges was determined using a 20 minute Reverse-

Phase HPLC method employing a 95/5 to 30/70 aqueous:organic gradient scheme on a C4 RP column.

5.2.5 Characterizing Complex Decoys

Scanning electron microscopy (SEM) was carried out at 150X, 500X, and 1000X magnifications to approximate gelatin pore size. SEM images were taken on an FEI Technai F20 XT Field Emission Transmission Electron Microscope with dehydrated gelatin hydrogels. mbhGelatin constructs of varying homogenate contents were subjected to rheological and mechanical testing to characterize homogenate effects on these properties. Rheological testing was carried out across oscillatory frequency and strain sweeps using an AR2000 rheometer. Elastic modulus, G', and loss modulus, G", were recorded. Frequency sweeps consisted of oscillatory measurements at a low fixed strain (1%) with increasing frequency amplitudes to determine the G' and G'' of the constructs as a function of frequency. The strain sweeps consisted of oscillatory measurements at a fixed frequency (1 Hz) with increasing strain amplitudes. Tanδ is the ratio of G'' to G' and is used in strain sweeps to help recognize the strain at which the gel's structure breaks mechanically. A release study was conducted by procuring 20mg sections of mbhGelatin at varied G:H ratios and adding to scintillation vials containing 20 mL of PBS. Across time points, 1 mL of bulk solution was sampled and replaced with fresh PBS. Samples were quantified for overall protein content using a Pierce BCA Protein Assay Kit (ThermoFisher Scientific, Waltham, MA). The loss of released material from sampling was accounted for when calculating cumulative release over time.

5.2.6 Retained Antigen-Specificity Analysis

2:1 mbhGelatin, Blank Gelatin, and $PLP_{139-151}$-conjugated gelatin constructs were embedded and cryosectioned (20 µm sections) onto microscope slides. Each sample was fixed

using 10% neutral buffered formalin and blocked with 1% bovine serum albumin. Samples were then incubated with mouse serum containing antibodies for $PLP_{139-151}$. Following the incubation, samples were washed, and bound antibody was detected using HRP-conjugated anti IgG. TMB substrate was incubated with the slides for 15 minutes, and pictures were taken to visualize PLP-specific binding.

5.2.7 Induction of EAE and Therapeutic Study

Experimental autoimmune encephalomyelitis was induced as previously described[15]. Briefly, 4-6-week-old, female SJL/J mice (n = 4/group) were induced with EAE under authorization approved from a protocol passed by the University's Institutional Animal Care and Use Committee. Mice were subcutaneously administered the $PLP_{139-151}$ autoantigen peptide epitope in complete Freund's Adjuvant with the intraperitoneal coadministration of pertussis toxin capsid. Intraperitoneal injection of pertussis toxin was repeated on day two post-induction. On day 4, mice received subcutaneous surgery for the implantation of either mbhGelatin, plpGelatin, Blank Gelatin, or Mock Surgery located between the shoulder blades. Over the course of 25 days, disease progression was monitored using a 5-point clinical scoring scheme which increases as a function of paralysis, including: 0, no clinical evidence of disease; 1, tail weakness or limp tail; 2, paraparesis (weakness or incomplete paralysis of one or two hind limbs); 3, paraplegia (complete paralysis of two hind limbs); 4, paraplegia with forelimb weakness or paralysis; and 5, moribund. In parallel throughout the study, weight change data was collected.

5.2.8 Detection of Anti-PLP IgG

PLP-specific IgG titers were assessed using methods previously described[19]. Briefly, Immulon 2HB 96-well plates were coated in an isoelectric PLP solution (pH 9.5) overnight at 4°C. Plates were blocked with 1% bovine serum albumin before serum from mice in the therapeutic

study was introduced in serial dilution. HRP-Conjugated anti-mouse IgG (Biolegend) was used to detect bound anti-PLP IgG as TrueBlue substrate was added as an indicator. The enzymatic conversion was stopped with a 2N sulfuric acid solution, and plates were read at 450 and 540 nm absorbances on a Spectramax M5 plate reader from Molecular Devices (San Jose, CA). For analyzing titer, linear regions across sample titration readings were fitted with linear regressions and extrapolated to their 1X concentration for comparison across samples.

5.2.9 Spleen Harvest and Splenocyte Isolation

Spleens were resected from mice and placed into 5 mL of sterile PBS. A wire mesh and the rubber stopper of a sterile 1 mL syringe was used to grind the spleen. The unlysed cell suspension was centrifuged, and the cell pellet was resuspended in 1 mL red blood cell lysis buffer (Sigma Aldrich, St. Charles, MO). The cells were incubated for 7 minutes to lyse splenic red blood cells. The reaction was quenched by adding 10 mL RPMI 1640 media containing 10% FBS to the mixture, and the suspension was centrifuged. The remaining splenocyte pellets were resuspended in fresh media (RPMI 1640 media containing 10% FBS and 1% Penicillin-Streptomycin) and counted for further analysis and experimentation.

5.2.10 Ex Vivo Screening with EAE Splenocytes

At peak of disease (Day 12), mixed EAE splenocytes were harvested and plated at 1.5 x 10^6 cells per well in a 24-well untreated plate containing either media alone (-PLP), soluble antigen rechallenge (+PLP), mbhGelatin sponge, or Blank Gelatin sponge. After 96 hours, sponges were minced with microscissors and the culture suspension was collected and passed through a cell strainer for further processing and analysis.

5.2.11 Fluorescent Staining and Flow Cytometry

Samples were collected and washed in FACS buffer containing 1X PBS + 5% fetal bovine serum + 0.1% sodium azide. Samples were resuspended in a solution containing Zombie Aqua viability stain (Biolegend) and were incubated for 20 minutes at room temperature. Following the incubation, fluorescent antibodies were added at manufacturer recommended concentrations for 30 minutes at 4°C. Samples were washed and run on a BD FACSFusion cytometer, where 100,000 events were collected per sample. Data were analyzed using FlowJo and GraphPad Prism.

5.2.12 Resazurin Cell Metabolism Assay

After 96 hours of incubation, samples were incubated with 75 µM resazurin (7-hydroxy-3H-phenoxazin-3-one 10-oxide) for 3 hours. Metabolic reductive capacity was measured by assessing changes in fluorescence (560 excitation, 590 emission, Spectramax M5, Molecular Devices, San Jose, CA). Background fluorescence was subtracted out by taking measurements of RPMI media alone.

5.2.13 Statistical Analysis

Statistical analysis was performed using an ordinary one-way ANOVA with uncorrected Fisher's LSD test. Statistical significance was set beginning at $p < 0.05$ and was assessed by comparing treatment values one group as a control (unless otherwise stated). All analyses were performed using GraphPad Prism software (GraphPad Software, Inc., San Diego, CA).

5.3 Results

5.3.1 Fabrication of Complex Decoys

Complex decoys were designed to recapitulate the phenomenon uncovered by $PLP_{139-151}$ peptide-conjugated, microporous collagen sponges in their impressive efficacy against EAE[15]. We

positioned complex decoys as a first translational step toward addressing the polyantigenicity of most authentic human autoimmune diseases. By incorporating primary tissue homogenate from the compartment implicated in disease, we hypothesized that comprehensive autoantigen coverage could be represented by a porous biomaterial for immunotherapeutic benefit. To investigate the incorporation of homogenized brain tissue into GelMA microstructures, we prepared mixtures of GelMA (7% w/w) with MBH at various Gelatin:Homogenate (G:H) ratios for photocrosslinking. Each mixture yielded microporous materials when exposed to UV light and lyophilized (**Fig. 1**). SEM imaging revealed that the homogenate appeared to be incorporated into the architecture of columnar pores. Increasing MBH content illustrated a trend of decreasing biomaterial porosity, particularly when homogenate composition was in excess to GelMA. Gelatin-alone hydrogels were produced with a ~50 μm pore size, and 3:1 G:H and 2:1 G:H closely mirrored this porosity. As homogenate was included in excess (1:1, 1:2, 1:3 G:H), pores were less prevalent and were roughly halved in size.

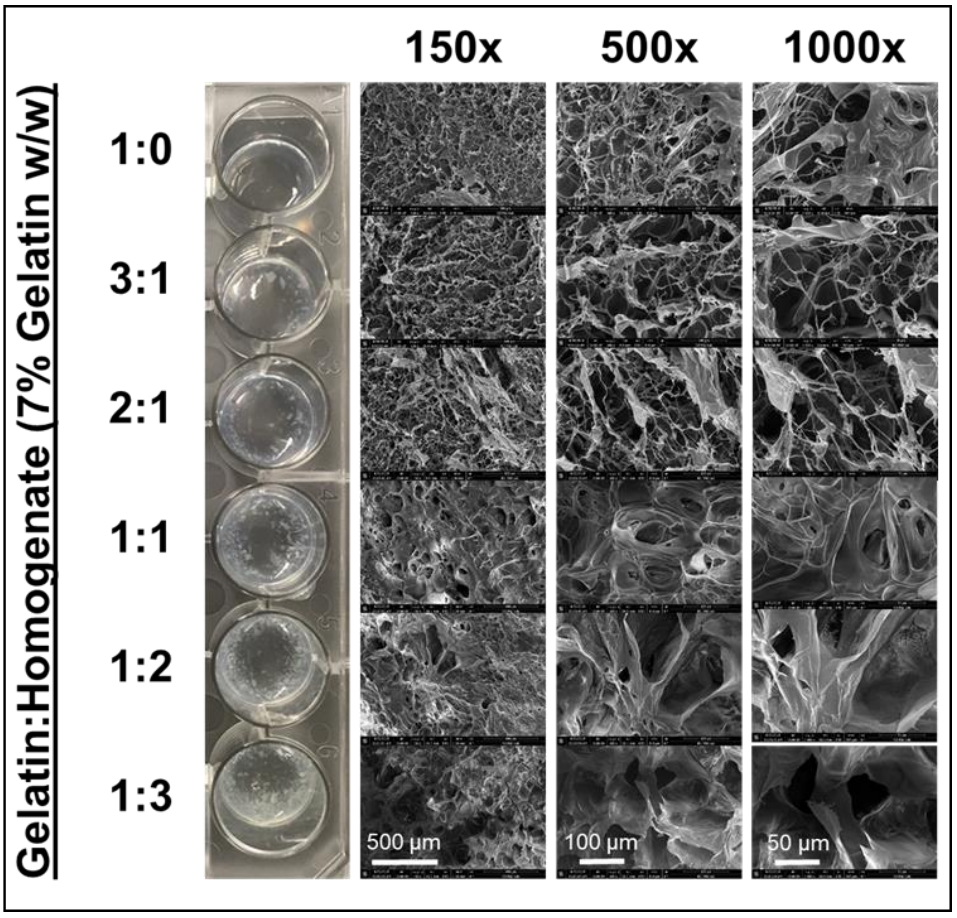

Figure 1. SEM of complex decoys for visualizing homogenate incorporation into gelatin methacrylate microstructures. The 7% gelatin methacrylate was mixed with varying ratios of mouse brain homogenate prior to photocrosslinking and lyophilizing to yield microporous biomaterials.

5.3.2 mbhGelatin Decoys are Persistent Depots that Incorporate Primary Tissue Homogenate and Retain Antigen-Specificity

To assess the influence of homogenate inclusion on GelMA material properties, we subjected the varied G:H ratio mbhGelatin constructs to a strain-sweep for rheological testing (**Fig. 2**). Most mbhGelatin materials exhibited similar deformation response curves excepting 1:3 G:H

(the extreme homogenate-containing hydrogel), which showed divergent behavior in its elastic modulus (**Fig. 2a)**. Shifts in rheological properties occurred at different strain points among the various ratios tested, so we further analyzed measurements at the discrete strain point of 0.32 (**Fig 2b**). G' values did not vary significantly at this point of separation, but a homogenate-dependent trend was evident in that increasing homogenate content led to increasing elastic modulus measurements. Conversely, changes in the viscous modulus, G", appeared to indicate that the inclusion of homogenate may have led to a similarly decreased readout across G:H contents, though 1:1 G:H exhibited a viscosity similar to gelatin-alone. The G"/G' ratio (tanδ) illuminated material propensities for being dominated by elastic or viscous properties. The inclusion of homogenate into the gelatin microstructures generally conferred a greater material resilience (noted through a G"/G' ratio of less than 1 across greater strain forces). This observation further suggested that the homogenate was successfully integrated into the architecture at some level.

To establish mbhGelatin as an implantable decoy therapeutic, it was important to assess the irreversibility of homogenate incorporation into the materials. Toward this end, we conducted a month-long release study of these constructs across the various G:H ratios (**Fig. 2c**). Release was dependent upon time and homogenate content, as released protein increased gradually over the course of the 31 days and was more pronounced in 1:3 G:H than in other groups. There appeared to be a slight burst release of unincorporated homogenate, as after 1 day both 3:1 and 1:3 G:H released significantly more protein than gelatin alone. After 31 days, however, 3:1 G:H cumulative release was statistically similar to gelatin alone while 1:3 G:H continued to increase.

Finally, it was necessary to investigate the retained discrete antigenicity of epitopes in homogenate after its incorporation into GelMA materials. We cryosectioned blank gelatin, $PLP_{139-151}$-conjugated gelatin, and 2:1 G:H gelatin onto microscope slides and used the materials as

substrates for an anti-PLP IgG ELISA. No anti-PLP IgG was detected on the blank gelatin sponge, and a definitively positive signal was evident with the peptide-conjugated gelatin (**Fig. 2d**). mbhGelatin exhibited an intermediate signal, indicating some binding. PLP represents just one of many material constituents of the CNS, so it was rational to observe a lower-intensity reading as the result of lower overall abundance.

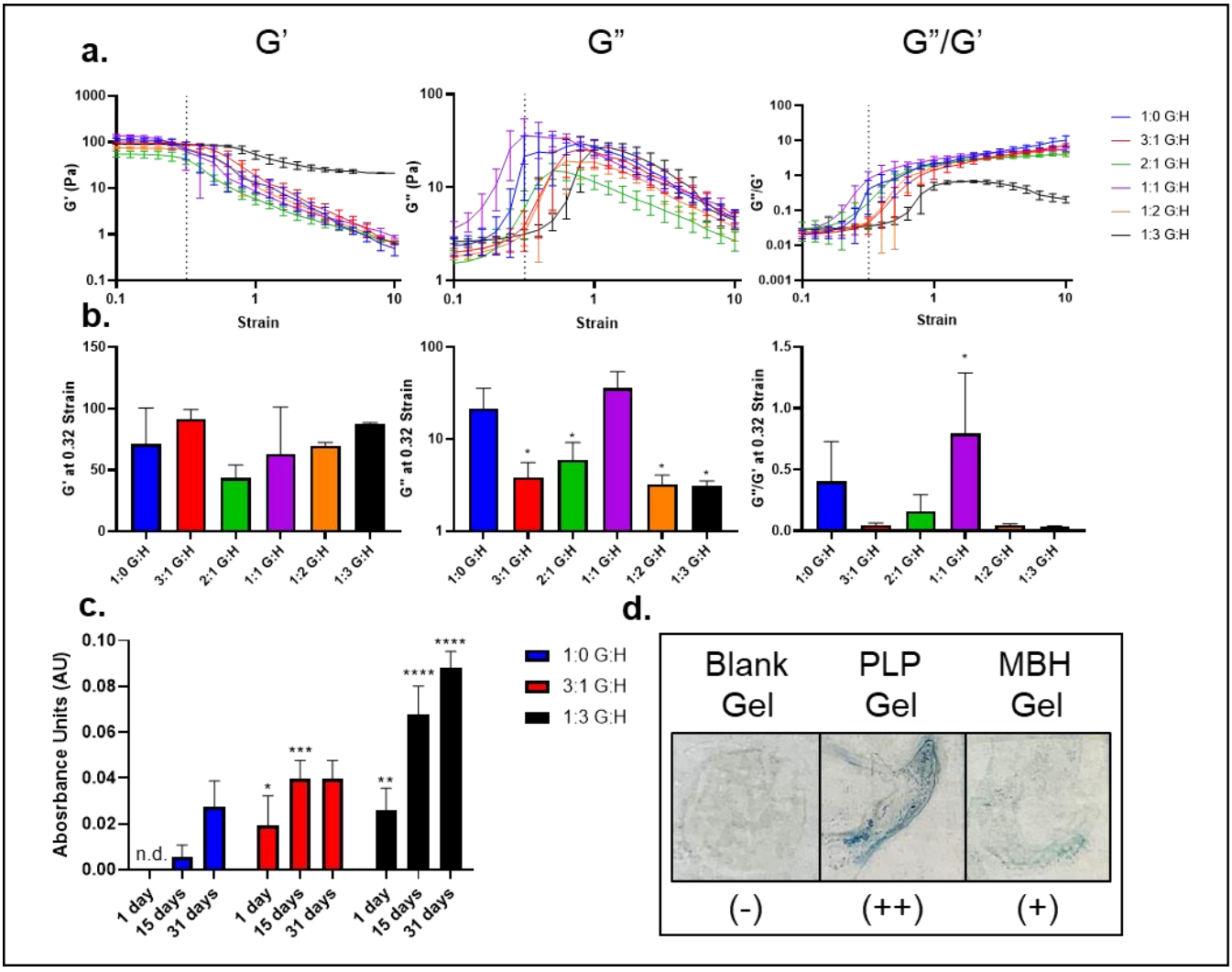

Figure 2. Material characterization of complex decoys of varied homogenate content. **a.** Rheological analysis across a strain sweep yielded storage modulus (G', left), loss modulus (G", middle), and tanδ (G"/G', right) information. **b.** To analyze strain sweep data with greater

resolution, G' (left), G"(middle), and G"/G' (right) are reported at 0.32 strain, a region of the greatest separation. **c.** A release study was conducted over the course of 31 days, in which data are reported for a blank gelatin sponge (1:0 G:H left), minimal homogenate sponge (3:1 G:H, middle), and maximal homogenate sponge (1:3 G:H, right). **d.** ELISA methods were used to detect the ability of anti-PLP-containing serum to bind cognate antigen. (Statistical analysis was performed against 1:0 G:H as a control. n = 3-4/group, *$p < 0.05$, **$p < 0.01$, ***$p < 0.001$, ****$p < 0.0001$).

5.3.3 mbhGelatin Decoys Elicit a Cellular Response and Amplify Antigen-Specific B cells ex vivo

2:1 G:H were selected for advancement to biological assays because they facilitated retained porosity (**Fig. 1**) with the most homogenate loading. EAE splenocytes were harvested at peak of disease and plated with vehicle, soluble $PLP_{139-151}$, blank gelatin sponges, or mbhGelatin (2:1 G:H) for 96 hours (**Fig. 3**). After the incubation, cell metabolism in response to the treatments was measured with resazurin (**Fig. 3a**). Both soluble antigen challenge and blank gelatin enabled a slight increase in metabolism after the interval, but mbhGelatin elicited over a four-fold increase in resazurin, suggesting greater cellular activity. In parallel, cells were harvested from wells and sponges and prepared for flow cytometry analysis **(Fig. 3b-g**). Gelatin biomaterials appeared to provide a favorable substrate for B cell viability; both blank gelatin and mbhGelatatin retained significantly more CD19+ cells than -PLP and +PLP, where mbhGelatin provided maximal retention. This B cell retention logically correlated inversely with CD3+ cell prevalence (**Fig. 3c**). Over 80% of surviving splenocytes in the -PLP and +PLP groups constituted T cells, while slightly less were present in blank gelatin and significantly fewer were appreciable after mbhGelatin treatment. Antigen presenting cells (CD11c+) were generally consistent among treatment groups

(**Fig. 3d**). CD19+CD11c+ antigen-presenting B cells were analyzed as a subset of interest that is implicated in autoimmunity (**Fig. 3e**), but only subtle differences were observed. mbhGelatin also maximally increased CD86 (**Fig. 3f**). This costimulatory marker was also significantly elevated by +PLP and blank gelatin. Finally, FITC-labeled soluble antigen arrays (SAgAs) incorporating multivalent PLP were used to detect anti-PLP B cell receptors (**Fig. 3g**). Few events were detected at baseline or after 96 hours with -PLP or +PLP incubation. One replicate of blank gelatin led to elevated PLP-specific B cells, but this amplification was not consistent as the other two readouts were comparable to other controls. mbhGelatin, however, evoked consistent and statistically significant amplification of antigen-specific B cells.

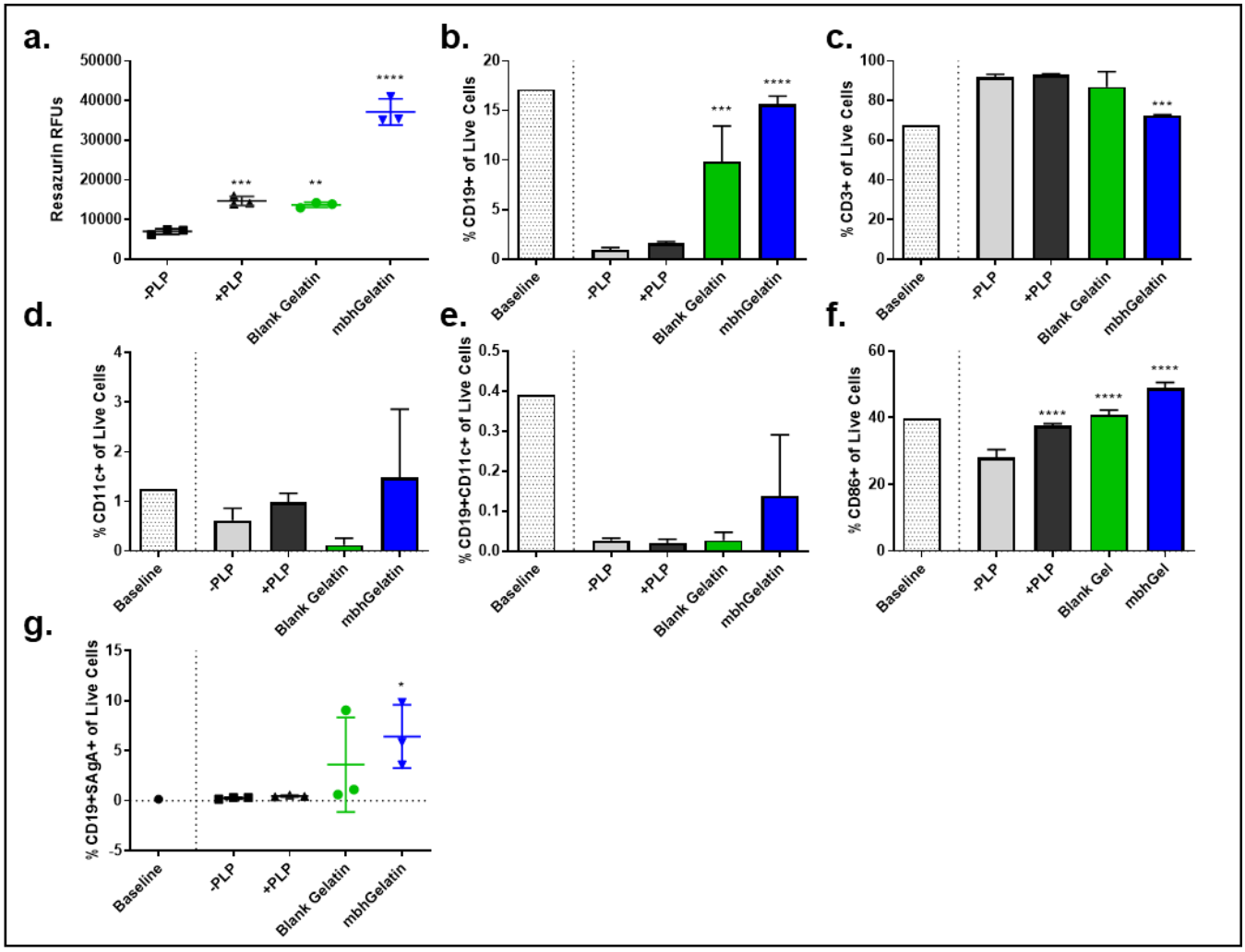

Figure 3. Ex vivo analysis of EAE splenocyte responses to complex decoys. **a.** The resazurin assay was used to assess changes in cell metabolism after incubating splenocytes for 96 hours with vehicle (grey), 25 µM PLP (black), blank gelatin (green), or mbh sponges (blue). After the incubation, flow cytometry was used to assess proportionality of populations expressing the markers CD19 (**b.**), CD3 (**c.**), CD11c (**d.**) as well as CD19+CD11c+ antigen-presenting B cells (**e.**) and costimulated CD86+ cells (**f.**). FITC labeled, dendrimeric PLP was used to quantify the presence of antigen-specific B cells as well (**g.**). (Statistical analysis was performed against –PLP as a control. n = 3/group, *p < 0.05, **p < 0.01, ***p < 0.001, ****p < 0.0001).

plpGelatin, but not mbhGelatin Decoys Suppress EAE in vivo. EAE mice were implanted with either mock surgery, blank gelatin, plpGelatin, or mbhGelatin on day 4 post induction (**Fig. 4**). plpGelatin suppressed disease as evidenced by clinical scoring, weights, cumulative score, and disease incidence (**Fig. 4a-d**, respectively). Only 3 of 4 plpGelatin-implanted mice developed EAE, while all mice in other groups exhibited symptoms to some degree (**Fig. 4d**). mbhGelatin did not alter disease course in EAE mice. Homogenate-containing biomaterials may have even exacerbated EAE symptoms, as 1 of 4 mbhGelatin mice succumbed to disease and died during the study. No mice were lost in the other control groups, and mbhGelatin trended slightly higher in cumulative disease score (**Fig. 4c**), though the increase was not statistically significant.

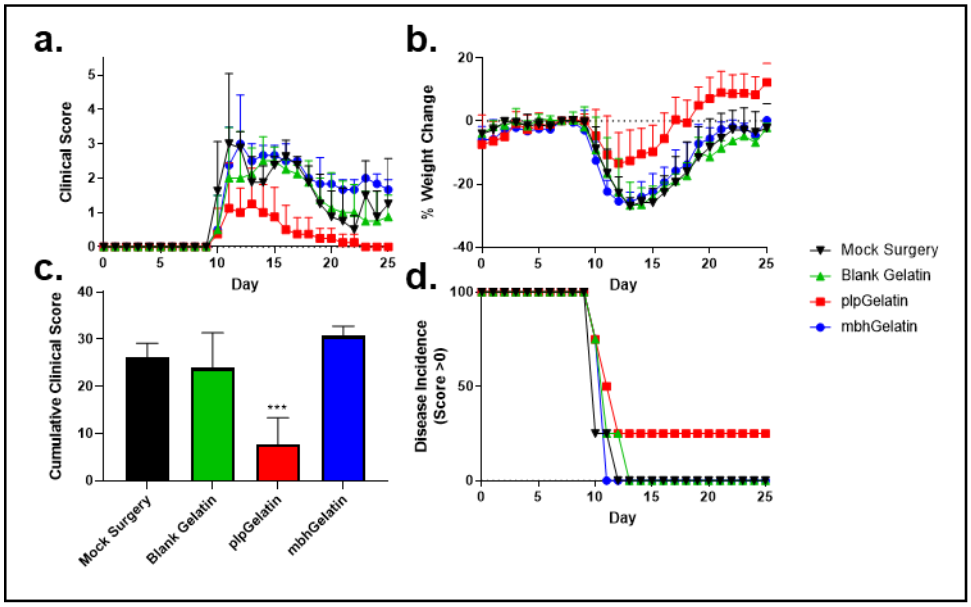

Figure 4. Clinical data from the in vivo implantation of EAE mice with complex decoys. Clinical scores (**a.**) and weights (**b.**) are reported for mice implanted with either mock surgery (black), blank gelatin (green), plpGelatin (red), or mbhGelatin (blue). **c.** Cumulative scores across 25 days are reported. **d.** the first incidence of disease was tracked across the study as well. (Statistical

analysis was performed against -PLP as a control. n = 4/group, *p < 0.05, **p < 0.01, ***p < 0.001).

5.3.4 EAE splenocytes are largely unchanged by prophylactic mbhGelatin implantation

After the 25-day therapeutic efficacy study, spleens and serum were harvested from mice in each group and processed for further analysis (**Fig. 5**). Spleen weights were measured upon harvest, where no significant differences were observed, although the one mouse that did not exhibit EAE symptoms in the plpGelatin group did exhibit a more massive spleen that was statistically determined to be divergent from the rest of the set (Grubbs outlier test, $\alpha = 0.05$, **Fig. 5a**). Generally, more splenocytes were harvested from plpGelatin-implanted mice, but this difference was not statistically significant (**Fig. 5b**). Serum from mice was used to determine anti-PLP IgG Titer among each group (**Fig. 5c**). plpGelatin exhibited a consistently slightly higher titer than other groups, and both mock surgery and blank gelatin each had one mouse with higher titer than others in the group. Flow cytometry was used to assess changes in cell populations after 96 hours of vehicle (-PLP, open bars) or antigen challenge (+PLP, solid bars, **Fig. 5d-i**). CD3+ cell proportionality among splenocytes was largely unchanged among groups after 96 hours, though they consistently constituted less in the +PLP group than with -PLP (**Fig. 5d**). CD19+ B cells increased with antigen challenge, and plpGelatin and mbhGelatin showed slightly elevated proportions, though not statistically significant (**Fig. 5e**). In terms of antigen-specific B cells, however, both blank gelatin and plpGelatin exhibited significantly higher proportions than mock surgery after antigen challenge (**Fig. 5f**). Splenic CD11c+ populations were not notably different between groups, however they increased in proportion after antigen challenge in the mock surgery

group while other groups showed a decrease after PLP incubation (**Fig. 5g**). mbhGelatin-implanted mice showed significantly higher costimulation than mock surgery controls (**Fig. 5h**). CD19+CD11c+ double positive cells were not different among groups (**Fig. 5i**). Finally, resazurin was used to quantify changes in cell metabolism among harvested splenocytes (**Fig. 5j**). Trends were strikingly similar between groups after 96 hours of incubation with vehicle, PLP, or mitogen Concanavalin A (ConA).

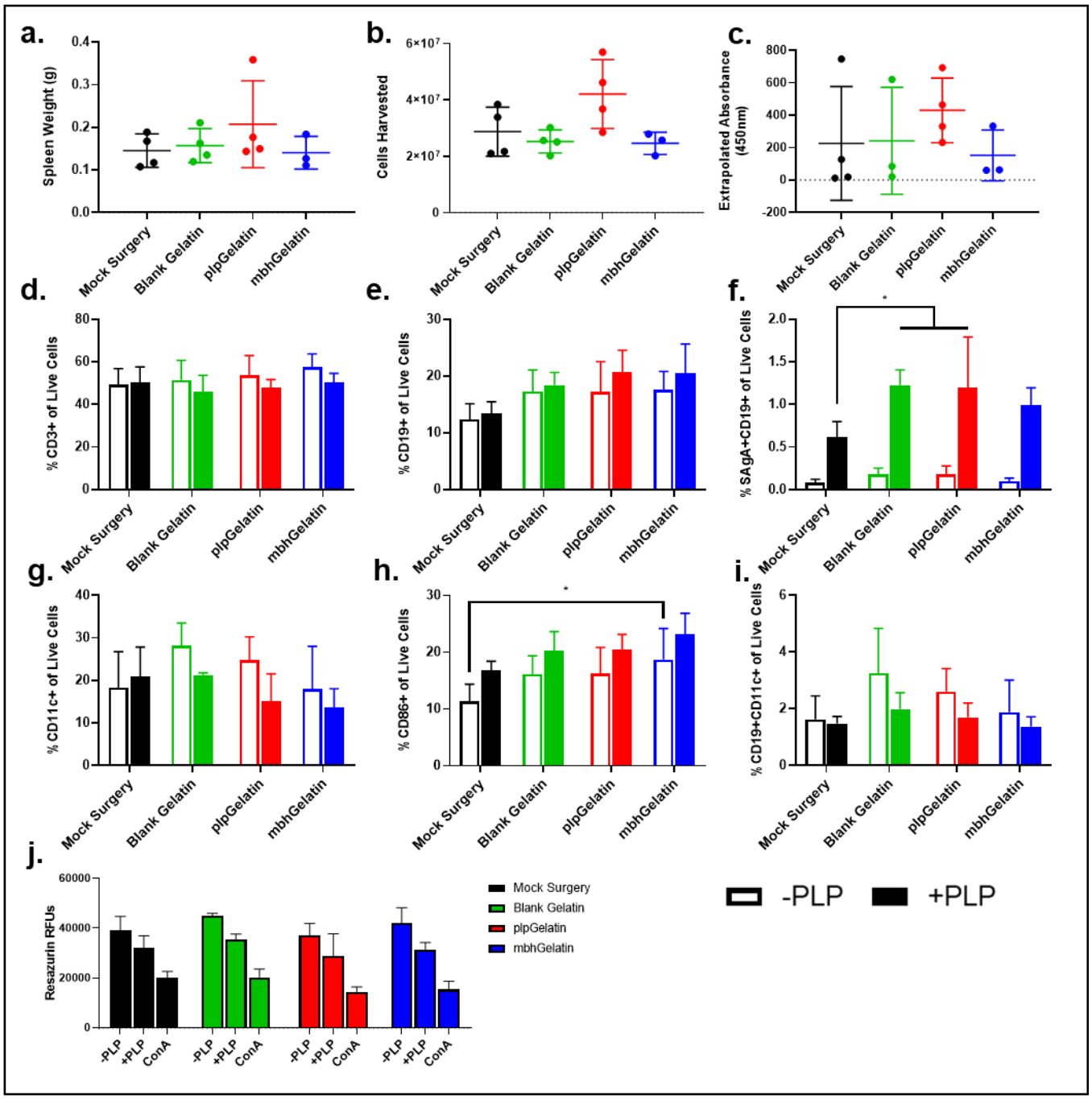

Figure 5. After the 25 day in vivo study, spleens were harvested and splenocytes were isolated. During isolation, spleens were weighed (**a.**) and harvested splenocytes were counted (**b.**). **c.** serum was harvested from mice and anti-PLP IgG was quantified. Splenocytes were incubated with (solid bars) and without (open bars) PLP rechallenge for 96 hours before being labeled for flow

cytometry. Data reflect marker expression for CD3 (**d.**), CD19 (**e.**), SAgA+CD19+ cells (**f.**), CD11c (**g.**), CD86 (**h.**), and CD19+CD11c+ antigen-presenting B cells (**i.**). **j.** resazurin cell metabolism is reported after 96 hour challenge with vehicle, PLP, or concavolin A. (Statistical analysis was performed against -PLP as a control. n = 3-4/group, *p < 0.05, **p < 0.01, ***p < 0.001, ****p < 0.0001).

5.4 Discussion

Our previous exploration of the decoy effect employed single epitope-conjugated microporous collagen sponges against an analogous single epitope model of autoimmunity ($PLP_{139-151}$-EAE) to illustrate that the antigen-specific exhaustion of autoimmune effector cells could prematurely return these populations to lymphoid organs and prevent disease[15]. Presently, we set forth to create a polyantigenic complex decoy as a first step to extrapolate these effects for authentic, polyclonal immune-mediated diseases. It was necessary to fabricate a microporous biomaterial that was immunologically inert, irreversibly associable with autoantigen, and antigenically functional. GelMA was selected as a constituent material for its biocompatibility and versatility in biological applications, and gelatin is chemically autologous to the collagen used in our previous application[20].

Photocrosslinkable GelMA was able to incorporate MBH and manifest as a microporous architecture (**Fig. 1, 2**). SEM imaging revealed that porosity was homogenate-dependent in determining size. As increasing amounts of homogenate were added prior to crosslinking the materials, we logically observed columnar formations of larger sizes and smaller pore diameters as a result. We theorized that a minimum pore diameter of 50 μm would be sufficient to facilitate unhindered cell and nutrient transfer[21, 22], and 2:1 G:H decoys enabled the highest loading of MBH

without falling below this threshold. Interestingly, as MBH mass equaled and exceeded that of GelMA in the formulation (1:1, 1:2, and 1:3 G:H), pore architecture changed from a thin, spider web-like phenotype to one more comparable to interpenetrating sheet-like structures (**Fig. 1**). In rheological testing analysis, it was apparent that the elastic modulus was slightly increased with greater inclusion of homogenate (**Fig. 2b**) 1:1 G:H sponges were consistently divergent from the rest of the set; it is unclear why this discrepancy emerged, but perhaps it is indicative of an intermediate transition occurring while the material is predominately GelMA versus becoming predominantly MBH. Nevertheless, G' and G" readouts across the strain sweep experiments follow the same response trends. This observation was to be expected, as GelMA hydrogels are largely fabricated to resemble the viscoelastic properties of authentic tissue. Therefore, both GelMA and MBH should conceivably present similar material properties and lead to these consistent trends.

The influence of MBH on the elastic moduli of mbhGelatin variants implies that the homogenate was incorporated to the GelMA structure since it contributed some material resilience[23]. However, mechanical testing alone cannot verify that MBH is irreversibly associated. To investigate the lasting immobilization of homogenate into the sponges, we conducted a month-long release study and found that after 31 days, mbhGelatin that is composed of a majority gelatin does not differ significantly from gelatin alone (**Fig. 2d**). This finding suggested that though some homogenate is unincorporated (being released early-on), tissue is retained in majority-gelatin materials. Combining SEM assertions (**Fig. 1**) with rheology and release trends (**Fig. 2**), 2:1 G:H materials were selected for further experimentation. Importantly, anti-PLP IgG bound with 2:1 G:H mbhGelatin to exhibit retained antigen functionality, fulfilling the last of our identified criteria for realizing a complex decoy (**Fig. 2d**).

Seemingly conflicting outcomes emerged between the *ex vivo* assays and *in vivo* therapeutic study (**Fig. 3, 4, 5**). Central to the apparent PLP-conjugated decoy mechanism our previous report was the activation and overstimulation of PLP-responsive cell subsets. Determinants of overstimulation conserved from PLP decoys were elevated cell metabolism and expression of costimulatory marker CD86, which were both significantly elevated by mbhGelatin during the *ex vivo* screen (**Fig. 3f**). However, these increases did not appear to confer exhaustion *in vivo*, as mbhGelatin-implanted mice exhibited the highest cumulative disease score (**Fig. 4c**) and no suppression of effector cells was evident as was the case with PLP-conjugated decoys from the previous work. CD86+ costimulation was higher in mbhGelatin splenocytes than in controls, but differences were slight and may have contributed to further destructive action rather than being substantial enough to cross a threshold into overstimulation and exhaustion.

Indeed, the line between immune action and exhaustion can be rather fleeting; these opposing results that stem from the same stimulus can be driven by a variety of factors[24-26]. Antigen valency is established as a major determinant[27-30]. Much work has been done to show the relationship between characteristics such antigen dose and persistence in tipping the balance between action and anergy[27, 31, 32]. In the present work, it rationally proceeds and was evident from **Fig. 2d** that plpGelatin was substantially more positive for anti-PLP IgG binding than mbhGelatin. Such a discrepancy could explain the difference in magnitude of costimulation and ultimately immune cell fates between exacerbation or amelioration of disease.

While included as a control group for the *in vivo* study, plpGelatin-implanted mice illuminate important qualities that the "decoy effect" harnesses to be therapeutically relevant. Mice treated with plpGelatin exhibited suppressed disease (**Fig. 4**), but one of the four mice in the group was protected from EAE symptoms altogether (**Fig. 4d**). Interestingly, this same mouse's spleen

was over twice as massive as nearly all others in the study (**Fig. 5a**). In the first exploration of antigen-specific decoys, engorged lymphoid organs were recognized as a consistent phenomenon in implanted mice that showed suppressed or no disease[15]. The fact that the spleen was engorged in this mouse for which disease was prevented illustrates that the phenomenon of premature splenic return may be critical to the overall driving mechanism of immune decoys.

Though mbhGelatin was not therapeutic, the polyantigenic biomaterial demonstrated an ability to amplify PLP-specific B cells *ex vivo* (**Fig. 3g**). Such functionality has the potential to demonstrate utility in characterizing autoimmunity for patients where tracking disease progression and status is difficult and expensive. For example, in MS, detectable autoimmune biomarkers are largely evidenced exclusively in the central nervous system[33]. Autoreactive cells are of low-prevalence in peripheral blood, and blood tests aiming to diagnose MS require elaborate single-cell and sequencing techniques[34]. Further development of mbhGelatin biomaterials could offer a lower-cost alternative for the amplification and analysis of MS biomarkers in the blood, but future studies are needed. Ongoing work would be beneficial in seeking to characterize *ex vivo* amplification in human patient samples and tie phenotypical changes back to discrete epitope specificities as a strategy to more precisely monitor and treat MS[35, 36].

There is undoubtedly a clinical need for precise immunotherapies that can selectively target aberrant autoimmune cells while preserving healthy host functions[37, 38]. Antigen-specific immunotherapy leads the charge toward this end, but solutions that can accommodate the heterogeneity and transience of autoimmunity are still needed. Ideated as an answer to this call but ineffective at treating disease, important lessons can be gleaned from immune decoys. Single-epitope decoys assert that establishing an immunological niche can be of great benefit for directing immunity[39, 40], but mbhGelatin illustrates that it is critical to consider additional properties such as

antigen loading density. Moving forward, perhaps new approaches will do well to deliver and retain immunomodulatory signals in disease-implicated compartments as niches of their own to confer broader coverage while limiting systemic effects.

5.5 Conclusions

MBH-containing, microporous complex decoys were successfully fabricated by mixing primary brain tissue with GelMA. Tissue was immobilized within the gelatin architecture and exhibited a retained ability to bind anti-PLP IgG. mbhGelatin decoys were able to amplify antigen-specific B cells among EAE splenocytes *ex vivo*. plpGelatin, but not mbhGelatin, suppressed disease *in vivo*, highlighting a key discrepancy in the exhaustion threshold needed to ameliorate disease. Future work is needed to refine polyantigenic decoys as viable, translatable solutions for treating human autoimmunity.

5.6 Acknowledgments

JDG was supported by the Madison and Lila Self Graduate Fellowship at the University of Kansas. JYS was supported by the Stella Fellowship of the Department of Pharmaceutical Chemistry at the University of Kansas. We gratefully acknowledge and thank Dr. Arghya Paul for providing the materials and expertise needed to prepare GelMA constructs.

5.7 References

1. Sabatos-Peyton, C. A.; Verhagen, J.; Wraith, D. C., Antigen-specific immunotherapy of autoimmune and allergic diseases. *Current opinion in immunology* **2010,** *22* (5), 609-615.
2. Carballido, J. M.; Santamaria, P., Taming autoimmunity: Translating antigen-specific approaches to induce immune tolerance. *The Journal of Experimental Medicine* **2019,** *216* (2), 247.

3. Steinman, L.; Ho, P. P.; Robinson, W. H.; Utz, P. J.; Villoslada, P., Antigen-specific tolerance to self-antigens in protein replacement therapy, gene therapy and autoimmunity. *Current opinion in immunology* **2019,** *61*, 46-53.
4. Northrup, L.; Christopher, M. A.; Sullivan, B. P.; Berkland, C., Combining antigen and immunomodulators: Emerging trends in antigen-specific immunotherapy for autoimmunity. *Advanced drug delivery reviews* **2016,** *98*, 86-98.
5. Kontos, S.; Grimm, A. J.; Hubbell, J. A., Engineering antigen-specific immunological tolerance. *Current opinion in immunology* **2015,** *35*, 80-88.
6. Mackay, I. R.; Carnegie, P. R.; Coates, A. S., Immunopathological comparisons between experimental autoimmune encephalomyelitis and multiple sclerosis. *Clin Exp Immunol* **1973,** *15* (4), 471-482.
7. Baxter, A. G., The origin and application of experimental autoimmune encephalomyelitis. *Nature Reviews Immunology* **2007,** *7* (11), 904.
8. Tuohy, V. K.; Kinkel, R. P., Epitope spreading: a mechanism for progression of autoimmune disease. In *Autoimmunity*, Springer: 2001; pp 39-48.
9. Quintana, F. J.; Farez, M. F.; Viglietta, V.; Iglesias, A. H.; Merbl, Y.; Izquierdo, G.; Lucas, M.; Basso, A. S.; Khoury, S. J.; Lucchinetti, C. F., Antigen microarrays identify unique serum autoantibody signatures in clinical and pathologic subtypes of multiple sclerosis. *Proceedings of the National Academy of Sciences* **2008,** *105* (48), 18889-18894.
10. Ayoglu, B.; Häggmark, A.; Khademi, M.; Olsson, T.; Uhlén, M.; Schwenk, J. M.; Nilsson, P., Autoantibody Profiling in Multiple Sclerosis Using Arrays of Human Protein Fragments. *Molecular & Cellular Proteomics* **2013,** *12* (9), 2657.
11. Miller, A.; Lider, O.; Weiner, H. L., Antigen-driven bystander suppression after oral administration of antigens. *Journal of Experimental Medicine* **1991,** *174* (4), 791-798.
12. Weiner, H.; Miller, A.; Zhang, Z.; Al-Sabbagh, A., Bystander suppression of type I diabetes by oral administration of glucagon. Google Patents: 2003.
13. Aharoni, R.; Teitelbaum, D.; Sela, M.; Arnon, R., Bystander suppression of experimental autoimmune encephalomyelitis by T cell lines and clones of the Th2 type induced by copolymer 1. *Journal of neuroimmunology* **1998,** *91* (1-2), 135-146.
14. Zonneveld-Huijssoon, E.; Roord, S. T.; de Jager, W.; Klein, M.; Albani, S.; Anderton, S. M.; Kuis, W.; van Wijk, F.; Prakken, B. J., Bystander suppression of experimental arthritis by nasal administration of a heat shock protein peptide. *Annals of the rheumatic diseases* **2011,** *70* (12), 2199-2206.
15. Griffin, J. D.; Song, J. Y.; Huang, A.; Sedlacek, A. R.; Flannagan, K. L.; Berkland, C. J., Antigen-specific immune decoys intercept and exhaust autoimmunity to prevent disease. *Biomaterials* **2019,** *222*, 119440.
16. Yue, K.; Trujillo-de Santiago, G.; Alvarez, M. M.; Tamayol, A.; Annabi, N.; Khademhosseini, A., Synthesis, properties, and biomedical applications of gelatin methacryloyl (GelMA) hydrogels. *Biomaterials* **2015,** *73*, 254-271.
17. Shirahama, H.; Lee, B. H.; Tan, L. P.; Cho, N.-J., Precise tuning of facile one-pot gelatin methacryloyl (GelMA) synthesis. *Scientific reports* **2016,** *6*, 31036.
18. Rohanizadeh, R.; Swain, M. V.; Mason, R. S., Gelatin sponges (Gelfoam®) as a scaffold for osteoblasts. *Journal of Materials Science: Materials in Medicine* **2008,** *19* (3), 1173-1182.
19. Griffin, J. D.; Christopher, M. A.; Thati, S.; Salash, J. R.; Pressnall, M. M.; Weerasekara, D. B.; Lunte, S. M.; Berkland, C. J., Tocopherol Emulsions as Functional

Autoantigen Delivery Vehicles Evoke Therapeutic Efficacy in Experimental Autoimmune Encephalomyelitis. *Molecular pharmaceutics* **2019,** *16* (2), 607-617.
20. Djabourov, M.; Lechaire, J.-P.; Gaill, F., Structure and rheology of gelatin and collagen gels. *Biorheology* **1993,** *30* (3-4), 191-205.
21. O'Brien, F. J.; Harley, B. A.; Waller, M. A.; Yannas, I. V.; Gibson, L. J.; Prendergast, P. J., The effect of pore size on permeability and cell attachment in collagen scaffolds for tissue engineering. *Technology and Health Care* **2007,** *15* (1), 3-17.
22. Lien, S.-M.; Ko, L.-Y.; Huang, T.-J., Effect of pore size on ECM secretion and cell growth in gelatin scaffold for articular cartilage tissue engineering. *Acta Biomaterialia* **2009,** *5* (2), 670-679.
23. Li, P.; Dou, X.-Q.; Feng, C.-L.; Zhang, D., Mechanical reinforcement of C 2-phenyl-derived hydrogels for controlled cell adhesion. *Soft Matter* **2013,** *9* (14), 3750-3757.
24. Kahan, S. M.; Zajac, A. J., Immune exhaustion: past lessons and new insights from lymphocytic choriomeningitis virus. *Viruses* **2019,** *11* (2), 156.
25. Schietinger, A.; Greenberg, P. D., Tolerance and exhaustion: defining mechanisms of T cell dysfunction. *Trends in immunology* **2014,** *35* (2), 51-60.
26. Wherry, E. J., T cell exhaustion. *Nature immunology* **2011,** *12* (6), 492.
27. Han, S.; Asoyan, A.; Rabenstein, H.; Nakano, N.; Obst, R., Role of antigen persistence and dose for CD4⁺ T-cell exhaustion and recovery. *Proceedings of the National Academy of Sciences* **2010,** *107* (47), 20453.
28. Hess, K. L.; Oh, E.; Tostanoski, L. H.; Andorko, J. I.; Susumu, K.; Deschamps, J. R.; Medintz, I. L.; Jewell, C. M., Engineering immunological tolerance using quantum dots to tune the density of self-antigen display. *Advanced functional materials* **2017,** *27* (22), 1700290.
29. Wang, H.; Mooney, D. J., Biomaterial-assisted targeted modulation of immune cells in cancer treatment. *Nature materials* **2018**, 1.
30. Dellacherie, M. O.; Li, A. W.; Lu, B. Y.; Mooney, D. J., Covalent conjugation of peptide antigen to mesoporous silica rods to enhance cellular responses. *Bioconjugate chemistry* **2018,** *29* (3), 733-741.
31. McKinney, E. F.; Lee, J. C.; Jayne, D. R.; Lyons, P. A.; Smith, K. G., T-cell exhaustion, co-stimulation and clinical outcome in autoimmunity and infection. *Nature* **2015,** *523* (7562), 612.
32. McKinney, E.; Smith, K., Metabolic exhaustion in infection, cancer and autoimmunity. *Nature immunology* **2018,** *19* (3), 213.
33. Miller, J. R.; Burke, A. M.; Bever, C. T., Occurrence of oligoclonal bands in multiple sclerosis and other CNS diseases. *Annals of Neurology: Official Journal of the American Neurological Association and the Child Neurology Society* **1983,** *13* (1), 53-58.
34. Rounds, W. H.; Salinas, E. A.; Wilks, T. B.; Levin, M. K.; Ligocki, A. J.; Ionete, C.; Pardo, C. A.; Vernino, S.; Greenberg, B. M.; Bigwood, D. W.; Eastman, E. M.; Cowell, L. G.; Monson, N. L., MSPrecise: A molecular diagnostic test for multiple sclerosis using next generation sequencing. *Gene* **2015,** *572* (2), 191-197.
35. Comabella, M.; Sastre-Garriga, J.; Montalban, X., Precision medicine in multiple sclerosis: biomarkers for diagnosis, prognosis, and treatment response. *Current opinion in neurology* **2016,** *29* (3), 254-262.
36. Derfuss, T., Personalized medicine in multiple sclerosis: hope or reality? *BMC medicine* **2012,** *10* (1), 116.

37. Carson, K. R.; Focosi, D.; Major, E. O.; Petrini, M.; Richey, E. A.; West, D. P.; Bennett, C. L., Monoclonal antibody-associated progressive multifocal leucoencephalopathy in patients treated with rituximab, natalizumab, and efalizumab: a Review from the Research on Adverse Drug Events and Reports (RADAR) Project. *The lancet oncology* **2009,** *10* (8), 816-824.
38. Rosenblum, M. D.; Gratz, I. K.; Paw, J. S.; Abbas, A. K., Treating human autoimmunity: current practice and future prospects. *Science translational medicine* **2012,** *4* (125), 125sr1-125sr1.
39. Bookstaver, M. L.; Tsai, S. J.; Bromberg, J. S.; Jewell, C. M., Improving vaccine and immunotherapy design using biomaterials. *Trends in immunology* **2018,** *39* (2), 135-150.
40. Kim, J.; Li, W. A.; Choi, Y.; Lewin, S. A.; Verbeke, C. S.; Dranoff, G.; Mooney, D. J., Injectable, spontaneously assembling, inorganic scaffolds modulate immune cells in vivo and increase vaccine efficacy. *Nature biotechnology* **2015,** *33* (1), 64.

6. Conclusions and Future Directions

6.1 Conclusions

In chapter 1, we explored the physical and chemical factors that dictate the transport and effects of parenterally delivered autoantigen formulations. Looking at established allergen desensitization regimens as a standard for optimal immune interfacing, we illuminated discrepancies between these small (10-70 kDa), soluble (GRAVY score <0), and slightly negatively-charged (PI ~5-7) entities and autoantigen counterparts, which often embody extreme characteristics outside of these ranges. Our conclusion from reviewing antigen-specific immunotherapy (ASIT) literature and clinical trials was that delivery systems and biomaterials not only enhance autoantigen delivery to secondary lymphoid organs, but are likely necessary to format self-antigens in a way to most effectively influence autoimmunity. This analysis served as the foundation from which the experimental works in this dissertation emerged. We leveraged three autoantigen delivery formats – soluble, particulate, and depot – to glean meaningful insights about physicochemical drivers of effect using experimental autoimmune encephalomyelitis (EAE) as a model of autoimmunity.

Chapter 2 initiated the scope of this dissertation by adopting the soluble antigen array (SAgA) as a platform to enumerate the role of valency in dampening autoimmunity. Prior to this work, the SAgA was well characterized to evoke B cell anergy and therapeutic tolerance by clustering B cell receptors. Past work had been done to assess delivery system properties such as structure, size, and solubility, but more nuanced components like ligand valency had not been explored. We hypothesized that by titrating this property, an optimal inhibitory configuration could be discovered to inform tailored SAgA design and future iterations. Both one- and two- signal SAgAs were evaluated in this analysis, and the inclusion of both revealed that autoantigen valency (not overall ligand valency) was the major driver of effect in autoreactive B cells and mixed

splenocytes. Antigen valency proved to correlate inversely and strongly with both acute measures of inhibition in a B cell line and downstream indicators of tolerogenesis in mixed splenocytes. We proposed a more optimally configured SAgA format expressing 4-7 autoantigen epitopes per 20 kDa hyaluronan backbone rather than the conventionally invoked 10 epitopes per backbone.

Particulate ASIT formulations for autoimmunity have been historically appealing for their similarities to vaccine formulations and ability to target immune-directive antigen-presenting cell populations. However, many of the tools for these approaches have been adapted from vaccine development where immunogenicity is desired. As a result, some vehicles for delivering autoantigen can cause inflammation which must be overcome by codelivering immunomodulatory drug. In chapter 3, we hypothesized that by developing a "functional" ASIT delivery vehicle, therapeutic efficacy would be contributed. We selected FDA-approved α-tocopherol emulsions (ETPGS) as a delivery system, as vitamin E is capable to mediate immunity through antioxidant mechanisms. We were able to deliver antigen with these formulations by developing a recipe to produce nanoparticles around 300 nm in diameter. ETPGS inhibited macrophage reactive nitrogen and oxygen species production *in vitro*, suggesting the antioxidant mechanism could inhibit innate immune actors.

We conducted a therapeutic study and discovered that the delivery of ETPGS containing autoantigen suppressed EAE *in vivo*. Following the therapeutic study with *ex vivo* analyses, however, it became apparent that the ETPGS delivery vehicle may not be enacting effect in the way we initially hypothesized. Both pro- and anti-inflammatory cytokines were elevated in mice treated with these formulations. Flow cytometric splenocyte analysis showed that cell phenotypes did not differ from controls. Ultimately, we assessed the production of autoantigen-specific IgG between the serum and central nervous system, and we discovered that a majority of IgG was

relegated to the periphery in the ETPGS plus autoantigen group. Further, we noted during the therapeutic study that the ETPGS formulations seemed to indefinitely persist at the injection site. We posited that rather than being tolerized, the autoimmune response may have been simply diverted from reaching the central nervous system by prioritizing and persisting near the autoantigen-rich subcutaneous depot formed by ETPGS. However, since ETPGS could hypothetically be evoking both immunomodulatory and "decoy" effects, we needed a new system to enable exploration of these claims.

Without definitive evidence for a decoy mechanism of therapeutic efficacy in autoimmunity, we set forth to design a biomaterial that could isolate and evaluate this functionality. Chapter 4 details the invention of the antigen-specific immune decoy (ASID), an immunologically inert biomaterial providing a substrate for irreversibly immobilized antigen formulation that was designed to persist at the site of implantation. We developed this microporous biomaterial by chemically conjugating autoantigen to the surface of collagen sponges. Antigen remained functional after conjugation to the surface and was undelivered due to the irreversibility of the conjugation scheme. We implanted ASIDs into EAE mice and found the biomaterials capable to prevent disease *in vivo*. ASIDs appeared to intercept disease-causing autoreactive cells. Effector immune cells appeared to be severely exhausted by antigen overstimulation within ASIDs, evidenced by high levels of costimulatory markers but a similarly high prevalence of apoptosis in response to autoantigen rechallenge. These cells did not appear to regain functionality, as a subsequent *in vivo* study revealed that ASID-implanted mice did not exhibit relapsing disease while control mice robustly relapsed. In all, ASIDs seemed to intercept and exhaust autoreactive cell subsets, prematurely returning them to secondary lymphoid organs where they did not regain functionality.

Chapter 5 set forth to advance from compelling validation of the decoy effect outlined in chapter 4 by translating the phenomenon to a format that might be conducive for treating authentic human disease. Chapter 4 detailed “simple” ASIDs decorated with the same peptide epitope used to induce autoimmunity in EAE mice. In human multiple sclerosis, a plethora of ever-changing autoantigens are targeted by the immune system. To account for this polyclonality, “complex” ASIDs were fabricated by integrating primary brain tissue homogenate into microporous collagenous hydrogels. We hypothesized that these decoys would present with the full palette of conceivable multiple sclerosis antigens while retaining discrete antigen specificity. To assess the latter of this supposition, we evaluated complex ASIDs both *ex vivo* and *in vivo*. *Ex vivo*, complex ASIDs behaved similarly to what we observed in simple ASIDs. Complex decoys stimulated antigen-presenting cells and led to the amplification of antigen-specific cell populations. These events are important precursors to cellular exhaustion. When complex decoys were implanted in EAE mice, however, therapeutic effect was elusive. This result indicated that a critical property was lost in translating ASIDs from simple to complex. As a result, ongoing work will shed light on this essential parameter.

6.2 Future Directions

In the midst of unexpected results from a first step in translating the decoy effect for human disease, we are brought back full-circle to indelible lessons from the foundational chapters of this dissertation. Chapters 1 and 2 illustrated the importance of antigen valency in directing the immune response. Indeed, the observation that low-valency SAgAs were most effective at tolerizing B cells and splenocytes stems from seminal work by Howard Dintzis. This determinant is a double-edged sword, however, as Dintzis taught us that on the other side of tolerogenesis is immunogenicity, brought on by high levels of antigen density. Reconciling this observation with the discrepancies

between simple and complex decoys, it seems that antigen valency may yet again be playing a critical role. Simple decoys consisted of a full surface saturation of autoantigen epitope, as the chemistry was carried out in excess. Conversely, complex decoys were ultimately fabricated with a half as much primary brain homogenate as gelatin, and the autoantigen epitope content within the heterogenous homogenate constitutes yet another vastly small fraction of total protein. While complex decoys were able to express some discrete epitope functionality that contributed to antigen-specific cell activation *ex vivo*, it is likely that the stimulatory threshold for cellular exhaustion was not met *in vivo*. As such, we must return to the single-epitope simple decoy system to investigate these claims. Future investigation into decoyed immunity should explore the role of autoantigen density for causing therapeutic effect. Much like valency was titrated in chapter 2, autoantigen conjugation should be discretely varied to evaluate constructs against EAE *in vivo*. We hypothesize that a threshold will become evident where autoantigen content lower in quantity will not protect against disease while higher loading will provide sufficient cellular exhaustion to prevent disease.

The step toward translating decoyed immunity in chapter 5 represents just one manifestation of extrapolating the success of the works in chapter 4. Simple decoys illustrate the power of engineered microenvironments in leveraging effect against the autoimmune response. The translation to complex decoys in chapter 5 strives toward accounting for the heterogeneity and polyclonality of human disease. While there is still promise for this platform with more intelligently-designed material properties, we may also be well-served to exploit immunological microenvironment engineering in alternate ways. One such avenue of interest could be to target the tissue compartment implicated in autoimmune destruction for delivering immunomodulatory factors to directly to instill an instructive depot at the site of inflammation where yet again, all

autoantigen epitopes are present. Advances in protein engineering have paved the way for opportunities such as the production of monoclonal antibodies consisting of specificities for regions such as the lesion microenvironment in multiple sclerosis or locales of islet destruction in type 1 diabetes. These specificities could be leveraged to deliver inhibitory factors or drugs to reestablish the microenvironment in a tolerogenic context to ultimately confer bystander effects and protection from disease.

The works presented in chapters 3 through 5 proceed in tandem and intuitively, however the lessons learned in chapter 2 provide the foundation for substantial future work within the SAgA platform as well. By elucidating that lower-valency conjugates (4-7 epitopes/backbone rather than 10) are most ideal for pursuing B cell anergy as a therapeutic mechanism, new research opportunities have emerged. To date, SAgAs have consisted of autoantigen grafted onto linear hyaluronan backbones. The utility of this material has been favorable the conjugation of arrays ranging from 10-20 ligands. However, taking to heart the low-valency design parameter outlined by chapter 2, new manifestations of these constructs can be ideated with similar size and solubility properties. Multi-armed polymers such as 4-arm poly(ethylene)-glycol backbones can provide a discrete number of functional handles for conjugation that overcomes heterogenous linear polymers in terms of scale-up manufacturability. Ongoing work around the SAgA platform may benefit from evaluating multi-arm configurations against classical linear ones to assess whether additional value may be grasped through adopting multi-dimensional backbones with similar molecular weights and hydrodynamic radii.